COPOLY(UREA-ISOCYANURATE)S AND THEIR HYBRID STRUCTURAL COMPOSITES FORMED BY REACTION INJECTION MOULDING, RIM

BY

XIAOQIU TAO

A Thesis submitted to
The University of Manchester / UMIST
for the degree of
Doctor of Philosophy
in the faculty of Technology

1993

Manchester Materials Science Centre

To my wife and parents

PUBLICATIONS

Various results and findings included in this thesis have been or will be published elsewhere. Details are given below.

1. Ryan, A. J.; Stanford, J. L; Tao, X., "Processing, Morphology and Properties of A Novel Matrix for Structural Reaction Injection Moulding, SRIM", *Eighth annual meeting of polymer processing society, PPS-8*, New Delhi, India, March 24-27, 1992.
2. Ryan, A. J.; Stanford, J. L.; Tao, X., "Supramolecular Structure and Properties of Rapidly Polymerised Isocyanurate-Based Copolymers", *4th European Polymer Federation Symposium on Polymeric Materials,* Baden Baden (Germany), September 27-October 2, 1992
3. Ryan, A. J.; Stanford, J. L.; Tao, X., "Morphology and Properties of Novel Copoly(ether-isocyanurate)s formed by Reaction Injection Moulding, RIM", *Polymer*, 1993, in press
4. Stanford, J. L.; Ryan, A. J.; Tao, X., "The deformation and fracture of structural composites formed by Reaction Injection Moulding", *2nd International Conference on Deformation and Fracture of Composites*, Manchester, UK, March 29-31, 1993
5. Stanford, J. L.; Ryan, A. J.; Tao, X., "Processing and properties of structural composites formed by Reaction Injection Moulding (SRIM)", Ninth annual meeting of polymer processing society, PPS-9, Manchester, England, April 5-8, 1993.
6. Tao, X.; Stanford, J. L., "Processing and properties of structural composites based on novel copoly(ether-isocyanurate)s formed by Reaction Injection Moulding, RIM", submitted to *Plastics, Rubber and composites Processing and Applications*, November, 1993.

DECLARATION

No portion of the work referred to in this thesis has been submitted in support of an application for another degree or qualification of this or any other university or other institute of learning.

ACKNOWLEDGEMENTS

The author would like firstly to thank his supervisor Dr. J. L. Stanford, and Dr. A. J. Ryan for their support, advice and guidance throughout the course of this work.

The author also wishes to thank all the technical staff at Manchester materials Science Centre whose hard work has mad this work possible. Particular thanks must go to Arthur Wilkinson, Adrian J. Birch and John Goodier for their assistance in operating the RIM equipment, Alan Jackson, Alec Redfern, Margaret Vernon for instruction with the preparation of laboratory equipment.

The author also wishes to thank British Council who funded this research under a TC award.

Finally, the author would like to express a special thanks to Xiao Hua Liu for her stalwart support, encouragement and unlimited patience.

ABSTRACT

Novel copoly(isocyanurate-urea)s, PUrI, have been produced by reaction injection moulding, RIM. The materials were formed from ≈ 2:1 weight ratio of polyisocyanate to amine-functionalised polyoxypropylene, POP, in the presence of an organic trimerisation catalyst (TMR), a quaternary ammonium carboxylate. Diamine- and triamine-POP, namely, D2000 and T5000 (M_n~2,000 and 5,000 g mol^{-1} respectively) were used and the polyisocyanate, Isonate M143, was based on 4,4'-diphenylmethane diisocyanate. In some cases an aromatic diamine chain extender, either 3,5-diethyltoluene diamine, DETDA, or methylene-bis-2,6-diisopropylaniline, MDIPA, was also used. Stoichiometric ratios, [NCO] / [NH_2], ranged from 7 to 30, and the reactant and mould temperatures used in RIM were 36 and 90 °C, respectively. Gel times were controlled by varying the catalyst concentration, and gel times as short as 5 s were achieved at 90 °C.

The kinetics of PUrI formation were monitored via an adiabatic temperature rise technique, and the data obtained were analysed using a specially developed kinetics model to give NCO fractional conversion-time profiles. Copolymerisation occurred via a two-step process involving rapid polyether-urea, soft segment (SS) formation followed by NCO-trimerisation to form a glassy polyisocyanurate, hard segment (HS) phase.

The morphologies and properties of the PUrI were studied using small angle X-ray scattering (SAXS), transmission electron microscopy (TEM), dynamic mechanical-thermal analysis (DMTA) and tensile stress-strain techniques. The RIM materials were stiff plastics with room-temperature Young's moduli between 1.5 and 0.7 GPa, and tensile strengths between 30 and 52 MPa, depending on morphology, and showed a SS glass transition temperature around -50 °C and a HS transition between 160 and 200 °C. Development of morphology is a result of competition between polymerisation kinetics, chemical gelation and (micro)phase separation. Diamine-based PUrI had isotropic, co-continuous morphologies with a size-scale of ≈ 100 Å and higher moduli than triamine-based PUrI which contained isolated glassy particles of ≈ 1μm.

Structural composites comprising a PUrI matrix and pre-placed mats of continuous-fibres were produced by RIM in cycle times of < 60 s. The mould temperature was 90 °C and SRIM composites were postcured at 150 °C for 1 hour. The matrix (D2/M/0.6), formed from M143 and D2000, showed the best combination of thermal and mechanical properties, and met the basic SRIM processing characteristic of low initial viscosity during mould filling, essential for minimising fibre mat movement whilst maximising mat penetration and fibre wetting by the PUrI reacting mixture. Various hybrid SRIM composites with fibre contents up to 40 % by volume were produced with single outer layers of unidirectional-fibre mats of either glass, carbon or Kevlar, and different numbers of inner layers of random-fibres of only glass.

SRIM composites were characterised using DMTA, linear thermal expansion, tensile stress-strain, interlaminar shear strength and single-edge notch (SENB) beam fracture tests. SENB fracture data were analysed using fracture mechanics to give values of K_{Ic} and G_{Ic}, which ranged, respectively, from 1.1 (matrix) - 10.0 MPa $m^{1/2}$ and 0.9 (matrix) -15.6 kJ m^{-2}. As expected, values of K_{Ic} and G_{Ic} parallel to the unidirectional fibre axes were greater than those perpendicular, and were greater for composites comprising outer plies of unidirectional glass rather than carbon.

Tensile properties varied with fibre volume fraction and fibre type. For example, hybrid composites comprising 6 % by volume of unidirectional carbon fibres and 26 % by volume of random glass fibres had unidirectional tensile modulus and strength values of 20 GPa and 260 MPa, respectively, at room-temperature and transverse values of 10 GPa and 174 MPa: the composite also showed excellent high-temperature behaviour with a modulus of 10 GPa at 200 °C. At a given volume fraction, tensile property data showed the modulus and ultimate elongation, parallel to the unidirectional fibre axes, to be determined mainly by the outer plies and to vary with fibre type, whereas the tensile strength varied only slightly. All of the tensile properties transverse to the unidirectional fibre axes were essentially independent of the outer plies and were determined by the inner random-fibre plies and the matrix. In general, experimental mechanical properties are shown to be in good agreement with those predicted by specially-modified composite theories.

Content

CHAPTER ONE

INTRODUCTION

1.1 Reaction Injection Moulding, RIM

1.1.1 Introduction

Reaction Injection Moulding, RIM, is a method for production of complex plastic parts directly from low viscosity monomers or oligomers [1]. These liquids are combined by impingement mixing just as they enter the mould. Solid polymer forms by cross-linking or phase separation and parts can often be demoulded in less than one minute.

RIM is quite different from conventional thermoplastic injection moulding (TIM) because it uses polymerisation, activated by the impingement mixing, in the mould rather than cooling to form a solid polymer. Fig.1.1 shows a schematic of RIM machine [1]. Two or more liquid reactants flow at high pressure, typically 100 to 200 bar (1500 to

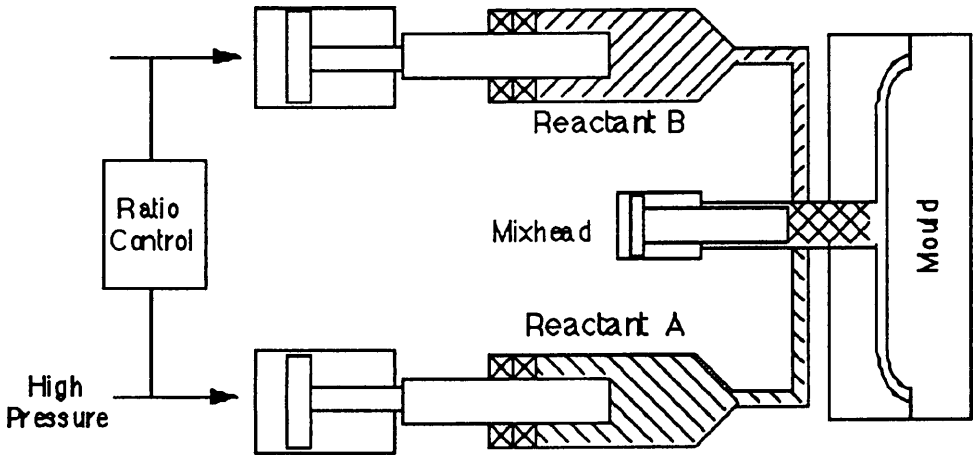

Figure 1.1 Schematic of a RIM machine [1]

3000 psi), into a mixing chamber. In the mix head the streams impinge at high velocity, mix and begin to polymerise as they flow out into the mould cavity. Because the mixture is initially at a low viscosity, low pressures, less than 10 bar are needed to fill the mould. The major reason for the growth of RIM is low viscosity during mould filling, which makes RIM different from thermoplastic injection moulding (TIM) (see Table 1.1[2]), and gives RIM several advantages (i) - (iii) over TIM in production of large moulding [3].

(i) Low energy consumption: Fig.1.2 shows the energy requirements to produce and to form various materials. Metal and many thermoplastics are energetically more expensive to produce than RIM polyurethanes [4].

(ii) Large part capability: Parts larger than 50 kg have already been produced via RIM [5]. TIM equipment to produce such parts would be cost prohibitive.

(iii) Low capital investment: Because RIM is a relatively low–pressure process, it utilises lower mould clamping forces and less expensive moulds.

Table 1.1 Comparison between typical RIM and TIM [2]

	RIM	TIM
Temperature: reactants	40 °C	200 °C
mould	70 °C	25 °C
Materials viscosity	0.1 - 1 Pa s	10^2 - 10^5 Pa s
Injection pressure	100 bar	1000 bar
Clamping force	50 ton / m^2	3000 ton / m^2

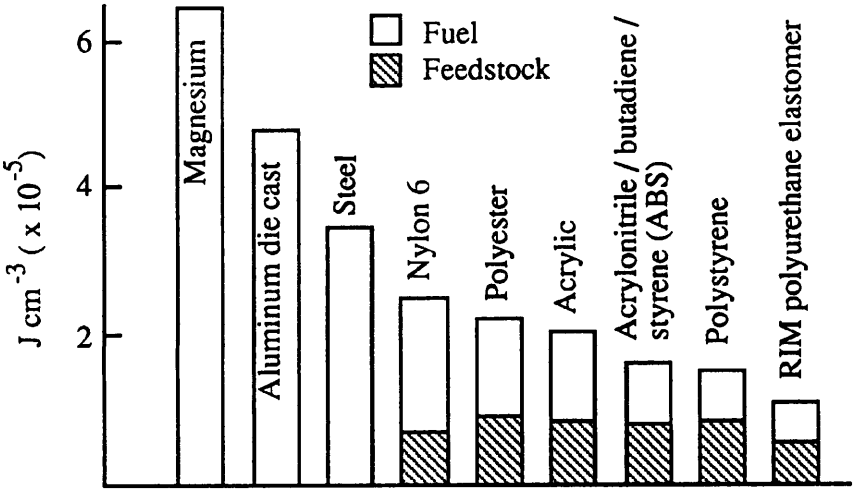

Figure 1.2 Energy consumption for the production and formation of several common engineering materials [4]

RIM may be broken into eight unit operations which are illustrated in Fig 1.3. Reactants are held in storage tanks under pressure, sometimes can be heated according to the formulation. The 'steady–state' conditions of temperature, pressure and reactant throughout

are achieved by means of high pressure metering (recirculation) of reactants through the mix–head (without impingement). In a shot cycle, mix–head design allows recirculation to be deverted to impingement, , and the metered mix and flow into the mould under low pressure, where they quickly polymerise and solidify sufficiently to withstand the stresses involved during demoulding.

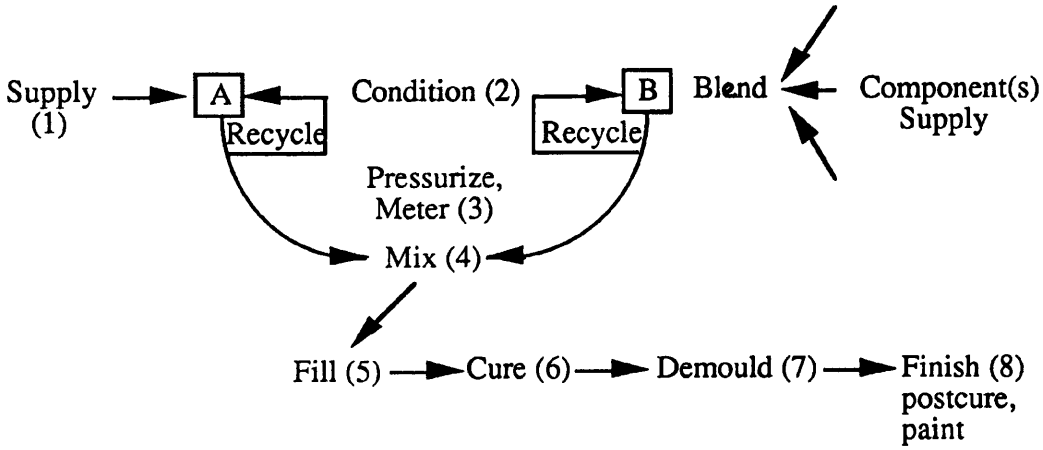

Figure 1.3 Schematic representation of the RIM process [1]

RIM developed from polyurethane rigid foam technology. Since the 1950's urethane elastomers and foam have been made by low pressure injection into flow–through rotating mixers. High pressure impingement mixing to produce urethane foams was first reported by Harries [6]. Pahl and Schluter [7] described the first RIM equipment with a self cleaning, recirculation mix-head. These machines were first used in Germany to produce integral–skin, rigid urethane foam for automotive and furniture [8-10]. Major growth of RIM was pushed by needs in the US automotive market. In 1972, Congress mandated the bumpers on all cars sold in the US withstand a 5 mile / hour impact without damage. Flexible polyurethane fascia on the front and rear of cars covering a steel beam mounted on shock absorbents were found to meet this requirement. RIM quickly proved the most economical way to make these large parts and production began in 1974. RIM production in the US grew from 2000 tons in 1974 to 17000 in 1978 [3]. Now there is a new trendency to develop Structural Reaction Injection Moulding composites, SRIM composites.

1.1.2 Impingement Mixing

High-jet velocity-impingement mixing, considered to be the heart of RIM process, differentiates RIM from other reaction moulding processes such as thermoset injection moulding or sheet moulding which are activated by heat transfer from hot mould walls. In RIM, polymerisation is activated by contact between reactants in the impingement mixing step, which frees RIM from heat transfer limitations making possible extremely fast moulding of large, thick, complex parts.

Despite its key role to RIM and considerable research, impingement mixing is still not well understood [1]. But due to the contribution of many researcher, such as Ranz [11], Fields, Thomas and Ottino [12], Wickert, Macosko, and Ranz [13], Machuga et al [14], the following model which contains the three main mechanisms active in impingement mixing has been generalised by Macosko [1] and is shown in Fig.1.4.

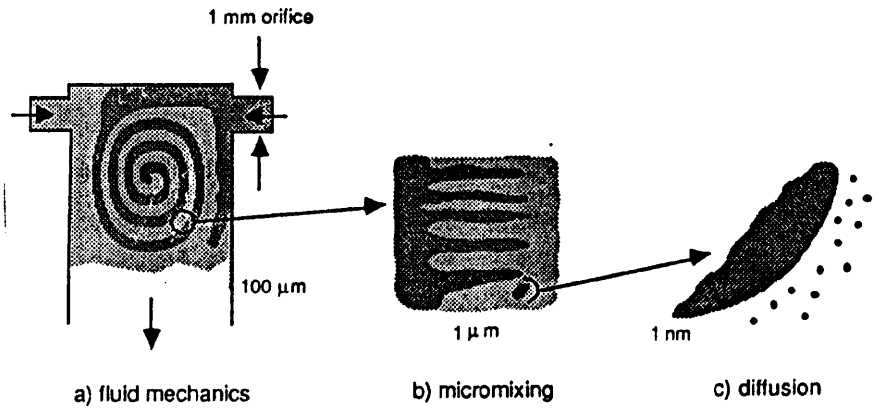

Figure 1.4 The three mechanisms active in impingement mixing of reactive liquids [1]

Thus, the fluid mechanics of impingement reduces the scale of segregation of reactants from the diameter of the inlet nozzles (1-3 mm) to a scale of the order of 100 µm in a manner independent of mix head design. Further reduction in scale results from fluid mechanical mixing during flow in combination with physiochemical effects at the interfaces between the two reactant streams. A pressure at the interface appear to drive one reactant rapidly into the other through tubules. The length of those tubules, and thus mixing is governed by reaction rate and the properties of resulting polymer (Fig.1.4b). Finally,

molecular diffusion takes over to bring all the components into molecular contact and near–complete reaction is eventually achieved.

1.1.3 Mixing–Head Design

The evolution of impingement mix–head design for RIM has been reviewed by Boden, Schulte and Wirtz [15]. Today all RIM mix–heads employ the following features:

(i) Recirculation of reactants near the mixing chamber to maintain temperature and dispersion and to permit rapid start up of mixing.

(ii) Rapid opening to control stoichiometry from start up of mixing.

(iii) Inlet nozzles or orifices which accelerate reactant jets to high velocity.

(iv) Chamber where streams impinge and initial mixing occurs.

(v) Some means to insure that the chamber is filled rapidly and proper impingement occurs from the beginning of shot.

(vi) Clean out piston to push all reactants out of the mixing chamber.

(vii) Some means to control the pressure in mixing chamber, and to obtain laminar flow of the discharged reaction mixture (Fig.1.5).

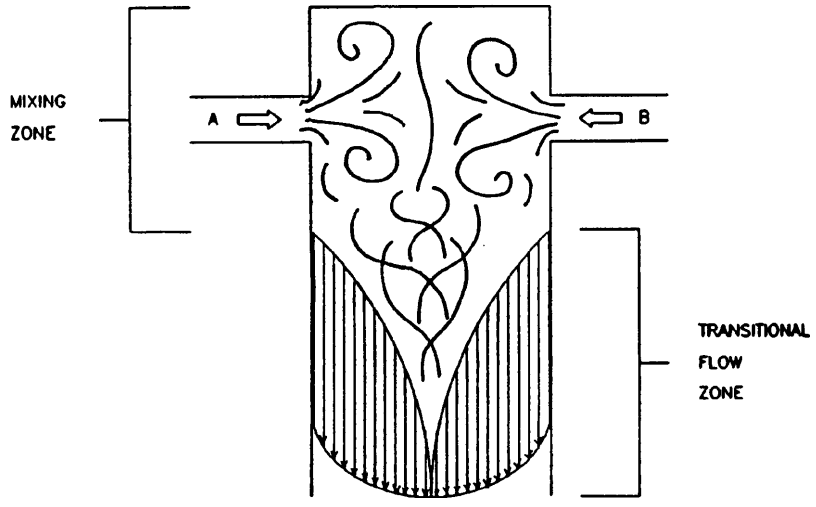

Figure 1.5 Schematic of flow patterns inside a RIM mix-head [18]

One of the first mix–head featuring recirculation and a remotely self–cleaning piston was that of the Krauss–Maffei design [16] shown in Fig.1.6. In recirculation mode reactant

flows through the grooves in the cleaning piston and back to the storage tanks. When the self–clean piston is retracted, reactants impinge in the mixing chamber. When the clean piston returns to its original position, impingement is interrupted and recirculation is re–established with the removal of residue material from the mixing chamber. In 1976, Krauss–Maffei patented [17] a twin piston design (Fig.1.7) which was aimed at improving throttling and smoothing over the earlier single piston mix–head (Fig.1.6).

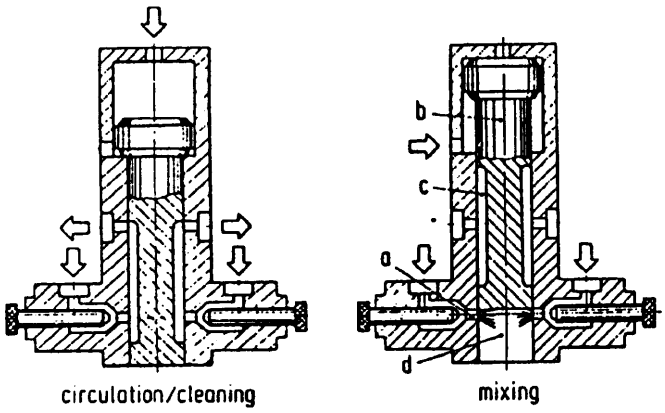

Figure 1.6 Krauss–Maffei mix-head [16]. In the closed or recirculation position, reactants recirculate through grooves (c) along the cylindrical clean-out piston (b). In the open position, reactants flow at high velocity through circular orifices (a), impinge in the chamber (d) and flow out to the mould cavity.

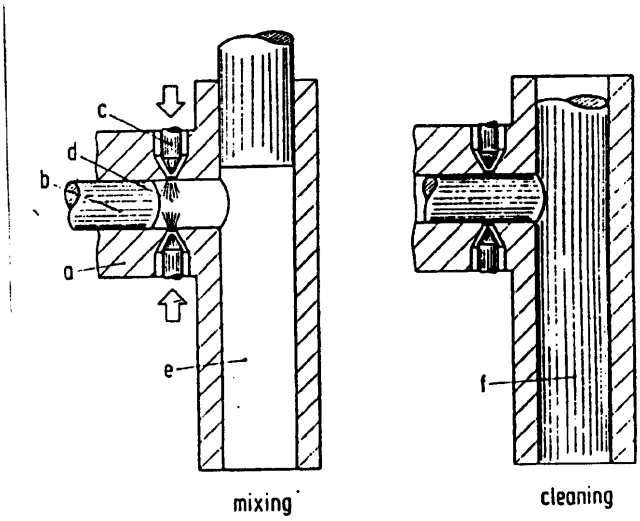

Figure 1.7 Schematic diagram of the Krauss–Maffei twin piston mix–head [15].
a. Mix–head. b. Control and mixing piston. c. Nozzle pintle.
d. Mixing chamber. e. Dispension chamber. f. Dispensing piston

Various designs of mix–head for mixing quality and exit flow properties have been investigated by Molnar and Lee [18]. They have classed the single piston design (Fig.1.6) as 'I' type, the right angled twin piston design (Fig.1.7) as the 'Long L' type, and an intermediate design with a smaller length mixing chamber as 'Short L' type. Glycerine and water were passed through simulated designs of mix–head, and the results are shown in Fig.1.8. The 'I' type was shown to give turbulent exit flow (poor smoothing) from the mix head (Fig.1.8a), while this flow was improved to laminar in the 'Long L' design (Fig.1.8c).

1.1.4 Mixing Quality

To achieve good mixing, intimate molecular contact must be occurred among the reactants. Mixing quality is normally assessed by visual inspection of a moulded part. If the polymer in the runner area is 'sticky or stringy', then poor mixing happens. The point at which efficient mixing occurs is usually considered to be at the onset of turbulent flow of both impingement streams. In general terms, the definition of turbulence for a liquid under flow is given when its Reynolds number, Re, the ratio of inertial to viscous force [19] reaches a critical value, Re_{crit}. There is no universal value of Re_{crit} for RIM and its value is dependent on a number of factors, including the specific properties of the chemical system and geometrical design of mix–head[20] Over the past decade there have been a number of semiquatitative studies investigating values of Re_{crit} for specific polyurethane [18] and polyurea [21–23] system, and there are a few studies investigating values of Re_{crit} for specific polyurea system [24]. But there is no report of Re_{crit} for copoly(isocyanurate–urea)s (PUrI).

1.1.5 RIM Reaction Kinetics

Commercial feasibility dictates that during RIM, the bulk copolymerisation must progress at a rate which allows polymer structure to develop sufficiently for a part to be demoulded with one minute [1]. The study of RIM reaction kinetics will be helpful to relate the development of polymer molecular weight to time and to temperature in the mould, with structure changes due to cross-linking and / or (micro) phase separation.

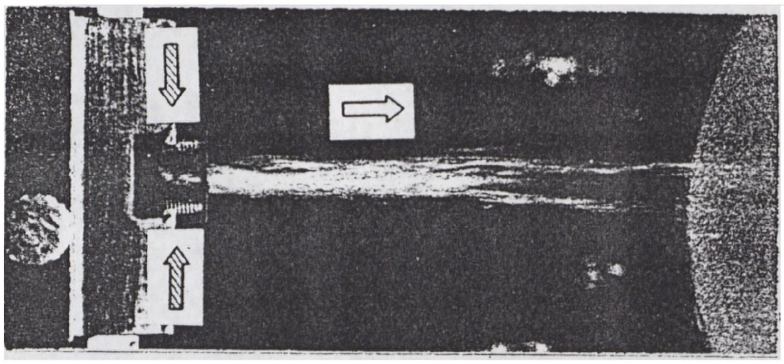

a)

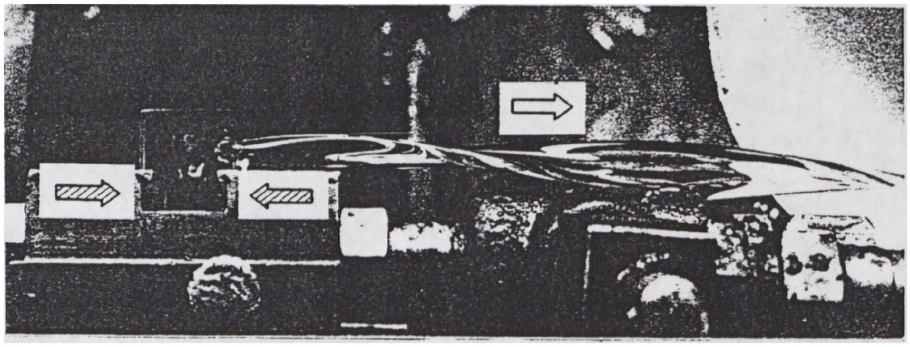

b)

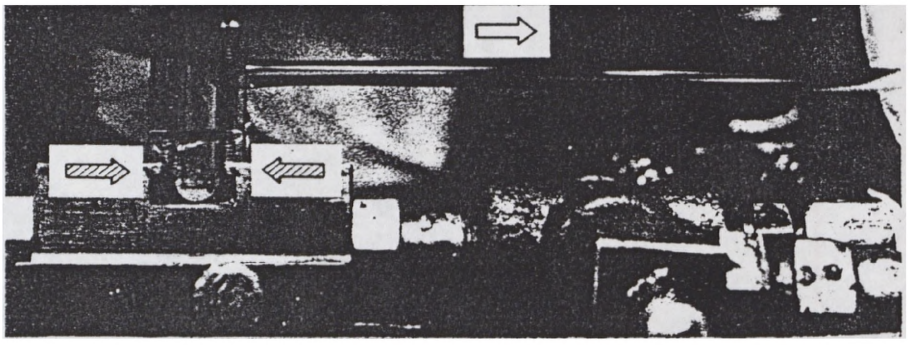

c)

Figure 1.8 Flow from the mix-head outlet of a glycerine-water mixture at Re = 100 (Re is Reynolds number of liquid flow, the ratio of inertial to viscous force [19]) for (a) I shape, (b) short L shape, and (c) long L shape mix-heads [18]

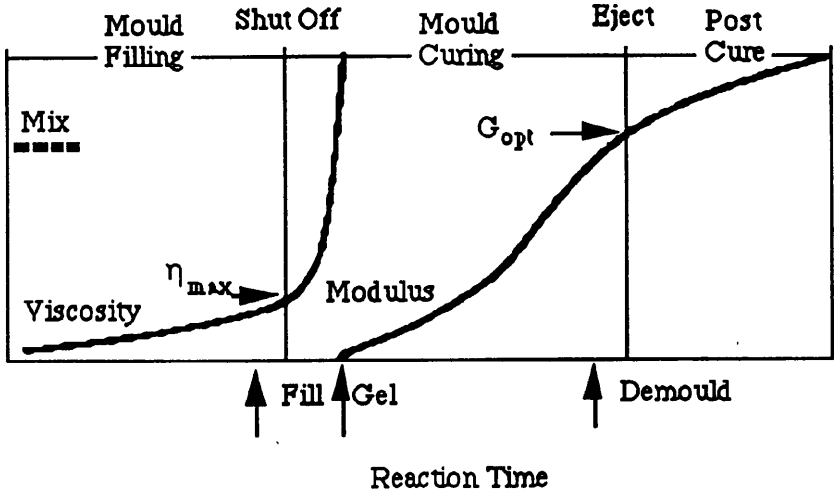

Figure 1.9 Rheological changes during a RIM cycle [1]

These structural changes result in the rheological variations shown in Fig.1.9 [1], and determine mould filling and curing of the polymer during the RIM process. During mould filling, the lower the viscosity of the reactants, the better. But following the mould filling step, very rapid gelation or solidification should occur, at which point the viscosity becomes infinite, to develop enough strength and modulus for quickly demoulding.

Several kinds of methods can be used to monitor RIM reaction kinetics. Fourier transform (FT) IR [25], which is an indirect method of monitoring end-group concentrations, is capable of monitoring several changes simultaneously, making it much more suitable for kinetic data acquisition during fast, bulk polymerisations [26-32]. Calorimetric methods, involving the measurement of the heat of reaction, are cruder but simpler than FTIR in both experimental technique and data analysis. The adiabatic temperature rise, ATR, technique [1,33] is particularly suited to monitoring the RIM reaction kinetics. ATR has been used to monitor the kinetics of bulk polymerisations including cross-linking polyurethanes [34,35], phase–separating, linear [35-37] and non-linear [35,38] copolymers, and poly(urethane–isocyanurate)s [39]. In addition, ATR has been used to judge the relative reactivities [40] and reaction kinetics of model compounds [41] in solution.

1.2 RIM Polymers

1.2.1 Basic Isocyanate Reaction

Isocyanate groups react easily with compounds which containing active hydrogens, i.e. a hydrogen which is replaceable by sodium. The reactivity of the isocyanate group is mainly determined by the pronounced electrophilic character of the C atom, further enhanced by conjugation with aromatic residence (R = Ar) as shown in chemical reaction equation (1.1).

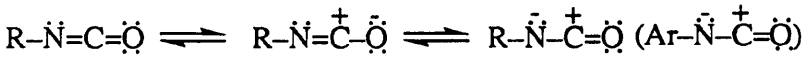

$$R\text{–}\dot{N}\text{=}C\text{=}\ddot{O} \rightleftharpoons R\text{–}\dot{N}\text{=}\overset{+}{C}\text{–}\overset{-}{\ddot{O}} \rightleftharpoons R\text{–}\overset{-}{\dot{N}}\text{–}\overset{+}{C}\text{=}\ddot{O}\ (Ar\text{–}\overset{-}{\dot{N}}\text{–}\overset{+}{C}\text{=}\ddot{O}) \qquad (1.1)$$

So electron withdrawing substituents in ortho- or para- positions in an aromatic ring increase the reactivity of the NCO group, whilst electron donating substituents lower its reactivity. Reviews on the reactions of isocyanates have been given by several papers [42-48]. Following are some of the important reactions used in RIM, which involve the isocyanate group and,

(a) alcohols to form urethanes,

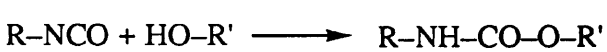

$$R\text{–}NCO + HO\text{–}R' \longrightarrow R\text{–}NH\text{–}CO\text{–}O\text{–}R' \qquad (1.2)$$

(b) amines to form ureas,

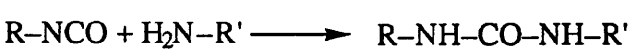

$$R\text{–}NCO + H_2N\text{–}R' \longrightarrow R\text{–}NH\text{–}CO\text{–}NH\text{–}R' \qquad (1.3)$$

(c) urethanes to form allophanates,

$$R''\text{–}NCO + R\text{–}NH\text{–}CO\text{–}O\text{–}R' \longrightarrow R''\text{–}NH\text{–}CO\text{–}N(R)\text{–}CO\text{–}O\text{–}R' \qquad (1.4)$$

(d) urea to form biuret.

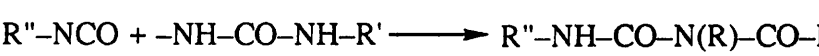

$$R''\text{–}NCO + \text{–}NH\text{–}CO\text{–}NH\text{–}R' \longrightarrow R''\text{–}NH\text{–}CO\text{–}N(R)\text{–}CO\text{–}NH\text{–}R' \qquad (1.5)$$

Reactions (1.4) and (1.5) result in cross-linking, but their rates are at least 100 times slower than those (reactions (1.2) and (1.3)) needed for RIM [41].

(e) Isocyanates react with water to form a carbamic acid, which is unstable and decomposes to an amine and CO_2. The amine then react with another isocyanate group to form a urea.

$$R\text{–}NCO + HOH \rightarrow R\text{–}NH\text{–}CO\text{–}OH \rightarrow RNH_2 + CO_2 \rightarrow R\text{–}NH\text{–}CO\text{–}NH\text{–}R \quad (1.6)$$

This reaction is important for the formation of low density of PU foam, but is unwanted in RIM.

Isocyanates also undergo self–condensation or addition reactions. Three of the most important of these reactions are

a) Dimerization

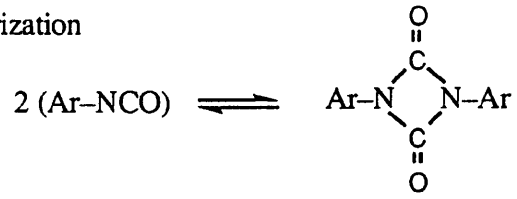

(1.7)

b) Trimerization

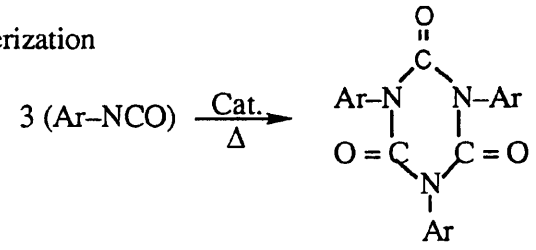

(1.8)

c) Uretonimine Formation

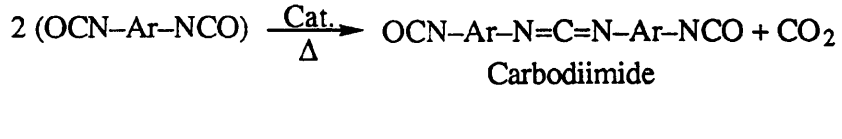

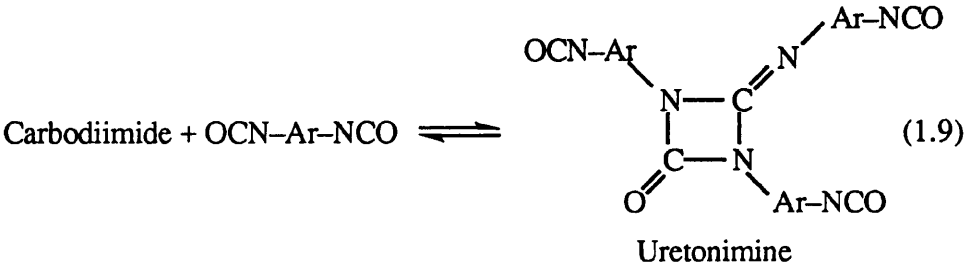

(1.9)

Dimer formation (1.7) is reversible, with dissociation being favoured at elevated temperatures. Isocyanurates are stable to much higher temperatures, and are used in some

RIM formulations to improve the thermal stability and mechanical properties of RIM products and are used as a matrix materials for SRIM [39, 49-57]. There are, however, no reports of PUrI used as matrix materials for SRIM composites.

1.2.2 Polymerisation to Form Segmented Block Copoly(urea-isocyanurate)s

RIM copolyureas are segmented copolymers, in which morphological structure, and consequently the properties, develop via (micro) phase separation of the constituent polymer blocks. The two phase, $[AB]_n$ type of RIM–copolymers is formed by the reaction of a diisocyanate with both of the following species:

(i) an amine-functionalised, high molecular weight prepolymer, usually a polyether, to form the soft segment (SS) oligomer.

(ii) a low molecular weight aromatic diamine (chain extender) to form the aromatic urea hard segment (HS) oligomer.

The RIM copoly(urea-isocyanurate)s (PUrI) are more complex due to another polytrimerisation of diisocyanates. These reactions are initiated during the impingement process of RIM. However the reaction of forming SS is much faster than the reaction of forming HS [58], which, in turn, is faster than polytrimerisation, which need a trimerisation catalyst. The low molecular weight aromatic diamine which reacts with the diisocyanate to form polyurea hard segment, is called a chain extender because in early polyurethane process the low molecular weight diol (equivalent to the aromatic diamine for polyurea) was added in a second, chain–extension step after prepolymer formation between the SS–prepolymer and excess isocyanate had occurred [4, 59].

The soft segment is so called since it is typically a soft rubber above its glass transition temperature, Tg^S, at room temperature, and is one of the phases in a PUrI. The hard segment sequences, however, are typically amorphous and glassy, well below their glass transition temperature, Tg^H, at room temperature, and together with polyisocyanurate, form another hard block phase, which is incompatible with the SS phase. The (micro) phase separation of the two phases is incomplete, and the two-phase morphology obtained, which dominates the physical properties of RIM PUrI, is influenced by the nature and

degree of (micro) phase separation as well as the chemical structure of the hard and soft segments. This will be fully discussed in Chapter 3.

1.2.3 RIM Precursors

1.2.3.1 Polyisocyanate

The most of RIM formulations are based on liquid variants of diphenylmethane diisocyanate, MDI. Crude MDI is a liquid mixture of 4,4'– and 2,4'– isomers and higher functionality methylene–bridged polyphenylene polyisocyanates in the ratio 40% : 2% : 58% respectively, and has a functionality ~2.7 [4]. Generally, it is not used directly in RIM since it leads to chain branching and cross-linking which inhibits phase separation.

MDI is synthesised from aniline. Firstly, aniline react with aqueous formaldehyde to form a mixture of condensation products, then isomerisation at 90 - 100 °C and washing with aniline give a mixture of amine functionalised chemicals. Phosgenation [60] of the amine mixture in chlorobenzene solution is carried out in two stage process to yield crude MDI. Phosgenation involves a cold and hot stage as follows:

Cold Stage (about 40 °C)

$$RNH_2 + COCl_2 \longrightarrow R\text{–}NH\text{–}COCl + HCl \qquad (1.10)$$

$$RNH_2 + HCl \longrightarrow R\text{–}NH_2\text{–}Cl \qquad (1.11)$$

$$RNH_2 + RNHCOCl \longrightarrow R\text{–}NH_2HCl + RNCO \qquad (1.12)$$

Hot Stage (about 100 °C)

$$R{=}NH_2HCl + COCl_2 \longrightarrow RNCO + 3HCl \qquad (1.13)$$

During the cold stage the amine hydrochloride and isocyanate are insoluble, inhibiting the reaction of the isocyanate with the amine. The reaction mixture is then heated to about 100 °C to convert the amine hydrochloride to isocyanate.

Crystallisation of crude MDI gives pure 4,4' MDI as a white crystalline solid (m.p. around 42 °C). Pure MDI dimerises at room temperature and this dimerisation can be inhibited by storing the material below –30 °C as solid or above 50 °C as a liquid.

Two routes are used to form low functionality, low viscosity modified MDI [61, 62]. One is the carbodiimide / uretonimine modification. When isocyanates are heated to between 150 and 300 °C, or to around 100 °C in the presence of phospholene oxides, carbodiimides are spontaneously formed.

$$2OCN\text{–}R\text{–}NCO \longrightarrow \underset{\text{Carbodiimide}}{OCN\text{–}R\text{–}N{=}C{=}N\text{–}R\text{–}NCO} + CO_2 \qquad (1.14)$$

Carbodiimide reacts further with isocyanates to form uretonimine.

A mixture of 15 mole % uretonimine with 85 mole % pure MDI forms a eutectic liquid mixture (about 0.2 Pa s at 25 °C) with a functionality of 2.1, such as M143 Isonate. The another route to liquified MDI modification is the formation of urethane or prepolymer modified MDI by vast excess of MDI reacting with a low molecular weight diol such as di– or tri–propylene glycol. These prepolymer modified MDI variants have a functionality of 2.0, but relatively high viscosity (about 1.0 Pa at 25 °C) due to hydrogen bonding between urethane groups and increased molecular weight. Gills et al [61] have investigated the effect of liquid MDI variants on the physical properties of RIM-PU. Using non–linear, uretonimine–modified MDI resulted in increased modulus, tensile strength and thermal stability, but using prepolymer modified MDI gave superior tear resistance and ultimate tensile strain. Blends of the uretonimine and prepolymer MDI, which allow choosing viscosity and functionality depending on the processing and material application requirements.

1.2.3.2 Soft–Segment Prepolymers

Polyoxypropylene, POP, soft–segment is most widely used in current RIM formulations. This low-cost polyether polyol is available in large quantities with wide range of molecular weights (200 to 6000 g mol^{-1}) and functionality (1 to 6) [63].

The polymerisation of propylene oxide is carried out anionically in solution. In the presence of strong base, the initiator, usually glycerol or trimethyl propane for triols, or propylene glycol or dipropylene glycol for diols, is heated at about 100 °C in a vacuum, to form the corresponding alkoxide ion and to evaporate the water,

$$ROH + KOH \longrightarrow RO^{-}K^{+} + H_2O \qquad (1.15)$$

Primary or secondary alkoxide ions may be formed from propylene oxide, since nucleophilic attack may occur at one of two sites on the non–symmetrical molecule. However, the attack at the primary carbon occurs preferentially by a factor of 20:1 [64] leading to a backbone with mainly head-to-tail units. As a consequence, the terminal hydroxyl group is usually a secondary one.

The formation of the less reactive (towards isocyanate) secondary hydroxyl groups in the polymerisation of propylene oxide is a disadvantage in terms of RIM-PU and PUU materials. However, this is usually overcome by capping the secondary hydroxyl tip with further polymerisation of ethylene oxide to provide about 80% primary hydroxyl termination [65].

For use in RIM–polyurea formulations the mainly secondary hydroxyl terminated POP is aminated by reaction with ammonia and hydrogen in the presence of nickel oxide catalyst at 900 °C and 200 atm [66]. The reaction rates of aliphatic amines with aromatic isocyanates is approximately 10 000 times greater than the rate of secondary hydroxyl groups with aromatic isocyanates.

1.2.3.3 Chain Extenders

Early RIM–PU systems used 1,4-butane diol, BDO, as chain extender in formulations with a primary hydroxyl–tipped POP diol and MDI [67-69]. BDO has been replaced by ethylene glycol, EG, which gives RIM–PU with higher application temperatures.

The advent of aromatic diamines has resulted in the production RIM-PUU [20, 70-72] and RIM-PUr [73-76] materials with improved physical properties. Diethylene toluene diamine (DETDA) is the most commercially important chain extender for RIM-PUr materials at present [1]. Its use in RIM first disclosed by the Bayer company [77]. DETDA is commercially available as an 80:20 mixture of the 2,4- and 2,6-isomers, and is manufactured by the alkylation of toluene diamine. Claims [41] have been made that the amino group in the 4 position of DETDA is more sterically hindered than the amino group in the 2 position, thus affecting reactivity. Any diamine developed for RIM diamine extender must meet certain criteria such as:

(i) proper reactivity towards isocyanate

(ii) solubility in polyamine

(iii) low toxicity

(iv) low price and good availability

(v) good physical properties in the RIM product

In order to increase the time for mould filling, diamine chain extenders with much less reactivity than DETDA have been developed. Nissen and Markovs [78] determined the reactivity of a variety of diorthoalkylmethylenebisanilines using a reaction exotherm technique in DMSO solvent to compare with DETDA in an attempt to identify a chain extender of reactivity suitable to RIM. Methylene bis–diisopropylaniline (MDIPA) having a reactivity of almost half that of DETDA was selected for PUU and PUr materials. Copolyureas containing MDIPA have been shown to have comparable physical properties to equivalent DETDA extender materials [79].

1.3 Structure–Property Relationships

1.3.1 Phase Separation Phenomena

RIM copolymers are loosely classed as (AB)n segmented block copolymers. The alternating blocks consists of hard glassy or crystalline segments and soft rubbery segments which are to some extent incompatible within each other, forming a two phase morphology

via a (micro)phase separation process. The physical properties of these materials are determined by the nature and extent of the morphological phase structure as well as the chemical nature of the copolymer formed and its processing conditions. The phase-separated nature of polyurethane block copolymers was first reported in 1966 by Cooper and Tobolsky [80] after examining the reasons for an unusually high modulus above Tg of their materials. The degree of (micro)phase separation which occurs during RIM copolymerisation is not only dependent on the dynamic incompatibility of the developing segments, but also on the reaction kinetics. If the copolymerisation is much faster than the rate of (micro)phase separation, then high molecular weight copolymer will form, leading to solidification before phase development has begun, further slowing down the rate of (micro)phase separation. If, however, the rate of copolymerisation is much slower than that of (micro)phase separation, hard block sequences can precipitate ((micro)phase separate) removing functional groups from the reaction mixture, therefore creating stoichiometric imbalances and hence limiting the development of molecular weight. Thus, due to the competitive kinetics of the RIM reaction, the two phase morphology developed in copolymers are seldom at equilibrium [81], and can often be easily modified by annealing [79, 82, 83].

1.3.1.1 The Thermodynamics of Phase Separation

The driving force for (micro)phase separation to occur in a RIM–copolymer system is the difference in solubility between the hard and soft blocks. In an attempt to explain this statement, the following description briefly reviews the thermodynamics of phase separation in polymer solutions and blends and (micro)phase separation in block copolymers. RIM copolymers can only be defined as ideal (AB)n block copolymers in the special case of complete reaction [84], which is not usually achieved. Instead, RIM materials are a complex mixture of homopolymers, free monomer and AB–type block copolymers.

Flory [85] and Huggins [86] originally proposed a liquid–lattice model which allow the entropy (ΔS_m) and enthalpy (ΔH_m) of mixing for polymer solutions to be calculated.

$$\Delta S_m = - k(N_1 \ln \phi_1 + N_2 \ln \phi_2) \tag{1.16}$$

$$\Delta H_m = \chi_{1,2} k T N_1 \phi_2 \tag{1.17}$$

where k is Boltzmann's constant, N_1 and N_2 are the number of solvent molecules and polymer chain segments and ϕ_1 and ϕ_2 their respective volume fractions. $\chi_{1,2}$ is the interaction energy per solvent molecule or chain segment and is commonly termed the Flory–Huggins interaction parameter. In general, thermodynamic considerations in the area of phase separation are often limited to the qualitative statement that the Gibbs free energy of mixing ΔG_m must be positive for phase separation to occur, that is, thermodynamic instability of the mixed state. Thus,

$$\Delta G_m = \Delta H_m - T \Delta S_m > 0 \tag{1.18}$$

and $\Delta G_m = 0$ determines the boundary between stable and unstable states, assuming the absence of specific interaction, such as hydrogen bondings. By substituting ΔH_m and ΔS_m from Eq (1.16) and (1.17) into Eq(1.18) and redefining the result in terms of hard (H) and soft (S) segments of a RIM copolymer gives

$$\Delta G_m = R T (N_H \ln \phi_H + N_S \ln \phi_S + N_H \phi_S \chi_{HS}) \tag{1.19}$$

In addition, the Flory–Huggins theory assumes $\chi_{1,2}$ to be independent of concentration and inversely dependent on temperature. However, in order to predict the behaviour of real polymer systems using Eq (1.19), it is required that an empirical temperature and concentration–dependent $\chi_{1,2}$ be used [87].

In fact, ΔG_m being positive is not a sufficient criteria for phase separation to occur, and the second derivative of free energy being zero defines the stability limit in terms of the free energy curve. Fig.1.13 illustrates a series of ΔG_m versus volume fraction HS curves at different temperatures for a binary mixture. Figs 1.14 and 1.15 show plots of ΔG_m and the second derivative $\partial^2 \Delta G_m / \partial^2 \Delta \phi_H$, respectively, versus volume fraction for binary mixture at a series of temperature, $T_1 < T_4$. The locus of the minima with common tangency (in

Fig.1.13) define the binodal or co-existence curve, represented as the solid line in Fig.1.15. This curve defines the composition of phases whose chemical potentials are equal and therefore would be in equilibrium if a phase separation process occurred.

The locus of the points at which $\partial^2\Delta G_m / \partial^2\Delta\phi_H = 0$ (in Fig.1.14) define a curve called the spinodal represented by dashed line. The phase diagram shown in Fig.1.15 illustrates a binary polymeric mixture with $\phi_H = \phi_S = 50\%$ and $N_H = N_S$. The maximum of the spinodal and binodal curves define the critical point (Tc, ϕ_{HC}). Above the coexistence curves (binodal) mixtures of species will be stable as a single homogeneous phase. Below the spinodal, such a homogeneous system is the thermodynamically unstable and must phase separate into an energetically more favoured state. The area between the binodal and spinodal curves is called the metastable region, in which phase separation will only occur if the energy barrier for the formation of nuclei is overcome. The chain length of the individual component polymers has an enormous effect on the phase diagram [88] and if the chain lengths of the two components are dissimilar, then the phase diagram will no longer be symmetrical. Experimental investigations [89] of the properties and phase behaviour of

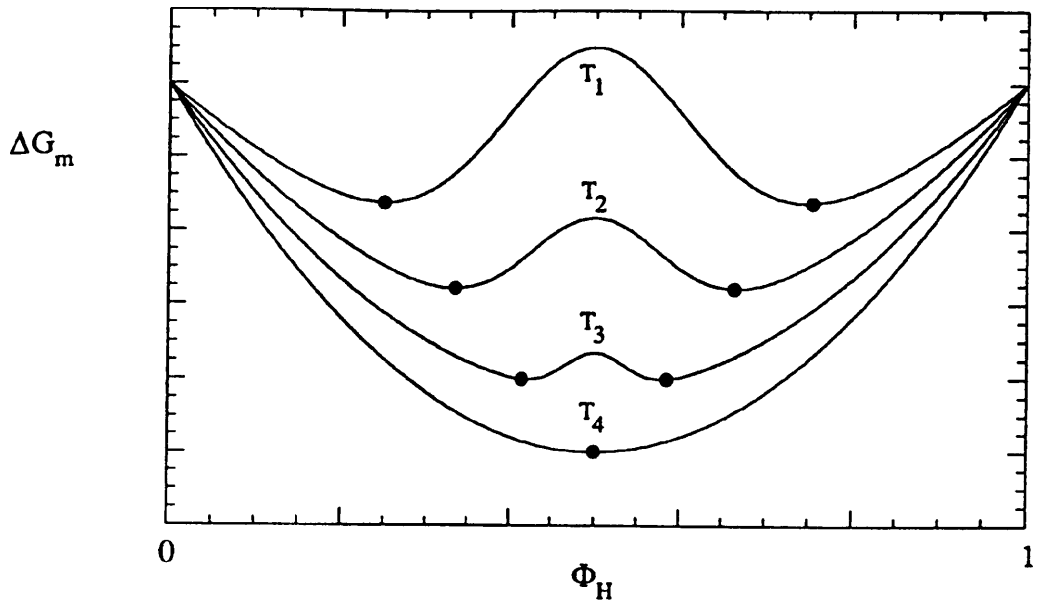

Fig.1.13 A series of ΔGm versus volume fraction of hard segment curves at different temperatures for a binary mixture, where $T_1 < T_4$ [63]

block copolymer / homopolymer blends have shown them to be extremely complex with several (micro)phase- and (micro)phase-separated and disordered (homogeneous) states. presumably the phase behaviour of RIM materials is even more complex due to their non–ideal (AB)n nature, thus discussion of their (micro)phase separation normally utilises simple, schematic phase diagrams [81].

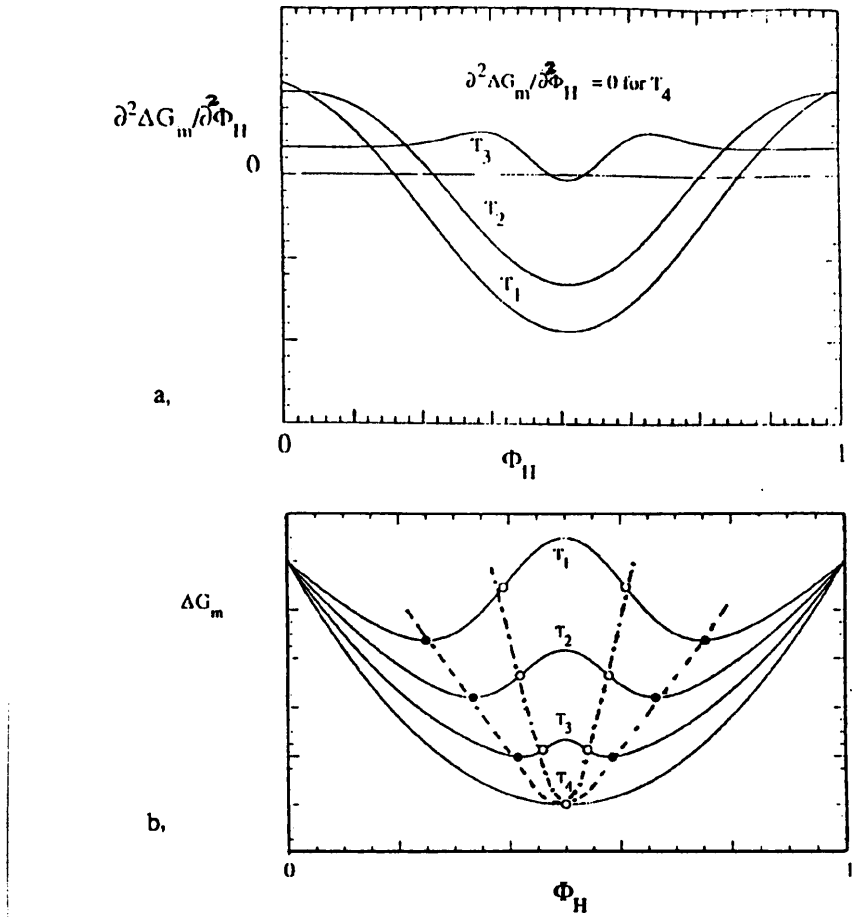

Figure 1.14 (a) $\partial^2\Delta Gm/\partial^2\phi_H$ versus fraction (ϕ_H) for a binary mixture at different temperatures T1 < T [63]
(b) ΔGm versus ϕ_H at different temperatures T1 < T4, showing the binodal and spinodal curves [63]

1.3.1.2 Mechanisms of Phase Separation

A generalised phase diagram for a polymer mixture is given in Fig.1.16. Conventionally the abscissa is the composition of the system and the ordinate temperature and/or reciprocal χN, where N is the degree of polymerisation ($N = N_H + N_S$). A system

position in phase diagram may be changed by temperature quenching or an increase in N (polymerisation).

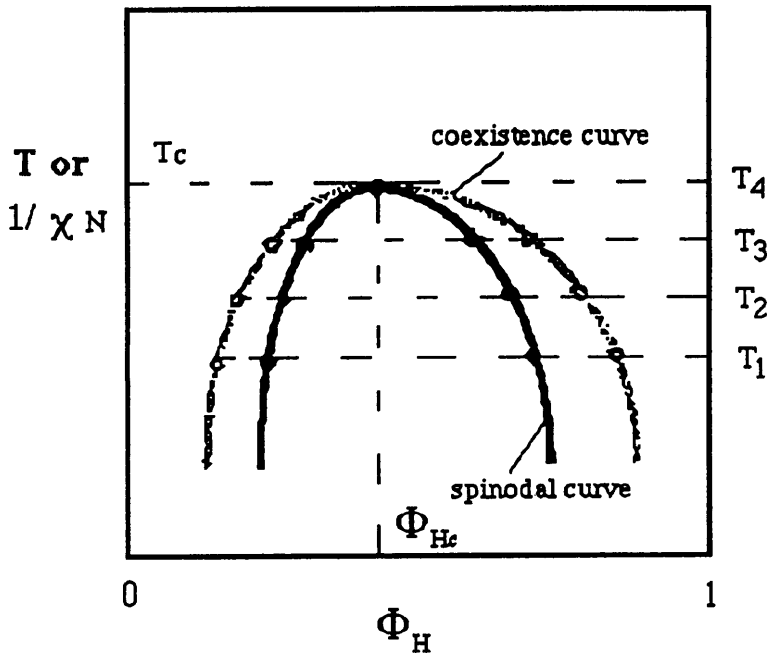

Figure 1.15 Phase diagram of temperature versus phase composition for a binary mixture [90]

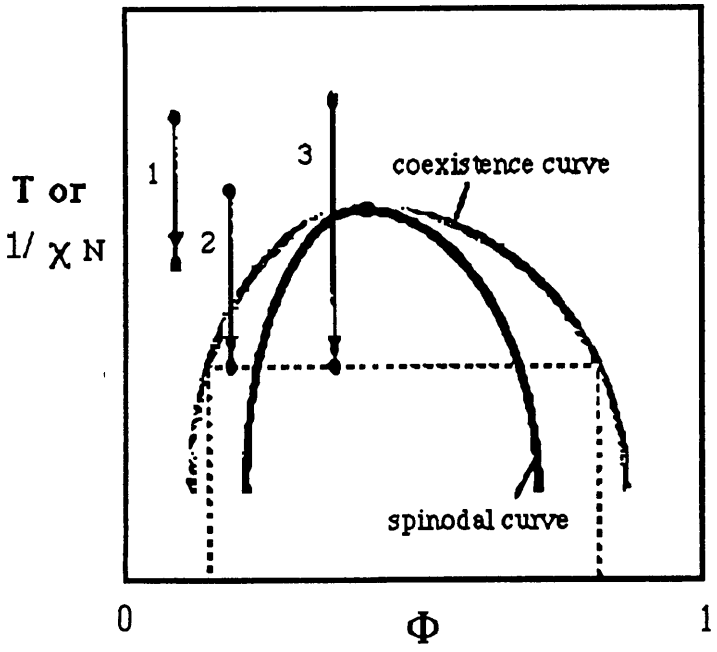

Figure 1.16 Generalised phase diagram for polymer mixture [90]

Three quenching (or polymerisation) processes are shown in Fig.1.16.

1. From a position in one–phase space to another in one –phase space; thus no phase change.

2 From a position in one–phase space to a position in the metastable region; phase separation may occur by nucleation and growth.

3 From a position in one–phase space to a position in the unstable region; phase separation must occur by a process of spinodal decomposition.

Hence depending on the composition of the system and the depth of quench or extent of polymerisation, one of two phase separation processes, I and II, may occur, and these are discussed in more detail in the following sections.

I Nucleation and Growth

Nucleation is the process of generating, within a metastable 'mother' phase, the initial fragments of a new, more stable phase. The formation of these initial fragments, or nuclei, requires an increase free energy of the system, resulting from undercooling into the binodal region. Once the energy barrier for phase separation has been overcome by the formation of nuclei, randomly in time and space, these nuclei grow into a separate phase fed by the metastable mother phase. The formation of new phase reduces the concentration of the mother phase in the immediate vicinity. Thus. the molecules or chain segments that feed the growth of the new phase diffuse from the unaffected region of the mother phase into the depleted volume. This so-called downhill diffusion process is shown schematically in Fig.1.17.

The early stages of phase separation by nucleation and growth are characterised by a continuous-phase / dispersed-phase morphology. The final sizes of the dispersed phase and the distance between them depend on the rate of nucleation, the rate of diffusion and the time available for growth. In RIM copolymerisation, the diffusion rate may be slowed by increasing viscosity on formation of high molecular weight early in the reaction, but increased by the reaction exotherm which would also decrease the rate of nucleation. In

addition, the time available for (micro)phase separation may be limited by the onset of hard segment vitrification.

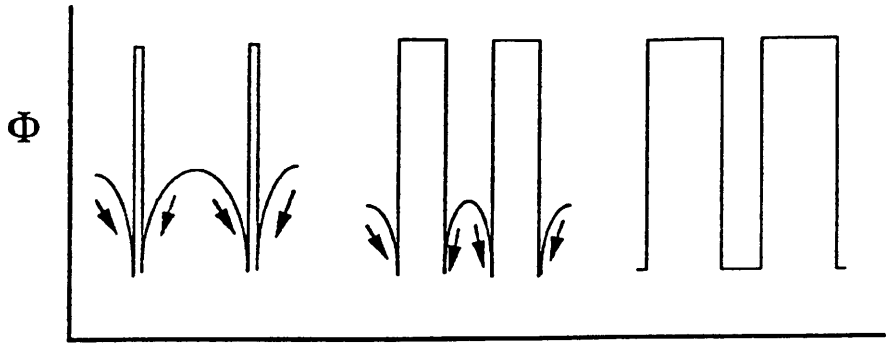

One-dimensional evolution of concentration profiles

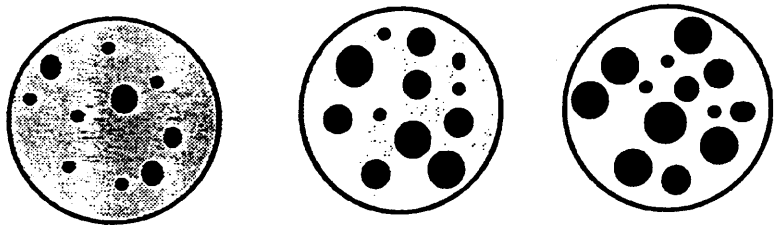

Two-dimensional representation of the resultant phase structure

Figure 1.17 Schematic representation of the nucleation and growth process [81]

II Spinodal Decomposition

The spinodal decomposition process is shown schematically in Fig.1.18, quenching from an initial state in one–phase space to final state in the unstable region, represented by case 3 in Fig.1.16. Spinodal decomposition is a kinetic process which generates a continuous growth of a separate phase. This growth originates from small amplitude fluctuations in density within an unstable mother phase. These fluctuations are stable about the mean composition in a stable region. However, on quenching into the unstable region the amplitude of these compositional fluctuations increases in a continuous manner. The phase that is richer in species A tends towards pure A and the phase richer in species B tends towards pure B, by diffusion against the concentration gradient. Thus phase separation occurs by a process called uphill diffusion. The decomposing system is characterised in the early stages of development by a co-continuity of the phases. However, this feature may be

lost at a later stage as the system seeks to minimise free energy by reducing interfacial area. As a consequence, this would lead to a continuous / dispersed morphology. It has been proposed [81,90] that during RIM copolymerisations, spinodal decomposition can result in a co–continuous morphology due to the vitrification of the HS phase during the early stages of (micro)phase separation.

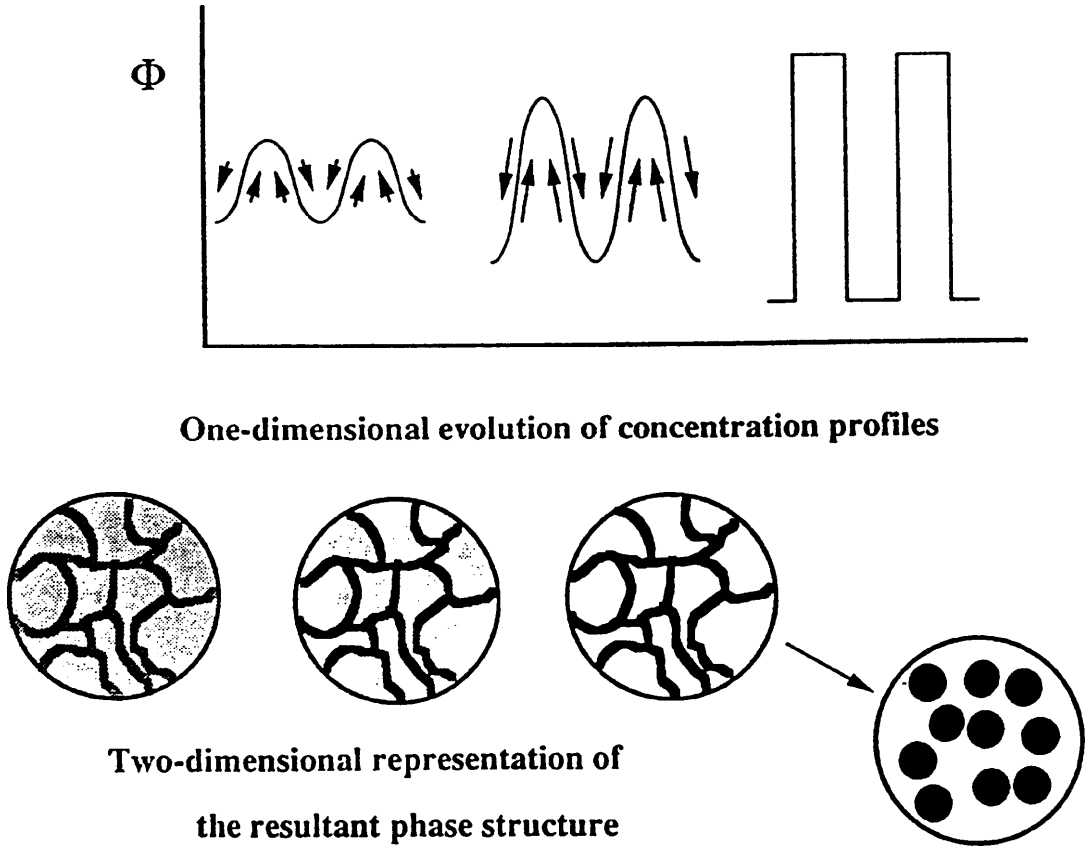

Figure 1.18 Schematic illustrations of the spinodal decomposition process [81]

1.3.2 Effects of Phase Separation on Physical Properties

The physical properties of copolymers is greatly effected by the two phase morphology from a (micro)phase separation process. Fig.1.19 schematically shows the effect of phase separation on modulus–temperature curve for a linear 50:50 block copolymer which comprises hard and soft segments with glass transition temperatures, Tg^H and Tg^S, respectively.

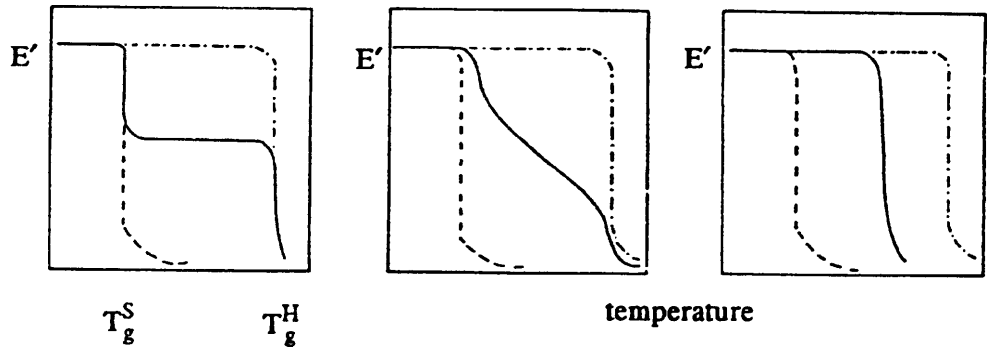

Figure 1.19 Schematic illustration of modulus–temperature behaviour of block copolymers (solid line) and the corresponding homopolymers (dashed line); (a) completely phase separated; (b) partially phase separated; (c) completely phase mixed.

The modulus-temperature profiles of the homopolymers showing glass transition behaviour are indicated by dashed lines in Fig.1.19. Fig.1.19a indicates the behaviour of a completely phase separated material. At Tg^S the block copolymer exhibits a drop in modulus followed by a modulus plateau prior to the onset of Tg^H where the modulus drops sharply as both segments are now in the rubbery state. A totally phase-mixed system (Fig.1.19c) exhibits only one transition, between those of the parent homopolymers, in which the modulus drops catastrophically as both segments of the copolymer enter the rubbery state. The modulus–temperature behaviour of partially (micro)phase separated copolymer is illustrated in Fig.1.19b. At temperatures slightly higher than Tg^S of the homopolymer, there is a small drop in modulus associated with a phase containing a large proportion of soft segments. A shallow negative slope follows, leading to a sharp drop in modulus, slightly between Tg^H for the pure homopolymer, as the phase with a composition higher in hard segment enters the rubbery state.

Hashimoto at al [91] have studied the effect of phase mixing and interphase broadening on the dynamic-mechanical response of block copolymers using specially-prepared, styrene-isoprene tapered block copolymers. It was observed that promotion of the formation of mixed-phase material, by incorporation of mixed blocks resulted in two effects.

One was to broaden the glass transition at Tg^S and Tg^H, and the second was to bring the positions closer together. These phenomena were attributed by the authors to domain-boundary mixing (interphase broadening) and mixing in domain (phase-mixing), respectively. Recently, the effect of morphology of PUrI on their properties was fully studied by Ryan, Stanford and Tao [92], using TEM, SAXS, DMTA, and tensile testing. The properties of PUrI were found to be greatly affected by morphology, which was determined by soft segment, hard segment, catalyst and post curing.

Many kinds of techniques can be used to study the phase separation of copolymers, such as DMTA, SAXS, TEM, SEM, FTIR, and all of these (except FTIR) are described in more detail in later chapters.

1.4 Composites Formed by Reaction Injection Moulding

Since the first automotive part came into production in 1975, RIM provides for the industry's needs for design freedom, part consolidation, and fast, accurate production. Complex shapes, variable wall thickness, soft lines, sharp corners, openings, and ribbons can be designed into RIM mouldings. Mini tooling changes can significantly alter the appearance of a RIM part, enabling the quick, economical response to changes in design required in the automotive market. Especially with large parts, RIM offers the advantages of part consolidation, reduced parts inventories, and reduced assembly operations. the excellent flow ability and processing characteristics of RIM products result in quick mould filling and short cycle times.

Over half of all RIM materials contain fillers. The main motivations are to improve dimensional stability and for better mechanical properties. The fillers can be milled fibres, flakes, which fill RIM to form Reinforced RIM (RRIM) materials, and continuous fibres which form structural RIM composites (SRIM). Fig.1.20 [1] shows general comparison of the coefficient of linear thermal expansion (CLTE) for typical materials.

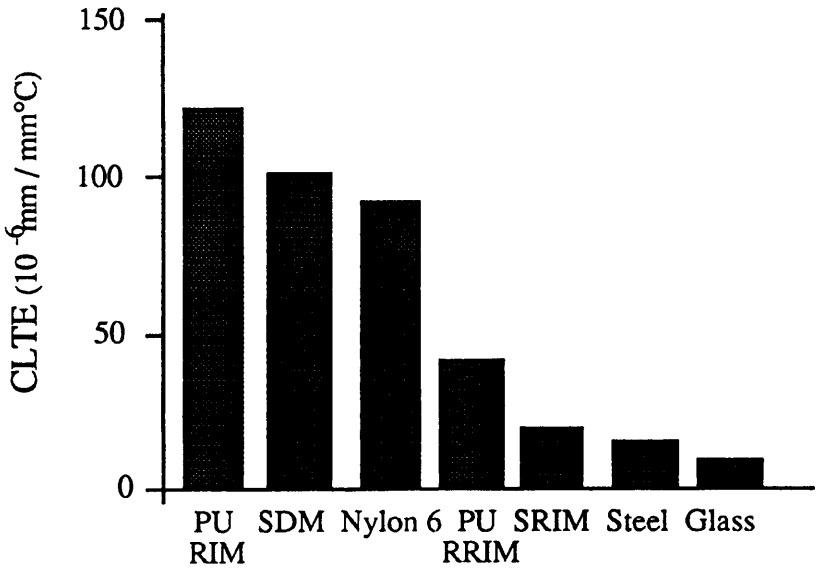

Figure 1.20 Comparison of the CLTE for typical RIM polyurethane, styrene dimethacrylate, nylon 6, RRIM polyurethane (10 vol% of 1.6 mm milled glass fibres), SRIM (styrene dimethactylate system injected into 10 vol% continuous fibreglass mat), steel and glass [1].

1.4.1 Reinforced Reaction Injection Moulding, RRIM

There are four types of fillers which have been studied extensively for use with RIM polyurethane formulations in RRIM:

(I) Chopped glass: They are made by bundling together hundreds of tiny glass filaments (10 to 20 μm dia.) with an adhesive. These strands can be chopped into fairly uniform lengths , such as 3 mm. When the chopped strands are dispersed in polyol the adhesive dissolves and the filaments separate. The high aspect ratio ($l / d \approx 100$) of these filaments greatly increase the viscosity of the mixture eventually becoming a solid–like mass. Cross et al. [93] gave a relation for the maximum volume fraction of fibres as a function of l / d. Coates and co-workers [94] found that 16% in the polyol was the maximum concentration at which they could process 1.5 mm chopped fibres (ICI WX6450, 17μm dia) in their RIM machine. These suspensions are very shear thinning. At the low shear rates encountered in emptying storage tanks and in recirculation they are very difficult to move but at the high shear rates encountered during impingement mixing and injection, this suspension viscosities are reduced to close those of polyols [94].

(II) Hammer milled glass: Milled glass is made by hammering glass filaments (about 10 to 20 μm dia) through a screen with a given opening. This opening represents the largest size fibre that will be present in the mixture. The length distribution is very large. For what is called 1.6 mm hammer milled fibre the average length is actually only 0.2 mm. Because the aspect ratio of milled fibres is low they can be loaded to at least 40 wt% in polyols and much easier to disperse and to pump than chopped fibres.

(III) Flake glass: They are made by shattering very large diameter, thin walled glass bubbles and passing the pieces through a sieve. The sieve opening size is used to designate the product; 0.4 mm is most frequently used in RIM. The flakes have a wide size range.

(IV) Mica: Mica is a plate–like mineral (muscovite, $K_2O\ 3Al_2O_3\ 6SiO_2\ 2H_2O$). As with flake glass, mica particles are segregated by sieving; 74 μm (200 mesh) has been used in RIM studies. These particles are thus on the average smaller than the glass flakes, but they are more regular in shape.

(V) Others: Other minerals have been tried in reinforced RIM systems. In particular, wollastonite ($CaSiO_3$), which is naturally rodlike particle with 10:1 aspect ratio, has been used [95]. Even talc and calcium carbonate, which are more spherical and much softer particles, do improve modulus when added to RIM polyurethanes [95]. Titanium dioxide and carbon black are added in small quantities for pigmentation rather than reinforcement.

Ferrarini and Cohen [96] have compared these four fillers in the same RIM formulation (Fig.1.21). All four fillers increase flexural modulus about three fold, and reduce heat sag about fourfold. In both properties we note that the fibrous fillers have much more anisotropy; there is a large difference (about 1.7 time) between samples cut parallel to the mould filling direction and perpendicular. This is even more apparent in the CLTE. In contrast plate-like particles will orient flat to the flow and thus properties with these fillers will show little dependence in the X, Y plane. The anisotropy of the fibrous fillers also manifests itself as warpage of large flat panels (0.6m x 1.2m x 3 mm).

Fig.1.21d shows that samples filled with chopped fibres have the greatest tensile strength. This is because they are long enough to break rather than pull out of the matrix. Both plate–like fillers, glass flakes and mica show lower tensile and impact strength than the fibrous fillers. Rice and Dominguez [97] also report lower puncture impact energy with plate fillers, especially mica at low temperature. It is again noticed in Fig.1.23d that the tensile strength of flake glass is the same in both mould directions and slightly higher than either chopped or milled fibre when measured perpendicular to the filling direction.

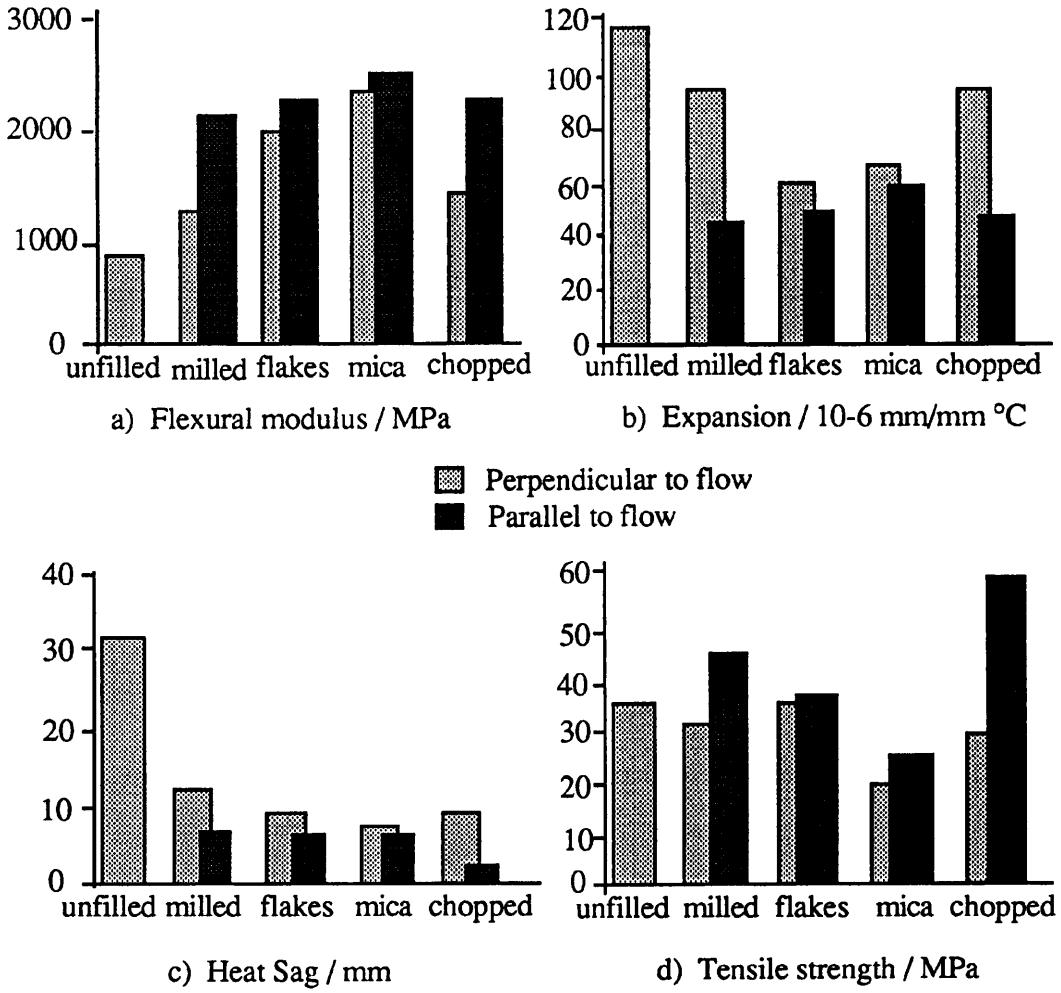

Figure 1.21 Properties of a high modulus polyurethane RIM formulation reinforced with various fillers: chopped glass (5 wt%, 1.6 mm chopped plus 10 wt%, 1.6 mm milled glass); mica (22 wt%); flake glass (22 wt%, 0.4 mm) milled glass (22 wt%, 1.6 mm). a) flexural modulus at 23 °C; b) CLTE from -30 to +30 °C; c) heat sag at end of 125 mm cantilever after 1 hour at 121 °C; d) tensile strength at 23 °C [97].

Despite their high reinforcement potential, problems with warpage, anisotropic properties, high viscosity in processing equipment and higher cost have kept chopped fibre from seeing much use. Milling fibres are used in long thin parts such as fascia where warpage is not as critical. To some extent, RRIM expands the range of application possibilities, but some special consideration need to be taken in processing RRIM (Table 1.2).

Table 1.2 Special consideration in processing RRIM [1]

Supply:	filler must not contaminate reactants (esp. water) high viscosity at low shear moving cavity recirculation pumps
Condition:	settling problems in tanks and lines use tank stirrers
Meter:	only lance pistons
Mix:	use viscosity at high shear to calculate Re_{crit} wear on nozzles . jambing clean out piston
Fill:	shear thinning of filled systems may reduce flow instabilities fibre orientation
Cure:	filler reduces T_{max}
Demould:	filler may remove mould release
Finish	harder to achieve glossy surface

1.4.2 Structural Reaction Injection Moulding, SRIM

As discussed in the previous section RRIM products have better thermal stability and improved modulus, compared with unfilled RIM materials. However, the strength and fracture properties of RRIM and RIM products are similar. Structural Reaction Injection Moulding(SRIM) is a development of the process capable of producing high performance materials, for example, E–modulus values between 4 and 18 GPa, coefficient of linear thermal expansion (CLTE) like metals, good impact properties even at low temperature, and good thermal stability. Possible application of SRIM include inner support panels, truck boxes, floor pans, instrument panel supports, front-end support and bumper beams. In

short, most of the secondary structure of a vehicle provides possible applications for SRIM. Depending on the properties available and the process involved, even the primary structure of a vehicle, the cross members, could be SRIM candidates. The second part of the definition is in the process. Reaction Injection Moulding involves the metering and mixing of two (or more) reactive components into a mould, which react in the mould to produce a polymer or polymer composite part in the shape of the mould. Traditionally, RRIM involved carrying the reinforcement into the mould with the reacting mixture. In SRIM, the reinforcement, which can be made of long, continuous fibres, is placed in the mould prior to the injection in the form of a mat, and the reacting mixture must flow through the mat. Fig.1.22 is schematic of a SRIM process [1].

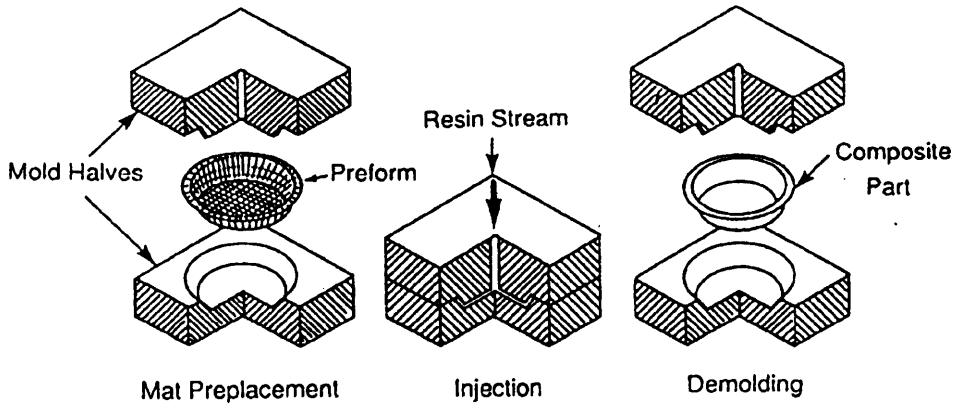

Figure 1.22 Schematic of the Structural RIM process [1].
(a) Placement of fibre preform in the mould cavity. (b) Closing of mould and injection of the reactive mixture. Curing in closed mould. (c) Opening of the mould and part ejection.

The advantage of continuous fibre reinforcement becomes clear in Table 1.3. SRIM can easily exceed the maximum fibre content of RRIM systems (about 25% by weight) because the fibres are already there, and there is no need to pump the glass into the mould. Glass fibre contents of 60 wt % and higher have been reported [98, 99]. Because of the high glass level of long fibres the flexural modulus and tensile strength of SRIM plaques are about five times that of RRIM. These high values approach those for laminated composites and metals, and thus open up load-bearing (structural) applications for SRIM.

Table 1.3 Typical properties of SRIM composites [1]

	Isocyanurate	Urethane	Acrylamate	Epoxy
Random Glass Mat (wt%)	38	44.8	40	40
Specific Gravity (g cm^{-3})	1.54	1.53	1.46	--
Void (v/v, %)	1.5	1.5	--	--
E_f (MPa at 25 °C)	8100	9600	8700	9200
Tensile Strength (MPa)	150	150	125	160
Elongation (%)	2.3	2.0	2.1	1.2
Izod Impact (J / m)	510	660	790	~800
Heat Distortion (°C)	184	189	240	>200
CLTE (m / m °C) x 10^{-6}	~20	--	27	18

Table 1.4 gives typical processing conditions [1] for the four systems described in Table 1.3. The viscosities are somewhat lower and gel times longer than those for typical RIM systems. This aids penetration into the fibre mats. The short demoulding times make SRIM attractive especially when compared to RTM and other labour intensive composites processes. Mould temperatures and pressures are similar to RIM and thus standard RIM equipment can be used for SRIM. The additional steps are concerned with getting the fibre into the mould as indicated in the unit operations in Fig.1.23. To compress the fibre mats SRIM requires mould clamp pressures of about 1 MPa, about double that for RIM.

Table 1.4 Typical processing conditions for SRIM resins [1]

	Isocyanurate	Urethane	Acrylamate	Epoxy
Viscosity at T_0				
A (mPa s)	130	175	250	100
B (mPa s)	45	50	30	100
Wt. ratio A / B	2.24	1.18	2.0	3.6
Initial Temp., T_0 (°C)	25	25 - 40	25	60 -70
Mould Temp., T_w (°C)	95	50 - 70	100	120 - 130
Mould Pressure (MPa)	1 - 5	--	0.2 - 0.4	--
Gel Time (s)	8	3 - 60	10 - 20	25
Demould Time (s)	45	30 - 300	50 - 70	75 - 300

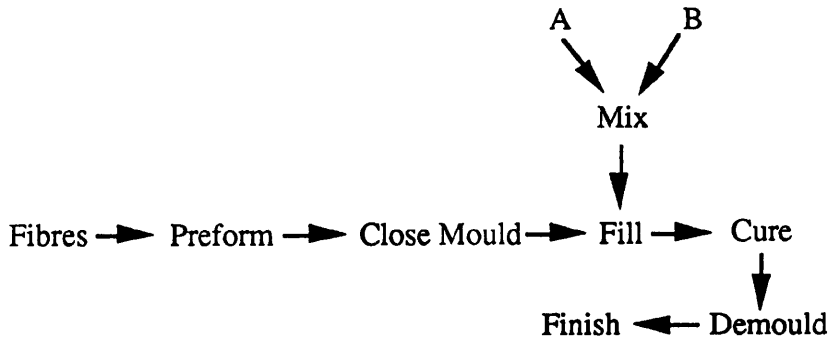

Figure 1.23 Unit operations for the SRIM process [1]

The preform may consist of one or more mats made from either glass, carbon or Kevlar fibres. The mats may be ether woven or non-woven, or ether uniaxially, biaxially or randomly oriented. The SRIM process benefits from the combination of two particularly successful technologies. The first, the RIM process, has already shown its capacity, mainly through the use of polyurethane chemistry, to produce complex-shaped, large, thin-walled parts with high volume, high quality, cheapness and reliability. The second, the preforming process, which until recently was mainly used for Resin Transfer Moulding process, is known to produce high content of long glass-fibre preforms. Useful reinforcing preforms for SRIM must now have three important properties [99]. The first condition is that it must be possible to produce a preformed structure from the fibres. The second, and most important point, concerns the distribution of fibres inside the mould cavity during mould filling. The third, the binder used to make the preform should not disturb the polymerisation(s) to form RIM material. Bad fibre distribution causes local shrinkage, distortion of the part and differences in mechanical properties. Additionally, it is necessary to have constant conditions of fibre distribution for mould filling within a part and from shot to shot. The fibre content, ply lay-up geometry and fibre orientation in individual plies influence the flow resistance at the specific location within the mould under the flow conditions such as velocity, and viscosity [100]. During mould filling, mat tearing is caused by the drag forces generated by resin flowing over the fibres. This is counter balanced by friction of the fibres against themselves and the mould wall. The drag force on isolated

cylinderical fibre is proportional to the viscosity and velocity of the fluid flowing over it [101]. For a given volume fraction of fibres the friction force should be constant. Thus for a particular mould, mat tearing will start if the drag force increases beyond a critical value. This can happen if viscosity or velocity increases.

Although further theoretical and experimental work is needed to better understand the limitations imposed by mat strength, it is possible to represent [1] the SRIM filling process, a qualitative mouldability diagram as shown in Fig.1.24 (where T_d is thermal degradation temperature, t_f is filling time). The SRIM process is typically carried out as a heat activated

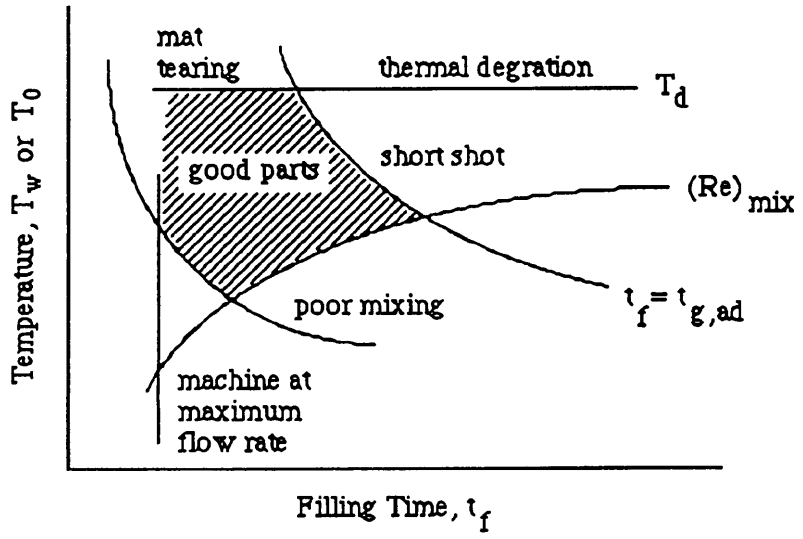

Figure 1.24 Mouldability diagram for filling in SRIM. Mixing orifices, volume fraction of glass fibres, and resin chemistry are fixed [1].

process; $T_0 << T_w$. Thus the maximum time to fill a given mould is controlled by the gel time ($t_{g,ad}$) at T_w. Degradation is also controlled by mould temperature (T_w). However, as in RIM, initial resin temperature (T_0) determines viscosity which controls mixing quality. Most SRIM parts are centre gated, and thus the mould is initially filled via radial flow. The highest velocity is at the gate where viscosity $\mu(T_0)$ is that of unreacted resin mixture at T_0. Thus, the initial drag force for mat tearing, can be controlled by the flow rate, Q, since it can be shown [1] that $t_f \propto 1/Q$, and by the initial temperature through viscosity $\mu(T_0)$.

One solution to difficult filling and for filling of large parts is to use multiple gating as discussed by Martin and Son [102]. An obvious problem with multiple gates in non-evacuated moulds is the trapping of air as the different flow fronts approach each other.

Many reactant systems have been studied for SRIM. These include: low-viscosity polyurethane systems [103-108], polyepoxides [104, 109-111], phenolics [112-114], urethane-acrylates [115-117], polyesters [118], acrylics [118] and urethane-isocyanurates [51, 106, 107, 119]. SRIM reinforcements are typically random, continuous-fibre mats of carbon, Kevlar or glass, with the latter being the most common. These mats have been used either as the single reinforcement or in admixture to make hybrid RIM composites. Table 1.5 [120] gives mechanical property data of SRIM composites from the literature.

Hostettler and McCormick [104] first reported the use of SRIM, which involved the use of carbon and Kevlar reinforcements with urethane and epoxy matrices. However, fibre wet-out was poor and consequently so were mechanical properties of SRIM composites (see mat. nos. 1 - 6). Since then, there have been a large number of reports on SRIM processing in the literature.

Polyurethanes: The use of unmodified RIM-PU systems for SRIM creates problems because of the relatively high initial viscosities (typically 0.6 - 1.0 Pa s) and fast rates of reaction of these systems. For example, Waddill [110] reported very poor fibre wet-out and Kleinholz met problems with mat distortion leading to irregular reinforcement distribution. Dominguez and Rice [105] claimed that delayed-action catalyst was required to modify standard RIM-PU formulations for SRIM. They successfully produced composites with up to 50% w/w of random , continuous glass-fibre reinforcements, as flat plaques (18 x 18 x 0.125"). Stanford [108] reported SRIM composites with up to 38% w/w unidirectional carbon fibre mat of 0 / 90° orientation. The preplaced mats were not displaced by the highly reactive RIM-PU matrix, however, these edge-gated materials did have an irregular distribution of the reinforcement through the thickness of the mouldings, giving a resin rich surface of good quality and exposed reinforcement "strike-through" on the other surface [108].

Table 1.5 Literature data for mechanical properties of SRIM composites [120]

Matrix	Reinforcement [a]	No. of Mats [b]	W_f [c]	V_f [d]	E_b [e]	S_f [f]	E[g]	σ_u [h]	Ref.	Materials
			%	%	GPa	MPa	GPa	MPa		Number
Polyurethane	Carbon, NW	-	15	-	4.7	94	-	-	104	1
Epoxy	Carbon, NW	-	10	-	4.65	74	-	-	104	2
Epoxy	Kevlar, NW	-	7.5	-	3.5	97	-	-	104	3
Polyurethane	Kevlar, NW	-	7.5	-	3.4	-	-	-	104	4
Epoxy	Glass, C, R	2	~15	-	6.3	209	7.3	130	110	5
PU form	Glass, C, R	2	-	10	-	21	>1.2	>13	107	6
Epoxy	Glass, C, R	2	40	-	9.3	244	12.1	158	111	7
	Glass, C, U	2 ↑								
Epoxy	Glass, C, R	1	53	34.2e[i]	24	786	29	442	111	8
	Glass, C, U	2 ↑								
	Glass, C, R	1								
	Glass (triaxial)	1	27							
Epoxy	0/+45/-45				5.1	104			109	9
	Glass, C, R	1								
	$CaCO_3$		18							
Epoxy	Carbon, C, PW	-	-	30/35	30	550	39	417	109	10
	Kevlar	3	-	9						
Epoxy	Glass, C, R	1	-	5	13.8	324	14.5	262	109	11
	Kevlar	3	-	9						

Table 1.5 continued

Matrix	Reinforcement [a]	No. of Mats [b]	W_f [c] %	V_f [d] %	E_b [c] GPa	S_f [f] MPa	E[g] GPa	σ_u [h] MPa	Ref.	Materials Number
Phenolic	Glass, R	-	60	~41e	12	227	-	156	114	12
Polyurethane	Glass, C, R	-	50	~32e	5.8	-	-	140	105	13
Styrene DMA	Glass, R	-	60	~32e	10 [j]	~230	-	-	123	14
	Carbon, R	1	N/A	-						
Acrylamate	Glass, R	N/A	30	-	7.6	154	7	88	115	15
	Carbon, R	1	N/A	-						
Isocyanurate	Glass, C, R	-	57.4	39.7	12.5	380	-	198	119	16
Isocyanurate	Glass, C, R	-	34.4	-						
	$CaCO_3$	-	22.6	-	10.4	279	-	-	119	17
Polyurethane	Carbon, C, U	2 → ↑	19	13.7e	-	-	10	112	108	18
Polyurethane	Carbon, C, U	4 ↑↑→→	38	29.3e	-	-	14	180	108	19
Acrylamate	Glass, C, R	3	37.6	21.8e	8.0	239	7.7	126	116	20
Acrylamate	Carbon	3 → ↑	32	-	31.2	345	26.2	255	116	21
PU foam	Glass, C, R	-	29	-	4	165	-	90	106	22
Polyurethane	Glass, C, R	-	40	23.5e	8.5	279	-	-	110	23
Isocyanurate	Glass, C, R	-	40	23.53	9.2	285	-	-	110	24
Isocyanurate	Carbon, C, U	-	30	22.5e	31	504	-	330	110	25
Isocyanurate	Glass, C, R	-	54	35.1e	15.9	414	-	219	110	26
Isocyanurate	Glass, C, U	-	50	31.6e	24.1	615	-	234	110	27
Isocyanurate	Glass, W	-	30	16.5e	6.3	145	-	159	106	28

Table 1.5 continued

Matrix	Reinforcement [a]	No. of Mats [b]	W_f [c] %	V_f [d] %	E_b [e] GPa	S_f [f] MPa	E[g] GPa	σ_u [h] MPa	Ref.	Materials Number
Polyester	Glass	-	23	-	5.6	-	-	-	118	29
	Filler	-	14							
Polyacrylic	Glass, W	-	40	23.5e	18	-	-	-	118	30
Polyacrylic	Glass,	-	20	-	9	-	-	-	118	31
	Filler	-	25							
Acrylamate	Glass	-	35	19.9e	6.1	165	9.7	98.5	117	32
Acrylamate	Glass	-	50	31.6e	10.4	313	12.5	201	117	33
Acrylamate	Glass	-	50	36.1e	14	219	15.2	193.6	117	34
Polyurethane	Glass	-	30	-	-	-	11.1	164.5	103	35

(a) C = continuous; R = random; NW = non woven; PW = plain weave; U = unidirectional; W = woven.

(b) Arrows denoted fibre orientation relative to material flow; parallel (↑) perpendicular (→); - number not given.

(c) / (d) W_f and V_f are weight and volume fractions of reinforcement, respectively.

(e) E_b = flexural modulus, (f) S_f = flexural strength, (g) E = Tensile modulus, (h) σ_u = Tensile strength.

(i) e = estimated, assuming specific gravity values: matrix 1.2; glass fibre 2.6 and carbon fibre 1.78.

(j) E' (dynamic flexural modulus) not E_b.

Several workers [106, 107] have reported successful SRIM processing of structural foam polyurethane systems (see mat. nos. 6 and 22). These systems typically have much lower reactivities than RIM-PU systems (gel times ~15s c.f. ~4s) giving lower processing viscosities, resulting in improved reinforcement "wet-out" and reduced mat displacement.

Low-viscosity PU resin systems, especially formulated for SRIM, are based typically on relatively low molar mass polyols of functionality of >2, giving a highly cross-linked polymer [104, 106, 121]. Nelson [106] reported a segmented PU resin system of this type with reactant viscosities of 90 - 130 and 400 - 600 mPa s for the isocyanate and polyol respectively, with a nominal gel time of 8 - 12s. This combination of low viscosity and reactivity allowed the moulding of composites containing up to 40% w/w of random, continuous glass-fibre mat, the mechanical properties of which are given in Table 1.5, material no. 22.

Phenolics: Brode and co-worker [113, 114] reported data on a phenolic SRIM composite produced in a 60s moulding cycle with 60% w/w glass reinforcement (see table 1.5 mat. no. 12). The static-mechanical and fatigue properties of this materials were found to be comparable with those of 60% w/w reinforced vinyl-ester and polyester-based composites, produced in a 10 minute cycle time compression moulding process.

Vinyl Monomer Based Systems: Vinyl monomer based SRIM systems have low initial viscosities, typically much less than 0.2 Pa s [122], and low reactivity with gel-times of ~10s and complete reaction times of ~180s. However, the processing of flammable, volatile monomers in a high speed, exothermic reactive process requires specialised equipment, with "spark free" electrical systems and suitable ventilation to prevent explosion. In addition, the high shrinkage of up to 20% for unfilled vinyl monomer SRIM systems, combined with the brittle nature of the highly-cross-linked polymers formed, can cause cracking problems. Thus, due to these problems, there have only been a limited number of SRIM studies performed.

Gonzalez and Macosko [123] reported a free radical polymerised SRIM system consisting of a 50:50 w/w mix of styrene and an aromatic dimethacrylate with 1% w/w butyl peroxide initiator. Composites containing 50% w/w of random, continuous glass fibre mat were produced, the mechanical properties of which are given in Table 1.5, mat. no. 14. Leadbitter and co-worker [118] reported the mechanical properties of SRIM composites with undefined polyester and polyacrylic matrices which are shown in Table 1.5, mat. no 29 - 31.

Epoxy Resin Systems: In addition to the brief studies of Hostettler and McCormick reported previously (see Table 1.5 mat. nos. 2 and 3) the use of epoxy-based system in SRIM was investigated in more detail by Waddill [106]. Plaque moulding (14 x 14 x 0.125") were produced by machine free-pour into an open, heated mould (100 - 150°C) containing pre-placed glass fibre mats. The mould was then closed and clamped, and polymerisation completed during a 90 - 180s curing cycle. The mechanical properties of the composite moulding produced are shown in Table 1.5, mat. no. 5.

Subsequent extensive development of the epoxy-SRIM process has been reported by Farris and co-workers [109, 111]. These studies utilised an evacuated mould (18 x 9 x 0.125") with various combinations of glass, Kevlar and carbon fibre reinforcements, and $CaCO_3$ particulate filler. The epoxy reactants had moulding viscosities of ~0.1 Pa s (60 °C) and were reported to develop 95% of their ultimate cure properties in 60s at 130 °C, a typical mould temperature. An SMC tool for the production of an automotive structural bumper brace was modified for epoxy-SRIM. The resultant mouldings had superior physical properties to the equivalent SMC components with significantly reduced part to part property variation. Examples of the composite mechanical properties achieved during these studies are shown in Table 1.5, mat. nos. 7 to 11.

Urethane-Isocyanurate Systems: Isocyanurate-based systems, in common with polyurethanes, utilise a polyisocyanate and a polyol component. The cyclo-trimerisation of isocyanates forms an isocyanurate, with the polyol acting as a rubber-toughening agent and

a catalyst carrier. Unlike polyurethane formation, urethane-modified polyisocyanurate systems do not build-up high molar mass during the initial stages of the reaction.

Carleton and co-workers [51, 119] discussed predicted in-mould conversions calculated from adiabatic exotherm studies and reported that the reaction initially produces low molar mass oligomers which rapidly combine to form a three-dimensional network during the latter stages of polymerisation. Thus, for a urethane-isocyanurate system a low initial viscosity of 65 mPa s for the reaction mixture was reported. Increasing the trimerisation catalyst content decreased the free-pour, machine gel-time from 44 to 18s, and the corresponding in-mould, gel-time from 12 to 8s which were shown to be suitable for SRIM. The shorter in-mould times are due to shear heat generated during the high flow-rate filling of the packed mould. The urethane-isocyanurates developed are versatile SRIM matrices and composites with over 57% w/w random, continuous glass fibre reinforcement were produced using both edge-gated and centre-gated moulds, gasketed for evacuation (see Table 1.5 mat. no. 16). In addition, hybrid composites with over 34% w/w glass and 22.6% w/w $CaCO_3$ were also produced (mat. no. 17). A supplementary report from the same laboratories [106] discussed the processing and mechanical properties of isocyanurate-SRIM composites containing continuous-glass and carbon fibre reinforcements, both random and unidirectional, with loadings of up to 54% w/w (see Table 1.5, mat. nos. 24 to 28). Interestingly, no indication of any inhibition of the isocyanurate polymerisation by the carbon reinforcement, as experienced by Hostettler and McCormick, was reported.

Urethane-Acrylates: Urethane-acrylate reactant systems often termed acrylamate resins, are especially designed as SRIM matrices [115-117] with low reactant viscosities (25 °C); viz. 0.4~0.6 and 0.15 Pa s for the polyol and isocyanate, respectively. Acrylamate systems produce rigid, highly cross-linked polymers within 60 to 120s, at mould temperature between 90 and 100 °C. Thus, acrylamate systems are readily processed by SRIM and composites with up to 55% w/w glass and carbon fibre reinforcements have been reported (see Table 1.5, mat. nos. 15, 20, 21, 32-34]. Acrylamate resins, known commercially as Arimax, are the most market-developed SRIM systems [123]. Applications

include spare tyre wells in the automotive industry, photocopier heat shields and satellite antennae.

Polyurethane, isocyanurate and acrylamate systems have an advantage over other chemical systems, in that standard RIM/RRIM machinery can be used to produce SRIM composites although Mazzoni and Corradi [125] have reported specialised SRIM equipment. SRIM machines are typically of low-medium throughout (< 2 kg s^{-1}) with high shot capacities, capable of producing large composite mouldings within 5 to 30s. The main differences in SRIM equipment are the clamping units, which are hinged and "book" to 90° to give the operator full access to the mould. Specialised SRIM clamping units have been reported [125] with a dual-platen, shuttle system for pre-forming mat reinforcements whose fibres are held by a thermoplastic binder. One mould is in the clamping unit being filled, while the other is in a service position at the side of the clamping unit. Mat is unwound to exact lengths over the mould by pneumatic conveying grippers and is then cut with a rotary knife. A heated plug then preforms the mat into the mould cavity which is then closed ready for filling. Problems encountered in the transition from what has until recently been a laboratory-based development process, to a full scale industrial production process, have been reviewed by Scrivo [126]. It is believed that S-RIM applications will expand in automotive industry.

1.5 Objective

There have been only limited reports [51, 106, 110, 119] of copoly(urethane-isocyanurate) based S-RIM, and no reports on SRIM materials based on copoly(urea-isocyanurate) (PUrI). Compared with RIM polyurethanes, RIM polyureas have superior thermal and mechanical properties [81]. Thus the main objective of the present work is to develop and study novel PUrI materials formed using RIM. Studies will be divided into two main areas:

I: The formation, morphology and properties of PUrI, suitable as matrices for SRIM

II: The development and characterisation of SRIM composites using pre-placed fibre mats and, as a matrix, one of the PUrI selected from I.

Following will discuss these two areas in more detail.

Initially, a series of PUrI copolymers will be formed by RIM using two different soft segment prepolymers, either a polyether diamine (D2000) or a polyether triamine (T5000), and uretonimine–modified MDI (M143). In addition, two different chain extenders, either diethylene toluene diamine (DETDA) or methylene bis–diisopropylaniline (MDIPA), will be used to form other PUrI. In all cases, an isocyanate-trimerisation catalyst, DABCO TMR catalyst (N-hydroxypropyl-trimethylammonium 2-ethylhexanoate in ethylene glycol solvent), will be used. Studies of the complex copolymerisation kinetics will be made using an Adiabatic Temperature Rise (ATR) technique, in order to establish the PUrI reaction chemistry necessary to produce a two-stage, viscosity-time profile suitable for SRIM processing. The kinetics data will be analysed to give a predictive model for the fractional conversion of isocyanate as a function of time for the various PUrI forming systems. The effects on PUrI morphologies and properties of catalyst content, PUrI composition and post-curing will be studied in detail.

The following techniques will be used to characterise the morphologies and properties of the PUrI: Rheometry, Adiabatic Temperature Rise (ATR), Small Angle X–ray Scattering (SAXS), Transmission Electron Microscopy (TEM), Scanning Electron Microscopy (SEM), Dynamic Mechanical-Thermal Analysis (DMTA), and tensile stress–strain testing.

One of the PUrI will be selected on the basis of its processing and properties for use as a matrix in the production of SRIM composites. Pre-placed reinforcement mats of either continuous glass, carbon or Kevlar fibres will be used with percentage volume fraction in the range 10 to 40%. Hybrid geometries involving unidirectional fibre mats as outer layers, randomly oriented glass fibre mats as inner layers, and combinations of glass-glass, carbon-glass, Kevlar-glass fibre mats will be used. The effects on composite properties of fibre

surface treatment using a silane coupling agent will also be studied. SRIM composites will be characterised using tensile stress-strain, dynamic mechanical-thermal, linear thermal expansion, and fracture (in-plane shear strength and single-edge notched bending) measurements. A composite model will be developed to analyse the tensile modulus and strength data of the hybrid SRIM composites.

CHAPTER TWO

PROCESSING OF COPOLY(UREA-ISOCYANURATE)S AS MATRIX FOR HYBRID SRIM COMPOSITES

2.1 Introduction

Isocyanurates are formed by the cycle trimerisation of isocyanates. Such reactions have been used [127] to form rigid foams by trimerisation of an isocyanate-terminated prepolymer. Since this first reaction, extension work has [50, 54, 56-58, 128-130] been done on isocyanurate-based foams and adhesives. Frisch [128] briefly reviewed the early development in the field of polyisocyanurates, and Reymore et al. [129] reviewed the chemistry and processing of polyisocyanurates foams and also presented a general mechanism for isocyanate trimerisation and suggested an explanation for the role of the catalyst. Since the end of 1970s, RIM urethane-isocyanurate elastomers have been prepared and studied [54, 56-58, 130]. More recently, isocyanurate-based polymers have become increasingly attractive as matrix materials for structural composites formed by reaction injection moulding, SRIM [131], due mainly to their good thermal and mechanical properties and also because the lower viscosity of the reactants allows easier mixing, and the initial viscosity increase with reaction time is slow and controllable.

As in the formation of polyurethane, polyisocyanurates formation via trimerisation reactions involves the use of isocyanates and a polyols. However, unlike polyurethanes, the reaction to form polyisocyanurates does not result in the development of high molecular weight in the early stages of reaction (Fig.2.1a-2.1b). The predicted conversions of isocyanate groups to urethane and isocyanate groups to isocyanates based on adiabatic exotherms, show that isocyanurates form slowly in the initial phases but rapidly reach high conversion at the end of reaction (Fig.2.2). Thus the reaction is one which forms many lower molecular weight species that subsequently react to form a three dimensional network [131].

During SRIM processing, low initial viscosity of reactant mixture is very important in order to achieve complete penetration of the pre-placed mats in the mould, as shown by the studies of Gonzalez and Macosko [132, 133]. In these studies, fluid flow of water through glass mats is described in term of Darcy's law, originally used to describe the

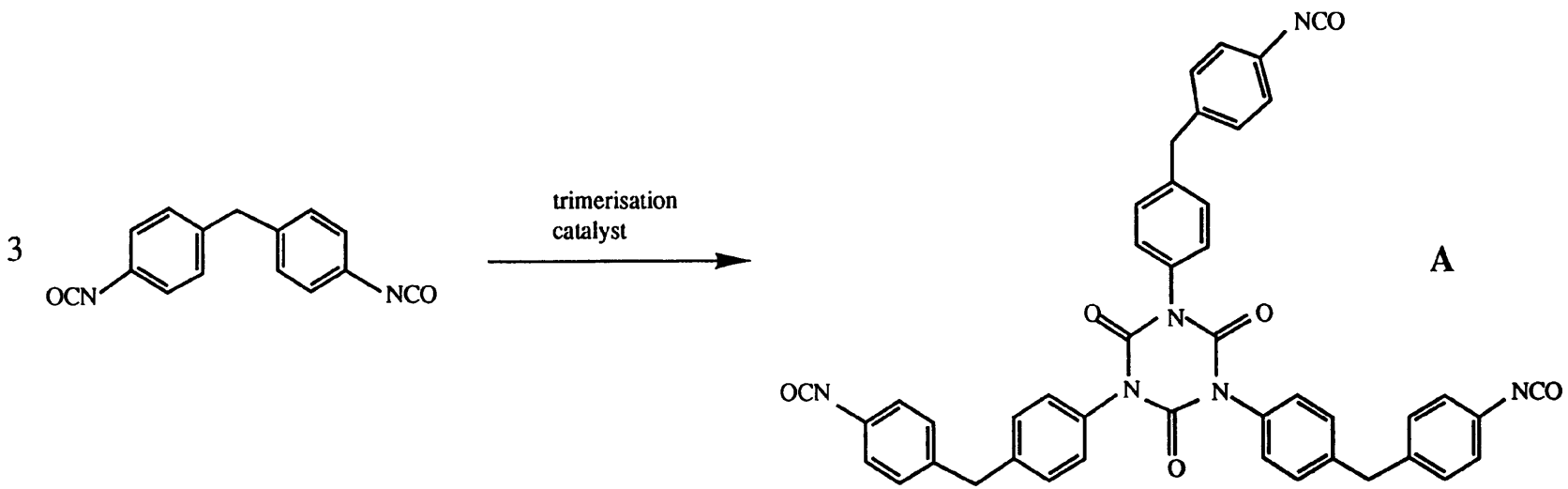

Figure 2.1a Polyisocyanurate formation (1)

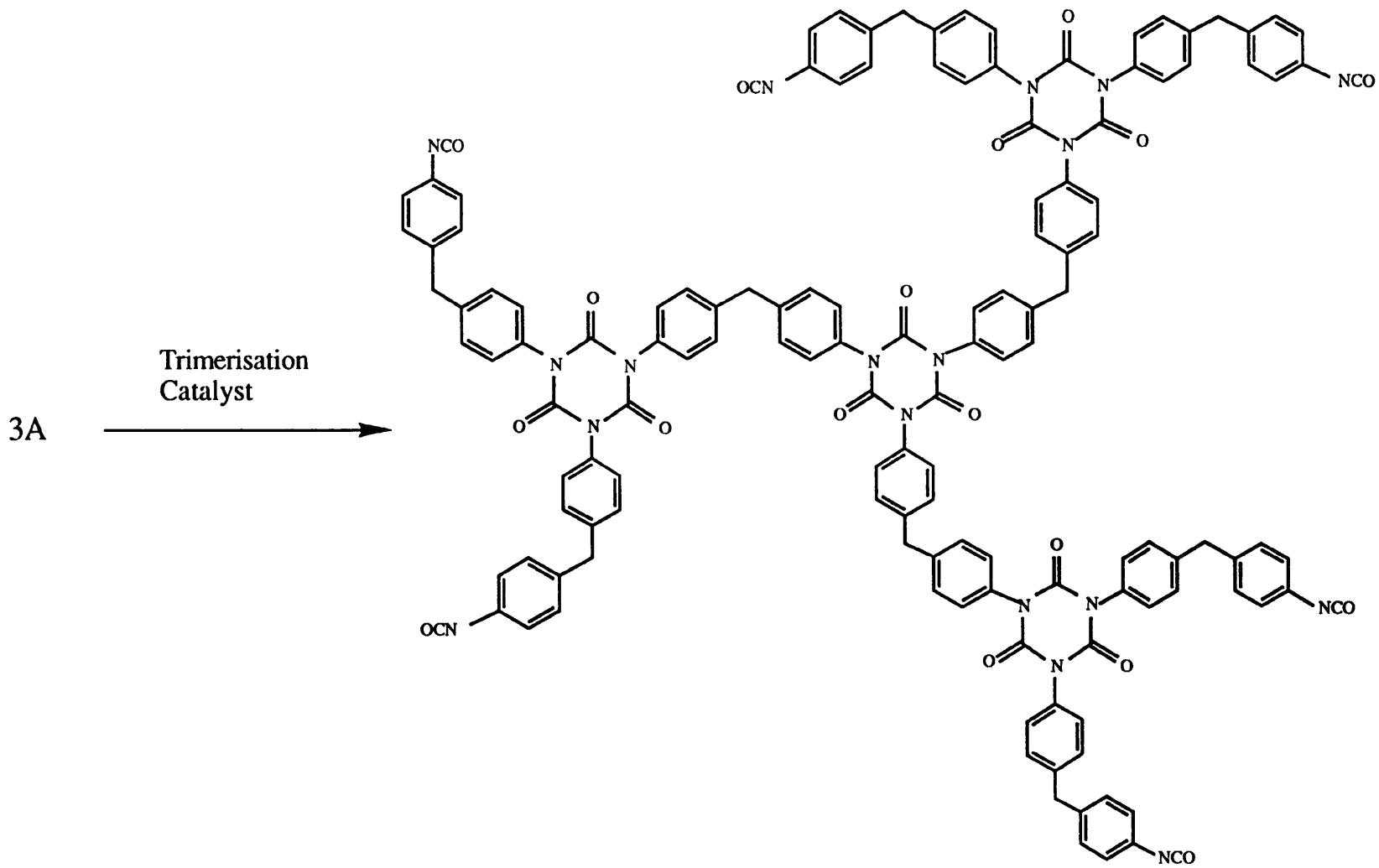

Figure 2.1b Polyisocyanurate formation (2)

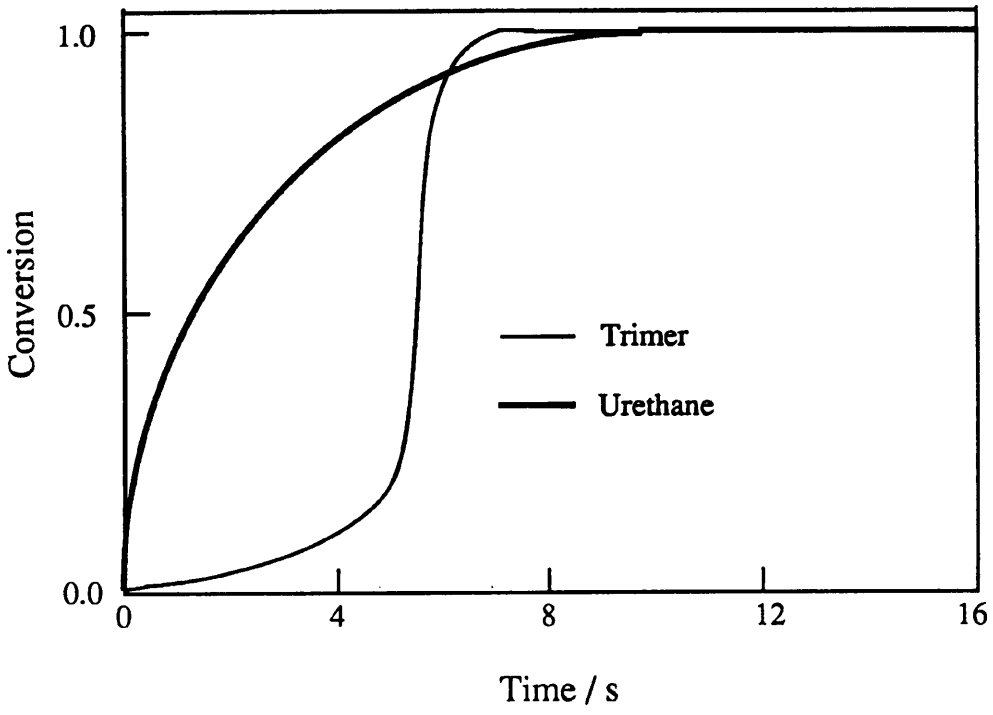

Fig. 2.2 Predicted in-mould conversions for urethane and isocyanurate

filtration of drinking water through sand. Darcy's law written as

$$V_x = (K_x / \eta)\, \Psi \qquad (2.1)$$

where V_x = Velocity of fluid in x direction, η = Viscosity of fluid, K_x = Permeability of mats in x direction, Ψ = Driving Gradient. Penetration is measured in terms of Permeability $K_x = (V_x / \Psi)\, \eta$. Thus for given conditions of V_x and Ψ, low η gives low K_x, which leads good penetration of the pre-placed mats.

Current commercial SRIM systems such as SpectRIM MM373^{TM} (ex. Dow Chemical) are based on aromatic polyisocyanates and polyether-polyols. In these copoly(urethane-isocyanurate)s, the polyol is used as a carrier for the trimerisation catalyst required for isocyanurate formation as shown in Fig.2.1. The polyol also provides control over mould filling viscosity [39, 131], gel-conversion and gel-time [54, 58, 106] during the SRIM processing. In addition, the polyol is incorporated into the copolymer as a rubber micro-phase and affects final mechanical properties by acting as a toughening agent for the

intrinsically brittle isocyanurate resin [56]. SRIM systems based on polyether-polyamines and polyisocyanates to form copoly(urea-isocyanurate)s are not commercially available despite the advantages in term of improving thermal stability and mechanical properties, of using amine-functionalised (rather than hydroxyl-functionalised) polyether to form RIM elastomer [134-136].

In this chapter, results of processing using RIM of eleven different copoly(urea-isocyanurate)s (PUrI) formulations are reported. The effects of polyether-polyamines, chain extenders and the concentration of the trimerisation catalyst on processing are presented and discussed.

2.2 Reactants

The materials studied in this chapter were prepared using four components: (i) a polyisocyanate, (ii) a polyether-polyamine, (iii) an aromatic chain extender and (iv) an organic catalyst. Materials were processed using RIM equipment in which two reactant streams are impingement mixed and moulded as rectangular plaque. The two reactant streams are designated, stream A and stream B: reactant stream A comprises the polyisocyanate, and reactant B comprises either a polyether-polyamine plus organic catalyst or a blend of polyether-polyamine plus an aromatic chain extender plus an organic catalyst (RIM equipment is described in details later).

2.2.1 Polyisocyanate (Stream A)

The polyisocyanate used in these studies was Isonate M143 (ex. Dow Chemical), described as liquefied 4, 4' - methylene diphenyl diisocyanate (MDI), and is a clear pale yellow, uretonimine-modified MDI product, as shown in Fig.2.3. Table 2.1 gives the composition of M143 and Table 2.2 gives the manufacturer's technical data.

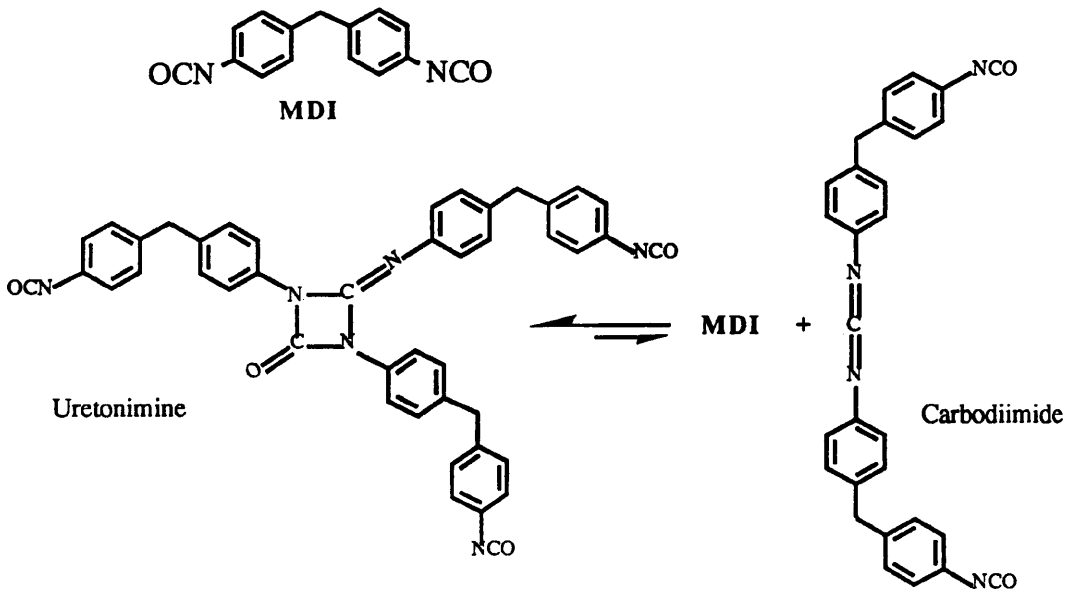

Figure 2.3 Idealised chemical structures of Isonate M143

Table 2.1 The composition of Isonate M143 [137]

Diphenylmethanediisocyanate, MDI	80 parts by weight
Uretonimine derivatives of MDI	20 parts by weight

Table 2.2 Technical data of Isonate M143 [137]

Functionality	2.17
Isocyanate equivalent	143.1
NCO / wt %	29.3
Viscosity / mPa s (25°C)	38
Specific gravity / g cm^{-3} (water = 1)	1.21

2.2.2 Polyether-polyamine (Stream B)

Jeffamine T-5000 triamine, Jeffamine D-4000, D2000 and D-230 diamines (ex. Texaco Chemical), described as polyoxyalkyleneamine, are amine-functionalised polyoxypropylene prepolymers with nominal number-average molar masses of 5000, 4000, 2000 and 230 g mol^{-1}, respectively. Their chemical structures are given in Fig.2.4-2.5. These materials are derived from hydroxy-functionalised precursors by a reductive amine process in which at least 80% of the secondary hydroxy end-groups are reported to be converted to amine groups [66]. The manufacturer's technical data for T5000, D4000, D2000, D230 are given in Table 2.3.

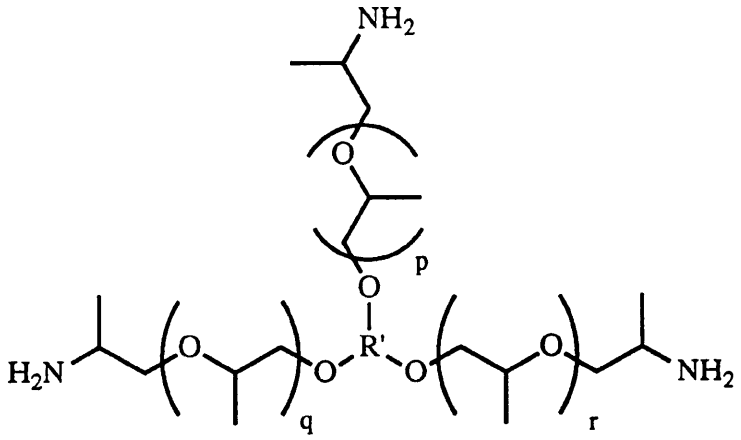

Figure 2.4 Idealised chemical structure of T-5000 [137]

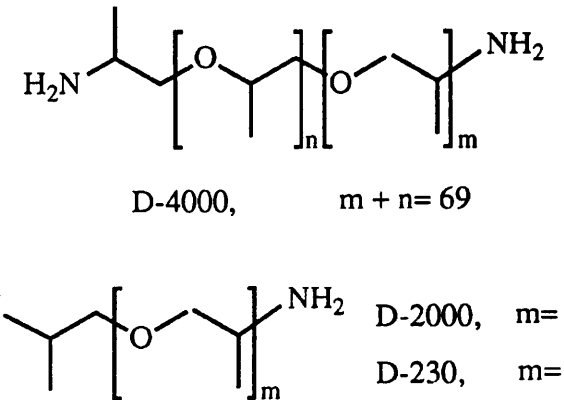

Figure 2.5 Idealised chemical structure of D-4000, D-2000 or D-230 [137]

Table 2.3 Manufacturer's technical data for polyamines [146]

Polyamine	T5000	D4000	D2000	D230
Nominal functionality	3	2	2	2
Specific gravity / g cm^{-3} (water = 1)	1.00	1.00	1.00	0.95
Viscosity / mPa s (25°C)	819	(a)	247	9
Max. water content / wt %	0.25	(a)	0.25	0.25
En, total acetylatables / g mol^{-1}	1563-1754	2000	962	115
Ena, total amine / g mol^{-1}	1923	2222	1000	119
Enla, primary amine / g mol^{-1}	1983	2273	1031	123
Total amine content / wt %	81-91	90	96	97
Primary amine content / wt %	79-88	88	93	94
Min. primary amine, % of total amine	97	98	97	97

(a) data not reported.

The experimental data from the various end-group analyses of the polyamine prepolymers are given in Table 2.4. It can be seen from the Table 2.4 that ›94% of the reactive groups in the polyether-polyamine prepolymers are amine groups, of which ›99% are primary amine groups. The non-amine groups (about 6%) are most probably residual secondary hydroxyl groups from the polyoxypropylene precursors [120].

Table 2.4 End group analysis results for polyamines [120]

Polyamine	D4000	T3000	T5000
En, total acetylatables / g mol^{-1}	2167± 20	1018 ± 14	1899 ± 10
Ena, total amine / g mol^{-1}	2304 ± 31	1077 ± 6	1964 ± 20
Enla, primary amine / g mol^{-1}	2304 - 2325 max.	1077 - 1086 max.	1970
Total amine content / wt %	94.1	94.5	96.7
Primary amine content / wt %	93.2 min.	93.6 min.	96.3

2.2.3 Chain Extenders (Stream B)

The aromatic diamine chain extender used was either 3,5-diethyltoluene diamine, DETDA (ex. Lonza AG), or methylene-bis-2,6-diisopropylaniline, MDIPA (ex. Lonza AG). Their chemical structures are shown in Fig.2.6.

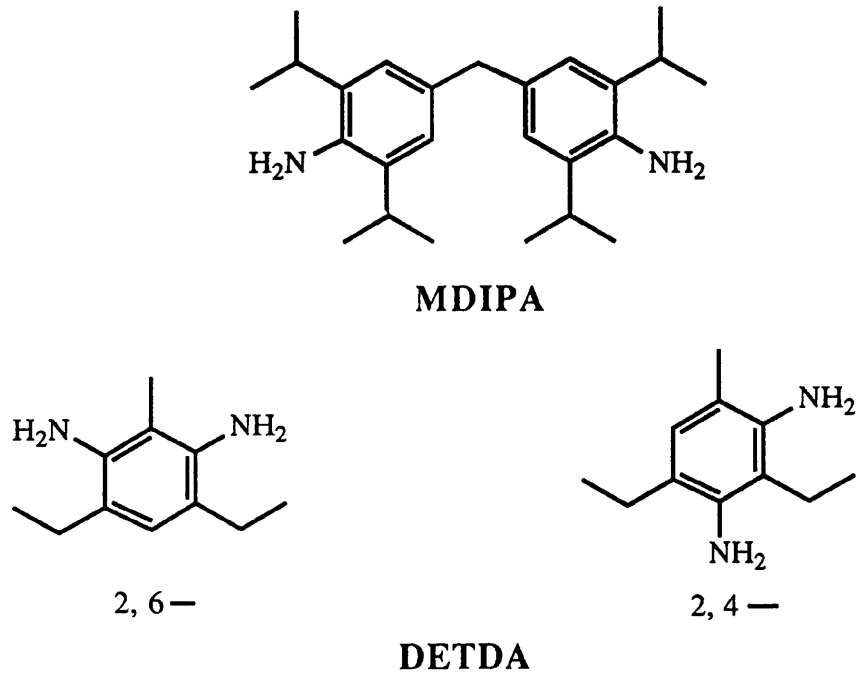

Figure 2.6 Chemical structures of chain extenders

DETDA was supplied as a dark-brown liquid. The manufacturer's technical data [139] claim that DETDA consists of an 80:20 mixture of the 2,4- and 2,6- isomers with a minimum assay of 97%, and with 3% of other amine. Ryan [20] reported purity to be 99.0% via GLC and an isomer ratio of 78:22 from NMR spectroscopy, confirming the manufacturer's specifications. Combustion analysis data for DETDA and MDIPA shown in Table 2.5 [20] were comparable with theoretical values calculated from the assumed structure of the aromatic amine chain extenders.

MDIPA was supplied as a brown glass with a T_g of -4 °C [139]. End group analysis data for DETDA and MDIPA are shown in Table 2.6 [138]. The En values of 91.7 and 186.2 g mol^{-1}, respectively, agree well with those calculated from the assumed structures.

Table 2.5 Combustion analysis data for DETDA and MDIPA [20]

Amine	C %	H %	N %
DETDA: Calculated for $C_{11}H_{18}N_2$	74.1	10.1	15.7
Determined (as received)	74.0	10.2	16.0
MDIPA: Calculated for $C_{25}H_{38}N_2$	81.9	10.5	7.6
Determined (as received)	81.6	10.5	7.6

Table 2.6 End group analysis data for DETDA and MDIPA [138]

Amine	DETDA	MDIPA
En / g mol^{-1}	91.7 ± 1.3	186.2 ± 3.1
Theoretical En / g mol^{-1}	89.14	183.3

2.2.4 Catalyst (Stream B)

For isocyanurate formation, the polyisocyanurate catalyst, DABCO TMR catalyst (ex. Air Products) was used. TMR is a quaternary ammonium carboxylate, N-hydroxypropyl-trimethylammonium 2-ethylhexanoate, in ethylene glycol solvent ($HOCH_2CH_2OH$). Its chemical structure is shown in Fig.2.7.

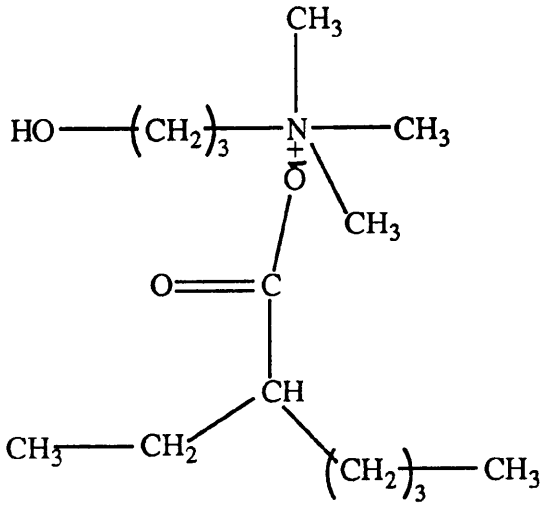

Figure 2.7 The chemical structure of TMR

The level of catalyst content in stream B is defined as the mass of TMR divided by the total mass of polyamine blend. That is

$$TMR = \frac{W_T}{(W_T+W_P+W_C)} \tag{2.2}$$

where W_T, W_P, W_C are the masses of TMR, polyamine and chain extender respectively.

2.3 Formulations

2.3.1 Reactant Ratio

The reactant ratio, r, is defined throughout the study as:

$$r = \frac{[NCO]}{[NH_2]_T} \tag{2.3}$$

where [NCO] is the concentration of isocyanate groups (equivalents per gram) and $[NH_2]_T$ is the total concentration of amine groups in the polyamine blend:

$$[NH_2]_T = [NH_2]_P + [NH_2]_C \tag{2.4}$$

where the subscripts P and C refer to polyether-polyamine and chain extender reactants respectively. Reaction of amine groups is considered to involve only one of the active hydrogen atoms.

$$RNH_2 + R'\text{-}NCO \rightarrow RNHCONHR'$$

2.3.2 Hard Segment Content

The weight percentage of hard segment content (%HS) is defined as the mass of the chain extender plus stoichiometric equivalent mass of polyisocyanate, divided by the total mass of the copolyurea. That is,

$$\%HS = \frac{(\frac{E_I W_C}{E_C} + W_C)}{(\frac{E_I W_C}{E_C} + W_C) + (\frac{E_I W_P}{E_P} + W_P)} 100\% \tag{2.5}$$

where E_P, E_C and E_I are the equivalent weights of the polyamine, chain extender and polyisocyanate respectively; W_P, W_C, are the masses of the polyamine and chain extender respectively.

2.3.3 Material Codes and Formulations

For convenience a shorthand, alphanumeric notation is used throughout this study to describe the materials and their subsequent thermal treatment. T5, D4, D2, D230, M, D and MD represent Jeffamine T5000, D4000, D2000, D230, Isonate M143, DETDA and MDIPA respectively; the number before D or MD indicates the value of %HS, the number after M indicates the level of TMR catalyst; and up or pc refers to non-postcured or postcured respectively. The following example shows how the code is applied to a particular PUrI, D2/20D/M/1.6/up.

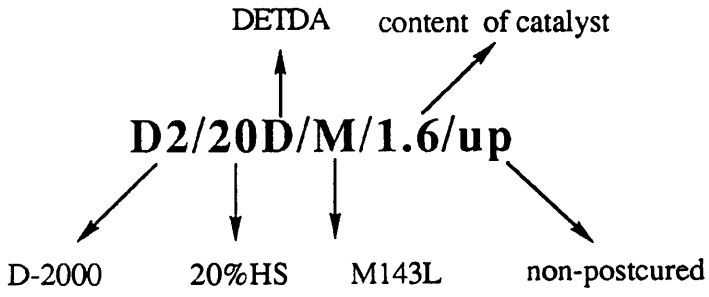

Figure 2.8 An example showing the code designation of materials

Table 2.7 gives the formulations of PUrI studied in this chapter.

2.4 Viscosity

The importance of understanding the rheological behaviour of the reactant component streams, and its effect on impingement mixing, has been described in Chapter 1. In order to obtain a greater understanding of the effects of temperature and chain extenders (in the case of stream B) on the rheological behaviour of reactant stream, a series of viscosity measurements were carried out as described in next section.

Table 2.7 The formulation[a] used to produce copoly(urea-isocyanuarate)s (PUr.I) via RIM

PUr.I	Stream A	Stream B							r[b]
	M143L	T5000	D4000	D2000	D230	DETDA	MDIPA	TMR	
T5/M/1.6	203.20	100.00						1.60	27.31
T5/20D/M/1.6	224.16	100.00				10.31		1.77	9.53
D4/M/1.6	203.20		100.00					1.60	31.55
D4-D230/M/1.6	203.20		93.08		6.92			1.60	14.20
D2/M/1.6	203.20			100.00				1.60	14.20
D2/M/1.2	203.20			100.00				1.20	14.20
D2/M/0.9	203.20			100.00				0.90	14.20
D2/M/0.6	203.20			100.00				0.60	14.20
D2/M/0.3	203.20			100.00				0.30	14.20
D2/20D/M/1.6	224.98			100.00		11.00		1.77	7.15
D2/20MD/M/1.6	236.20			100.00			16.20	1.86	8.83
D230/M/1.6	203.20				100.00			1.60	1.69

(a) reactants used in stream A and B are in parts by weight (g)

(b) r is stoichiometric ratio given as $\frac{[NCO]}{[NH_2]}$ (see Eq(2.3))

2.4.1 Test Method

The viscosities of reactant blends were measured using a Rheometrics RMS 800 / RDSII (Rheometrics, Inc) equipment fitted with a parallel plate fixture whose geometry is shown in Fig. 2.9.

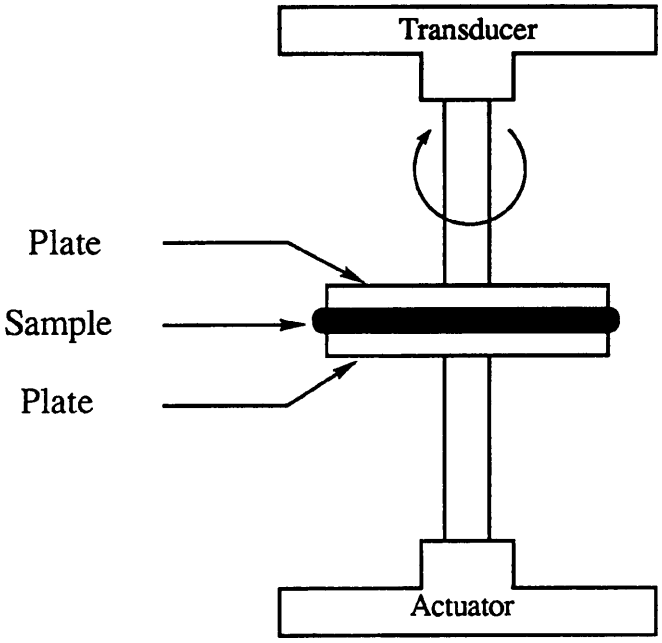

Fig.2.9 The fixture geometry of parallel plate

For viscosity measurement using the parallel plate geometry, the relationship between strain rate, γ (s^{-1}) , and actuator angular velocity, θ' (radians / s) is given as

$$\gamma = K_r \theta' \tag{2.6}$$

where the constant K_r is determined from the ratio of plate radius to plate gap. Typically, the plate radius R was 25 mm and the gap H was varied depending on a fluid. The shear stress, τ (Pa), developed in the fluid depends on the transducer torque, M (g cm), according to the equation

$$\tau = M K_\tau \tag{2.7}$$

where $K_\tau = 2G_c / \pi (R / 10)^3$ = stress constant, and $G_c = 98.07$ (Pa / g). The viscosity η (Pa s) of a fluid can be calculated using equations (2.6) and (2.7) as following

$$\eta = \tau / \gamma \tag{2.8}$$

A fluid is said to be Newtonian if the viscosity is independent of the shear rate. For a non-Newtonian fluid, if the viscosity of a fluid decreases as shear rate is increased, the fluid is described as being shear thinning or pseudoplastic. In the present study, R was fixed as 25 mm, H was approximately 1 mm, and γ varied from 100 to 1000 s^{-1}. For $\gamma <$ 100 s^{-1}, the reactant blends were thinning or pseudoplastic; for $\gamma >$ 100 s^{-1}, the viscosities of reactant blends were constant, and the fluid became Newtonian. For example Fig.2.10 shows viscosity plots for D2000 at five temperatures.

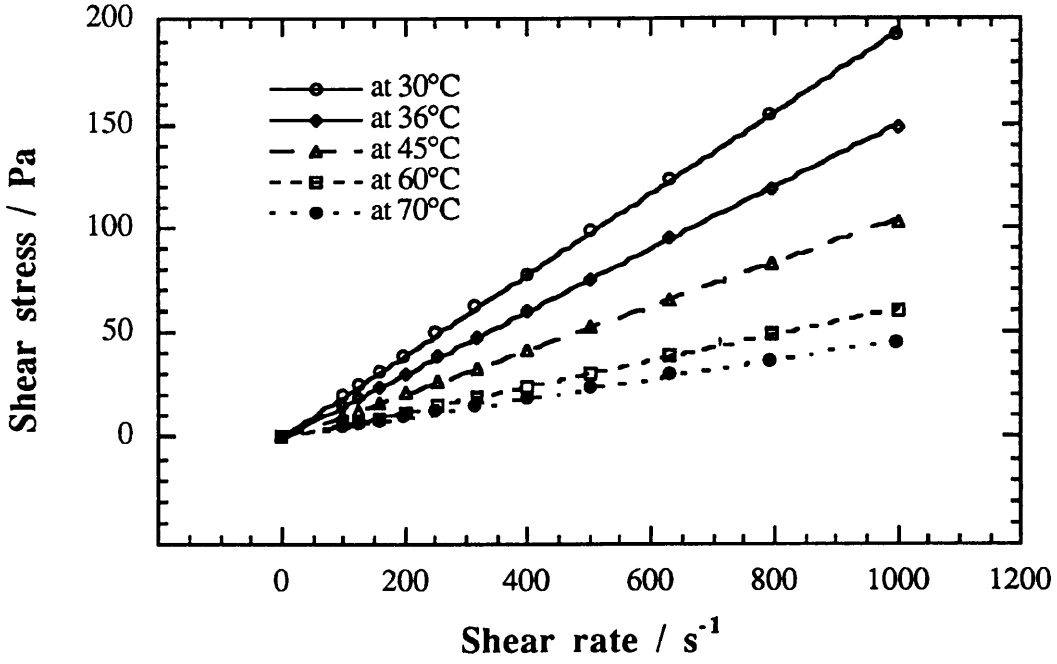

Fig.2.10 The dependent of shear stress on shear rate for D2000 at different temperatures

2.4.2 Results and Discussions

The viscosities of the various reactant blends were measured at five different temperatures in range of 30-70 °C, so as to include the specific processing temperature,

36°C. The results are given in table 2.8.

Table 2.8 The experimental data of viscosities of reactant blends

Blends	M_n / g mol^{-1}	E_n / g mol^{-1}	Viscosity / Pa s				
			30 °C	36 °C	45 °C	60 °C	70 °C
D2000	2000	962	0.194	0.150	0.104	0.061	0.046
D2/20D[(a)]	990	492	0.231	0.167	0.112	0.063	0.046
D2/20M	1224	608	0.265	0.192	0.126	0.069	0.048
D4-D230	2000	962	0.413	0.324	0.226	0.136	0.099
D4000	4000	2000	0.658	0.499	0.341	0.201	0.147
T5000	5000	1754	1.018	0.766	0.518	0.296	0.212
T5/20D	1452	648	1.089	0.793	0.516	0.279	0.194

(a) the viscosities of DETDA at 25 °C and 40 °C are reported [142] to be 0.180 and 0.100 Pa s respectively

Fig.2.11 shows the effect of number average molecular weight (M_n) on viscosities. Clearly, as the molecular weight increases, the viscosity increases for linear polymers, which is predicted by equation [142] $\log\eta = n \log(M_z) + K$, where n is a constant whose value lies between 1.75 and 3.4, M_z is z-average molecular weight ($M_z > M_n$), and constant. For branched T5000, the relationship is much complicated. The introduction of chain branching appears to have the same effect on the viscosity-shear rate curve as broadening of the molecular weight distribution, which increases the viscosity. When D230 was added to D4000 (D230 has similar chemical structure to D4000, but much lower viscosity), the viscosity of D4-D230 blend is decreased, as predicted by the rule-of-mixtures . However, because the molecular weight distribution of D4-D230 blend is much wider than that of D2000, the viscosity of the D4-D230 blend is still much higher than that of D2000, even they have the same number average molecular weight. Fig. 2.12 shows this clearly.

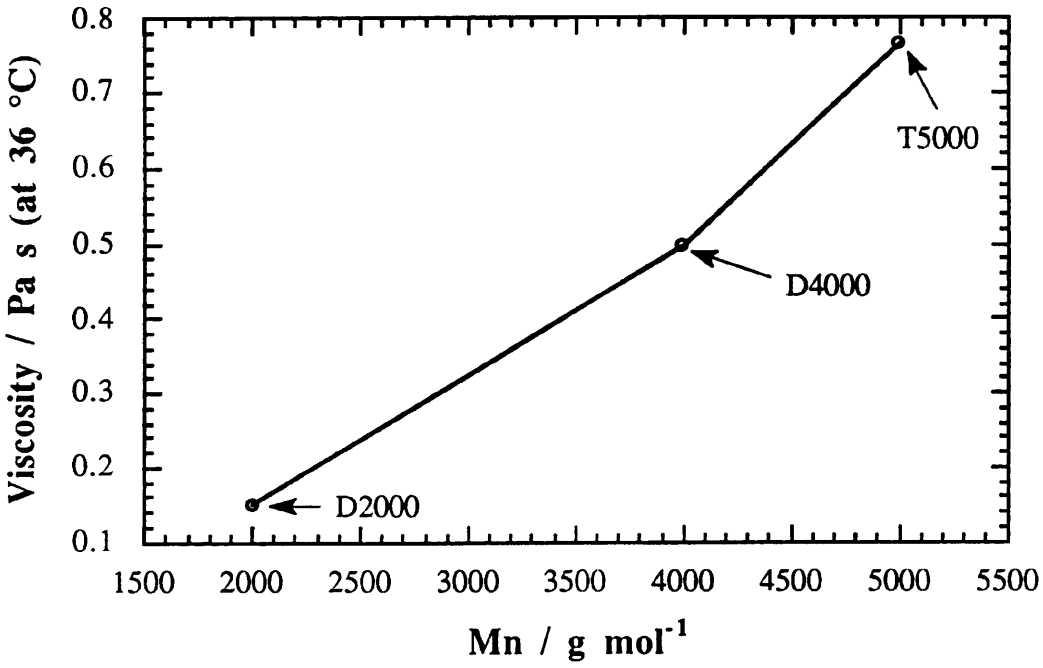

Fig.2.11 The effect of molecular weight on viscosities of amine functionalised polyethers

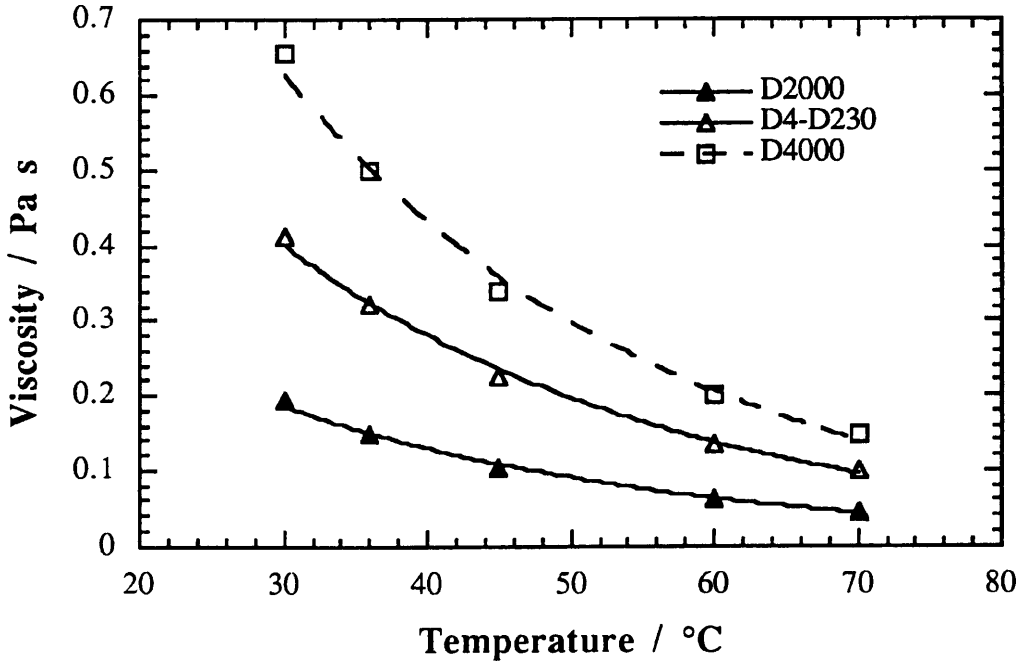

Fig. 2.12 The effect of molecular weight distribution on the viscosities

When the lower viscosity chain extender, DETDA, was added to D2000, the viscosity of D2/20D blend did not decrease as predicted by the rule-of-mixtures, especially at lower temperatures (see Fig.2.13), and this is probably due to chemical interactions and secondary bonding involving the amine groups of DETDA and the ether oxygens of D2000. This may be further supported by the fact that as temperature increases, the difference between the viscosities of D2000 and D2/20D decreases and may be due to the interactions breaking down. The study on T5000 and T5/20D shows the similar result to that of D2000 and D2/20D, and at 70°C, the viscosity of T5/20D is even lower than that of T5000.

The dependence of the viscosity on temperature can be interpreted using the Arrenius equation. For Newtonian liquid, the viscosity-temperature behaviour follows, approximately, the Arrenius [142] equation

$$\eta = A\, e^{E/RT} \tag{2.9}$$

where A is a constant, E is the activation energy for viscous flow, R is the gas constant (8.314 J mol^{-1} K^{-1}), and T the absolute temperature (K). A plot of $\ln(\eta)$ versus 1/RT should therefore be linear with slope E. Data for each reactant blend is analysed accordingly and from which the value of E is calculated. The results are shown in Fig.2.14 and Table 2.9.

Table 2.9 Values of E for reactant blends

	D4-D230	D2000	D4000	T5000	D2/20D	D2/20M	T5/20D
M_n / g mol^{-1}	2000	2000	4000	5000	990	1224	1452
E_n / g mol^{-1}	962	962	2000	1754	492	608	648
E / kJ mol^{-1}	31.0	31.3	32.3	33.9	34.7	36.7	37.2

The increase in the activation energy for viscous flow caused by addition of DETDA is shown by comparing D2000 with D2/20D, and T5000 with T5/20D. The increase is therefore thought to be due to the increase in molecular interactions between amines and

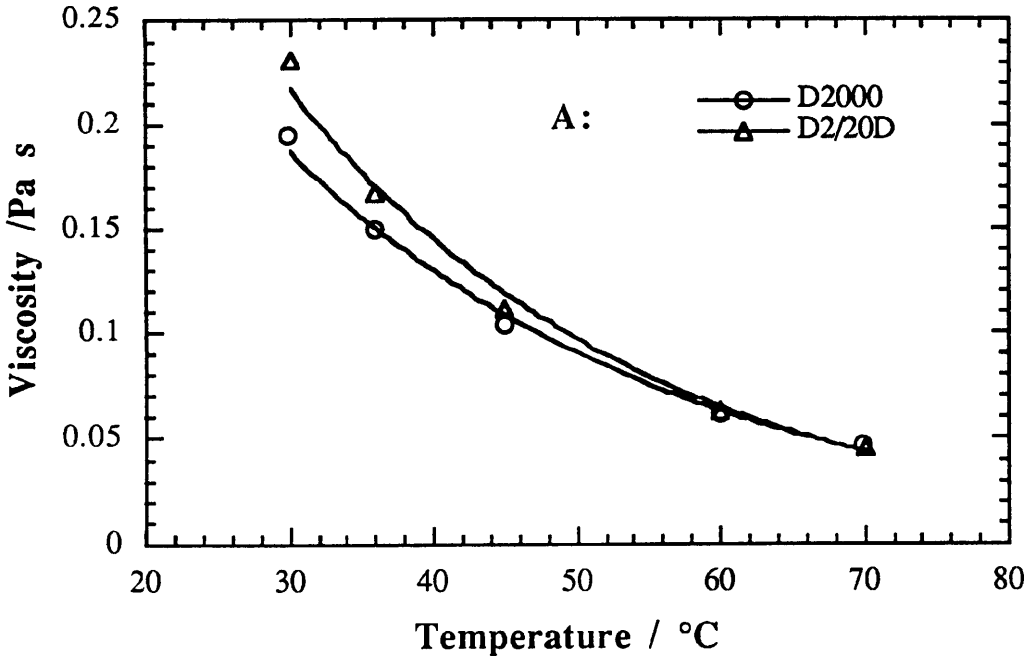

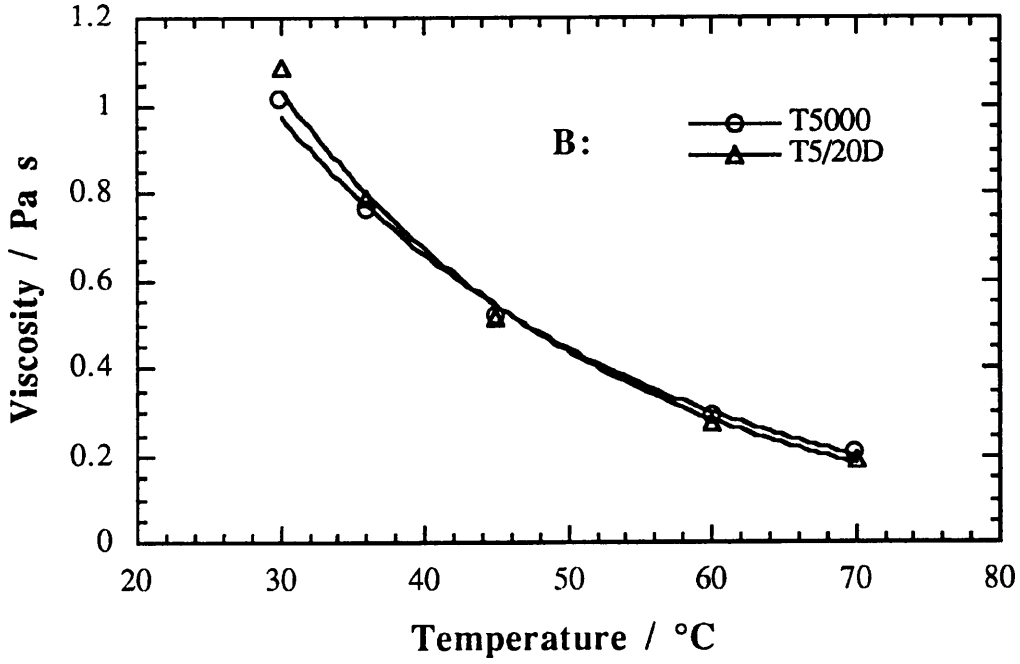

Fig. 2.13 The effect of chain extenders on the viscosity of amine functionalised polyethers. A: DETDA / D2000: B: DETDA / T5000

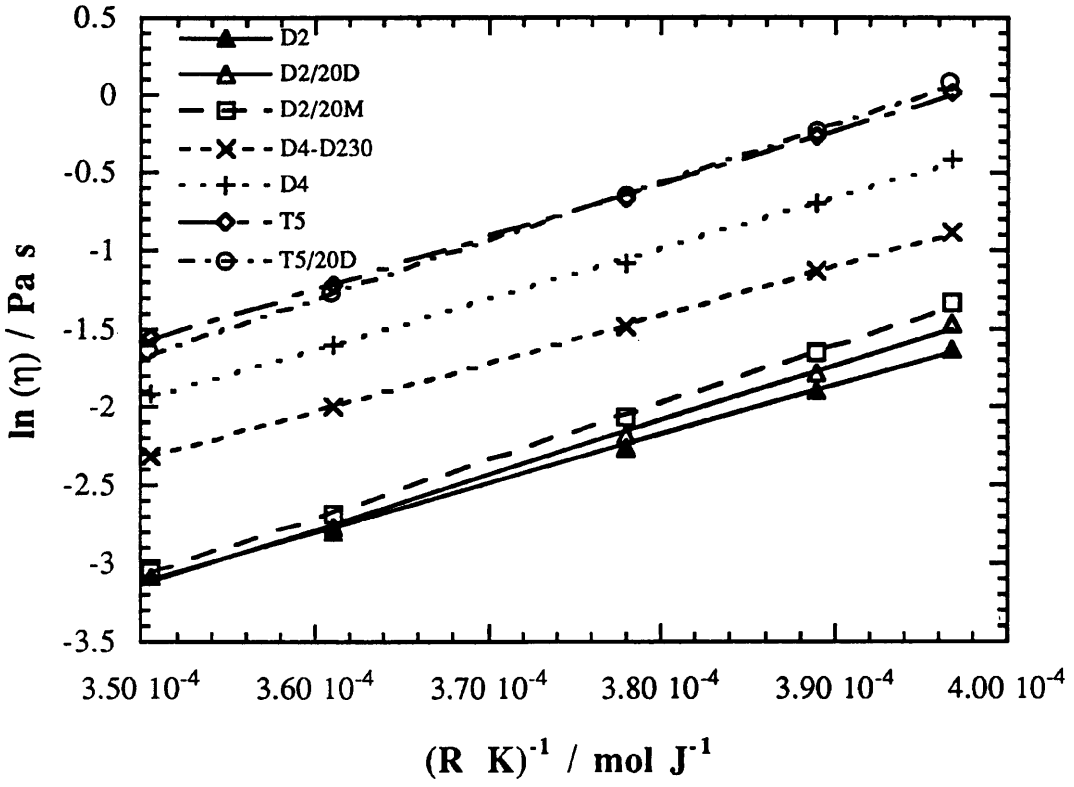

Fig. 2.14 The effect of temperature on the viscosities

ether oxygens (comparing their E_n in Table 2.9). The bigger jump of E from D4000 to T5000, compared with from D2000 to D4000, Probably suggests the contribution of branching. The increase in the activation energy for viscous flow along the series D4-D230 < D2000 < D4000 < T5000 < D2/20D < D2/20M < T5/20D indicates that the dependence of viscosities on temperature follows the same order. In other wards, the viscosity of T5/20D blend, which has the biggest activation energy, is the most sensitive to temperature.

2.5 Reaction Injection Moulding, RIM: Experimental

2.5.1 The RIM Equipment

The RIM equipment used throughout the study was based on a machine originally designed and constructed at UMIST [140] and later modified [141] to process fast reaction polyurethanes, poly(urethane-urea)s and polyureas. A comprehensive description of the

modified HP15 RIM machine has been reported by Wilkinson [120]. The essential features necessary to understand the operation of the machine will be dealt with in this section.

Illustrated in Fig. 2.15 is a schematic representation of the HP15 RIM machine. The polyamine holding tank is pressurised with air and fitted with a motorised stirrer. The polyisocyanate tank is pressurised with dry nitrogen gas supplied from cylinder. Any moisture present in the supply to the polyisocyanate side could lead to a build-up of solid urea products within the pipe lines connecting the tank to the displacement cylinder and mix-head. Such urea depositions tend to break down and , although the equipment is fitted with filters to trap solid debris, some invariably reach the mix-head, block the pin hole and cause blockage. Apart from these differences, the equipment is essentially identical for both the polyamine and polyisocyanate sides. Hence, a generalised description for both will suffice as follows.

Metering is the delivery of reactants to the mix-head at a constant desired flow rate and is achieved by using axial piston pumps driving one-stroke, hydraulic displacement cylinders. The output of hydraulic fluid from the axis piston pumps may be varied using a Vernier adjustment. The hydraulic fluid enters the bottom port of the vertically-mounted displacement cylinder, forcing the piston to rise. Consequently, reactant is forced out from the top port of the cylinder at a rate dependent on the pump setting. With valve V_1 closed, the reactant is delivered to the mix-head. After the displacement piston has risen to a pre-determined height (dictated by the cycle time), the output of the axial piston pump is diverted back to the tank and V_1 is opened. The pressurisation on the storage tanks forces reactant back into the top port of the displacement cylinder, moving the lance piston to its fully-down position.

The equipment incorporates a Krauss-Maffei MK 8 / 12-UL-2K mix-head. This device based on the principal of mixing by impingement and also allows recirculation of reactants near the mixing chamber so as to maintain their temperature. A schematic representation of a cross-section through the mix-head is given in Fig. 2.16. The head is of the 'long L' design, with an 8 mm diameter mixing chamber (4 cm^3 capacity) leading to a

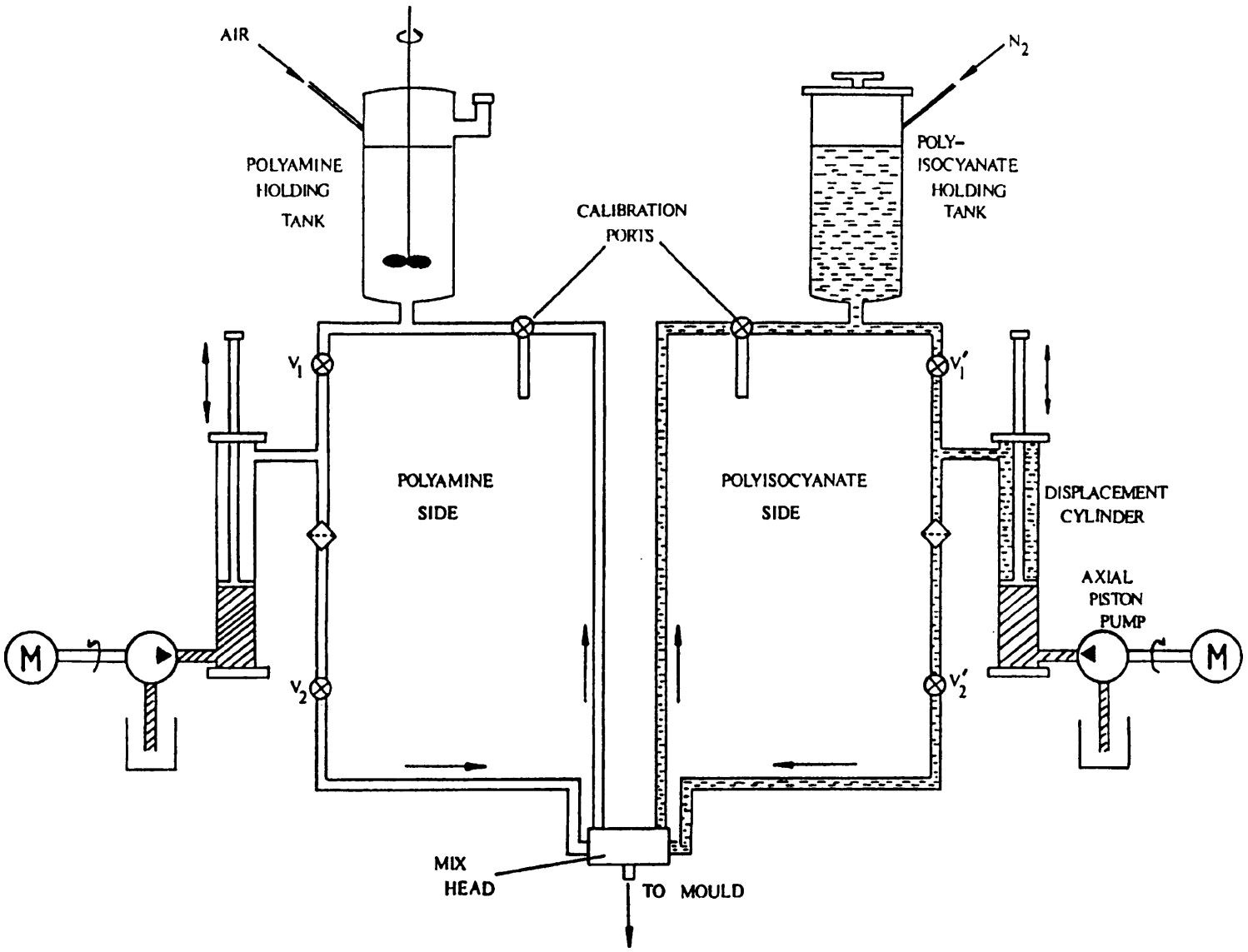

Figure 2.15 Schematic illustration of the UMIST HP15 RIM equipment [63]

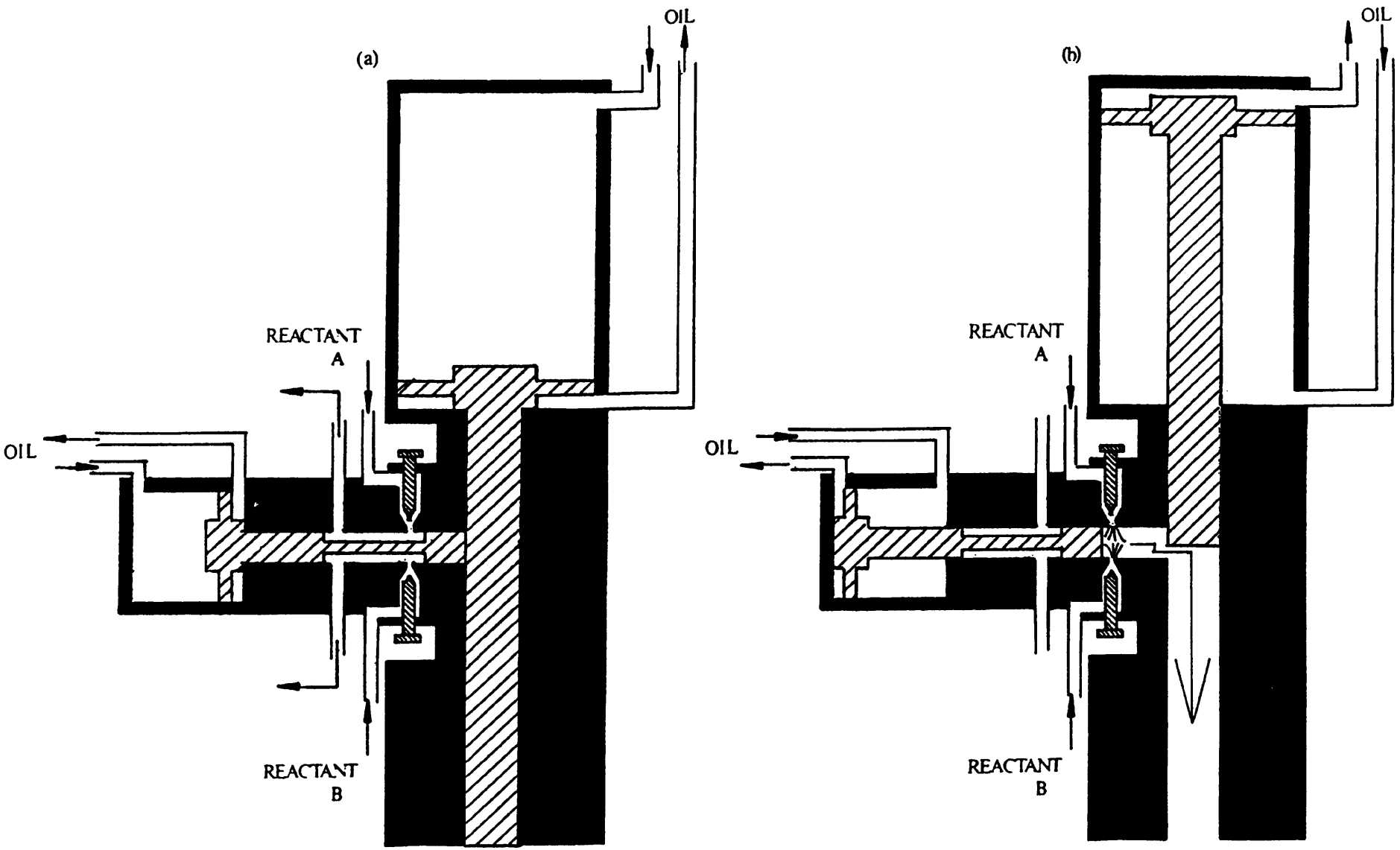

Figure 2.16 Schematic representation of the Krauss-Maffei 'long L' type mix-head. (a) recirculation mode; (b) mixing mode [63].

12 mm diameter dispensing chamber, each of which has a self-cleaning piston. Mixing efficiency was evaluated by Molnar et al [18] using ATR data and high-speed photographic visualisation techniques. In this way, various types of mix-head were compared and it was shown that 'L'-types give better mixing than conventional single piston, 'I'-type, mix-heads and provide much more laminar-like flow from the outlet nozzle.

Reactants (polyamine blends and polyisocyanate) flow separately to the mix-head and pass through nozzle and pintle assemblies before entering the mixing chamber. Such assembly can be externally adjusted so that a pintle can be positioned within the fixed circular diameter of the nozzle. The tapered nature of the pintle and nozzle allows the thickness of annular orifices to be varied. Depending on the viscosity and deliver rate of the reactants, the desired pressure of the reactants can be achieved by adjusting the size of the annular-orifices. Typical pressure value for polyamine blends is 3000 psi (207×10^5 N m^{-2}), which corresponds to reactant velocities of approximately 100 m s^{-1} [138]: typical pressure value for the polyisocyanate is 2000 psi. Such pressures are required to obtain turbulence during impingement, which is essential for efficient mixing. In general terms, turbulent flow of a liquid can be achieved when its Reynolds number, Re, the ratio of inertial to viscous forces, exceeds or equals a critical value, Re_{crit}. The determination of Re will be discussed in section 2.5.2.

During recirculation (Fig.2.16a), reactants enter the mixing chamber from the nozzle and pintle assemblies, but do not impinge because the small piston (in the mixing chamber) is in the closed position. This piston has machined grooves along its length which keep the reactants separate, transferring them to the outlet port and back to their respective holding tanks.

During a mixing cycle (Fig. 2.16b), recirculation is achieved first and then under automatic control from a series of timers and relays, the hydraulics to the mix-head piston are operated sequentially. The sequential operation is as follows [138]:

(1) The large dispensing piston is withdrawn, followed by rapid activation of the small piston. Reactants impinge from diametrically-opposed nozzles under turbulent

conditions and flow into the dispensing chamber. A degree of laminar-like flow is achieved as the reacting mixture exits the chamber under relatively low pressure.

(2) After the desired shot time, the small piston is rapidly closed, expelling the remaining material and re-establishing recirculation.

(3) Almost instantaneously the rapid downward (closing) motion of the dispensing piston cleans the remaining material out of the head.

(4) The reacting mixture flows through a baffle-type after-mixer and a dam-gate, then into the mould (the design of the mould is fully discussed by Ward [52]). The cavity of the mould is 150×450×3 mm.

The heating of the mould was provided by the circulation of oil through channels machined through the top and bottom platens of the tool. A Conair Churchill 3-200 oil heater with a temperature controller was used to deliver oil, at the appropriate temperature (max. 185 °C), through steel-braided hoses to the inlet channels at the back of the mould. Oil returns to the heater via outlet ports. The maximum attainable temperature of the mould cavity and gating arrangement is 176 ± 2°C. A mould temperature of 90 ± 2°C was used throughout this study.

2.5.2 Reynolds Number and RIM Processing

In RIM Processing, efficient mixing can be achieved when turbulent conditions are achieved. The degree of turbulence is defined in terms of the Reynolds number, Re, which is the ratio of the kinetic or inertial forces, which promote mixing, to the viscous forces which oppose mixing. In its simplest form for flow in a circular orifice, Re is given [143] as

$$Re = \frac{4\,Q}{\pi\, d\, \eta} \tag{2.10}$$

where d is the nozzle orifice diameter (m), and η is the dynamic viscosity of the fluid (Pa s), and Q is the volumetric throughput. However, in practice, the application of equation (2.10) to commercial mix-heads is difficult because of their complicated geometries. The mix-head

utilised in this study has a complex orifice arrangement, and a simple definition of d is impossible. For this reason, alternative expressions have been derived [20, 143, 144] which eliminated d, such as,

$$Re = \frac{4 W K}{\pi \eta^2} \sqrt{2 g \rho \Delta P} \qquad (2.11)$$

where W is the mass throughput (kg s^{-1}), ΔP is the pressure drop (MPa)on entering the mixing chamber and K is a nozzle factor to account for die swell of the reaction stream and drag during flow through the mix-head orifice [144]. The value of K for a Krauss-Maffei mix-head has been reported [144, 145] to be between 0.8 and 0.83. The term g in Eq (2.11) is the gravitational constant (9.81 m s^{-2}). Values of Re are calculated from Eq (2.11), and the results and processing parameters are given in Table 2.10.

Table 2.10 Processing Parameters and Re

Reactant Blends	Q kg s^{-1}	$\eta^{(a)}$ Pa s	Re	ΔP MPa	ρ kg m^{-3}
D2000	0.070	0.150	1411	20.7	1000
D2/20D	0.070	0.167	1268		
D2/20MD	0.070	0.192	1103		
D4-D230	0.069	0.324	653		
D4000	0.069	0.499	424		
T5000	0.069	0.766	276		
T5/20D	0.070	0.793	267		
M143	0.140	< 0.038	> 7520	13.8	1210

(a) data at 36 °C from Table 2.8

The experimental operating procedures used to form PUrI are summarised in the flow chart shown in Fig 2.17 [138]. A more detailed description of the various operating stages, A-F, is given below.

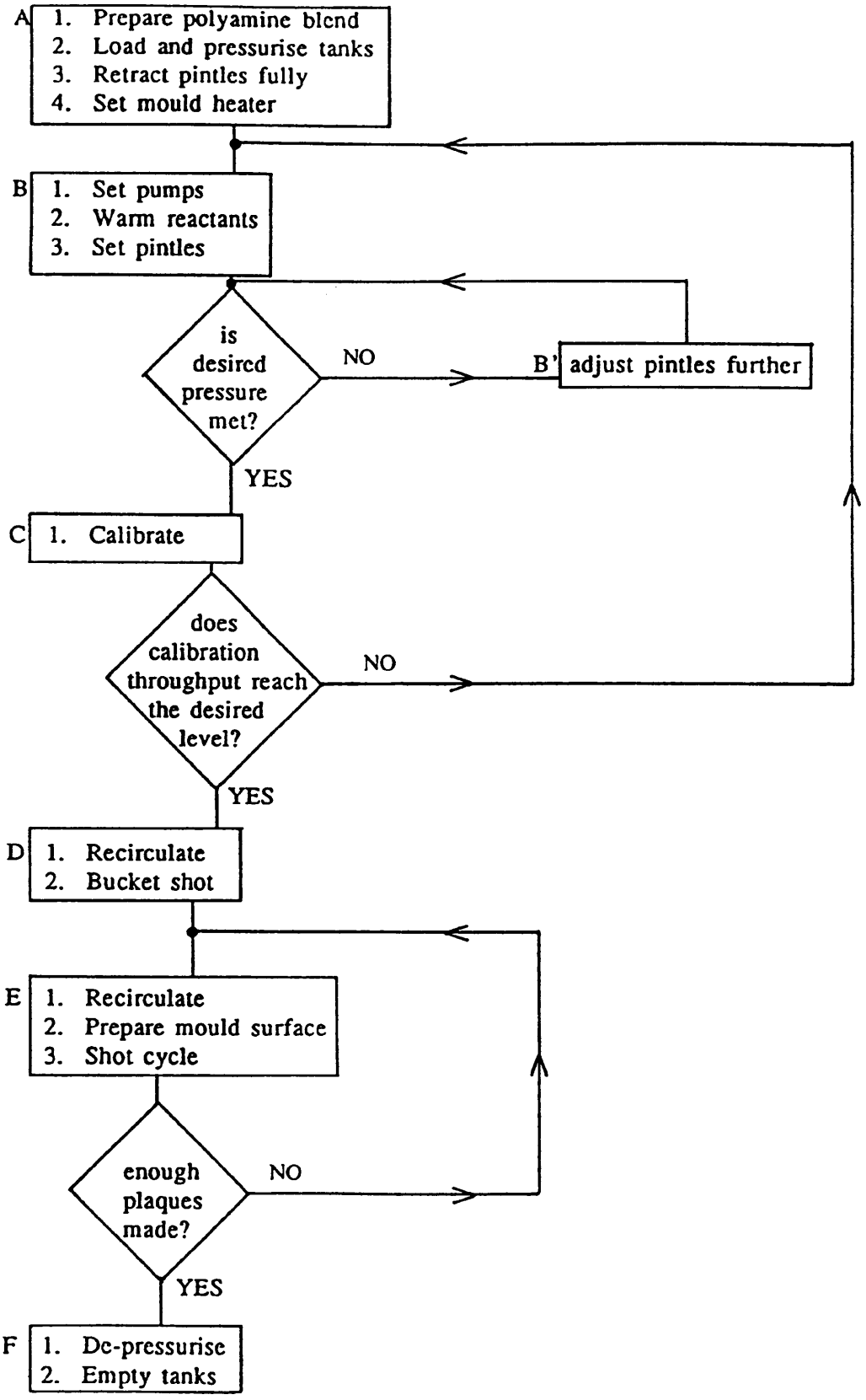

Figure 2.17 Operation flow diagram for HP 15 RIM machine [63].

Stage A

1. The desired formulation of chain extender, catalyst and polyamine were tared and mixed in an open drum. In formulations containing MDIPA, the MDIPA was first melted at 80 °C prior to tarring and mixing.

2. The polyamine and polyisocyanate tanks were filled and pressurised.
3. The pintle in the mix-head were drawn back fully to avoid high pressures being developed as high viscous (cold) reactants were first recirculated.
4. The mould heater was set to achieve the desired mould cavity temperature (90 °C). The mould was closed to avoid excess heat loss.

Stage B

1. The pumps were set via the Vernier adjustment to achieve an approximate throughput based on stoichiometry.
2. Reactants were recirculated at low pressure through the mix-head to achieve the desired temperatures, 36 °C.
3. As the reactants approached the desired temperature, the pintles on the mix-head were inserted to develop the desired processing pressure.

Stage C

1. The reactants were recirculated at the processing temperature and pressure. Mid-way during the movement of the displacement pistons for a two second period, the returning stream was diverted to a tared container via the calibration port (Fig 2.15). The mass throughput was determined.

(NB: stages B and C were repeated until the desired conditions for processing and of stoichiometry had been obtained.)

Stage D

1. Recirculation was used to maintain reactant temperature.
2. A plastic bag was placed in a 1L beaker, and this was placed underneath the mix-head. The mix-head hydraulics were initiated and a 1.2 s shot was dispensed

into the bag. This operation is known as a 'bucket shot' and was used to assess the suitability of the system for moulding in term of solidification time and mixing quality (visual homogeneity).

Stage E

1. Assuming the bucket shot was successful, the reactants were recirculated further to maintain the temperature.
2. The mould surface was cleaned and coated with 1711 mould release agent. The mould was closed and kept shut during moulding with using a hydraulic press.
3. The reactant mixture was dispensed into the mould. Five minutes later, the mould was opened and the resultant plaque removed.

Stage F

1. The tanks were de-pressurised with the displacement lances in the full-up position (cylinders empty of reactant).
2. The polyamine blend lines were uncoupled at the mix-head and placed into an appropriate drum (e.g. for waste or for storage). The tank was re-pressurised forcing all remaining reactant out of the holding tank and lines and into the drum. polyamine side was cleaned by repeated recirculation and draining with dioctyl phthalate (DOP), plasticiser (flushing).

2.6 Adiabatic Temperature Rise (ATR)

2.6.1 Test Method

A micro-RIM machine was used during ATR study, and a schematic diagram of the experimental set-up is shown in Fig.2.18. Reactant systems used to form PUrI were injected into a paper cup (200 cc) through a glass fibre-reinforced polypropylene pipe of 25 cm length. The paper cup was insulated by a block of polyurethane foam, and two J-type thermocouples were located around the centre of the cup, 5-10 mm above the bottom of the cup. The time to cover these thermocouples by reacting mixture, i.e. delay time for temperature measurements, is ~0.1s. Temperature data were collected with an A / D

converter and a Macintosh II microcomputer. ATR Experimental shows that the experimental set-up shown in Fig.2.18 is very efficient to be used to obtain ATR data.

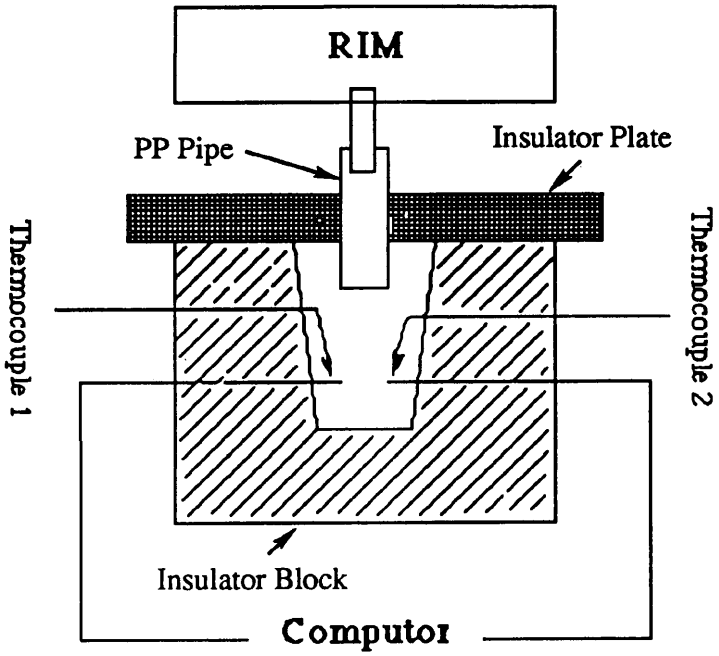

Figure 2.18 A schematic diagram of the experimental set-up used to obtain ATR data

The quality of mixing of a reactant system can be assessed by comparing ATR data obtained from different locations within the same reactant mixture in the paper cup of the experimental set-up in Fig.2.18. Such compression experiments can be carried out by using two thermocouples simultaneously again as shown in Fig.2.18. Fig.2.19 shows typical data for D2/20MD/M/1.6, and since the data from two thermocouples are essentially coincident, it may be concluded that good quality of mixing of a reactant system is achieved.

2.6.2 Analysis of ATR Data

To obtain accurate ATR data, a temperature correction must be applied to account for (i) heat rises due to viscous dissipation from reactants passing through the RIM mix-head and (ii) for heat losses due to conduction through the insulation block. In order to analysis ATR data, the following assumptions can be used [41, 37]:

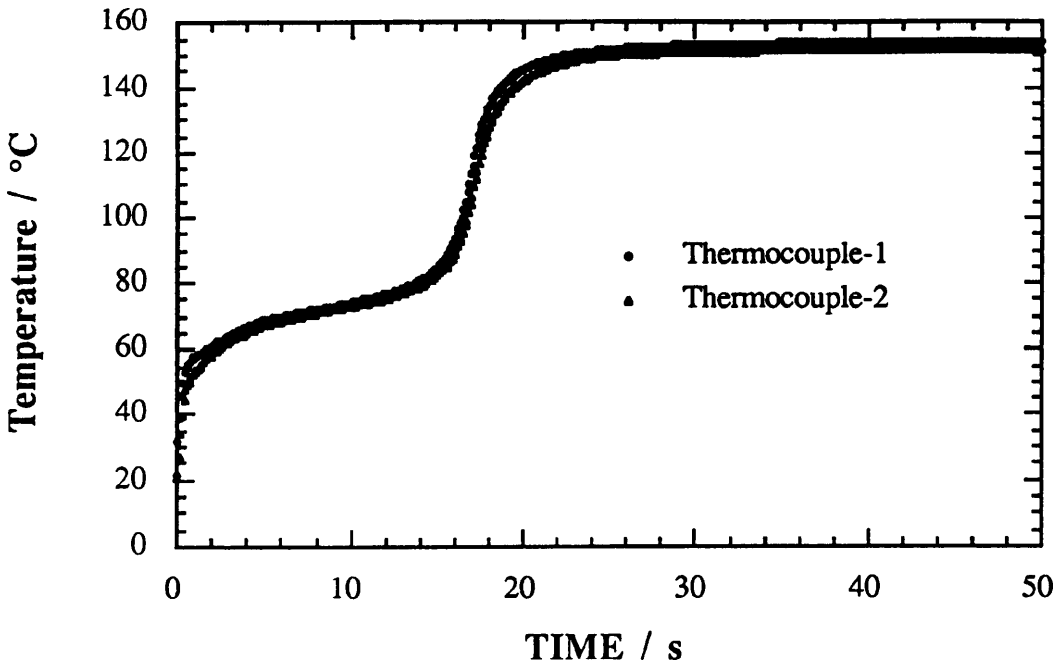

Fig. 2.19 Mixing quality of mix-head for D2/20MD/M/1.6

(a) constant heat(s) of reaction over the temperature range,

(b) the heat capacity and density of the reactant system remain constant over the temperature range,

(c) the reactant mixture becomes homogeneous rapidly after impingement,

(d) no heat sources other than the reaction(s) contribute to ATR,

(e) no restrictions due to diffusion control affect the reaction rate(s).

The energy balance for a single irreversible reaction is [41]:

$$\rho C_p \frac{dT}{dt} = (-\Delta H_r) r_a - U (T-T_{amb}) \qquad (2.12)$$

where U is the heat transfer coefficient per unit volume, r_a is the reaction rate, ΔH_r is the heat of reaction, C_p is the heat capacity, ρ is the density, t is the reaction time, T is the temperature at time t, and T_{amb} is the ambient temperature. The reaction rate can be

expressed in terms of the initial concentration, C_o, of the limiting reactant, and the extent of reaction ($\alpha = (C_o - C) / C_o$), so that Eq (2.12) can be rewritten as

$$\rho C_p \frac{dT}{dt} = (-\Delta H_r) C_o \frac{d\alpha}{dt} - U (T-T_{amb}) \tag{2.13}$$

The heat transfer coefficient can be determined using a non-reactive system for which the energy balance simplifies to

$$\rho C_p \frac{dT}{dt} = - U (T-T_{amb}) \tag{2.14}$$

and with the assumption of constant ρ and C_p, Eq(2.14) can be integrated to give

$$\ln (T - T_{amb}) = \ln (T_o - T_{amb}) - \frac{U}{\rho C_p} (t - t_o) \tag{2.15}$$

where t_o (= 0) is initial reaction time, and T_o is initial temperature of the reactant mixture (at t_o), and is defined as the weight-average temperature of the reactants

$$T_o = \frac{T_1 W_1 + T_a W_a}{W_1 + W_a} \tag{2.16}$$

The value of U can be calculated from the slope of a plot of $\ln (T - T_{amb})$ vs $(t - t_o)$, which enables the temperature correction term, $U (T-T_{amb})$ in Eq(2.13) to be applied. A subtraction of 2 °C [37] must also be applied to T in Eq(2.13) to correct for the viscous dissipation heat rise resulting from impingement. Such corrections then allow temperatures and fractional conversion to be directly related according to

$$\alpha = \frac{\rho C_p (T - T_o)}{- \Delta H_r C_o} \tag{2.17}$$

The heat of reaction is calculated from the maximum temperature, T_{ad},

$$-\Delta H_r = \frac{\rho C_p (T_{ad} - T_o)}{C_o} \tag{2.18}$$

Combining Eqs (2.17) and (2.18) gives the final expression for α for a single reaction system as

$$\alpha = \frac{T - T_o}{T_{ad} - T_o} \qquad (2.19)$$

However, Eq(2.19) developed for only a single reaction system is not applicable to the present copoly(urea-isocyanurate) (PUrI) systems such as that shown in Fig.2.19. In the case of PUrI, more than one reaction occurs during copolymerisation and the situation is more complicated, and requires the development of alternative energy balance expressions which, in particular, cover the two cases: (i) polyether diamine + polyisocyanate, and (ii) polyether diamine + chain extender + polyisocyanate. In general, the alternative energy balance expressions may be subsumed into a single expression which may be applied to multi-sequence reaction systems.

Firstly, an alternative energy balance expression is developed for the particular case of the three reaction system (ii) shown in Fig.2.20. Table 2.11 summaries the reactants involved in the three reactions and gives comparative reaction rate data for each step in terms of the time taken to achieve 25% conversion of isocyanate groups. Table 2.11 shows that reaction (1) occurs firstly, and in the case of large excess of isocyanate, it gives isocyanate group tipped urea; reaction (2) occurs secondly, and in the case of large excess of isocyanate, it gives isocyanate group tipped aromatic urea; finally, all of the isocyanate groups (of urea, aromatic urea and M143) polytrimerise to give PUrI (reaction (3) in Fig.2.20 only shows the trimerisation of M143, but applies to products from reactions (1) and (2)).

Table 2.11 The time for 25% conversion of reactions

Reaction	(1)	(2)	(3)
Reactants	D2000 + M143	Chain extender + M143	Polytrimerisation of M143
Time / s	~ 10^{-3} [34]	15 [34]	50 [(a)]

(a) no literature data available: value obtained from ATR data in present study.

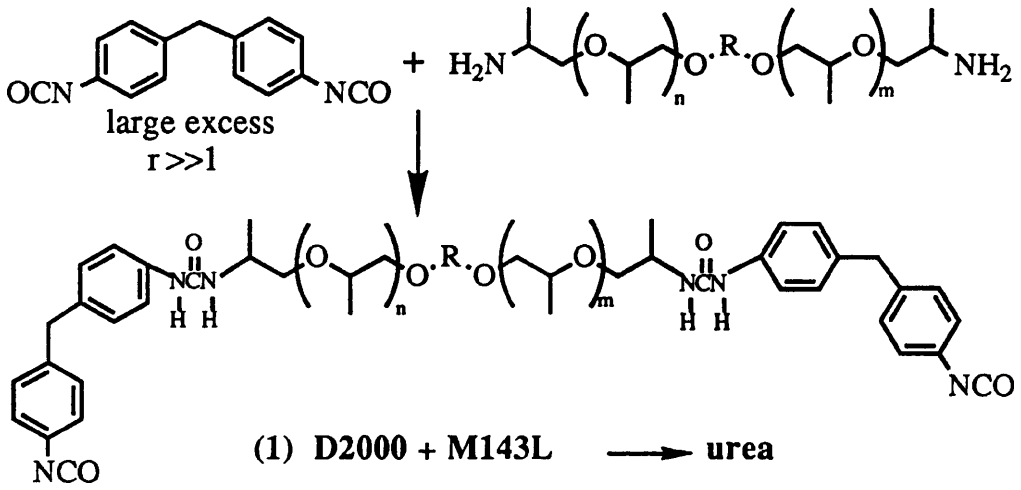

(1) D2000 + M143L ⟶ urea

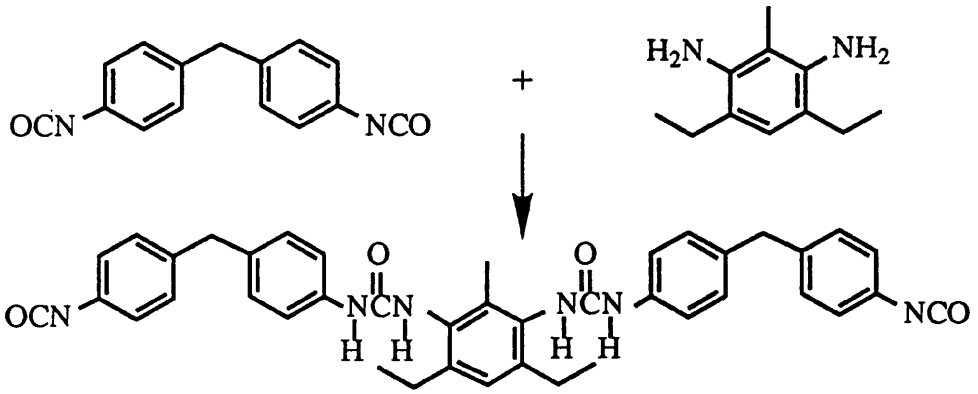

(2) chain extender + M143L ⟶ urea

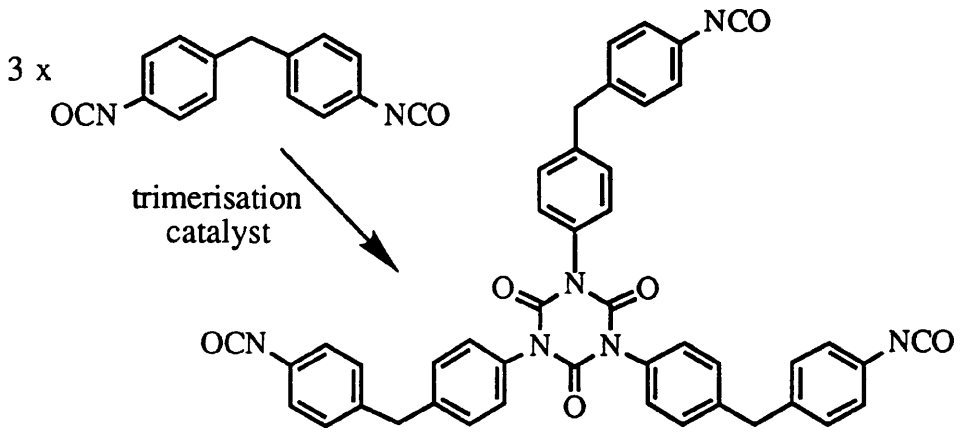

(3) polytrimerisation of M143L

Figure 2.20 Reaction scheme for the three-reaction system D2000 + DETDA + M143, The three reactions are shown as (1), (2) and (3).

Based on these data in Table 2.11, it may assumed to a first approximation that three reactions are sequential, thus simplifying the ATR analysis. The previous assumptions (b), (c), (d), and (e) on page 75 are still valued and are used to develop the new expression. Thus, for the system involving three sequential irreversible reactions, such as D2/20D/M, the energy balance is

$$\rho C_p \frac{dT}{dt} = -(\Delta H_1 + \Delta H_2 + \Delta H_3) r_a - U (T - T_{amb}) \tag{2.20}$$

where ΔH_1, ΔH_2, and ΔH_3 (ΔH_I) are the heats of reaction for reaction (1) occurring between t_o and t_1), reaction (2) occurring between t_1 and t_2 and reaction (3) occurring between t_2 and t_3, respectively. Using corrected temperature data, Eq(2.20) can be written as

$$\rho C_p \frac{dT}{dt} = -(\Delta H_1 + \Delta H_2 + \Delta H_3) r_a = -(\Delta H_1 + \Delta H_2 + \Delta H_3) C_o \frac{d\alpha}{dt} \tag{2.21}$$

where α is the fractional conversion $(C_o - C) / C_o$ of isocyanate groups. Rearranging Eq(2.21):

$$d\alpha = \frac{\rho C_p}{-(\Delta H_1 + \Delta H_2 + \Delta H_3) C_o} dT \tag{2.22}$$

Integrating Eq(2.22) from To to T, corresponding to $t = t_o$ to $t = t$ ($t \le t_1$) with $\Delta H_2 = \Delta H_3 = 0$ gives

$$\alpha = \frac{\rho C_p (T - T_o)}{-\Delta H_1 C_o} \tag{2.23}$$

When reaction (1) is complete at $t = t_1$, the fractional conversion, α_1, of isocyanate groups is

$$\alpha_1 = \frac{\rho C_p (T_1 - T_o)}{-\Delta H_1 C_o} \tag{2.24}$$

where T_1 and T_o are the temperatures at reaction time t equal to t_1 and t_o, respectively. Combining Eqs (2.23) and (2.24) gives the fractional conversion, α, of isocyanate groups occurring via reaction (1) corresponding to $t_o \le t \le t_1$. That is,

$$\alpha = \alpha_1 \frac{T - T_o}{T_1 - T_o} \qquad t_o \le t \le t_1 \tag{2.25}$$

Integrating Eq(2.22) from t_1 to t ($t_1 < t \leq t_2$), corresponding to T_1 to T ($\Delta H_1 = \Delta H_3 = 0$), gives

$$\alpha - \alpha_1 = \frac{\rho\, C_p\, (T - T_1)}{-\Delta H_2\, C_o} \tag{2.26}$$

When reaction (2) is complete at $t = t_2$, the fractional conversion, α_2, of isocyanate groups is

$$\alpha_2 - \alpha_1 = \frac{\rho\, C_p\, (T_2 - T_1)}{-\Delta H_2\, C_o} \tag{2.27}$$

where T_2 is the temperature at $t = t_2$. Combining Eqs (2.26) and (2.27) gives the fractional conversion, α, of isocyanate groups occurring via reactions (1) and (2) corresponding to $t_1 \leq t \leq t_2$.

$$\alpha = (\alpha_2 - \alpha_1)\frac{T - T_1}{T_2 - T_1} + \alpha_1 \qquad t_1 \leq t \leq t_2 \tag{2.28}$$

Similarly, for the third reaction corresponding to $t \geq t_2$, the total fractional conversion, α, is

$$\alpha = (1 - \alpha_2)\frac{T - T_2}{T_{ad} - T_2} + \alpha_2 \qquad t_2 \leq t \tag{2.29}$$

where T_{ad} is the maximum adiabatic temperature rising. Thus the conversion of isocyanate groups at any time t is obtained by relating t to t_1 and to t_2, and then by applying the appropriate Equation from the three expressions given in Eq(2.30).

$$\alpha = \begin{cases} \alpha_1 \dfrac{T - T_o}{T_1 - T_o} & t_o \leq t \leq t_1 \\ (\alpha_2 - \alpha_1)\dfrac{T - T_1}{T_2 - T_1} + \alpha_1 & t_1 \leq t \leq t_2 \\ (1 - \alpha_2)\dfrac{T - T_2}{T_{ad} - T_2} + \alpha_2 & t_2 \leq t \end{cases} \tag{2.30}$$

For the first reaction, rewriting Eq(2.24) gives

$$-\Delta H_1 = \frac{\rho\, C_p\, (T_1 - T_o)}{\alpha_1\, C_o} \tag{2.31}$$

For the second reaction, rewriting Eq(2.27) gives

$$-\Delta H_2 = \frac{\rho\, C_p\, (T_2 - T_1)}{(\alpha_2 - \alpha_1)\, C_o} \tag{2.32}$$

Similarly, for the third reaction, the reaction heat, ΔH_3, is

$$-\Delta H_3 = \frac{\rho\, C_p\, (T_{ad} - T_2)}{(1 - \alpha_2)\, C_o} \tag{2.33}$$

If heat capacity is a linear function of temperature (Cp = a + b T), by repeating previous analysis except of using a + b T to replace Cp, then Eq(2.30) is modified as

$$\alpha = \begin{cases} \alpha_1 \dfrac{a\,(T - T_o) + \frac{b}{2}(T^2 - T_o^2)}{a\,(T_1 - T_o) + \frac{b}{2}(T_1^2 - T_o^2)} & t_o < t \le t_1 \\ (\alpha_2 - \alpha_1) \dfrac{a\,(T - T_1) + \frac{b}{2}(T^2 - T_1^2)}{a\,(T_2 - T_1) + \frac{b}{2}(T_2^2 - T_1^2)} + \alpha_1 & t_1 < t \le t_2 \\ (1 - \alpha_2) \dfrac{a\,(T - T_2) + \frac{b}{2}(T^2 - T_2^2)}{a\,(T_{ad} - T_2) + \frac{b}{2}(T_{ad}^2 - T_2^2)} + \alpha_2 & t_2 < t \end{cases} \tag{2.34}$$

and Eqs(2.31), (2.32), and (2.33) is modified as

$$-\Delta H_1 = \frac{\rho}{\alpha_1\, C_o}\left[a\,(T_1 - T_o) + \frac{b}{2}(T_1^2 - T_o^2)\right] \tag{2.35}$$

$$-\Delta H_2 = \frac{\rho}{(\alpha_2 - \alpha_1)\, C_o}\left[a\,(T_2 - T_1) + \frac{b}{2}(T_2^2 - T_1^2)\right] \tag{2.36}$$

$$-\Delta H_3 = \frac{\rho}{(1 - \alpha_2)\, C_o}\left[a\,(T_{ad} - T_2) + \frac{b}{2}(T_{ad}^2 - T_2^2)\right] \tag{2.37}$$

For more complicated, n sequential reactions, by repeating the analysing method used above, the fractional conversion, α, is expressed as

$$\alpha = (\alpha_j - \alpha_{j-1}) \frac{a\,(T - T_{j-1}) + \frac{b}{2}(T^2 - T_{j-1}^2)}{a\,(T_j - T_{j-1}) + \frac{b}{2}(T_j^2 - T_{j-1}^2)} + \alpha_{j-1} \qquad t_{j-1} < t \le t_j \tag{2.38}$$

and corresponding equation for the reaction heats are

$$-\Delta H_j = \frac{\rho}{(\alpha_j - \alpha_{j-1})\, C_o} \left[a\,(T_j - T_{j-1}) + \frac{b}{2}(T_j^2 - T_{j-1}^2) \right] \qquad (2.39)$$

where j = 1, 2, ...n, $\alpha_o = 0$, $\alpha_n = 1$, and $T_n = T_{ad}$.

Eqs (2.38) and (2.39) will be used to predict fractional conversion, α, of isocyanate groups at any time, t, and to calculate ΔH_I (isocyanate groups polytrimerise to form polyisocyanurate)and ΔH_2 (MDIPA reacts with MDI to form isocyanate group tipped aromatic urea) under the experimental conditions. The basic data required in calculation using Eqs(2.38) and (2.39) are given in the Table 2.12.

Table 2.12 The basic data required in calculation using Eqs(2.38) and (2.39)

C_p [(a)]	C_o	T_o	ρ	ΔH_1[(a)]	ΔH_2[(b)]	α_2	α_1
kJ K^{-1} kg^{-1}	eq L^{-1}	K	kg L^{-1}	kJ eq^{-1}	kJ eq^{-1}		
$1.82 + 2.01\times10^{-3}$ T	5.57	310.49	1.19	111	94	$\frac{1}{r}$ (c)	$\frac{\beta}{r}$ (d)

(a) see reference [37], (b) see reference [41], (c) referring to r = [NCO] / [NH_2],
(d) referring to β = [aliphatic NH_2] / ([aliphatic NH_2] + [aromatic NH_2]).

The Eqs(2.38) , (2.39) and data in Table 2.12 have been applied to each of the systems in Table 2.13.

(1) For D2/M/1.6, T5/M/1.6, D4-D230/M/1.6, two reactions occur (n = 2). Eq (2.39) is used to calculate T_1 (j = 1); t_1 (at $T = T_1$) and T_{ad} can be read from the respective experimental ATR curves. Then Eq (2.38) is used to calculate the fractional conversion of isocyanate groups at any time. From Eq (2.39), $-\Delta H_I$ can be also calculated by putting j = 2.

(2) For D2/20D/M/1.6 and T5/20D/M/1.6, three reactions occur (n = 3). T_1 (j = 1) and T_2 (j = 2) can be obtained from Eq (2.39); t_1 (at $T = T_1$), t_2 (at $T = T_2$), and T_{ad} can

Table 2.13 Kinetics parameters derived from Eqs (2.38) and (2.39)

PUr.I[a]	r	C_0 / eq L^{-1}	α_1	α_2	β	T_1 / K	T_2 / K	T_{ad} / K	ΔH_1 / kJ eq^{-1}	ΔH_2 / kJ eq^{-1}	t_1 / s	t_2 / s	t_g / s
D230/M	1.69	5.57	0.592	(b)	(b)	436	(b)	436	(b)	(b)	~ 0.1	(b)	~ 0.1
D2/M	14.2	5.57	0.070	(b)	(b)	325	(b)	430	62	(b)	0.6	(b)	~ 9
D4-D230/M	14.2	5.57	0.070	(b)	(b)	325	(b)	422	53	(b)	0.7	(b)	~ 26
T5/M	27.0	5.57	0.037	(b)	(b)	318	(b)	405	49	(b)	0.6	(b)	~ 42
D2/20D/M	7.15	5.57	0.064	0.140	0.46	324	338	427	57	94 [c]	0.4	~2	~ 14
D2/20MD/M	8.83	5.57	0.061	0.113	0.54	324	330	426	60 [d]	71	0.7	2.1	~ 17
T5/20D/M	9.30	5.57	0.073	0.108	0.32	324	331	408	47	94 [c]	0.5	~2	~ 41

(a) the catalyst level for all PUr.I in this table is 1.6%

(a) not applicable

(c) reference [41].

(d) average value of 62 for D2/M and 57 for D2/20D/M.

be read from the ATR curve. Fractional conversion of isocyanate groups at any time, α, can be calculated from Eq.(2.38) and $-\Delta H_I$ can be calculated from Eq(2.39) by putting j = 3.

(3) For D2/20MD/M/1.6, T_1 (j = 1), t_1 (at $T = T_1$), and T_{ad} can be determined as for other systems. If the average value of $-\Delta H_I$ obtained from other systems is taken as the value of $-\Delta H_I$ for D2/20MD/M/1.6, T_2 can be calculated from Eq (2.39) (when j = 3), and t_2 read from the ATR curve. Then reaction heat of MDIPA with M143, and fractional conversion of isocyanate groups at any time can be calculated by Eqs (2.39) (when j = 2) and (2.38) respectively.

In the cyclotrimerisation of diisocyanate, gelation is predicted [58] to occur at 50% conversion of isocyanate groups. Based on this conversion and experimental, the gelation time, t_g, of the reaction systems for forming PUrI can be evaluated. All the kinetics calculation results are given in Table 2.13.

Comparing value of t_g, it is clear that the system D230/ M/1.6 is too fast for RIM processing. The values of ΔH_I calculated for the different systems should be constant. However, the result in Table 2.13 indicate a decreasing order of D2/M/1.6 > D2/20MD/M/1.6 > D2/20D/M/1.6 > D4-D230/M/1.6 > T5/M/1.6 > T5/20D/M/1.6. This order appears to be consistent with the content of polytrimerisations. Fig.(2.21)and (2.22) show the effects of chain extenders on isocyanate conversion. Addition of chain extenders to D2 increases the gelation times of reaction systems, however, addition of chain extender to T5 decreases the gelation time very slightly. Fig (2.23) shows that increase of functionality and molecular weight distribution of polyamine increases the gelation times of reaction systems.

ATR studies were also carried out on the polyisocyanurate to establish reaction kinetics of cyclotrimerisation. 50 ml M143 was put into a paper cup, using the same experimental set-up as shown in Fig.2.18, but without micro-RIM, the required amount (see Table 2.14) of TMR was added dropwise into the cup with rapid stirring. The ATR curves

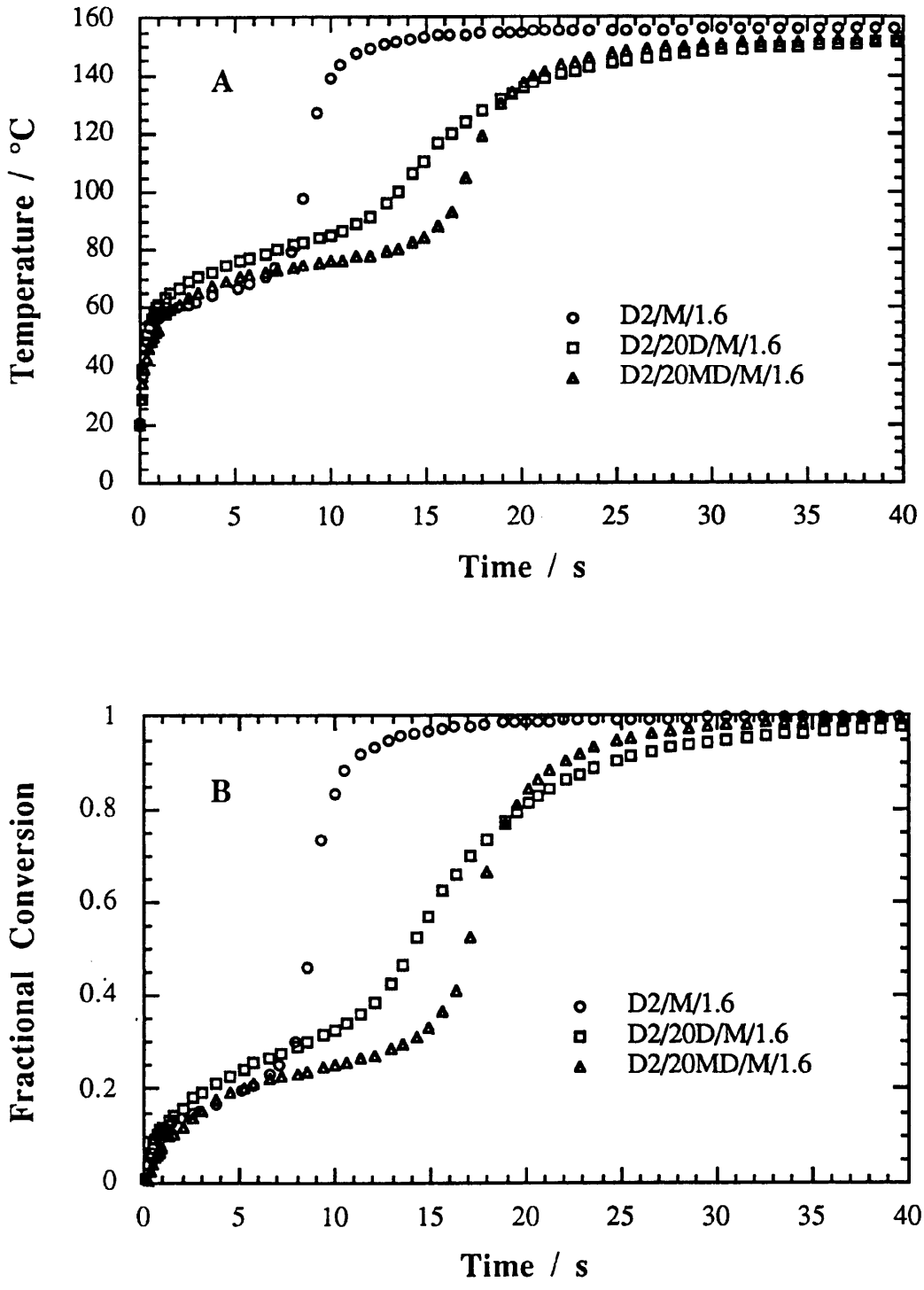

Fig 2.21 The effect of chain extender on reaction kinetics of D2-based PUrI

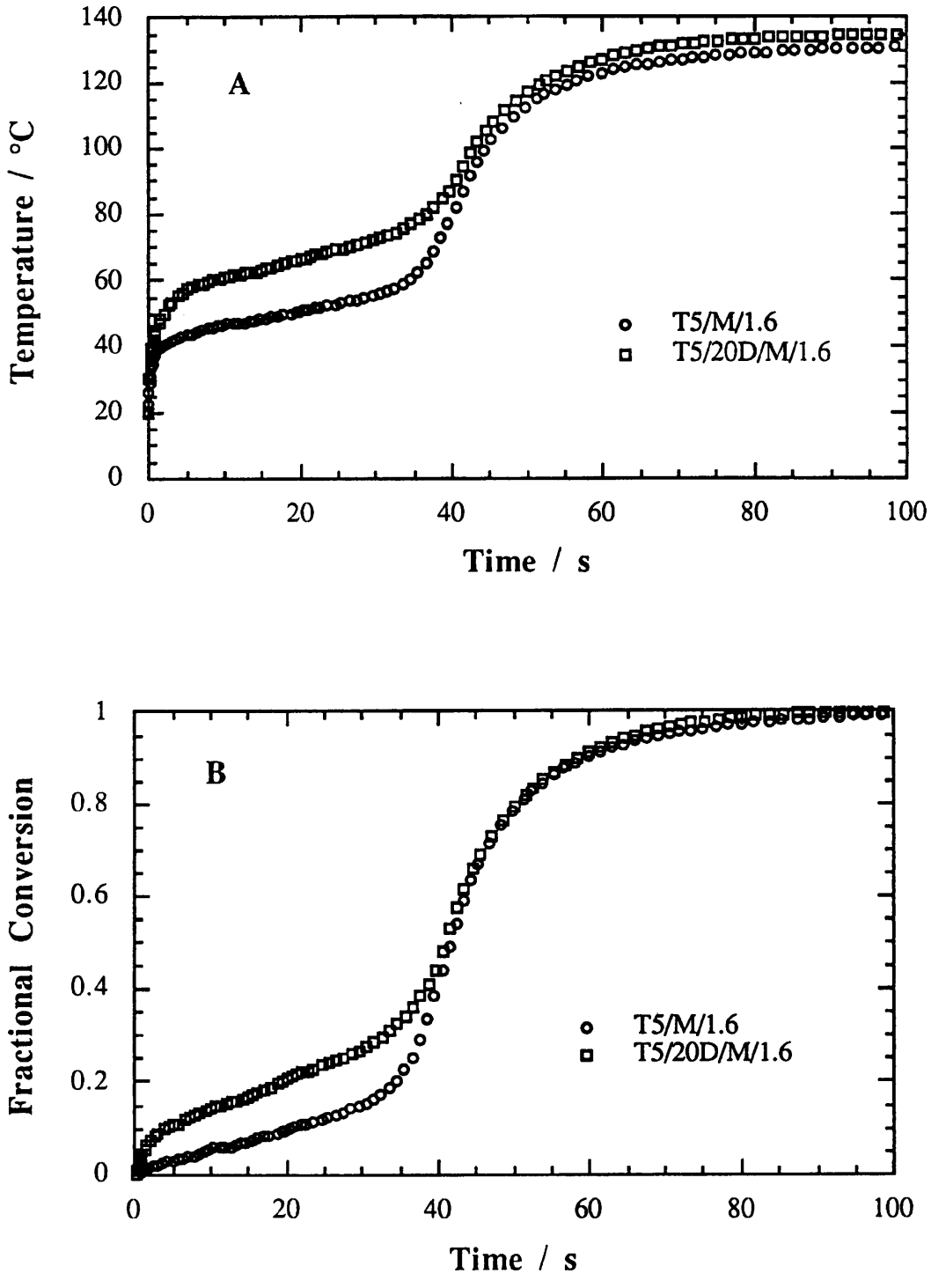

Fig 2.22 The effect of chain extender on reaction kinetics of T5-based PUrI

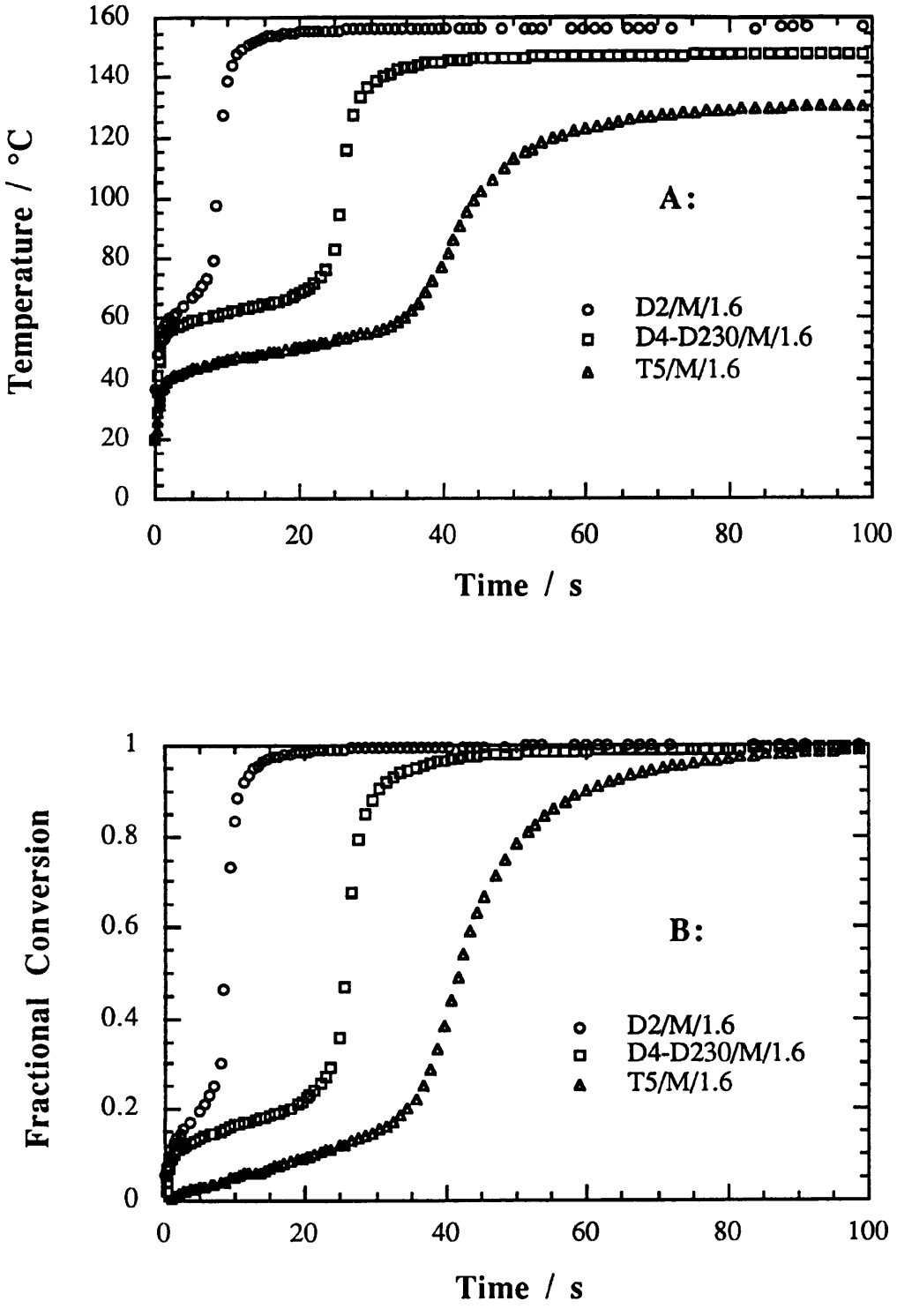

Fig 2.23 The effect of polyamines on reaction kinetics of PUrI

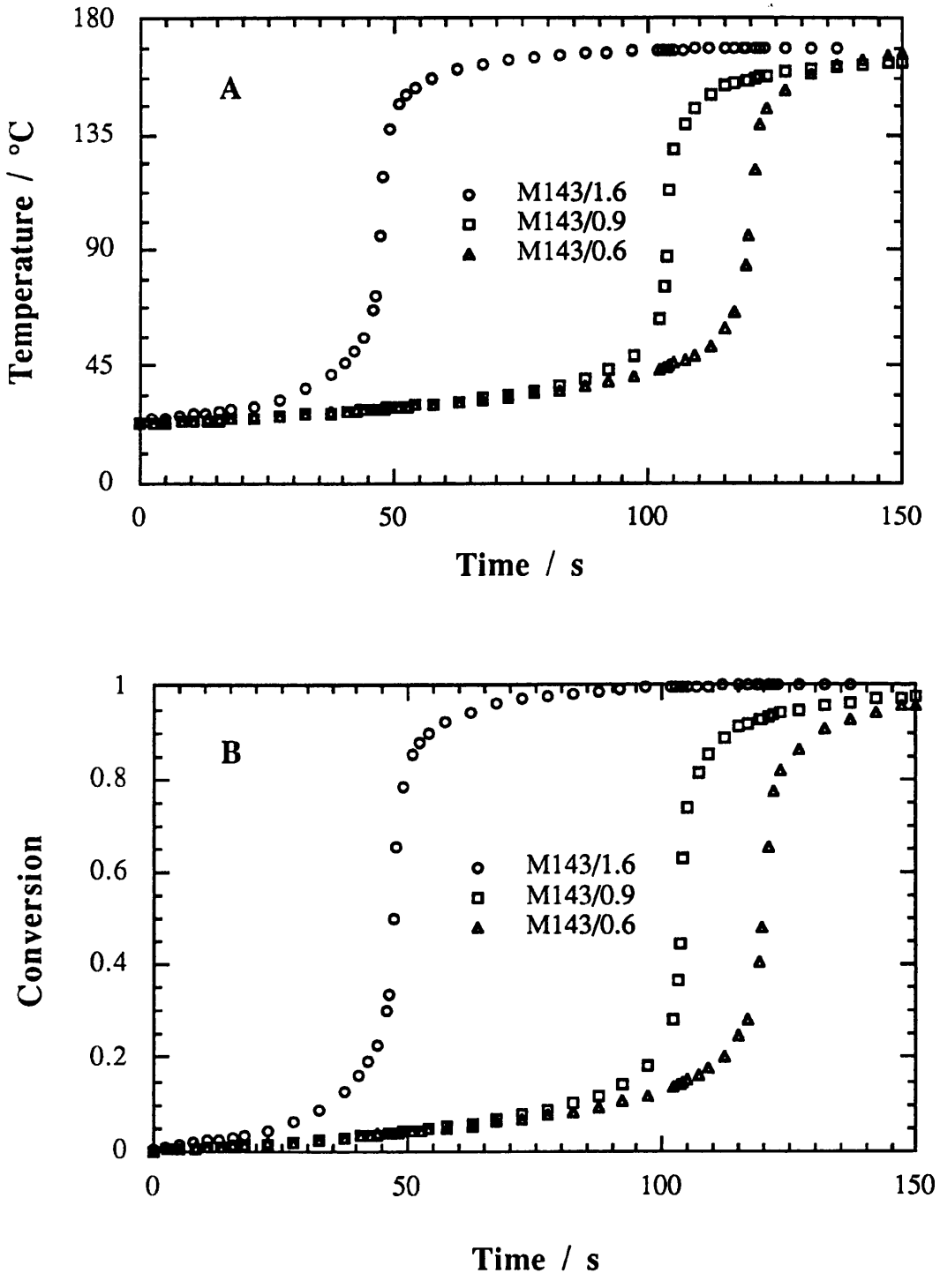

Fig 2.24 The catalyst content on reaction kinetics of pure polyisocyanurate

are shown in Fig.2.24, and the results summarised in Table 2.14. It is clear that the fractional conversion of isocyanate groups in polyisocyanurate is only 80% of that in D2/M/1.6. It is also noticed that increasing the content of catalyst decreases the gelation time.

Table 2.14 Experimental data and calculation results for pure polyisocyanurate

	$T_{ad}^{(a)}$ / K	T_{ad} / K	t_g / s	$\alpha_{max}^{(b)}$
M143/1.6[c]		442	48	0.8
M143/0.9	478	440	104	0.8
M143/0.6		446	120	0.8

(a) using Eq(2.39), where j = 1, ρ = 1.21 kg L^{-1}, C_o = 8.46 eq L^{-1}, T_o = 311 K (38 °C), ΔH_I = 62 kJ eq^{-1}(the polytrimerisation heat of reaction (2) in D2/M/1.6 system), C_p = 1.82 + 2.01x10^{-3} T, and α = 1, the theoretical value of T_{ad}, $T_{ad}^{(a)}$, is calculated. (b) α_{max} is defined as $(T_{ad} - T_o) / (T_{ad}^{(a)} - T_o)$. (c) the figure 1.6 in M143/1.6 means that the catalyst (TMR) content in M143/1.6 is the same as that in D2/M/1.6, in terms of equivalent weight of isocyanate to per gram of TMR.

The effect of catalyst level on the reaction kinetics of D2/M has been studied by Birch [148]. The RIM machine HP-15 [63] and the temperature measuring method described by Pannone [41] were used. The results which are shown in Fig.2.25 clearly indicates that as catalyst content decreases, the rate of the reaction becomes also decreases. In the case of D2/M/0.6, the time to gelation is 1.7 times longer than that for D2/M/1.6. The gelation time for D2/M/1.6 system in the study [148] is longer than that in present study, probably due to different kinds of RIM machine, different temperature measuring methods, and different T_o.

It should be noticed that Eq (2.38) is developed based on the energy balance of multi-step reactions so as to predict the fractional conversion, α, at any time. This energy balance approach is different from that usually based on the reaction kinetics, as for example in Willkomn's [76] work, in which the kinetic equation (2.40) was used to predict fractional conversion (α) of isocyanate groups during RIM polyurea formation. In this work [76] reaction of isocyanate groups with aliphatic amine group was assumed to be instantaneous,

so that only the reaction of isocyanate groups with aromatic amine groups was considered. The reaction order of either 2 or 3 was also assumed in order to calculate α according to Eq(2.40).

$$\frac{d\alpha}{dt} = A \exp\left(\frac{-E_a}{RT}\right) C^n_{NCO}\, C^m_{NH2} \qquad (2.40)$$

where E_a is the reaction activation energy, R is the gas constant, T is the temperature, C_{NCO} and C_{NH2} are concentrations of isocyanate and aromatic amine groups respectively. The reaction orders of NCO and NH_2 are n and m, respectively.

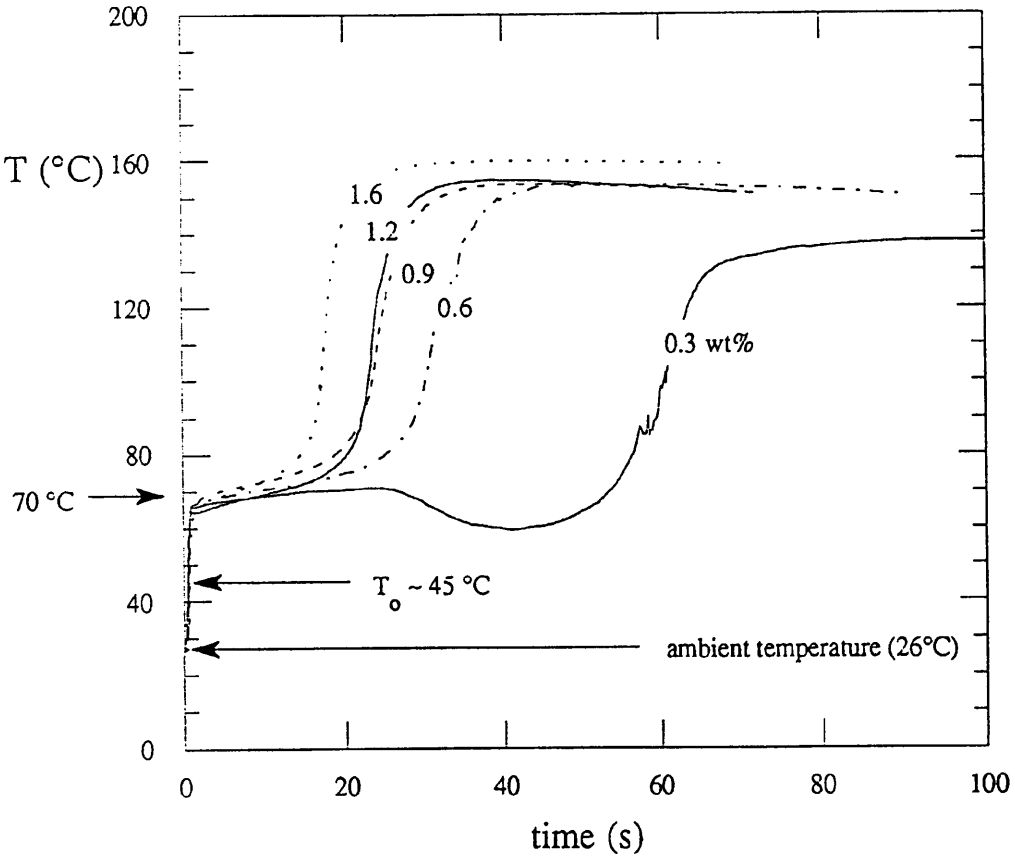

Fig 2.25 The effect of catalyst level on the reaction kinetics of D2/M (Numbers against each curve refer to the catalyst content)

2.7 Summary and Conclusions

In this chapter, novel copoly(isocyanurate-urea)s, PUrI, have been produced by reaction injection moulding, RIM. The materials were formed from ≈ 2:1 weight ratio of

polyisocyanate to amine-functionalised polyoxypropylene, POP, in the presence of an organic trimerisation catalyst (TMR), a quaternary ammonium carboxylate. Diamine- and triamine-POP, namely, D2000 and T5000 (M_n~2,000 and 5,000 g mol^{-1} respectively) were used and the polyisocyanate, Isonate M143, was based on 4,4'-diphenylmethane diisocyanate. In some cases an aromatic diamine chain extender, either 3,5-diethyltoluene diamine, DETDA, or methylene-bis-2,6-diisopropylaniline, MDIPA, was also used. Stoichiometric ratios, [NCO] / [NH_2], ranged from 7 to 30, and the reactant and mould temperatures used in RIM were 36 and 90 °C, respectively. Gel times were controlled by varying the catalyst concentration, and gel times as short as 5 s were achieved at 90 °C. The processing of eleven PUrI systems was studied by means of Reynolds number, Re, and Adiabatic Temperature Rise, ATR. Six of the systems, D2/M/1.6, D2/20D/M/1.6, D2/20MD/M/1.6, T5/M/1.6, T5/20D/M/1.6, and D2/M/0.6, were successfully processed by HP-15 RIM machine to produce PUrI block polymer materials.

The viscosity study shows the effect of chain extenders and polyamines on the Re of polyamine blends.

(1) By increasing in molecular interactions between amines and ether oxygens, addition of chain extenders, DETDA and MDIPA, increases the viscosities of polyamine blends, T5/20D, D2/20D, D2/20MD, and decreases their Re.

(2) As the increase of molecular weight or changing molecular structure from linear to branching, the viscosity of polyamine blend increases, and their Re decreases.

(3) The dependence of the viscosity on temperature can be determined by the activation energy for viscous flow, E. So temperature will effect the viscosity in order of T5/20D > D2/20D > D2/20MD > T5 > D4 > D2 > D4-D230 according to their E, so does Re.

Based on an energy balance approach for the reactions involved, two equations were developed to calculate fractional conversions of the limiting reactant and the heat of reaction

for the case of n sequential reactions. The equations derived to analyse the ATR experimental data were as follows:

$$\alpha = (\alpha_j - \alpha_{j-1}) \frac{a\,(T - T_{j-1}) + \frac{b}{2}(T^2 - T_{j-1}^2)}{a\,(T_j - T_{j-1}) + \frac{b}{2}(T_j^2 - T_{j-1}^2)} + \alpha_{j-1} \qquad t_{j-1} < t \leq t_j \qquad (2.38)$$

$$-\Delta H_j = \frac{\rho}{(\alpha_j - \alpha_{j-1})\,C_o}\left[a\,(T_j - T_{j-1}) + \frac{b}{2}(T_j^2 - T_{j-1}^2)\right] \qquad (2.39)$$

where α, α_{j-1}, α_j are the fractional conversions of the limiting reactant at times t, t_{j-1}, t_j, respectively; t_{j-1} and t_j are, respectively, the initial and final times of the jth reaction, where j=1, 2.....n; α_o(=0) and α_n(=1) are, respectively, initial and final conversions. T, T_{j-1} and T_j are, respectively, adiabatic temperatures at times t, t_{j-1}, t_j; T_n, the temperature rise for the final reaction corresponds to the measured (total) maximum adiabatic temperature, T_{ad}. ΔH_j is the heat of reaction of the jth reaction, ρ is the density of reactant mixture, C_o is the concentration of limiting reactant, and a and b are constants.

The Eqs(2.38) and (2.39) were successfully applied to the present systems. The analysis results of ATR data showed that copolymerisation occurred via a two-step (or three-step) process involving rapid polyether-urea, soft segment (SS) formation followed by NCO-trimerisation to form a glassy polyisocyanurate, hard segment (HS) phase. The T5-based reaction systems had longer gelation times than D2-based systems. Increasing the molecular weight distribution of the polyamine as in D4-D230 blend, or adding chain extenders to D2, increased the gelation times of the reaction systems. However, for T5-based systems, adding chain extender had little effect on gelation times. The reaction kinetics studies showed that for all PUrI reaction systems, very low fractional conversions of isocyanate groups were achieved during initial stages, which therefore limited the viscosity build-up during initial stages of the RIM process. This control of the viscosity-time profile was shown to be very important for the successful production of SRIM composites.

CHAPTER THREE

MORPHOLOGY AND PROPERTIES OF RIM COPOLY(UREA-ISOCYANURATE)S

Introduction

Copolyisocyanurate network-forming systems involve multiple competitive reactions and produce materials with complex morphologies. In these materials the chemical structure of the polymer and the competition between polymerisation reactions, micro-phase separation and vitrification, determine morphology which strongly influences resulting materials properties. The work reported [50, 54, 57, 106, 119, 149] to date has dealt solely with copoly(urethane-isocyanurate)s and has been restricted to studies of chemical (adiabatic) kinetics and mechanical properties but without detailed reference to morphology. In contrast, the morphologies of the related block copolyurethanes have been studied extensively in attempts to interpret their thermal and mechanical properties. The techniques used to characterise morphology include small angle X-ray scattering (SAXS), wide angle X-ray diffraction (WAXD), transmission electron microscopy (TEM), scanning electron microscopy (SEM), and Fourier transform infra-red spectroscopy (FTIR). Such studies have been the subject of a number of reviews [127, 150, 151].

In this chapter, the effects of polyether-polyamine functionality and the incorporation of aromatic diamine chain extenders on the copoly(isocyanurate-urea) (PUrI) morphology are characterised by SAXS and TEM. Correlations between morphology and dynamic mechanical-thermal and tensile stress-strain properties of a systematic series of PUrI are established.

3.1 Dynamic Mechanical Thermal Analysis (DMTA)

3.1.1 Test Method

DMTA data were obtained on a Polymer Laboratories machine at frequency of 1 Hz in the temperature range -100 to 300 °C at a heating rate of 5 °C min^{-1}. A double cantilever bending geometry was used for beam samples (3 x 10 x 45 mm) to obtain dynamic flexural moduli and mechanical damping as functions of temperature. A schematic diagram of the DMTA specimen mounting is shown in Fig.3.1. The DMTA data are average values from three specimens.

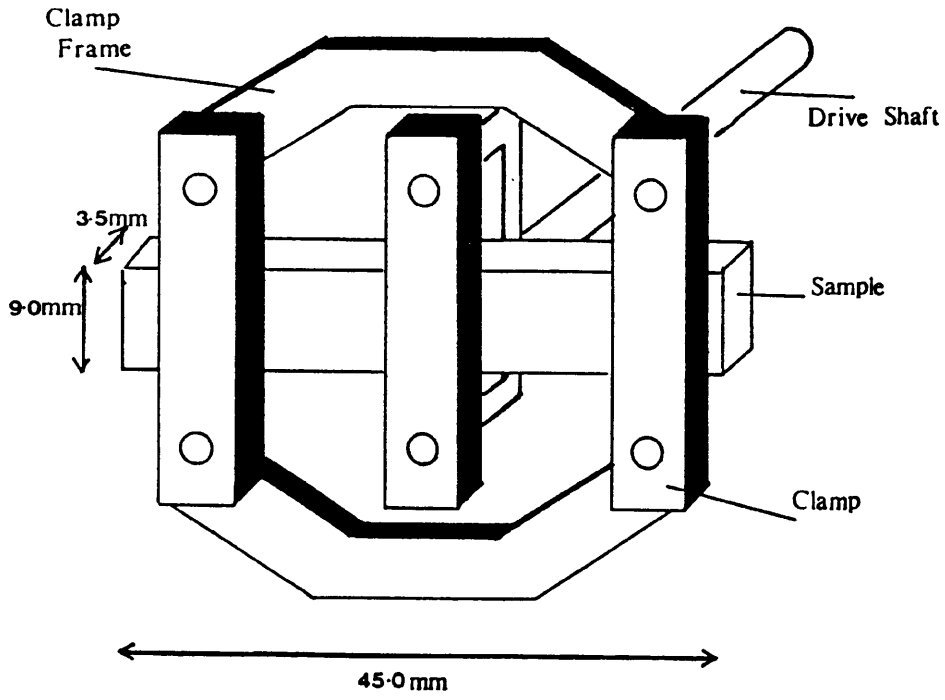

Figure 3.1 The schematic of DMTA Specimen Mounting - dual cantilever

3.1.2 Results and Discussion

3.1.2.1 Effect of Soft Segment Structure

DMTA data provide modulus-temperature and molecular relaxation behaviour of the (micro)phase separated RIM-copolymers. The effect of soft segments on DMTA data of PUrI are given in Fig.3.2 and Table 3.1 and 3.2.

Several peaks of varying intensities and sharpness are shown by the damping curve (tanδ) in Fig 3.2b. They are designated α, ß, γ in order of decreasing temperature according to convention [150]. The lowest temperature peak (γ) is associated with soft segment glass transition at Tg^S between – 42 and –34 °C. The next peak (ß) around 70 °C is broad and

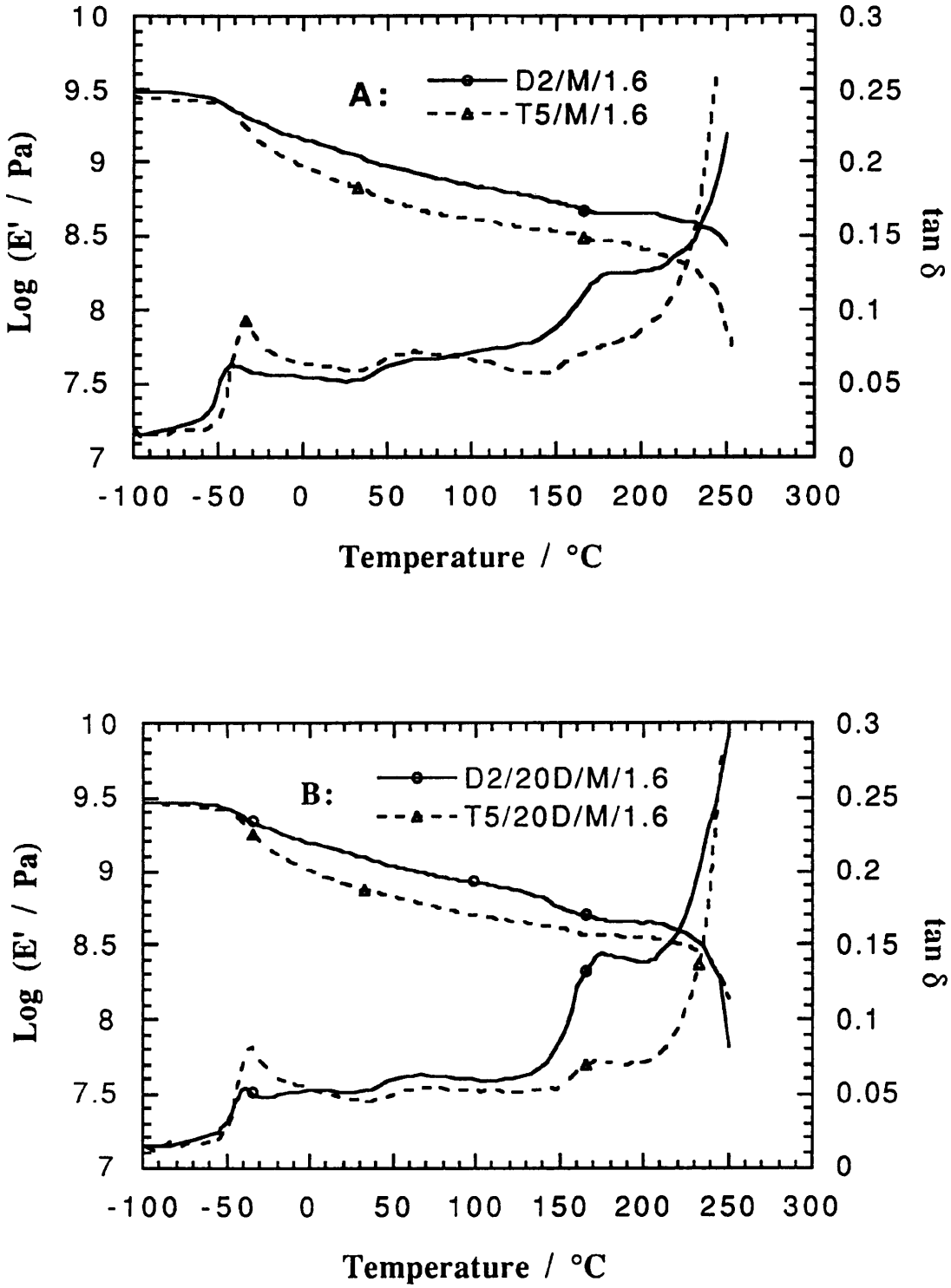

Figure 3.2 The effect of soft segment structure on DMTA curves of PUrI post-cured at 150 °C for 1 Hr. A: without chain extenders and B: with chain extender DETDA.

Table 3.1 The effect of soft segments on molecular relaxation of PUrI post-cured at 150 °C for 1 h.

Sample	r	γ (Tg^S) / °C	tanδ at Tg^S	ß / °C	α (Tg^H) / °C	tanδ at Tg^H
D2/M/1.6	14	– 42	0.063	~ 70	180	0.125
T5/M/1.6	27	– 34	0.093	~ 66	174[(a)]	0.074
D2/20D/M/1.6	7	– 39	0.054	~ 67	175	0.145
T5/20D/M/1.6	9	– 35	0.082	~ 72	172	0.073

(a) observed as a shoulder in tanδ

Table 3.2 The effect of soft segment structure on DMTA Modulus-temperature data of PUrI post-cured at 150 °C for 1 h.

Sample	$\frac{E'(-50\ °C)}{E'(60\ °C)}$	$\frac{E'(60\ °C)}{E'(100\ °C)}$	$\frac{E'(100\ °C)}{E'(200\ °C)}$	$\frac{E'(-50\ °C)}{E'(200\ °C)}$	tanδ at Tg^S
D2/M/1.6	2.99	1.21	1.11.	5.54	0.063
T5/M/1.6	4.92	1.31	1.51	9.73	0.093
D2/20D/M/1.6	2.50	1.19	1.88	5.35	0.054
T5/20D/M/1.6	4.11	1.25	1.33	6.83	0.082

attributed to co-operative relaxations of the mixture of soft segment and polyisocyanurate. The highest temperature peak (α), which appears as a shoulder sometimes, is related to the polyisocyanurate glass transition at Tg^H between 172 and 180 °C, which is around the values reported by Nelson [106]. Fig.3.2 and Table 3.1 show that when polyether diamine D2000 is replaced by polyether triamine T5000, tanδ at Tg^S increases in intensity and becomes sharper, but tanδ at Tg^H decreases in intensity. The increasing of intensity at Tg^S is mainly related to the big difference in equivalent weight between D2000 and T5000. The equivalent weight of T5000 is 1900 g mol^{-1}, approximately double that of D2000 (975 g mol^{-1}) This suggests that it is easier for T5000 to form a purer soft segment phase, with

sharper phase boundaries. Stoichiometric ratio, [NCO] / [NH2], may also affect morphology and properties. Lower [NCO] / [NH2] ratio, which means less polyisocyanurate of D2000-based PUrI, may be responsible for the increases in intensity of tanδ at Tg^H. Corresponding modulus-temperature data show that the storage modulus curve for T5000-based PUrI have a bigger decrease compared with D2000-based PUrI, around Tg^S, as exemplified by the modulus ratio values of E'(-50 °C) / E'(60 °C) in Table 3.2. Table 3.2 also shows, in the temperature range of -50 to 200 °C, the storage modulus of T5000-based PUrI decrease much more than those of D2000-based PUrI, as exemplified by the modulus ratio values of E'(-50 °C) / E'(200 °C) in Table 3.2. It is quite clear that T5000-based PUrI are more temperature dependent than D2000-based PUrI.

3.1.2.2 Effect of Hard Segment Structure

When either DETDA or MDIPA is added to PUrI-forming systems, it reacts with MDI to form aromatic polyurea hard segments, which are mixed with glassy aromatic polyisocyanurate structure. The different morphologies produced have been studied using TEM and SAXS, and the results are presented in later Section 3.3. Figure 3.3 and Tables 3.3 and 3.4 show the effects of hard segments on DMTA data of PUrI.

The addition of chain extender, DETDA, increases the store modulus of both D2-based and T5-based PUrI, decrease the intensity of tanδ at Tg^S, and in corresponding, increases the thermal stability of both D2-based PUrI and T5-based PUrI in terms of E'(-50 °C) / E' (60 °C). However, the addition of chain extender, DETDA, only increases the thermal stability of T5-based PUrI, but not for D2-based PUrI in terms of E'(-50 °C) / E' (200 °C) due to the increase of tan δ at Tg^H for D2-based PUrI. However, the addition of MDIPA decreases the intensities of tanδ at both Tg^S and Tg^H, thus increase the thermal stability of D2-based PUrI in terms of both E'(-50 °C) / E' (60 °C) and E'(-50 °C) / E' (200 °C). Table 3.4 shows that the modulus–temperature dependence of PUrI is improved by the addition of hard segments, and even better by addition of MDIPA.

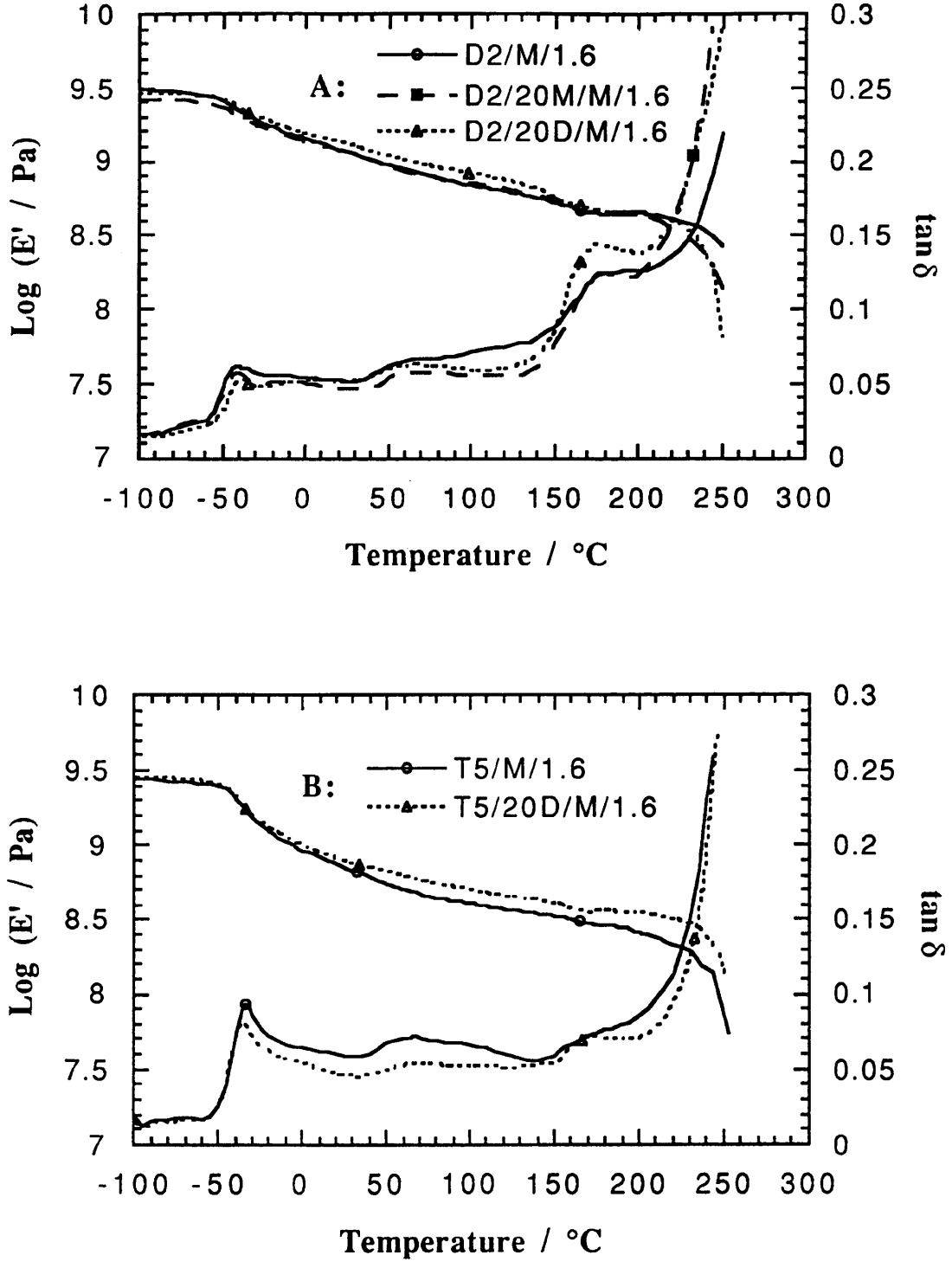

Figure 3.3 The effect of hard segments on DMTA data of PUrI post-cured at 150 °C for 1 h. A: the addition of chain extenders to D2-based PUrI and B: the addition of chain extenders to T5-based PUrI

Table 3.3 The effect of hard segments on DMTA relaxation data for PUrI post-cured at 150 °C for 1 h.

Sample	γ (Tg^S) / °C	tanδ at Tg^S	β / °C	α (Tg^H) / °C	tanδ at Tg^H
D2/M/1.6	– 42	0.063	~ 70	180	0.125
D2/20D/M/1.6	– 39	0.054	~ 67	175	0.145
D2/20M/M/1.6	– 42	0.058	~ 71	182	0.124
T5/M/1.6	– 34	0.093	~ 66	174(a)	0.074
T5/20D/M/1.6	– 35	0.082	~ 72	172(a)	0.073

(a) shoulder shown in tan δ curves

Table 3.4 The effect of hard segments on DMTA modulus-temperature data of PUrI post-cured at 150 °C for 1 h.

Sample	$\frac{E'(-50\ °C)}{E'(60\ °C)}$	$\frac{E'(60\ °C)}{E'(100\ °C)}$	$\frac{E'(100\ °C)}{E'(200\ °C)}$	$\frac{E'(-50\ °C)}{E'(200\ °C)}$	tanδ at Tg^S
D2/M/1.6	2.99	1.21	1.11	5.54	0.063
D2/20D/M/1.6	2.50	1.19	1.88	5.35	0.054
D2/20M/M/1.6	2.70	1.19	1.68	5.06	0.058
T5/M/1.6	4.92	1.31	1.51	9.73	0.093
T5/20D/M/1.6	4.11	1.25	1.33	6.83	0.082

3.1.2.3 Effect of Thermal Treatment

As mentioned in Chapter 1, the two-phase morphologies developed in RIM–copolymers are rarely in equilibrium due to the dynamic nature of the RIM process and can often be easily modified by thermal treatment. Fig.3.4, Table 3.5 and Table 3.6 show the effects of post curing on DMTA data for D2/M/0.6.

For non–post cured (up) D2/M/0.6, the tanδ curves show that there is only a shoulder around – 40 °C (γ peak); but when D2/M/0.6 is post cured at 150 °C for 1 h, the γ peak not only shifts to – 48 °C, but also becomes sharper and higher. The α peak also shifts from 166 to 203 °C. Besides, when D2/M/0.6 is post cured at 150 °C for 1 h, the storage

curves in Fig.3.4 show that the modulus of D2/M/0.6 is greatly enhanced by post-curing. The values in Table 3.6 also show that postcuring at 150 °C for 1h. reduces the dependence of the storage modulus of D2/M/0.6 on temperature, however further increasing postcuring temperature from 150 to 180 or 200 °C increases the dependence of storage modulus of D2/M/0.6 on temperature. These observations suggest that thermal treatment greatly affects the thermal dynamic properties of D2/M/0.6, due to the enhancement of (micro)phase separation. The values of tanδ at Tg^S in Table 3.5 imply that increasing post curing temperature enhances (micro)phase separation. Table 3.7 suggests that post curing has similar effects on (micro)phase separation of all the RIM PUrI. However T5000-based PUrI are less affected by post curing than D2000-based PUrI, due to the higher equivalent weight of T5000, which facilitates (micro)phase separation. Table 3.8 shows that post-curing enhances the thermal stabilities of all RIM materials in terms of E'(-50 °C) / E'(200 °C), maybe due to the further reactions caused by post-curing.

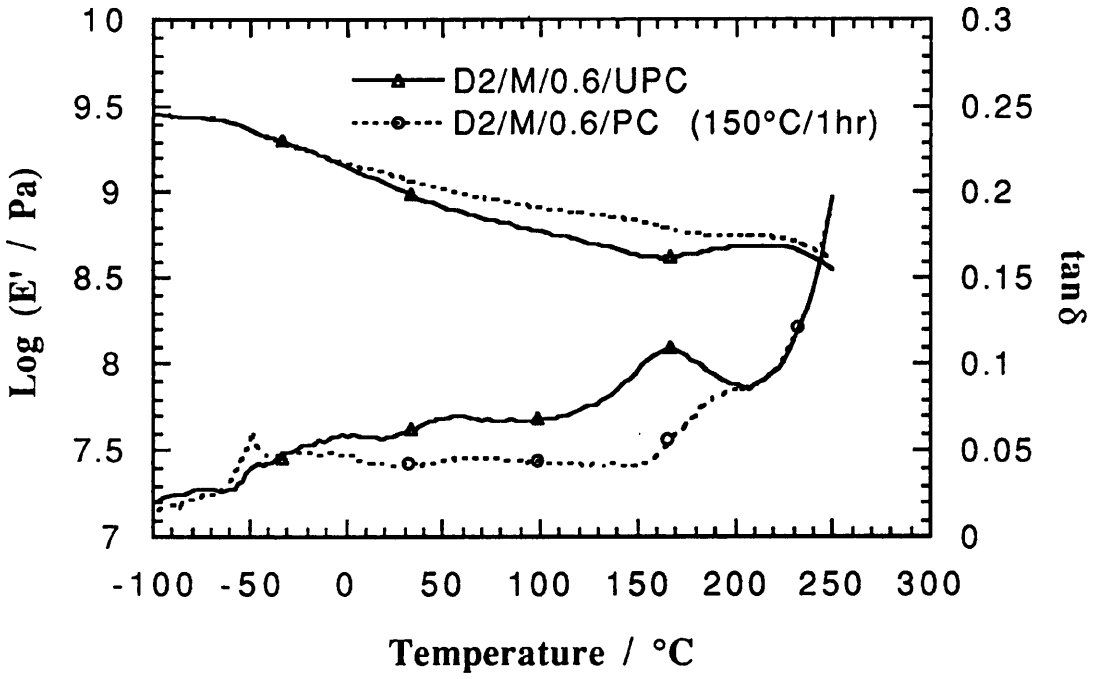

Figure 3.4 The effects of post curing (150 °C / 1hr.) on DMTA curves of D2/M/0.6

Table 3.5 The effect of post curing on DMTA relaxation data of D2/M/0.6

Post Curing	γ (Tg^S) / °C	tanδ at Tg^S	ß / °C	α (Tg^H) / °C	tanδ at Tg^H
up	– 40[a]	0.042	~ 54	166	0.108
150 °C, 1h.	– 48	0.062	~ 72	203[a]	0.084
180 °C, 1h.	– 47	0.067	~ 70	(b)	--
200 °C, 1h.	– 46	0.075	~ 69	(b)	--

(a) shoulder appearance; (b) α peak did not appear below 220 °C, at which temperature thermal-oxidation occurred

Table 3.6 The effect of post curing on DMTA modulus-temperature data of D2/M/0.6

Post Curing	$\frac{E'(-50\ °C)}{E'(60\ °C)}$	$\frac{E'(60\ °C)}{E'(100\ °C)}$	$\frac{E'(100\ °C)}{E'(200\ °C)}$	$\frac{E'(-50\ °C)}{E'(200\ °C)}$	tanδ at Tg^S
up	3.08	1.29	1.20	4.77	0.042
150 °C, 1h.	2.34	1.24	1.40	4.06	0.062
180 °C, 1h.	2.69	1.26	1.46	4.95	0.067
200 °C, 1h.	2.78	1.23	1.45	5.00	0.075

Table 3.7 The effects of post curing on DMTA relaxation data of RIM materials

Materials [a]	γ (Tg^S) / °C	tanδ at Tg^S	ß / °C	α (Tg^H) / °C	tanδ at Tg^H
D2/M/up	- 10[c]	0.046	~ 71	158	0.085
D2/M/pc [b]	- 42	0.063	~ 70	180	0.125
D2/20D/M/up	- 37[c]	0.038	~ 70	159	0.132
D2/20D/M/pc [b]	- 39	0.054	~ 67	175	0.145
D2/20M/M/up	- 39[c]	0.040	~ 73	165	0.118
D2/20M/M/pc[b]	- 42	0.058	~ 71	182	0.124
T5/M/up	- 34	0.082	~ 70	174	0.080
T5/M/pc [b]	- 34	0.093	~ 66	174[c]	0.074
T5/20D/M/up	- 35	0.070	~ 72	163	0.075
T5/20D/M/pc[b]	- 35	0.082	~ 72	172[c]	0.073

(a) The catalyst concentration for all materials is 1.6%; (b) post cured at 150 °C for 1 h.
(c) shown as shoulder.

Table 3.8 The effect of post-curing on DMTA modulus–temperature data of RIM materials

Materials [a]	D2/M		D2/20D/M		D2/20M/M		T5/M		T5/20D/M	
	up	pc [b]	up	pc [b]	up	pc [b]	up	pc [b]	up	pc [b]
E'(-50 °C) / E'(200 °C)	5.88	5.54	5.59	5.35	5.26	5.06	11.30	9.73	7.94	6.83

(a) The catalyst concentration for all materials is 1.6%; (b) post cured at 150 °C for 1 hr.

3.2 Tensile Properties

The tensile properties of the various RIM copoly(isocyanurate–urea)s (PUrI) in terms of Young's modulus (E), ultimate stress or strength (σ), ultimate strain (ε) and tensile toughness (U_t, the total area under a stress-strain curve) have be determined.

3.2.1 Test Method

Data were obtained on an Instron 1122 universal Testing Machine at 20 ± 3 °C. Dumb-bell specimens (ASTM D3039–76) having an overall length of 150 mm, a neck length of 60 mm, a width of 12.5 mm and a thickness of around 3 mm were used (Fig.3.5). The gauge length was 75 mm and the extension rate 10 mm min^{-1}. Strains were recorded to within ± 0.05% using a 0-10% strain-gauge extensometer clamped directly onto the central portion of a dumb-bell specimen. The tensile properties reported are the mean of at least five tests.

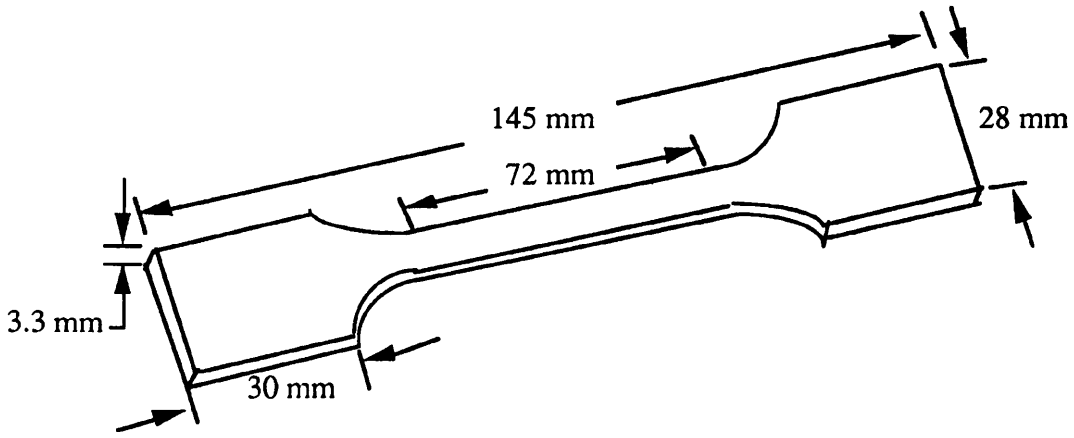

Figure 3.5 The configuration of tensile test specimen

3.2.2 Results and Discussion

The effects of soft segment and hard segment structures on tensile properties are shown in Fig.3.6 and Table 3.9.

Table 3.9 The effects of soft segments and hard segments on tensile properties of RIM PUrI post-cured at 150 °C for 1 h.

Sample	E / GPa	σ / MPa	ε / %	U_t / MJ m^{-3}
D2/M/1.6	1.38 ± 0.07	38 ± 2.7	3.8 ± 1.5	0.89 ± 0.53
D2/20D/M/1.6	1.46 ± 0.12	50 ± 1.9	6.0 ± 1.5	2.08 ± 0.78
D2/20M/M/1.6	1.27 ± 0.06	39 ± 2.6	5.1 ± 0.4	1.24 ± 0.18
T5/M/1.6	0.72 ± 0.06	30 ± 6.4	11.6 ± 4.4	2.31 ± 1.42
T5/20D/M/1.6	0.80 ± 0.04	42 ± 4.8	15.3 ± 3.6	4.86 ± 1.65

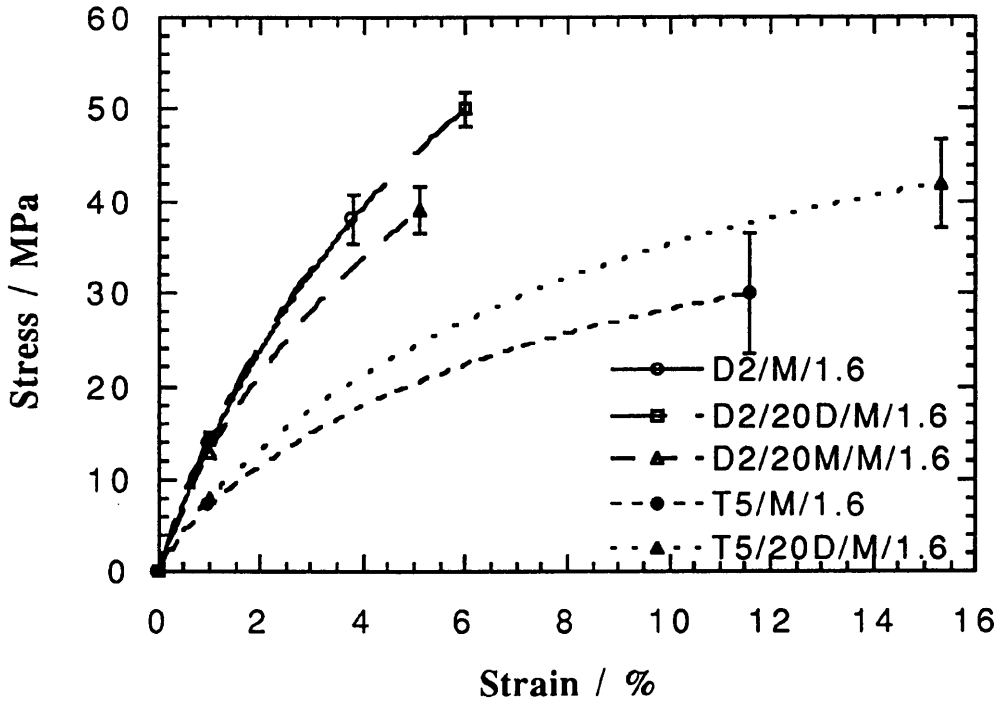

Figure 3.6 The stress-strain curves of RIM PUrI post-cured at 150 °C for 1 hr.

Obviously, D2000-based PUrI have superior modulus and strength, but lower ultimate strain and tensile toughness properties, due to their totally different morphologies (to be discussed in section 3.3). The addition of chain extender, DETDA, producing hard segment, results in increases on the tensile properties of PUrI, particularly, their toughness.

The effect of post-curing on the tensile properties of PUrI is shown in Table 3.10. Post–curing at 150 °C for 1 hr greatly enhances the tensile properties of D2/M/0.6, due to enhancement of (micro)phase separation as shown in section 3.1 and increase of cross-linking density. However, further increasing post-curing temperature, and thus increasing (micro)phase separation and larger (micro)domain size in PUrI (see section 3.3), has a deleterious effect on the tensile properties, which suggests there is optimum point of (micro)phase separation for the best tensile properties.

Table 3.10 The effect of post-curing on tensile properties of D2/M/0.6

Post-curing	E / GPa	σ / MPa	ε / %
UP	1.26 ± 0.12	38 ± 2.2	10.0 ± 1.6
150 °C, 1hr	1.45 ± 0.06	52 ± 0.6	8.7 ± 0.6
180 °C, 1hr	1.46 ± 0.10	44 ± 3.0	6.2 ± 0.8
200 °C, 1hr	1.33 ± 0.1	40 ± 2.3	5.6 ± 1.5

3.3 Morphology–Property Relationships in PUrI

3.3.1 Small Angle X-ray Scattering (SAXS)

3.3.1.1 SAXS Experimental

SAXS measurements were made on beamline 8.2 on the Synchrotron Radiation Source (SRS) at the SERC Daresbury Laboratory, Warrington, UK, and the schematic is shown in Fig.3.7. The white radiation from the bending magnet is monochromated by a cylindrically bent Ge(111) monochromator with an asymmetric cut of 10.5 ° and giving a

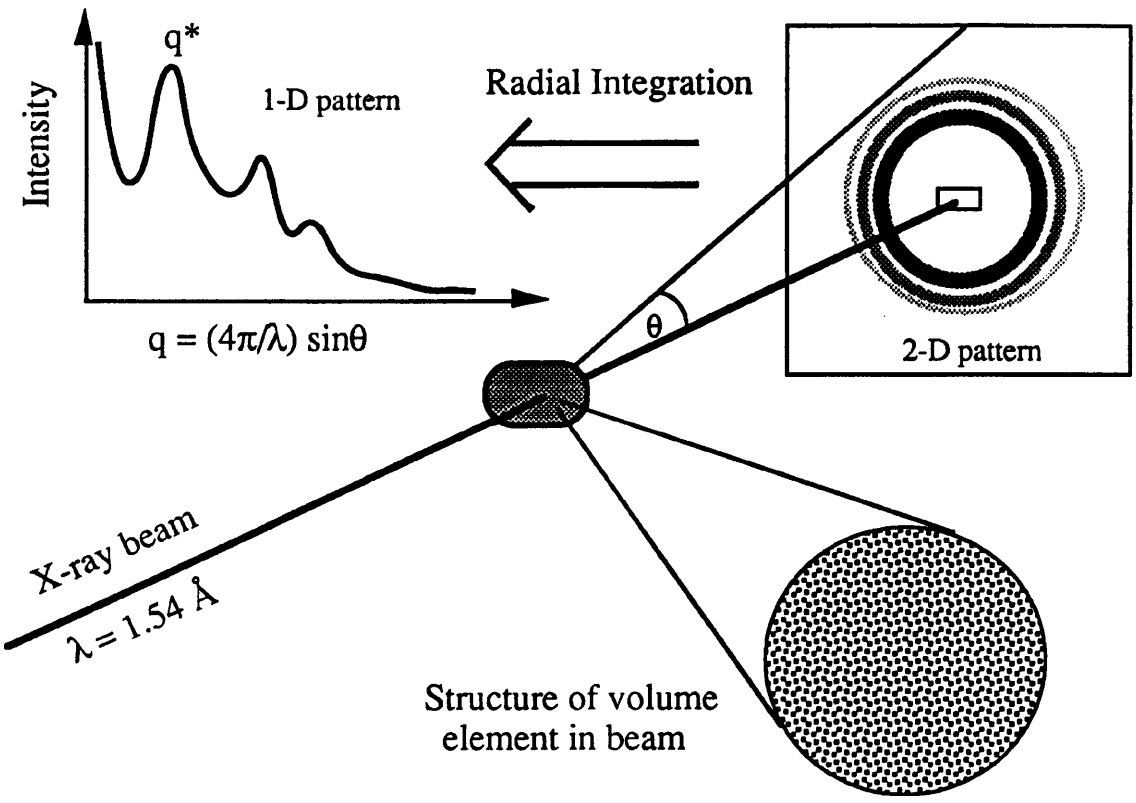

Figure 3.7 A schematic diagram of the SAXS experimental

horizontal compression ratio of 13:1 for the incoming beam. The distance from the tangent point of the storage ring to the monochromator is 20.0 m. The horizontal acceptance of the monochromator is approximately 5 mrad and the alignment is such that 1.52 Å radiation is selected. An uncoated, fused-quartz mirror receives the monochromated radiation under a glancing angle of about 4 mrad. The mirror, which is cylindrically bent and 0.7 m in length, effectively cuts-off all of the higher harmonics transmitted by the monochromator and focuses the radiation in the vertical plane. By varying the bending radius the radiation can be focused in the horizontal plane in the range of 0.2 to 4.5 m behind the sample stage. The beamline is kept under high vacuum and four sets of slits are used for beam size definition and reduction of parasitic scatter. A highly-collimated beam is produced with a typical cross section of 0.3 x 4 mm^2 in the focal plane. With the SRS operating at 2 GeV and 200 mA, a flux of 4 x 10^{10} photons s^{-1} is generated at the sample position. A vacuum chamber is

placed between the sample and detector in order to reduce air scattering and absorption. Both the exit window of the beam-line and the entrance window of the vacuum chamber are made from 15 μm mica, the exit window of the vacuum chamber is made from 10 μm Kapton film. A beamstop is mounted just before the exit window to prevent the direct beam from hitting the detector. The camera is equipped with a multiwire quadrant detector which has an opening angle of 70° and an active length of 0.2 m. This detector measures intensity in the radial direction and is only suitable for isomorphous scatters. The spatial resolution of the detector is 500 μm and it has an advantage over single-wire detectors in that the active area increases radially.

The scattering pattern from an oriented specimen of wet collagen (rat-tail tendon) was used to calibrate the sample-to-detector distance (3.5 m). The specimens for SAXS were prepared by cutting strips 3 *x* 10 *x* 50 mm from RIM plaques. Scattering patterns were taken by fixing the ends of the specimens onto the entrance window of the vacuum chamber so that the X-rays could pass uninterrupted and data were collected for one-minute per specimen. Parallel-plate ionisation detectors, placed before and after the sample record the incident and transmitted intensities, thus enabling differences in the specimens attenuation factors (a function of transmission and thickness) to be monitored. The experimental data were corrected for background scattering (subtraction of the scattering from the empty camera), attenuation factor and the positional linearity of the detector. The reproducibilities of the spatial resolution and integrated intensities were ±1% and ±2% respectively.

3.3.1.2 SAXS Data Analysis

A peak or a shoulder in $I(\mathbf{q})$ gives a general indication of the presence of a periodic structure in the system. The most common practice for determining the periodicity is to use Bragg's law in the calculation of a domain spacing, d, from the location of the peak maximum, $\mathbf{q}_{max}$, in an intensity versus scattering vector plot .

$$d = \lambda / 2\sin\theta_{max} = 2\pi / \mathbf{q}_{max}$$

Most SAXS experiments do not fulfil all the requirements for calculation of Bragg diffraction spacings and assumptions of one- or three-dimensional order in a system and the subsequent calculation of its correlation function is a more appropriate method of calculating the periodicity [154]. Furthermore, the shoulder in the bare intensity data in Fig.3.8 is weak making unambiguous determination of q_{max} difficult if not impossible.

For the copolymers in the present study, more precise information regarding microstructural periodicity is obtained if the morphology is assumed to globally isotropic but locally lamellar. The data can then be analysed to give a one-dimensional Bragg spacing, 1-d. This analysis is done by applying the Lorentz correction, q^2, to the observed scattered

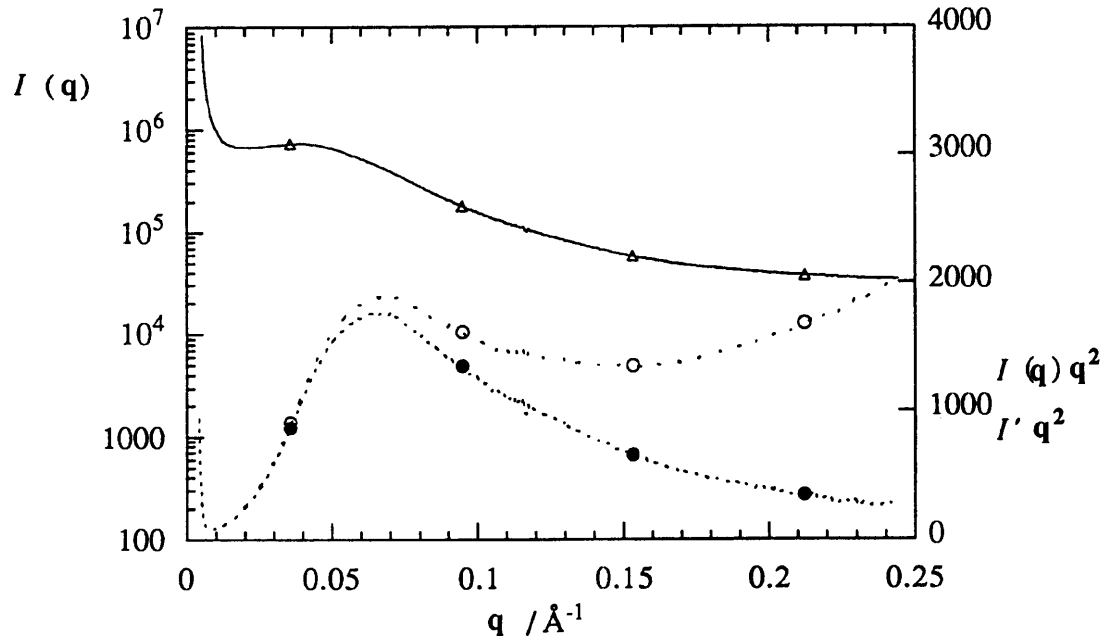

Figure 3.8 Scattering curves for D2/M/0.6 showing the three stages of data analysis. The uppermost curve (Δ) is the bare intensity, $I(q)$, versus q. The middle curve (o) is the Lorentz-corrected intensity , $I(q)\ q^2$, versus q. The lower curve (•) of $I''q^2$ versus q is the Lorentz-correction of the bare intensity with the thermal background subtracted

intensity $I(q)$. Fig.3.8 is a plot of $I(q)$ and $I(q)\ q^2$ versus q for D2/M/0.6. The upturn of $I(q)\ q^2$ at high q in Fig.3.8 indicates a positive deviation from Porods Law [155], caused by either a strong thermal fluctuation background or isolated segmental mixing. In a well-segregated system with sharp phase boundaries, $I(q)\ q^2$ should tend to zero at high q. The deviation must be corrected for before the data can be analysed further.

For materials with sharp phase boundaries, Porod's Law [155] predicts a fall off of $q^{-1/4}$ in scattered intensity at large angles.

$$\lim_{q \to \infty} I(q) = (K_p / q^4) + I_b$$

The quantity I_b arises from density fluctuations and K_p is the Porod constant. Note the strong positive deviation in the Porod plot ($I(q)q^4$ versus q^4). illustrated in Fig.3.9 for

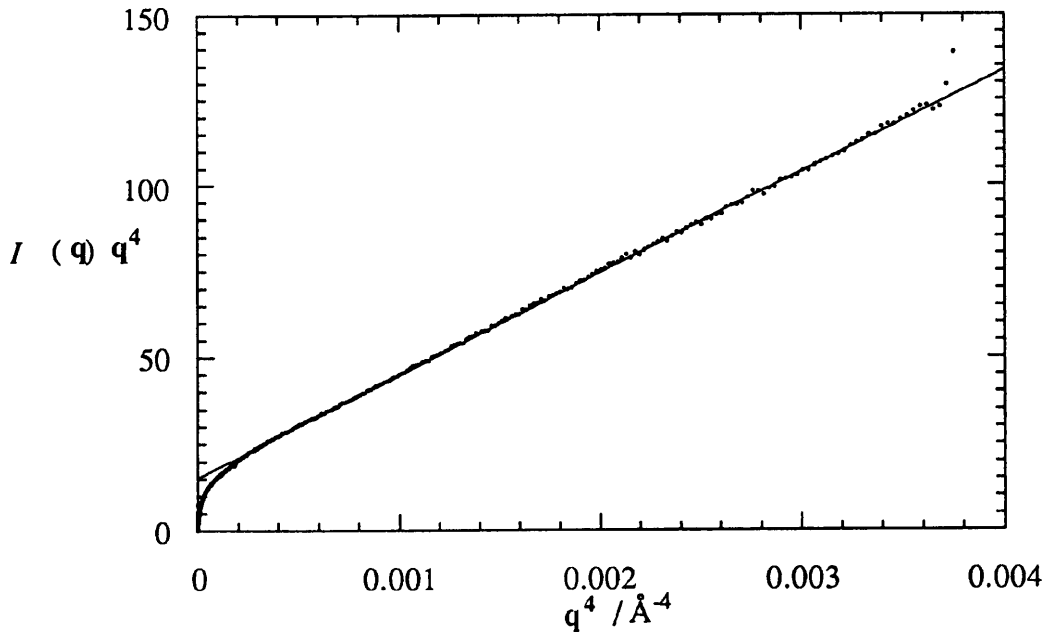

Figure 3.9 A Porod plot of $I(q)q^4$ versus q^4 for D2/M/0.6. The symbols (•) are data points and the solid line is a regression analysis of the linear part the curve giving values of K_p = 15.4 and $I_b = 2.95 \times 10^4$.

D2/M/0.6. Positive deviations from Porod's law are caused by thermal density fluctuations and/or isolated mixing of one type of segment in the other [150]. A regression analysis of the linear part the curve gives values of K_p = 15.4 and $I_b = 2.95x\ 10^4$. I_b must be subtracted from the raw intensity data before both 1-d and the invariant are calculated.

The filled symbols in Fig.3.8 are values of $I'\mathbf{q}^2$ {= $(I(\mathbf{q}) - I_b)\mathbf{q}^2$} versus q and the artificial upturn of $I(\mathbf{q})\ \mathbf{q}^2$ at high **q** has been corrected. For the calculation of the Bragg spacing, the maximum in $I'\mathbf{q}^2$ versus **q** is taken as **q***, so that

$$1\text{-d} = 2\pi/\ \mathbf{q}^*$$

The peak value from $I(\mathbf{q})$ versus **q** gives a *d* spacing of ≈150 Å whereas the peak value from $I'\mathbf{q}^2$ versus **q** gives a 1-d spacing of 95 Å Furthermore the removal of the thermal background has also resulted in a small shift in the peak position of the Lorentz corrected data. The peak in the uncorrected $I(\mathbf{q})\ \mathbf{q}^2$ versus **q** gives a *1-d* spacing of 93 Å. Theoretically [156], *d* is expected to be 23% greater than 1-d, and the greater deviation (58%) in the present results could be due to some instrumental broadening of *I*. The fully-corrected 1-d spacing will be used in the discussion that follows.

The ideal electron density variance, $\langle\eta_0^2\rangle$, of a perfectly separated, two-phase system with sharp phase boundaries, is defined by

$$\langle\eta_0^2\rangle = \phi_1^0(\rho-\rho_1^0)^2 + \phi_2^0(\rho-\rho_2^0)^2$$

where ρ is the average electron density of the material and ϕ^0 and ρ^0 are, respectively, the volume fractions and electron densities of the two pure phases. The value of $\langle\eta_0^2\rangle$ represents the maximum degree of micro-phase separation. The electron density variance of a real system will be lower than this value, since complete micro-phase separation is seldom achieved. In this case the actual electron densities of the phases (ρ_1 and ρ_2) are closer to the average leading to a decrease in electron density variance of the real system defined by

$$\langle\eta^2\rangle = \phi_1(\rho-\rho_1)^2 + \phi_2(\rho-\rho_2)^2$$

The value of $\langle\eta^2\rangle$ will thus range from zero for a homogeneous mixture to $\langle\eta_0^2\rangle$ for a fully micro-phase-separated block copolymer and is useful as an indication of the degree of micro-phase separation.

Experimentally, the electron density variance may be calculated from

$$\langle\eta^2\rangle = \frac{Q}{2\pi i_e} = \frac{1}{2\pi i_e}\int_0^\infty \left(I(\mathbf{q})-I_b\right)\mathbf{q}^2\,d\mathbf{q} = \frac{1}{2\pi i_e}\int_0^\infty I'\,\mathbf{q}^2\,d\mathbf{q}$$

where I' (= $(I(\mathbf{q}) - I_b)$) is the intensity corrected for the thermal background, i_e is the Thompson scattering factor and the quantity Q is known as the invariant (being independent of the size or shape of the structural heterogeneities). The experimental invariant can therefore be used to characterise structure development as well as the degree of micro-phase separation. Determination of the electron density variance, $\langle\eta^2\rangle$, requires absolute invariant data which in turn require absolute intensity measurements. The absolute intensity requirement is not readily feasible on synchrotron SAXS cameras which have pseudo pin-hole optics [154]. Calculation of the absolute invariant also requires extrapolations from $\mathbf{q} = 0$ to the first data point, and from the last data point to $\mathbf{q} = \infty$. The biggest contribution to the magnitude of Q, however, is the area under the $I'\mathbf{q}^2$ versus $\mathbf{q}$ curve and this may be evaluated from the experimental data via a Simpson's Rule summation. A relative invariant, Q', has been calculated by summation of the area under the $I'\mathbf{q}^2$ versus $\mathbf{q}$ curve between the first reliable data point, $\mathbf{q} = 0.01$ Å, and the last reliable data point $\mathbf{q} = 0.24$ Å. Due to the arbitrary nature of the intensity measurement, the value of Q' has arbitrary units. However, Q' gives a quantitative indication of the relative degree of micro-phase separation for these materials.

3.3.2 Transmission Electron Microscopy (TEM)

The simplest electron microscope has two image-forming lenses and is an exact analogy of the compound light microscope, as shown diagrammatically in Fig.3.10. The illumination coming from an electron gun is concentrated on the specimen by a condenser

lens. After passing through the specimen the electrons are focused by the objective lens into a magnified intermediate image. This image is further enlarged by a projector lens and the final image is formed on a fluorescent screen or a photographic film.

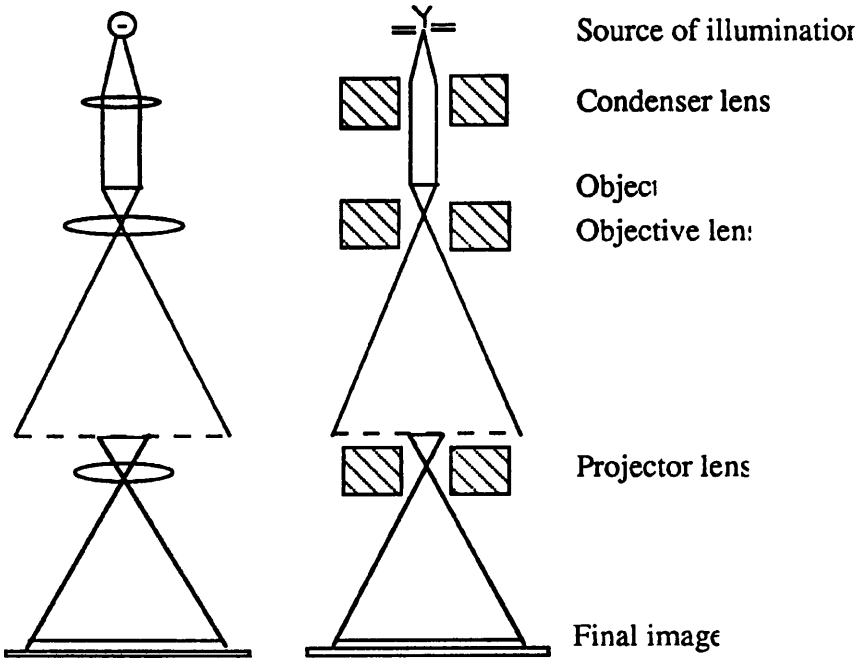

Figure 3.10 Light microscope and the equivalent two-stage electron microscope

Electron lenses can conveniently be made to magnify 50 - 200 times, and the simple two-stage TEM would have a magnification of about 10 000 times. The objective lens would typically resolve detail down to 5 nm, which would require an overall enlargement of 50 000 to be seen readily by the naked eye. This is achieved by using a simple magnifying glass on the fluorescent image, or a photographic enlargement of the image recorded on the photographic film.

The practical realisation of an electron microscope, however is larger and more complex than the diagram suggests for several reasons:

I The electron beam illumination must be generated and used in high vacuum. The body of the microscope is an airtight tube continuously evacuated to a pressure of

10^{-4} mbar or below. The electron path length within the tube may be more than one metre.

II Electron lenses are bulkier than glass lenses, and must be powered from appropriately stabilised electrical supplies.

Thus, as well as the electron–optical column of lenses with associated vacuum pumps, there will be also an electric power unit to supply the lenses with current and provide a high voltage of 50, 100 or even 1000 kV to accelerate the electrons.

When the design and construction of electron lenses is sufficiently good to reveal details beyond the 5 nm resolution level, it is desirable to employ more than two stages of magnification in order to see and record the final detail. Three imaging lenses enable magnification of up to ~ 500 000 or so to be achieved, and resolutions obtained down to fractions of a nanometer. Several current microscopes employ five or six image lenses, and cover range of 50 ~ 500 000 times without change of specimen position, with minimum image rotation and distortion, and permitting selected–area diffraction to be carried out over a wide range of magnification. There is a further advantage to be gained by distributing the magnification between a large number of lenses, in terms of the overall reduction in column length, and the more rigid construction that can be achieved. The latter is an essential feature when very high magnifications are involved.

During this section, TEM samples were microtomed using a Reichert-Jung Ultracut E with a freshly-prepared, wet glass knife at room temperature (Fig.3.11). The knife trough was filled with distilled water and thin sections were floated onto 500-mesh copper TEM grids. Optical reflection indicated, by the gold colour, that sections were < 40 nm thick (special care needs to be paid to obtain thin enough specimen). A Phillips 301 Transmission Electron Microscope operated at 100 kV and magnifications between 7 500 and 28 000 was used with Grade IV Ilford film. Microtomed thin sections were observed directly without any support film. To minimise electron beam damage of the samples and to avoid radiation artefacts, special precautions were taken by focusing on one area and translating to an

adjacent area for recording. Contrast was enhanced by underfocus of the objective lens [163].

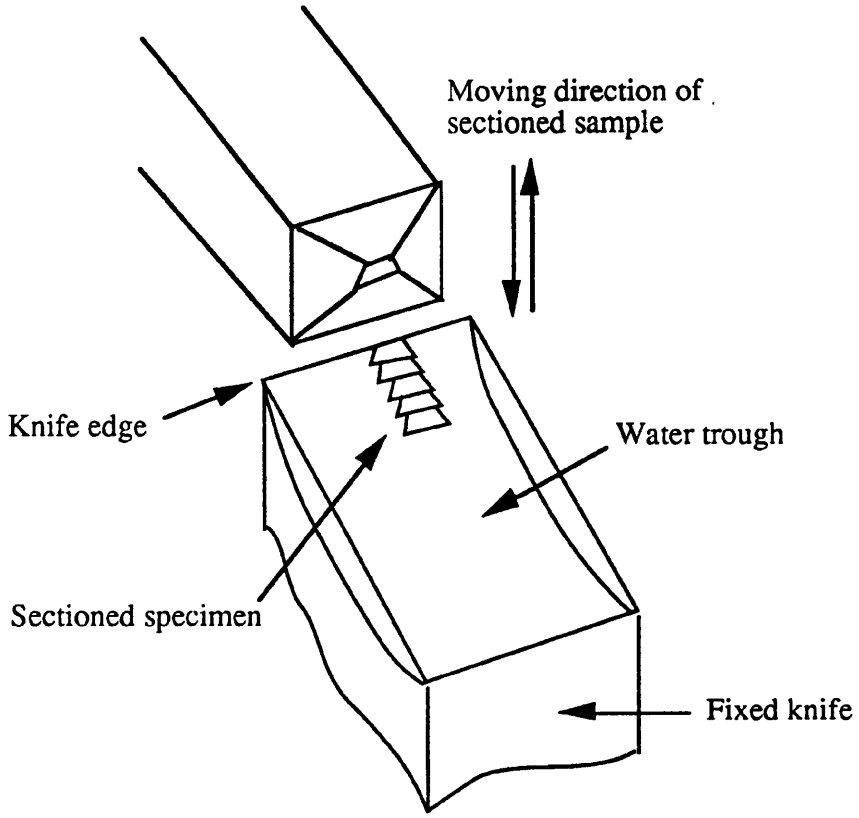

Figure 3.11 A schematic diagram showing the sectioning of a sample for TEM analysis

3.3.3 Results and Discussion

The RIM materials were stiff plastics with room-temperature Young's moduli between 1.5 and 0.7 GPa. The macro-network structure of these PUrI is not easy to visualise but the values of modulus suggest that there is a continuous glassy phase [81]. The simplest materials are formed from two of the components, *viz.* the polyisocyanate and either the polyether diamine or the polyether triamine, and these materials comprise 33% by weight (43% by volume) polyether and 67% by weight (57% by volume) highly-crosslinked polyisocyanurate. Assuming that the impingement mixing process produces a homogeneous mixture on the molecular level, the stages of polymerisation can then be described . In the initial stages of copolymerisation, -NCO-tipped, polyether-urea oligomers are formed by the

nearly instantaneous [37] reaction between aliphatic -NH_2 groups and the large stoichiometric excess of isocyanate groups. The remaining isocyanate groups then undergo trimerisation reactions, at a rate determined by the catalyst content and temperature, to form a highly-crosslinked material. Good connectivity between the polyisocyanurate and polyether microphases is ensured by the initial formation of the urea bonds. During the polymerisation process there is a large increase in average molecular weight and a change in chemical structure causing both rapid microphase separation and polyisocyanurate vitrification, which quench the system to produce an incompletely-reacted material with a non-equilibrium morphology.

There is strong experimental evidence to support the existence of a microphase-separated morphology. The micrographs in Fig.3.12 for D2/M/0.6 show a two-phase morphology, with a dominant wavelength of ≈ 100Å, which looks similar to Cahn's [157] computer simulation of a co-continuous, spinodal structure. Previous studies of RIM copolyureas indicate that the dominant mechanism of morphology formation is spinodal decomposition [90] which is initiated at low conversions of isocyanate groups. The diffraction patterns in Fig.3.8 and the Porod plot in Fig.3.9 correspond to the structure in Fig.3.12a, and suggest a well-ordered system with a size scale of ≈ 100 Å and sharp phase boundaries: the SAXS data are in good agreement with the TEM (The positive deviation in the Porod plot comes from either isolated glassy segments or a strong thermal fluctuation in electron density [154]). The DMTA curves in Fig.3.4 confirm the microphase-separated nature of this material. The polyether glass transition is observed as a peak in tan δ and a drop in modulus at ≈ -50 °C. The isocyanurate glass transition is also observed as a peak in tan δ and a drop in modulus (followed by a rubbery plateau) at higher temperatures (>150 °C). The effects of processing and chemistry on the morphology and properties of the novel PUrI are dealt with in more detail in the specific sections below.

3.3.3.1 Effects of Thermal Treatment

Simple materials with a relatively low catalyst content (D2/M/0.6) have a low rate of trimerisation and have been subjected to a series of heat treatments. These materials have

been shown to have the least complete reaction on demoulding, and are therefore the most susceptible to changes caused by heat treatment (annealing).

The TEM micrographs in Fig.3.12 are for unstained specimens which were (a) as-moulded, (b) annealed at 150°C for one hour and (c) annealed at 180 °C for one hour. The as-moulded material has a poorly defined structure. Image definition is due entirely to density differences between the microphases and is sharpened considerably by annealing at 150 and 180 °C. The real-space image is similar to Cahn's [157] computer simulation of a random co-continuous spinodal structure and is also reminiscent of a TEM of a segmented copolyurethane morphology described by Thomas [158] as "a random-platelet ". The characteristic length in the micrographs is estimated to be ≈ 100 Å and this does not change on annealing, and the dominant feature of the series of images (a to c) is the increase in phase-contrast with the annealing temperature.

Lorentz-corrected and thermal background-subtracted scattering patterns are presented in Fig.3.13. The assumption of a random lamella morphology and use of the Lorentz correction is, to some extent, suggested by TEM micrographs. The Lorentz-corrected scattering curves are essential for the calculation of the relative invariant, Q', and illustrate the improvement in electron density difference (phase purity) on annealing. The Q' values in Table 3.11 show a 40% increase on annealing. The value of Q' is independent of the size of the scattering centres and is only a function of the electron density difference between the highly-crosslinked glass and the rubbery polyether. Changes in Q' correspond to changes in the degree of microphase separation and are in qualitative agreement with the contrast in the TEM micrographs. The 1-d spacings obtained are 95, 95 and 150 Å, respectively, for the as-moulded, 150 °C- and 180 °C-annealed materials. The 1-d for the highest-temperature material is much larger than the value obtained for the as-moulded and 150 °C-annealed materials, and could be due to Ostwald ripening [159] on annealing lightly-crosslinked structures. The discrepancy between length scales estimated from TEM and 1-d values, calculated precisely from SAXS, is insignificant and is overwhelmed by the correlations between techniques in terms of microphase contrast.

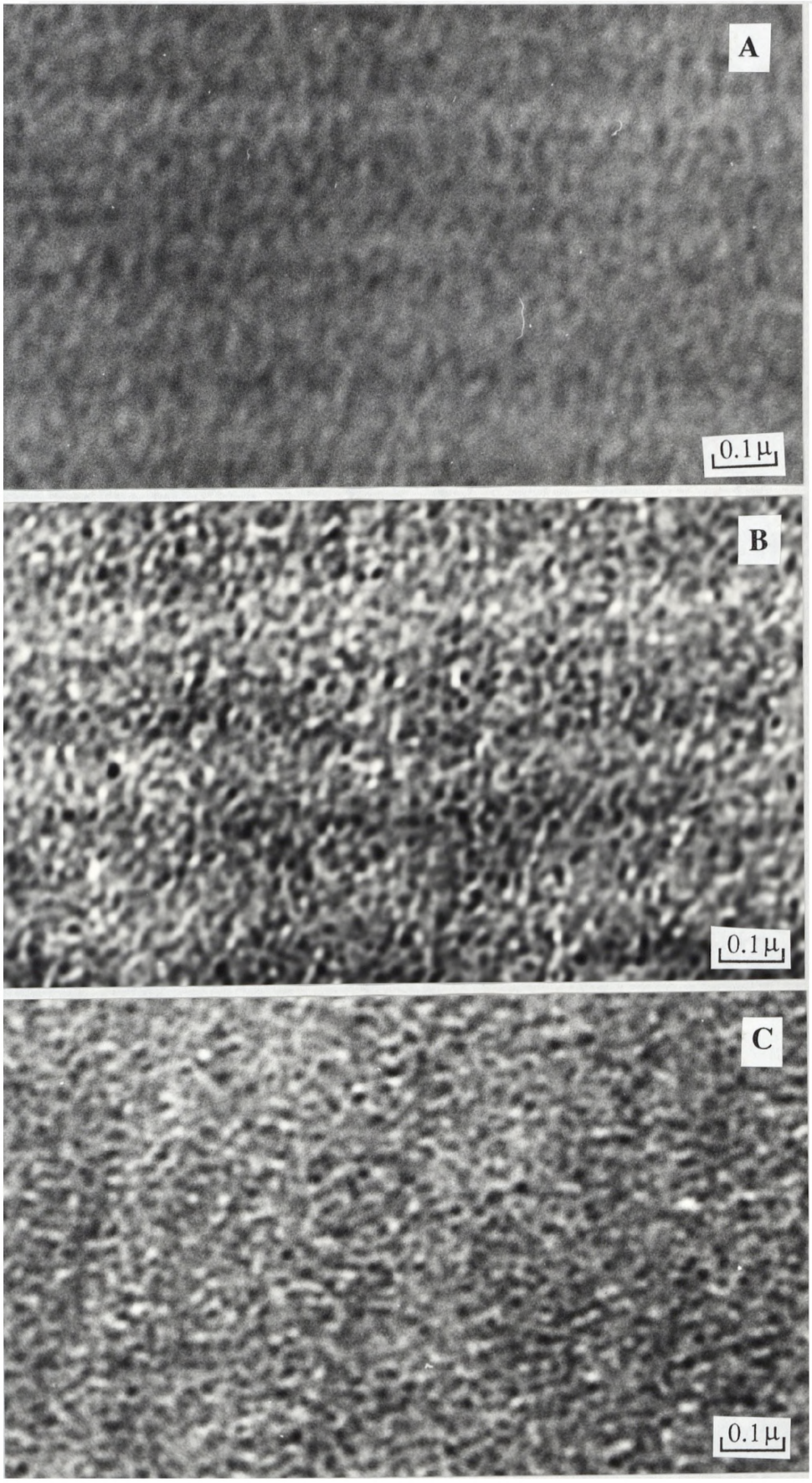

Figure 3.12 TEM micrographs of D2/M/0.6. (A) as-moulded; (B) annealed 1 hour at 150 °C; (C) annealed 1 hour at 180 °C.

Table 3.11. Composition, morphology and tensile properties of RIM PUrI post cured at 150 °C for 1 hr.

Copolymer	$\emptyset_{pe}$[b]	1-d / Å	Q'	L / Å	E / GPa	σ / MPa	ε / %
D2/M/1.6	0.43	112	214	110	1.38±0.07	38±2.7	3.8±1.5
D2/20D/M/1.6	0.38	74	180	70	1.46±0.12	50±1.9	6.0±1.5
D2/20M/M1.6	0.37	116	188	110	1.27±0.06	39±2.6	5.1±0.4
T5/M/1.6	0.43	153	198	150	0.72±0.06	30±6.4	11.6±4.4
T5/20D/M/1.6	0.39	98	187	100	0.80±0.04	42±4.8	15.3±3.6
D2/M/0.6/upc[a]	0.43	95	180	100	1.26±0.12	38±2.2	10.0±1.6
D2/M/0.6/150[a]	0.43	95	257	100	1.45±0.06	52±0.6	8.7±0.6
D2/M/0.6/180[a]	0.43	150	247	100	1.46±0.10	44±3.0	6.2±0.8

[a] upc refers to the as-moulded material; 150 and 180 refer to the materials annealed at 150 °C and 180 °C for one hour.

[b] Volume fraction polyether.

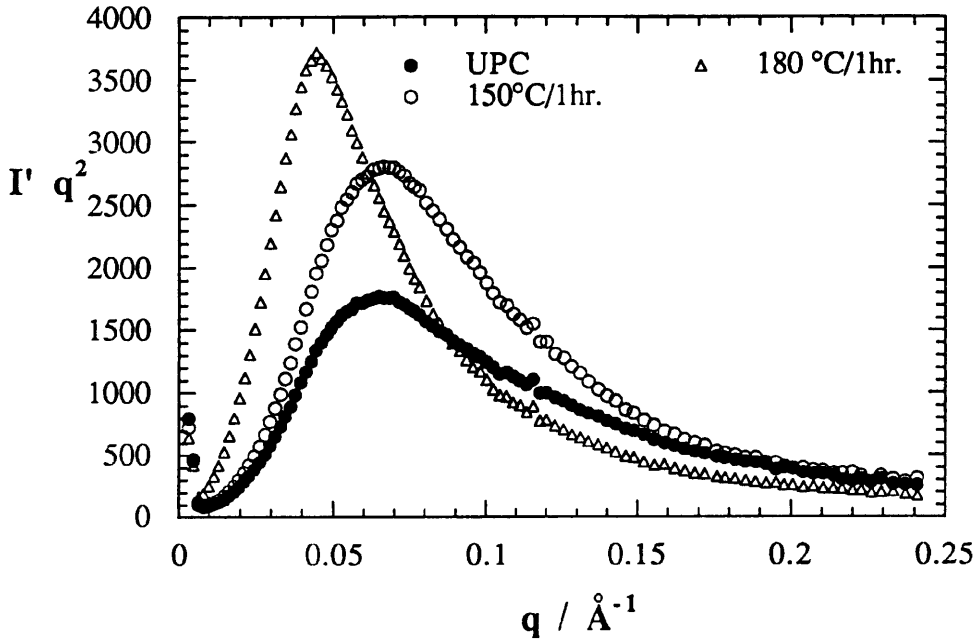

Figure 3.13. Lorentz-corrected SAXS patterns for D2/M/0.6.

The structural changes which occur on annealing D2/M/0.6 materials are readily explained by the differences in the DMTA curves of Fig.3.4 and by the tensile stress-strain data in Table 3.9. At low temperatures (< -60 °C) both as-moulded and annealed materials have moduli (≈ 3 GPa) and low damping typical of a glassy polymer. As temperature exceeds -50 °C, the modulus begins to fall and tan δ increases. The thermal sensitivity of the modulus and damping of the as-moulded and annealed materials is quite different. The annealed material has a sharp peak in tan δ associated with the soft segment glass transition temperature at ≈ -45 °C, whereas tan δ rises gradually with temperature for the as-moulded material, clearly indicating that the polyether-rich microphase is much purer in the annealed material. For both materials the moduli decrease at the same rate up to 0 °C and above this temperature, the as-moulded material has much lower moduli and higher damping than the annealed material due to its lower degree of crosslinking and microphase separation. The as-moulded material has a weak peak in tan δ and a corresponding change in slope of E'

at ≈ 70 °C and this feature, often observed in other RIM copolyureas[81, 135], is normally ascribed to the break-down of hydrogen bonding between ether-oxygens and urea groups. Both modulus-temperature curves have inflections at ≈ 160 °C. For the as-moulded material, E' gradually increases and there is a corresponding peak in tan ∂, and this behaviour is associated with two opposing processes, *viz.*, a glass-rubber relaxation and a preceding crosslinking reaction. Between 160 to 200 °C, the annealed material shows an initial decrease in E' followed by a modulus plateau with the corresponding tan ∂ values rising to a shoulder, and this behaviour is associated with a relaxation in the isocyanurate-rich microphase. Above 220 °C, E' begins to decrease and tan ∂ increases rapidly for both materials as thermal-oxidative degradation occurs. Generally the DMTA data show the as-moulded material to be incompletely reacted and poorly micro-phase separated; annealing increases the modulus (by forcing the reaction toward completion thereby increasing crosslinking density) and reduces damping (by improving the level of microphase separation). Tensile stress-strain data confirm one of the effects of annealing, that is, an increase in crosslinking density which explains an increased Young's modulus and reduced ultimate elongation with annealing. The interpretation of the damping behaviour, as regards improvement of phase purity with annealing, is in good agreement with the SAXS and TEM.

3.3.3.2 Effects of Hard Segment Structure

The addition of a hindered aromatic diamine (typically used as chain extenders in RIM polyureas [1, 37, 81, 90, 120, 135, 136]) was investigated. The addition of chain extender was observed to significantly increase the mould-filling viscosity of these systems (see chapter 2). The overall polymerisation still comprises effectively a two-stage reaction process involving instantaneous capping of the polyether diamine followed by competitive reaction of the remaining isocyanate groups, either in trimerisation reactions to form isocyanurate or with the aromatic diamine chain extender to form ureas. The relative rates of reaction are determined by the chemical structures of the diamine, the concentration of the trimerisation catalyst and the temperature. The parent D2/M/1.6 material comprises 33% by

weight polyether, whereas the two materials containing aromatic polyurea hard segments (D2/20D/M/1.6 and D2/20M/M/1.6) comprise 28% by weight polyether.

The TEM micrographs of D2/20D/M/1.6 and D2/M/1.6, see Fig.3.14(a) and 3.14(b) respectively, show real-space images similar to those in Fig.3.12 (In fact comparison of 3.12(b) and 3.14(b) shows the effect of doubling the concentration of trimerisation catalyst: namely, a slight increase in the domain spacing but a decrease in contrast). According to the TEM, the material containing DETDA, D2/20D/M/1.6, has a poor contrast structure with a smaller size-scale than D2/M/1.6. These qualitative observations are in good agreement with the SAXS data in Fig.3.15, where the *1-d* spacings obtained from the Lorentz-corrected scattering curves are 74 Å and 114 Å for the material with DETDA (D2/20D/M/1.6) and that without DETDA (D2/M/1.6); the corresponding relative invariants are 180 and 214. The addition of DETDA to the formulation prevents full development of the electron density difference and reduces the observed domain spacing. The aromatic urea (which has a high Tg [81, 135]) must co-exist with both the polyether and the polyisocyanurate; it is possible that the addition of polyurea causes vitrification to occur at an earlier stage of structure development (i.e. smaller sizes and lower Q' values).

The two TEM micrographs of D2/20M/M/1.6 in Figures 3.14(c) and 3.14(d) show a different morphology to those discussed above. The lower magnification micrograph features a random array of spherical inclusions, with a mean diameter of 1.5 μm which is beyond the resolution of the SAXS experiment. These inclusions account for ≈ 20 % of the total volume, and are obviously neither pure polyisocyanurate nor pure polyurea. The higher magnification micrograph shows these inclusions to be superimposed on a background pattern similar to the real-space images in Fig.3.12, 3.14(a) and 3.14(b). Furthermore, the inclusions have internal structure of the same length-scale as the background pattern. These observations are supported by the SAXS data in Fig.3.15 where D2/20M/M/1.6 has comparable 1-d and Q' values to the parent D2/M/1.6 material. The matrix in D2/20M/M/1.6 must therefore have the same composition (in terms of electron

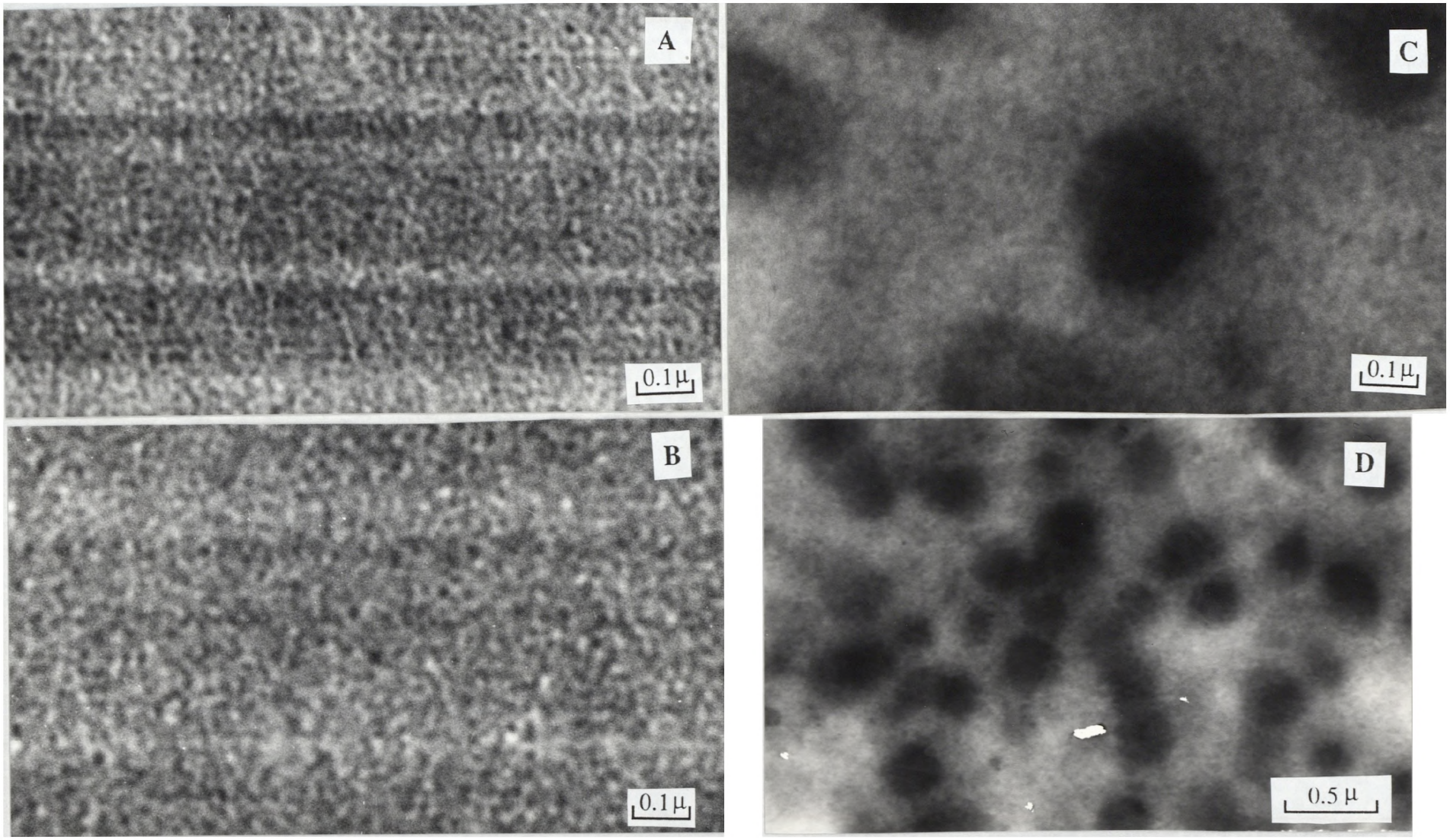

Figure 3.14 TEM micrographs of (a) D2/20D/M/1.6; (b) D2/M/1.6; (c) and (D) D2/20M/M/1.6

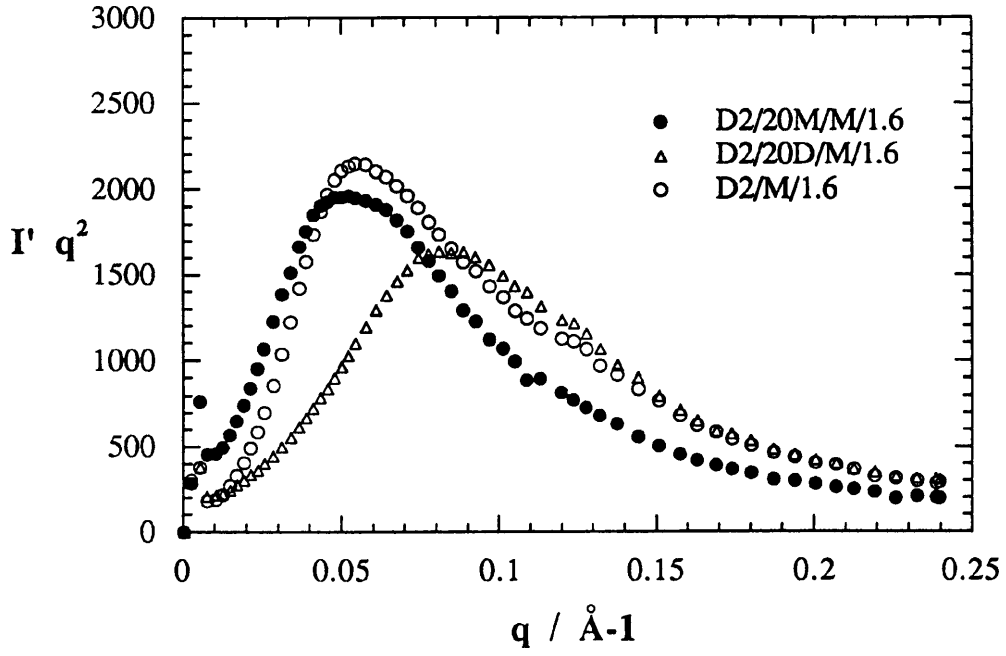

Figure 3.15 Lorentz-corrected SAXS patterns for (Δ) D2/20D/M/1.6; (o) D2/M/1.6; and (•) D2/20M/M/1.6.

density modulation) as D2/M/1.6 and the extra aromatic glass must be contained in the inclusions. The upturn in $I'q^2$ at low q for D2/20M/M/1.6 is most likely due to particle scattering from these inclusions.

The mechanism leading to the formation of inclusions has not been observed directly but is a result of competition between polymerisation kinetics, chemical gelation and (micro)phase separation. Specifically, MDIPA reacts with diisocyanate at a rate faster than that of the trimerisation of the diisocyanate although chemical gelation (at isocyanate-conversions of ≈ 50%) must occur after the onset of microphase separation (1-d ≈ 100Å). NCO-tipped-MDIPA maybe nucleate MDI before chemical gelation. The narrow size

distribution of the inclusions is a feature of heterogeneous nucleation and growth, and frozen by chemical gelation. In contrast for D2/20D/M/1.6, NCO-tipped-DETDA can not nucleate maybe due to its different molecular structure, and is incorporated in the trimerising material. Consequently the morphology shows only the microphase-separated morphology without large inclusions.

The dynamic mechanical spectra in Fig.3.3 illustrate the effects on modulus and damping of both chemical-structure and morphology. In each case the polyether glass transition is observed as a peak in tan δ and a drop in modulus at ≈ -30 °C. The isocyanurate glass transition is also observed as a peak in tan δ and a drop in modulus (followed by a rubbery plateau) at the higher temperature of ≈ 175 °C. The observation of two glass transitions confirms the existence of a microphase-separated morphology. The effects of morphology may be observed in the modulus-temperature behaviour. Both D2/20D/M/1.6 and D2/M/1.6 materials appear to have a co-continuous morphology from TEM. However, the D2/20D/M/1.6 material has a higher volume fraction of organic glass, and it therefore has a higher modulus than D2/M/1.6 over the entire temperature range. The D2/20D/M/1.6 and D2/20M/M/1.6 materials have the same volume fractions of organic glass, although D2/20M/M/1.6 has a discontinuous structure with glassy inclusions and consequently has a lower modulus above the polyether glass transition. The tensile stress-strain data in Table 3.8 confirm the relation between modulus, as determined by DMTA, and morphology . The weak feature in tan δ and corresponding changes in slope of E' observed at ≈ 50 °C for all three materials, are similar to those discussed previously for the as-moulded D2/M/0.6 material. This behaviour is an indication of phase mixing [76, 81, 120, 135].

Comparison of the DMTA and SAXS data for D2/M/1.6/150 and D2/M/0.6/150 shows the former to have poorer microphase separation as evidenced by the lower Q' value and the existence of the higher phase-mixed tan δ peak, despite the phase-mixed material having a bigger 1-d spacing.

3.3.3.3 Effects of Soft Segment Structure

The two TEM micrographs of T5/M/1.6 in Fig.3.16(a) and 3.16(b) show a morphology similar to that discussed for D2/20M/M/1.6. The lower magnification micrograph features a random array of spherical inclusions with a mean diameter of 1.9 μm, accounting for ≈ 25% of the volume. The higher magnification micrograph shows these inclusions to be superimposed on a background pattern, similar to the real-space images in Fig.3.12, 3.14(a) and 3.14(b), with a characteristic length of ≈ 150 Å. Furthermore, the inclusions have internal structure of the same length-scale as the background pattern. These observations should be compared with those made for d2/M/1.6, whose micrograph forms Fig.3.14(b), noting that the only difference between D2/M/1.6 and T5/M/1.6 is in the replacement of the 2000 molecular weight diamine with a 5000 molecular weight triamine. The increase in the characteristic size in the morphology is expected since the radius of gyration, Rg, of T5000 is ≈ 1.8 times greater than that of D2000. However, the existence of the spherical inclusions of what must be isocyanurate-rich material, is unexpected.

SAXS data for T5/M/1.6 and the homologous D2/M/1.6 material are presented in Fig.3.17, and the 1-d spacings of 153 and 112 Å, respectively, are in good agreement with TEM. The relationship between Rg and degree of polymerisation, N, according to De Gennes [160] is $Rg \sim N^{2/3}$. Furthermore, for strongly-segregated block copolymers, Helfand and Wasserman [161] have shown the observed domain spacing to be directly related to Rg, that is $1\text{-}d \sim Rg \sim N^{2/3}$. Assuming the RIM PUrI to be strongly-segregated block copolymers, then a 1.8 increase in the radius of gyration should lead to a change of equal magnitude in the observed 1-d spacing. The similarity in the values of Q' indicate that the matrix in T5/M/1.6 has essentially the same composition (in terms of electron density) as D2/M/1.6, since the relative invariant measures only the square of the electron density difference. The inclusions must be contain aromatic glass, so that the volume fraction of glassy material in the lamellar matrix is reduced. Thus from geometric considerations the observed value of 1-d is reduced compared with that predicted for the well-segregated block copolymer. The upturn in $I'q^2$ at low q for T5/M/1.6 is again most likely due to particle scattering from these inclusions.

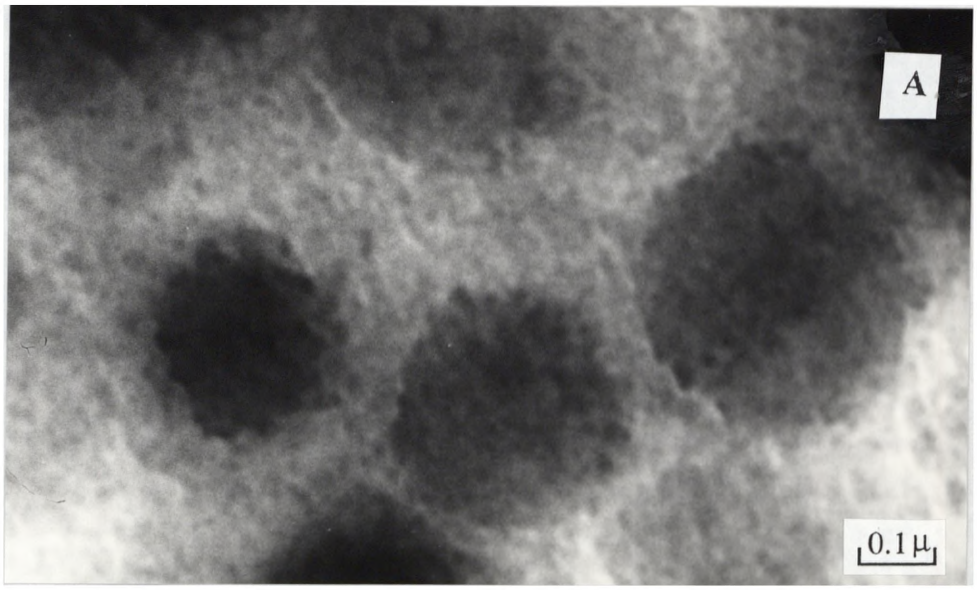

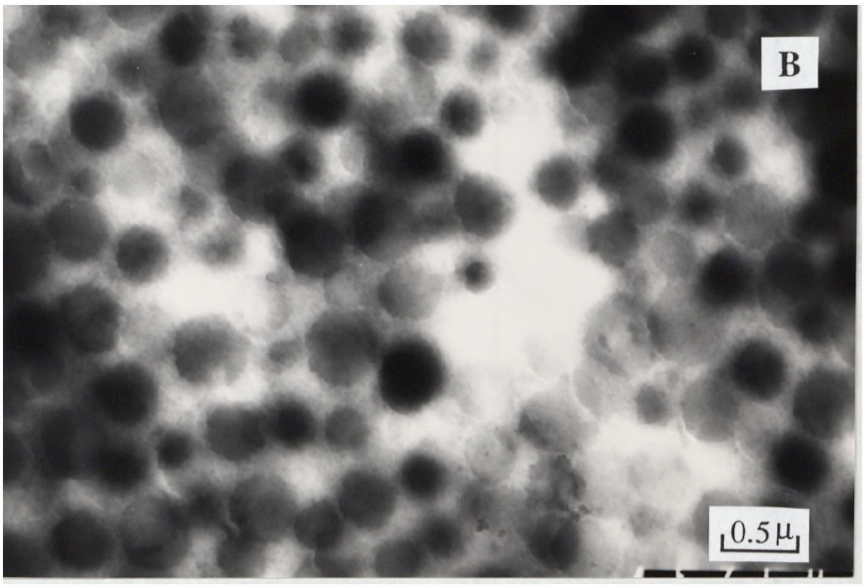

Figure 3.16 TEM micrographs of (A) and (B) T5/M/1.6.

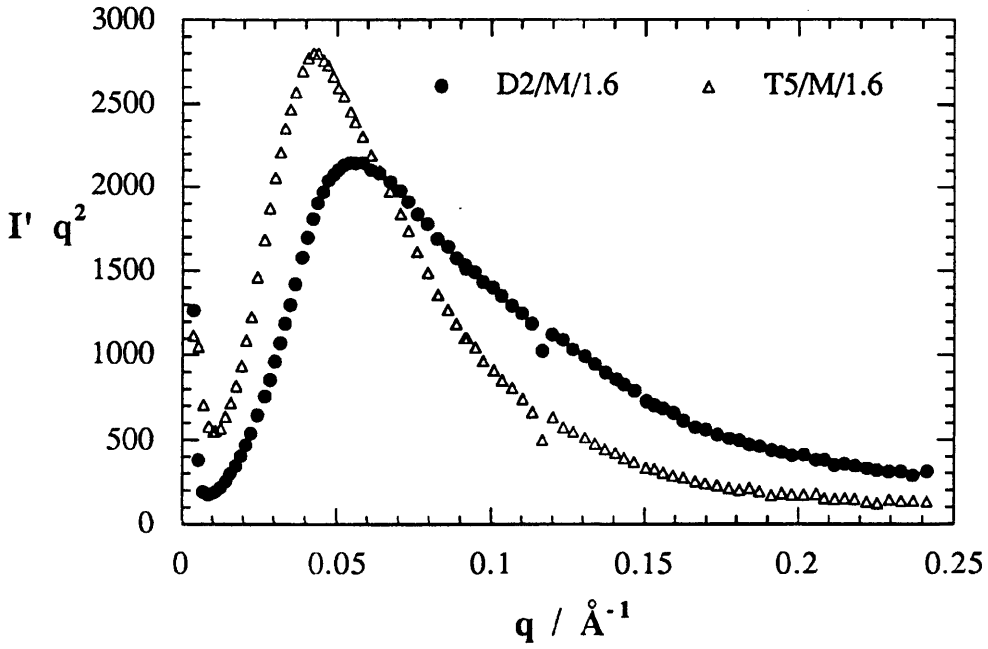

Figure 3.17 Lorentz-corrected SAXS patterns for (•) D2/M/1.6; and (Δ) T5/M/1.6.

The effects of morphological differences on dynamic mechanical behaviour are illustrated in Fig.3.2a for D2/M/1.6 and T5/M/1.6. Replacing D2000 by T5000 results in a more intense polyether glass transition at ≈ -30 °C. For both materials, the isocyanurate glass transition is observed as a shoulder on a rising tan δ curve and a drop in modulus (followed by a rubbery plateau) at ≈ 175 °C. The large difference in the modulus-temperature behaviour above the polyether glass-transition is due to morphology. The T5/M/1.6 material has the same volume fraction of organic glass as D2/M/1.6 but shows a lower value of modulus over the entire temperature range. Both materials appear to have a co-continuous morphology from TEM, except that in T5/M/1.6 there is also a discontinuous structure of glassy inclusions. The tensile stress-strain data in Table 3.8 confirm this behaviour. Furthermore, T5/M/1.6 also has the weak peak in tan δ and a corresponding change in the slope of E' at ≈ 70 °C associated with the break-down of hydrogen bonding between ether-oxygens and urea carbonyls, these features are an indication of phase mixing.

The incorporation of chain extender into T5- systems results in similar changes in morphology and mechanical properties as discussed for D2-systems. Thus, the data in Table 3.11 for T5/20D/M/1.6 compared to T5/M/1.6, and the data for D2/20D/M/1.6 compared to D2/M/1.6, show that the addition of DETDA-based hard segment leaves the morphology qualitatively unchanged with reductions in L, 1-d and Q'. Furthermore addition of DETDA results in higher values of modulus, strength and ultimate elongation. The different morphologies of the D2- and T5- systems, therefore, are related solely to the molecular architecture (linear versus branched) of the polyether oligomers and indicate that structure develops during the initial stages of polymerisation since the amines react almost instantaneously and their reaction products dominate the subsequent thermodynamic processes occurring during solidification.

Impingement mixing of amine-functionalised polyether oligomers with MDI does not always lead to the formation of a perfect mixture, as shown by Willkomm [76]. The most probable distribution could only be achieved by using very high Reynolds numbers (> 800) for mixtures of polyether diamines and MDI at a stoichiometric ratio r=10. When T5000 is mixed with MDI at r = 10, an inhomogeneous "stringy" solid was extruded from the mixhead irrespective of Reynolds number. The stringy structure corresponds to the initial striations formed during the impingement mixing process. Chemical gelation occurred in milliseconds, a time-scale equivalent to the residence time of the materials in the mixhead. Theoretically [162], chemical gelation occurs only in the stoichiometry interval, $f\text{-}1 \geq r \geq 1/f\text{-}1$, for $RA_2 + RB_f$ polymerisations. That chemical gelation occurs in the reaction between a diisocyanate and a triamine (f = 3) indicates that a local stoichiometry of $r \leq 2$ exists in the striations. The loosely crosslinked system sets the initial (block copolymer) morphology with 1-d = 150 Å at very low (< 20 %) conversions of isocyanate groups, and starts to exclude the unreacted diisocyanate from the gel by microsyneresis (squeezing). A heterogeneous nucleation and growth process accounts for the nearly monodisperse size distribution of the inclusions which are subsequently crosslinked .

3.4 Summary and Conclusions

A series of novel RIM PUrI have been formed by reacting a polyisocyanate and a polyether polyamine (and an aromatic diamine chain extender) in the presence of an organic catalyst. A polyether diamine (D2000) and a polyether triamine (T5000) were used to study the effects of functionality on the morphology and properties of PUrI. An aromatic diamine chain extender, either DETDA or MDIPA, was also used in some systems to modify the glassy isocyanurate structure resulting in the formation of tougher materials. Properties of RIM materials were shown to be dependent on their non-equilibrium morphology which resulted from competition between polymerisation kinetics, chemical gelation and (micro)phase separation. DMTA confirmed the existence of a microphase-separated morphology, the scale of which was determined by SAXS and TEM. The degree of segmental mixing, inferred from the DMTA modulus-temperature dependence between the polyether (≈ -50 °C) and isocyanurate (160-200 °C) glass transition temperatures, was in good agreement with that measured by the invariant Q' from SAXS. The high modulus (≈ 1.5 GPa) materials, D2/M and D2/20D/M, were shown by SAXS and TEM to have an isotropic, co-continuous morphology (1-d ≈ 100 Å). Replacing D2000 with T5000 resulted in materials with heterogeneous morphologies irrespective of variations in composition or processing conditions. Materials which were shown by TEM to contain isolated glassy particles (≈1μm) were formed when chemical gelation occurs at low isocyanate conversions (50%) and had lower moduli (≈ 0.7 GPa) than those with the isotropic morphology. In system based on D2000 and MDIPA, MDIPA maybe act as nucleus which also resulted in the formation of isolated glassy particles. The morphology and properties of D2/M/0.6 PUrI were also affected by annealing (150 °C / 1 hr, 180 °C / 1 hr, 200 °C / 1 hr). Tensile stress-strain data showed that annealing increased Young's modulus (from 1.26 to 1.45 GPa) and reduced ultimate elongation (from 10% to 8.7%), due to increase in crosslinking density. The DMTA (sharper and higher γ (T_g^s) peaks), in good agreement with the SAXS (Q' increased from 180 to 257) and TEM(clearer definition of morphology), showed enhancements of phase purity on annealing. The results of these

studies have therefore established correlations between processing, morphology and the dynamic mechanical-thermal and tensile stress-strain properties for a systematic series of PUrI.

CHAPTER FOUR

PROCESSING AND THERMAL PROPERTIES OF HYBRID SRIM COMPOSITES

4.1 The Processing and Thermal Properties of SRIM Hybrid Composites

4.1.1 Reinforcements and their surface treatments

Four kinds of reinforcements were used during the study. Three of the reinforcements, ROVLOK NON-WOVEN reinforcements (ex. Heinsco), are unidirectional glass, carbon, Kevlar fibre mats respectively. The fourth of reinforcement is randomly oriented, continuous glass-fibre mat, M8610 (ex. Owens-corning). Tables 4.1, 4.2, and 4.3 give some technical data for the ROVLOK reinforcements used in the study.

Glass fibre reinforcements were surface treated using Dow Corning Z-6020 silane, which is a reactive chemical containing an alkylamine organic group and a trimethoxysilyl inorganic group. The chemical formula of Z-6020 is

$$(CH_3O)SiCH_2CH_2CH_2NHCH_2CH_2NH_2$$

and is designated N-(β-aminoethyl)-δ-amino-propyltrimethoxysilane.

Surface treatment involved the immersion of glass Mats in a 0.1 % (v/v) aqueous solution (pH = 3-4.5) of the silane for five minutes at room temperature. The coated mats were put into an oven at 120°C for 20 minutes, and then stored in the open air place for a few days to complete dryness. The surface-treated glass mats were ready for the production of composites.

Carbon fibre and Kevlar fibre reinforcements were treated with an experimental proprietary silane coupling agent (ex. Dow Corning). The surface treatment procedure was the same as for Z-6020.

In addition, untreated reinforcements and reinforcements surface-treated with higher level (0.5% v/v) of silane were also used in the production of SRIM composites. Unless otherwise specified, the processing and properties of the SRIM composites reported refer to reinforcements which were treated with 0.1% (v/v) of silane.

Table 4.1 General unidirectional ROVLOK specification [164]

Product Description	Unidirectional Reinforcement Fibre Sheet with Binder Web on each surface
Width Tolerance	± 2% (on widths 300 mm and above) of specified width
Weight of Reinforcement	± 4% of specified weight per square metre
Binder Web	Proprietary polyester copolymer
Weight of Web	6.5 ± 1.5 g m^{-2} on each surface

Table 4.2 Reinforcement fibres [164]

VERLOK	084 M19 15 micron E glass, epoxy and polyester compatible. (Silenka)
GRAFLOK	Tenax HTA Standard Modulus (AKZO)
ARALOK	Kevlar 49 (Du Pont)

Table 4.3 ROVLOK reinforcements [164]

Reinforcement	Type	Density / g m^{-2}.
E Glass Fibre (VERLOK)	Unidirectional	300
Carbon Fibre (GRAFLOK)	Unidirectional	200
Aramid Fibre (ARALOK)	Unidirectional	175

4.1.2 SRIM Processing and Composites Codes

The RIM machine and the mould used to process SRIM composites were as described in Chapter 2. The matrix formulation, D2/M/0.6, was chosen for the production of SRIM composites because of its lower reactant viscosity, and better mechanical and thermal properties of the finally-formed copoly(urea-isocyanurate) (PUrI), as reported in Tables 2.10, 3.4, 3.6 and 3.7.

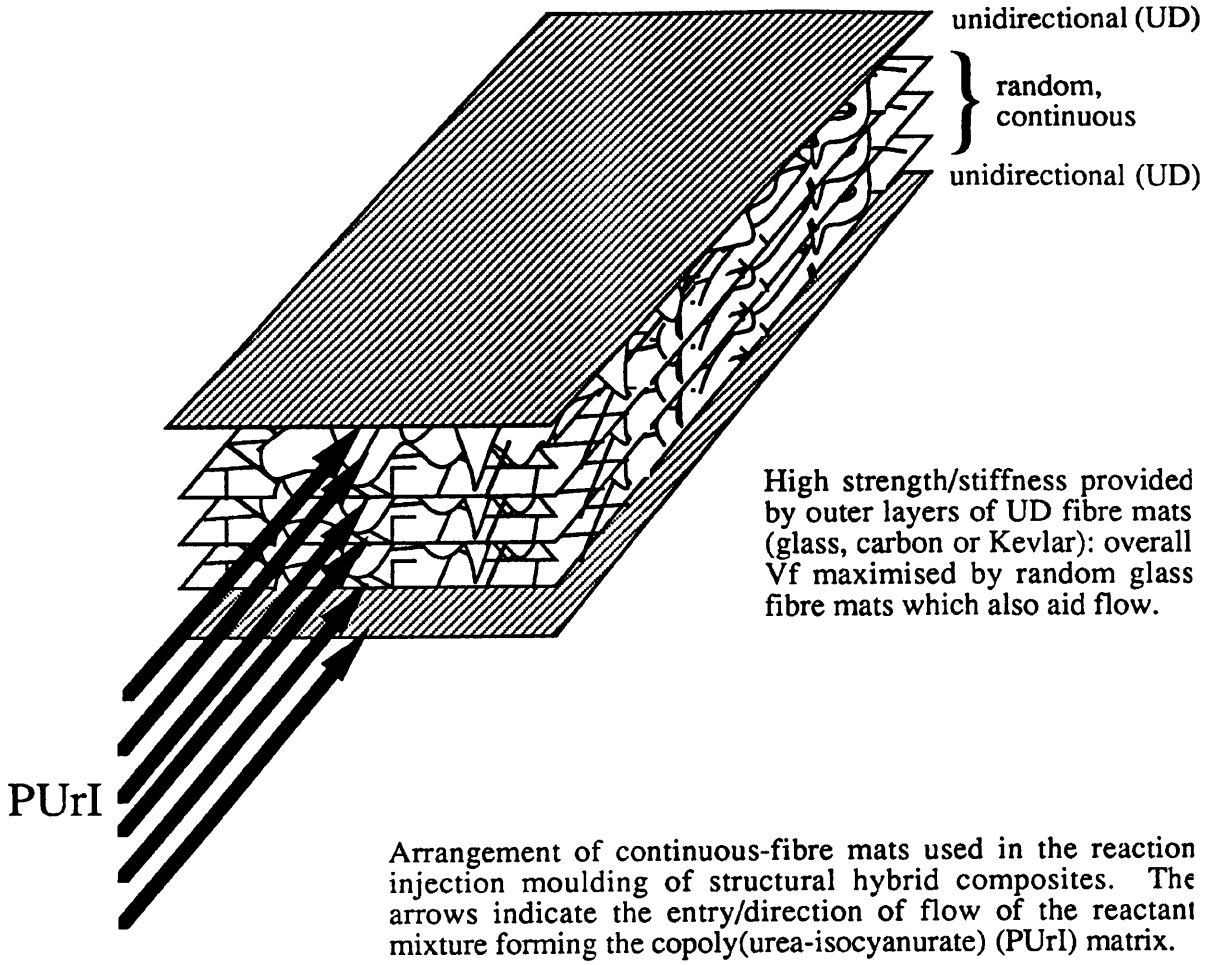

Figure 4.1 Reinforcement geometry for SRIM composites

All reinforcement mats were cut to give dimensions slightly smaller than those of the mould, and were packed into the mould as shown as in Fig.4.1, in which, the outer (top and bottom) layers were unidirectional fibre mats, providing high strength and high modulus for SRIM composites, and inner layers were randomly-oriented continuous glass fibre mats, M8610, facilitating flow of the reactant mixture during SRIM processing. Different reinforcement packing geometries were also studied, they were alternately packing of four layers GRAFLOK and three layers M8610, and alternately packing of three layers M8610 and two layers GRAFLOK. The processing procedure and parameters was the same as that described in section 2.5.3 for the production of PUrI, except that reinforcement mats were pre-placed in the mould. SRIM composites were moulded as rectangular plagues (150 x 400

x 3.3 mm) using PH-15 RIM machine. A polyisocyanate:polyamine mass ratio of 2:1 was used throughout. Initial reactant and mould temperature were 36 and 90 °C respectively: typical gel time was ~4 s with mould filling occurring in 1.5 s, and demould time were ~5 minutes. To achieve good mixing in an impingement mixing device, nozzle Reynolds numbers (Re) must exceed a critical value , generally quoted as ~300 for polyurea formulation [1]. A constant value of Reynolds number, Re ~ 1200, for the polyamine D2000 reactant stream was used throughout the present study, and Re for the polyisocyanate reactant stream was always > 1500. Mixing was therefore good and the materials showed no visible striations or gel-lines. All materials were post-cured at 150 °C for 1 hour. Table 4.4 gives the codes used to designate different SRIM composite produced.

Throughout this Chapter and Chapter 5, the specimens for thermal and mechanical property tests were taken from SRIM composite plaques in directions of longitudinal and / or transverse to the fibre axes of the outer, unidirectional fibre mats (see Fig.4.2). The longitudinal direction also corresponds to the mould-fill direction of the reactant mixture.

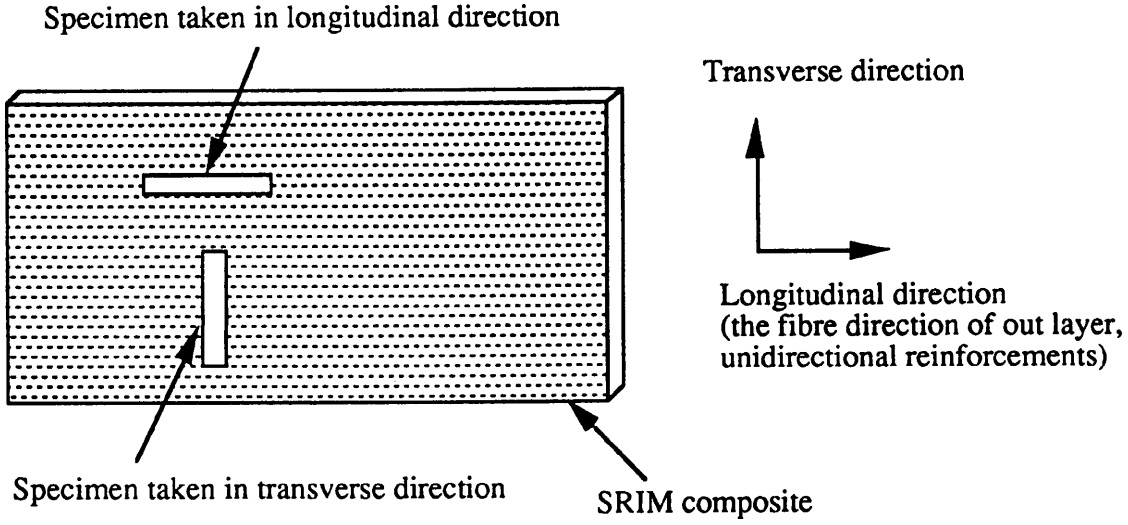

Figure 4.2 Sampling of specimens from SRIM composites for thermal and mechanical tests

Table 4.4 Desciption and designation codes of SRIM composites

SRIM composite codes	Top layer (Unidirectional)	Inner layers (Random)	Bottom layer (Unidirectional)
2GR	0	2 x M8610	0
2GL/2GR	1 x VERLOK	2 x M8610	1 x VERLOK
2GL/3GR	1 x VERLOK	3 x M8610	1 x VERLOK
2GL/4GR	1 x VERLOK	4 x M8610	1 x VERLOK
2GL/5GR	1 x VERLOK	5 x M8610	1 x VERLOK
2GL/6GR	1 x VERLOK	6 x M8610	1 x VERLOK
2CL/2GR	1 x GRAFLOK	2 x M8610	1 x GRAFLOK
2CL/3GR	1 x GRAFLOK	3 x M8610	1 x GRAFLOK
2CL/4GR	1 x GRAFLOK	4 x M8610	1 x GRAFLOK
2CL/5GR	1 x GRAFLOK	5 x M8610	1 x GRAFLOK
2KL/2GR	1 x ARALOK	2 x M8610	1 x ARALOK
2GW/2GR	1 x woven fibre mat	2 x M8610	1 x woven fibre mat
CL/GR/CL/GR/CL	1 x GRAFLOK	1 x M8610, 1 x GRAFLOK, 1 x M8610	1 x GRAFLOK
GR/CL/GR/CL/GR/CL/GR	1 x M8610	1 x GRAFLOK, 1 x M8610, 1 x GRAFLOK, 1 x M8610, 1 x GRAFLOK	1 x M8610

4.1.3 Reinforcement Volume Fraction (ϕ_f)

The reinforcement mats were cut into ~20 x 20 mm specimens which were accurately weighted, and used to determine composite densities. Table 4.5 gives the densities of the reinforcement mats, and the values are the average of at least eight determinations. Table 4.6 gives the densities of reinforcement fibres.

Table 4.5 The densities of reinforcement mats

Reinforcement mats	Density / g m^{-2}	
	Experimental	Manufacturer [164]
M8610	462 ± 10	(a)
VERLOK	302 ± 5	300
GRAFLOK	210 ± 12	200
ARALOK	170 ± 8	175

(a) Not available.

Table 4.6 The densities of reinforcement fibres

	E glass fibre	carbon fibre	Kevlar 49
Density / g m^{-2} (a)	2.54	1.78	1.45

(a) (Heinsco Ltd)-private communication

The weight, W_a, of D2/M/0.6 matrix in air, and the weight, W_w, in water were measured, from which the density of matrix, d_m, was determined using

$$d_m = \frac{W_a}{(W_a - W_w) / d_w} \tag{4.1}$$

where d_w (= 0.996 g cm^{-3}) is the density of water. The density, d_c, of a composite was determined using the same procedure.

The volume fraction of reinforcements was calculated as following:

For the composite specimen of the length L, width B, and thickness h (h ≈ 3.3 mm), its weight, W_c, is

$$W_c = B\ L\ h\ d_c \tag{4.2}$$

Assuming the weight of binder was 6.5% of reinforcements. The weight, W_{uf}, of two unidirectional reinforcement layers is

$$W_{uf} = 2 \times 0.935 \times B\ L\ d_u \tag{4.3}$$

where d_u is the density of the unidirectional reinforcement mats. The weight, W_{rf}, of N layers of M8610 random glass mats is

$$W_{rf} = N\ B\ L\ d_r \times 0.935 \tag{4.4}$$

d_r is the density of M8610 mats. The weight, W_m, of matrix is

$$W_m = W_c - W_{uf} - W_{rf} \tag{4.5}$$

Thus, using Eq(4.2) to (4.5), the volume fraction, ϕ_{uf}, of unidirectional reinforcements is

$$\phi_{uf} = \frac{2 \times 0.935 \times B\ L\ d_u}{d_{uf}\ B\ L\ h} = \frac{2 \times 0.935 \times d_u}{h\ d_{uf}} \tag{4.6}$$

where d_{uf} is the density of fibres in the unidirectional reinforcements. The volume fraction, ϕ_{rf}, of M8610, random glass fibre mats is

$$\phi_{rf} = \frac{0.935 \times N\ B\ L\ d_r}{d_{rf}\ B\ L\ h} = \frac{0.935 \times N\ d_r}{h\ d_{rf}} \tag{4.7}$$

where d_{rf} is the density of E glass fibre (= 2.54 g cm^{-3}). The volume fraction, ϕ_m, of matrix is

$$\phi_m = \frac{W_c - W_{uf} - W_{rf}}{d_m\ B\ L\ h} = \frac{h\ d_c - (2\ d_u + N\ dr) \times 0.935}{h\ d_m} \tag{4.8}$$

where d_m is the density of matrix (= 1.19 g cm^{-3}).

Thus, the volume fraction, ϕ_b, of voids is

$$\phi_b = 1 - \phi_{uf} - \phi_{rf} - \phi_m \tag{4.9}$$

Table 4.7 gives the reinforcement volume fractions of reinforcements for all SRIM composites. The effects of reinforcement volume fraction on heat sag, CLTE and thermal dynamic properties of SRIM composites will be discussed in following sections.

4.2 Heat Sag

The heat sag test is used extensively in the PU industry to rank RIM-materials in the order based on the thermal dimensional stability, and is generally conducted according to ASTM D3769–81, using a jig shown schematically in Figure 4.3. A critical analysis of

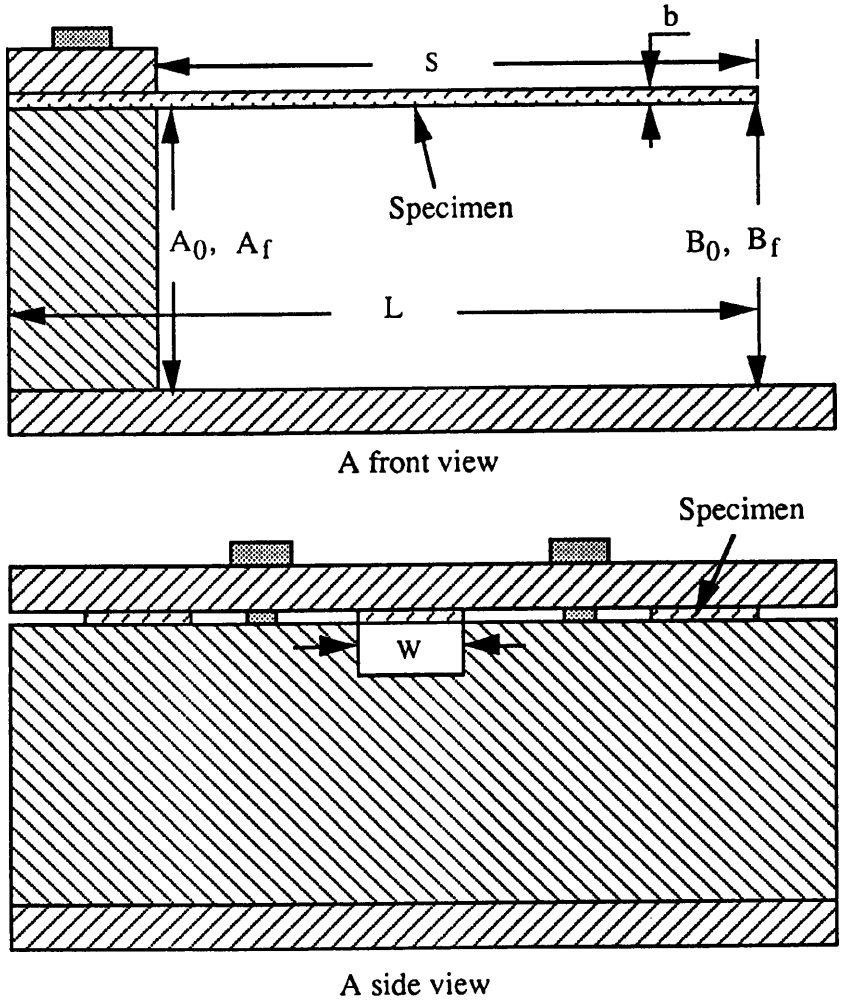

Figure 4.3 A schematic diagram of the jig used for heat sag measurements

Table 4.7 Reinforcement volume fraction of SRIM composites

Materials	ϕ_f / %		ϕ_m / %		
	ϕ_{uf}	ϕ_{rf}	Control	0.1% Silane	0.5% Silane
2GR	0	10.7 ± 0.1	69.4 ± 1.4	68.2 ± 2.6	67.9 ± 1.8
2GL/2GR	6.9 ± 0.1	10.7 ± 0.2	67.8 ± 1.5	63.5 ± 1.8	63.3 ± 2.4
2GL/3GR	7.0 ± 0.2	16.3 ± 0.3	62.6 ± 2.0	57.3 ± 1.9	58.9 ± 2.5
2GL/4GR	6.8 ± 0.1	21.1 ± 0.3	59.8 ± 3.6	57.1 ± 3.5	(a)
2GL/5GR	6.8 ± 0.2	26.5 ± 0.4	54.1 ± 2.4	53.3 ± 2.5	(a)
2GL/6GR	6.6 ± 0.2	30.9 ± 0.5	(a)	50.1 ± 1.7	(a)
2CL/2GR	6.4 ± 0.1	10.7 ± 0.3	(a)	63.0 ± 2.9	(a)
2CL/3GR	6.4 ± 0.3	16.0 ± 0.4	(a)	57.3 ± 4.8	(a)
2CL/4GR	6.3 ± 0.2	21.1 ± 0.7	(a)	54.9 ± 3.6	(a)
2CL/5GR	6.4 ± 0.2	26.3 ± 0.5	(a)	52.8 ± 2.5	(a)
GR/CL/GR/CL/GR	6.7 ± 0.5	16.8 ± 0.6	(a)	64.0 ± 1.5	(a)
CL/GR/CL/GR/CL/GR/CL	13.4 ± 0.6	16.5 ± 0.6	(a)	53.1 ± 1.8	(a)
2KL/2GR	6.3 ± 0.3	10.7 ± 0.4	(a)	64.2 ± 1.7	(a)

(a) Not determined

standard D3769 has been reported by Dominguez and co–workers [105]. They concluded that the heat sag of a RIM elastomer was mainly dependent on the sample overhang, sample thickness and the experimental temperature. Results for high-modulus ($E \geq 0.6$ GPa) RIM materials obtained using the conditions specified in ASTM D3769 proved statistically meaningless. It was recommended that the sample overhang should be at least 155 mm for high-modulus materials. In this section, the heat sag tests were carried out using a jig shown in Figure 4.3, and three specimens, taken in the longitudinal direction from SRIM composites (see Figure 4.2), of dimensions 250 (L) x 25 (W) x 3.3 (b) mm. The pre-measured specimens were clamped in the jig with a 200 mm unsupported overhang. After 5 ± 0.2 minutes, the distances A_0 and B_0 were measured. The jig was then placed in an air–circulating oven at 200 ± 1°C for 60 ± 1 minutes. After removal, within 5 ± 0.2 minutes, the distances A_f and B_f were measured. The initial sag (room temperature, 5 minute interval) was calculated as [A_0–B_0] (mm) and the final sag as [(A_f–B_f)–(A_0–B_0)] (mm), the results being reported as the average of the three specimens and given in Table 4.8.

Table 4.8 The heat sag data for SRIM composites

Materials	Total volume fraction / %	Heat sag / mm
D2/M/0.6 (matrix)	0	25.49 ± 0.44
2GR	10.7	0.74 ± 0.31
2GL/2GR	17.6	negligible[(a)]
2GL/3GR	23.3	negligible[(a)]
2GL/4GR	27.9	negligible[(a)]
2GL/5GR	33.3	negligible[(a)]
2CL/2GR	17.1	negligible[(a)]
2CL/3GR	22.4	negligible[(a)]
2CL/4GR	27.5	negligible[(a)]

(a) no measurable sag within accuracy of digital calliper's measurement

From Table 4.8, it is clear that the dimensions of D2/M0.6 (matrix) changed significantly, and is useless as a structural material at 200 °C. However, with addition of fibre reinforcements, at volume fractions excess of 18%, the thermal stability of matrix was greatly improved. The dimensions of SRIM composites remained essentially constant even with overhangs of 200 mm at 200 °C for one hour.

4.3 Thermal Expansion

Coefficient of linear thermal expansion (CLTE) is a very important physical property of materials, especially when different materials are used together, and for this reason their CLTE must be matched. In this study, the CLTE was measured using the equipment that was designed and constructed in the Materials Science Centre of University of Manchester / UMIST. Test specimens, 3.3 x 3.3 x 10 mm, were taken from SRIM composites in both longitudinal and transverse directions as shown in Fig.4.2. Figure 4.4 is a schematic diagram of the specimen holder used for CLTE experiments. Special care was required to ensure that the top and bottom surfaces of a specimen were parallel. When a specimen was placed in the specimen holder, the holder was then put into a fine furnace in which the temperature was controlled to within ± 0.1 °C.

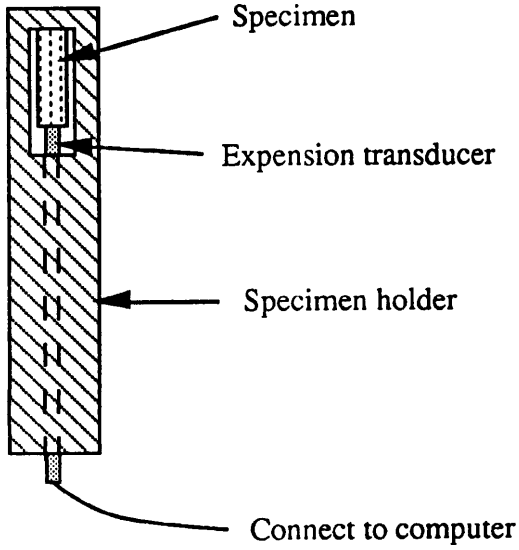

Figure 4.4 A schematic of specimen holder for CLTE experimental

CLTE experiments were first carried out on the unfilled PUrI matrix (D2/M/0.6), conditioned prior to testing in their different ways. The conditioning used is summarised in Table 4.9.

Table 4.9 Storage conditions of matrix specimens for CLTE experimental

Specimen	Conditioning
A	Post cured at 150 °C for 1hr., and stored in a desiccator at 20 °C for 24 h.
B	Post cured at 150 °C for 1hr., and stored in a room environment for 24 h.
C	Post cured at 150 °C for 1hr., and immersed in water at 20 °C for 24 h.

The determination of CLTE involved a heating program comprising several thermal cycles as shown in Fig.4.5. In the first cycle, the furnace was heated from 30 to 155°C at a rate of 1°C min^{-1}, and then cooled from 155 to 30 °C at a rate of -1°C min^{-1}. This process was repeated in the second and third cycles. The thermal expansion was measured by a very sensitive transducer, which can detect dimensional changes down to 10^{-3} μm, recorded by a computer. Transducer data (~200 data points) was collected every four minutes over a total time period, typically 12.5 hours, and also used to carry subsequent calculations. Figure 4.6–4.8 show the thermal expansion dL / L (expressed as the change in length, dL, divided by original length, L) versus temperature diagrams of specimens of A, B, C.

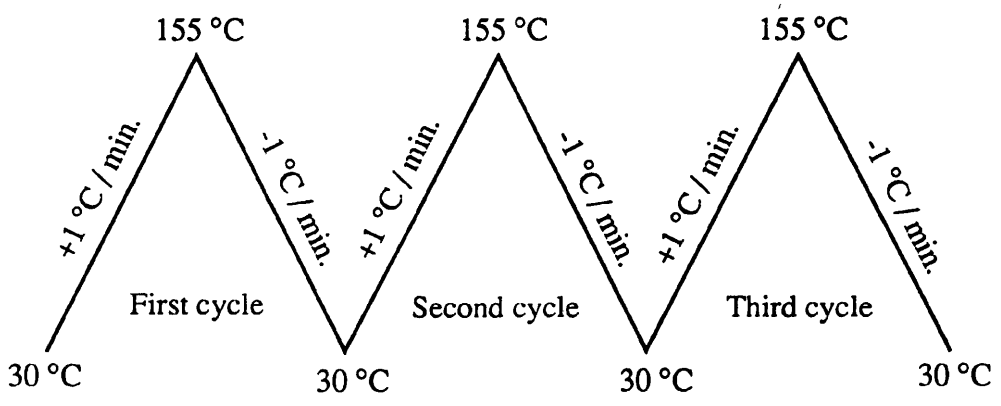

Figure 4.5 Heating programme used in CLTE experiments on matrix (D2/M/0.6)

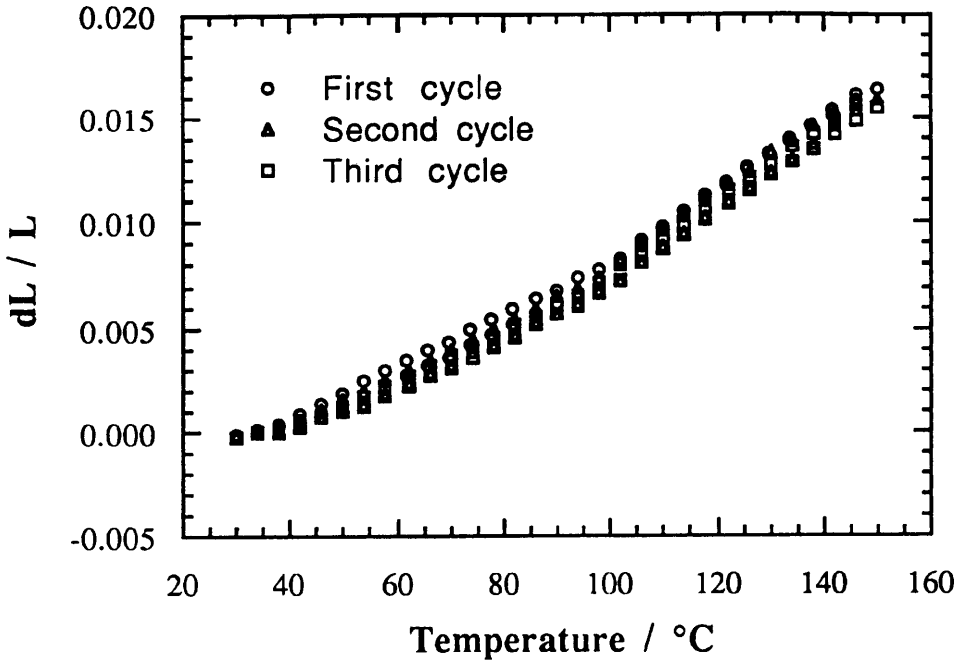

Figure 4.6 Plot of dL / L versus temperature for PUrI matrix, D2/M/0.6 (specimen A stored in desiccator)

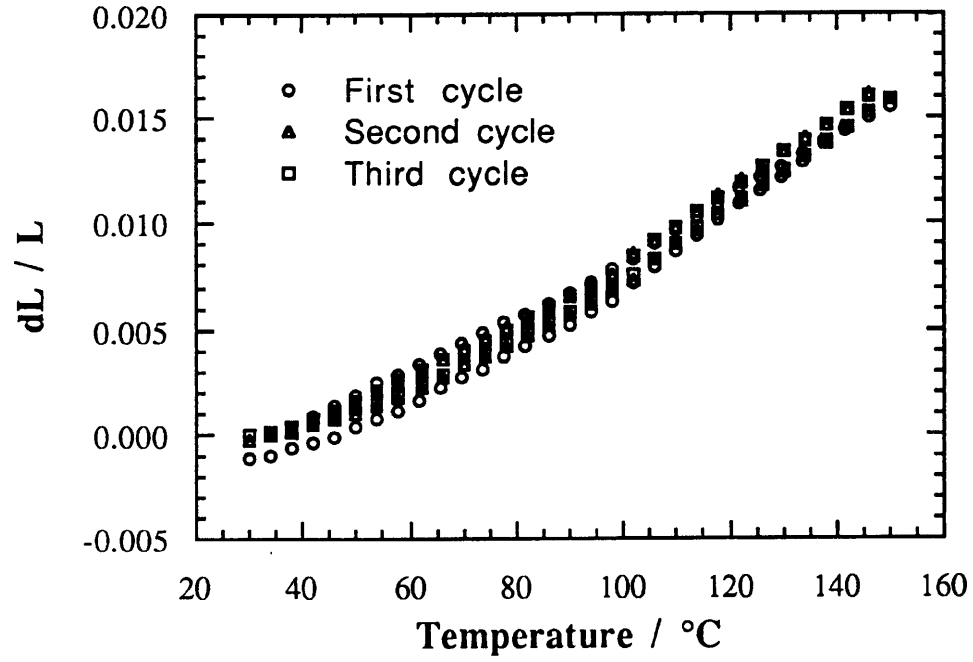

Figure 4.7 Plot of dL / L versus temperature for PUrI matrix, D2/M/0.6 (specimen B stored in air)

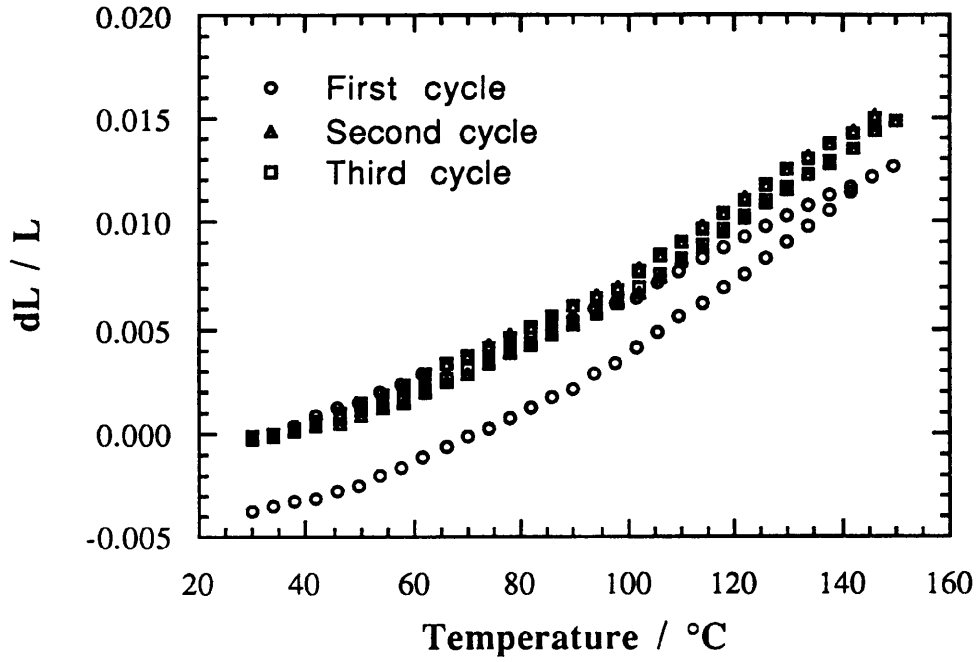

Figure 4.8 Plot of dL / L versus temperature for PUrI matrix, D2/M/0.6 (specimen C immersed in water)

In Figure 4.6, the thermal expansion curves obtained from the three cycles show reasonable agreement with the contraction curve during cooling stage following the expansion curve during heating stage. In Figure 4.7 and Figure 4.8, the contraction curves of the second and third cycles also show reasonable agreement, and follow the expansion curves. However, the contraction curve of the first cycle does not follow the expansion curve, particularly for the specimen C which contracted more than it expanded during its first cycle. The differences between Figure 4.6-4.8 show the big effects of storage conditions on the first cycle, but not on the second and third cycles.

An explanation of the thermal behaviour of specimen C can be proposed in relation to the chemical structure of PUrI. The matrix materials (D2/M0.6) comprise many polar urea groups (-NCON-), and carbonyl groups (C=O) attached to isocyanurate rings, which are capable of forming hydrogen bonds. The structure of PUrI is therefore capable of absorbing

moisture or water which then strongly interact with polar groups. During the first cycle, the absorbed water is steadily moved in heating stage, but in cooling stage, the loss of the absorbed water is significantly reduced. Thus, in Figure 4.7 and 4.8, the contraction curves of cooling stages during the first cycle does not follow the expansion curves of heating stages. Clearly the absorbed water has an effect on the first cycle, but no effect on the second and third cycles. Similar phenomena were observed for SRIM composites, and values of the CLTE in this study were calculated from the either the second or the third cycles. Change in slope of dL / L versus temperature in all plots at ~110 °C associates with β transition which also exists in the tan δ - temperature curves of DMA experimental as a very broad peak (70 - 130 °C).

In the case of SRIM composites, a heating programme for CLTE experiments (Fig.4.9) similar to that described for the matrix was used, except that an upper temperature of 200 °C (cf. 155 °C) was used. Figure 4.10 - 4.15 show plots of dL / L versus temperature. Change in slope of dL / L versus temperature in all plots (~110 °C) associates with β transition of the matrix. Figure 4.16 - 4.22 were diagrams of CLTE versus temperature. Table 4.10 was main results of CLTE for SRIM composites. values of the CLTE of common engineering materials are given in Table 4.11 for comparative purposes.

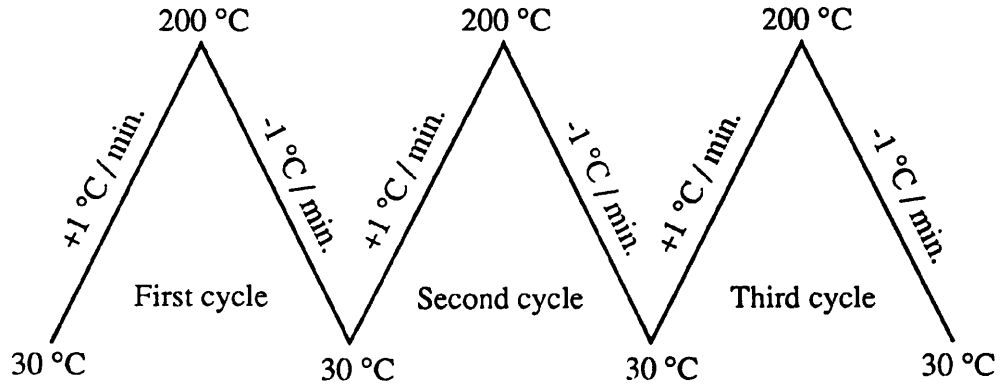

Figure 4.9 The heating programme used in CLTE experiments on SRIM composites

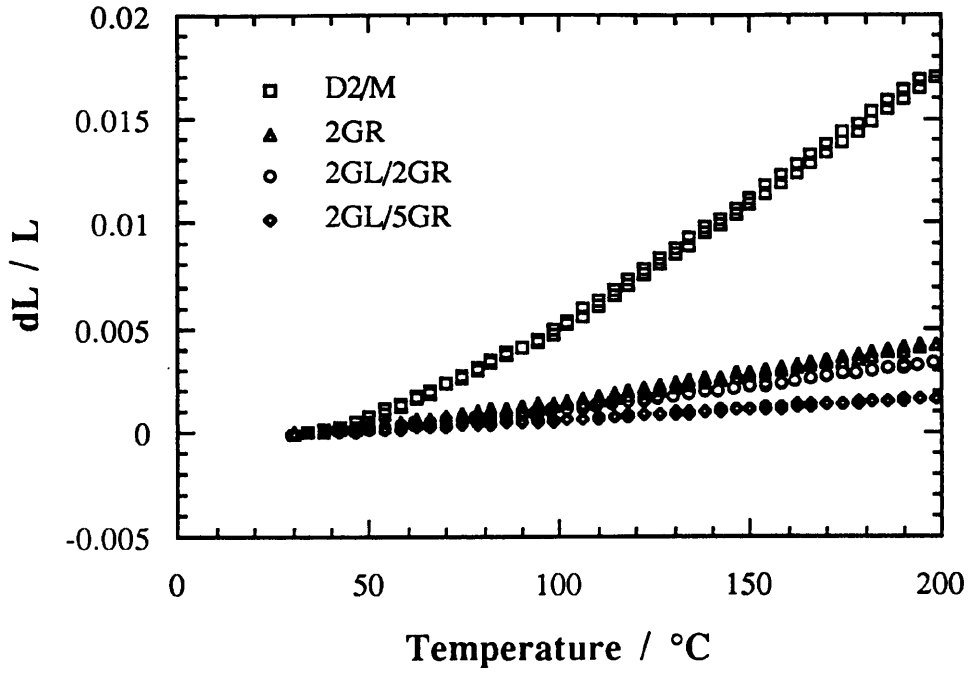

Figure 4.10 Plots of dL / L versus temperature (the second cycle) for glass-glass SRIM composites tested in longitudinal direction.

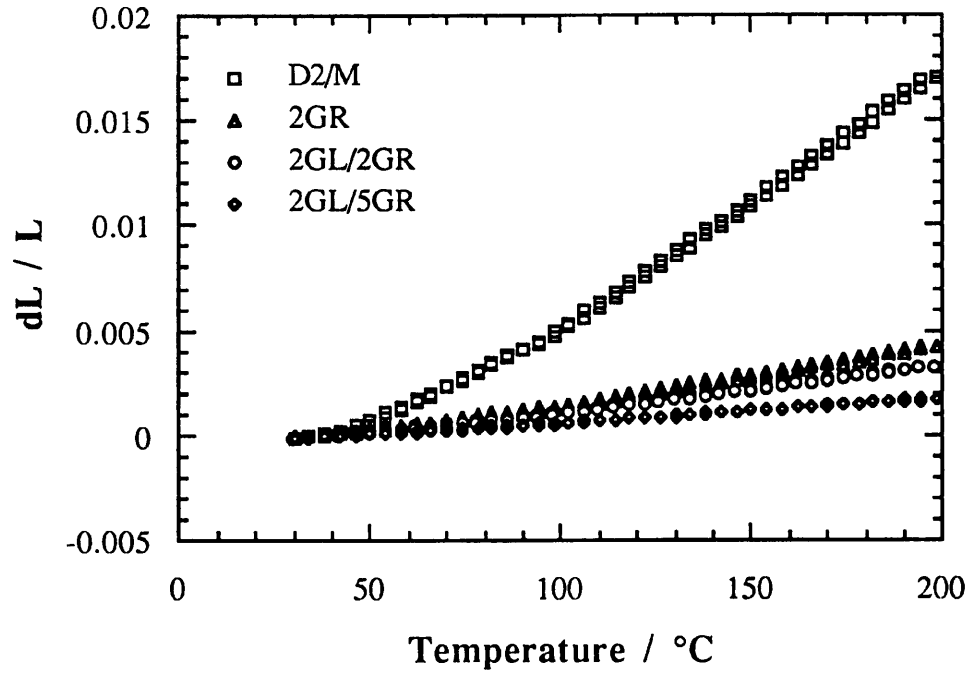

Figure 4.11 Plots of dL / L versus temperature (the second cycle) for glass-glass SRIM composites tested in transverse direction.

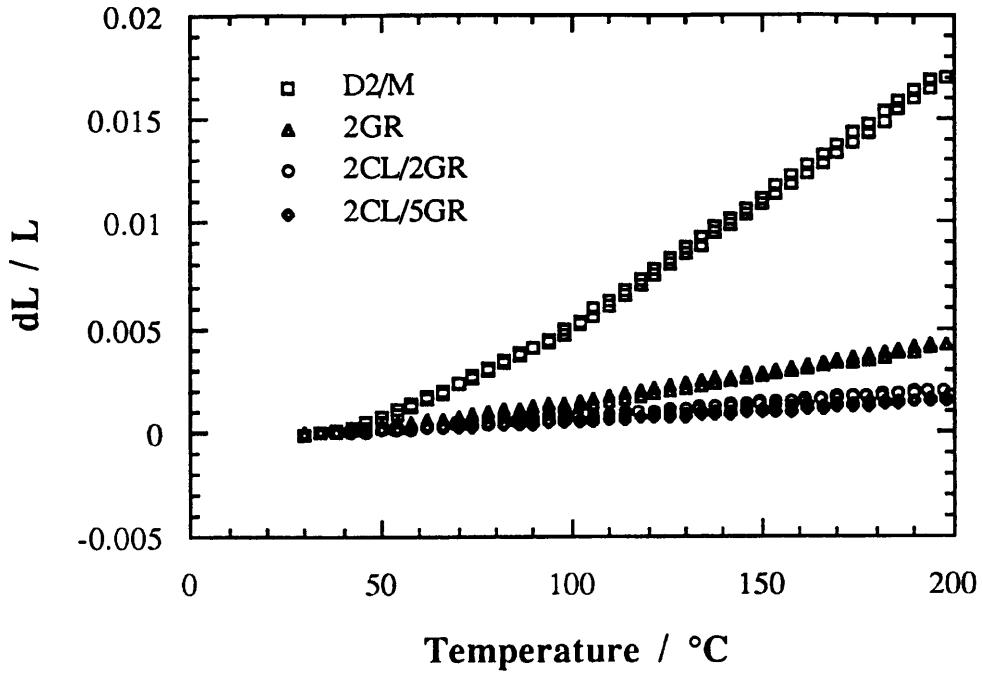

Figure 4.12 Plots of dL / L versus temperature (the second cycle) for carbon-glass SRIM composites tested in longitudinal direction.

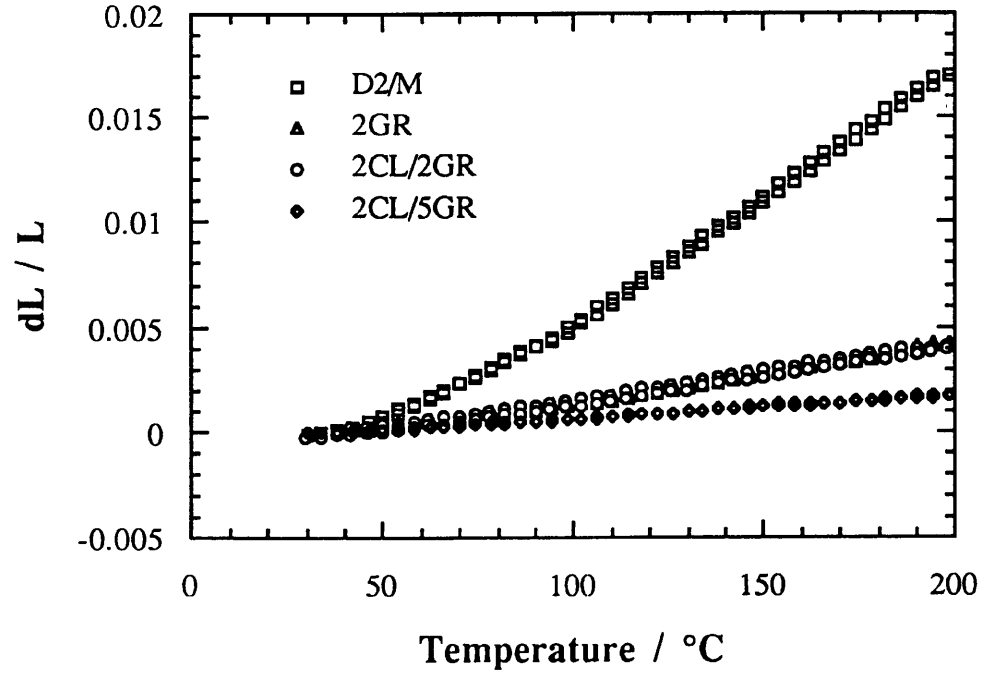

Figure 4.13 Plots of dL / L versus temperature (the second cycle) for carbon-glass SRIM composites tested in transverse direction.

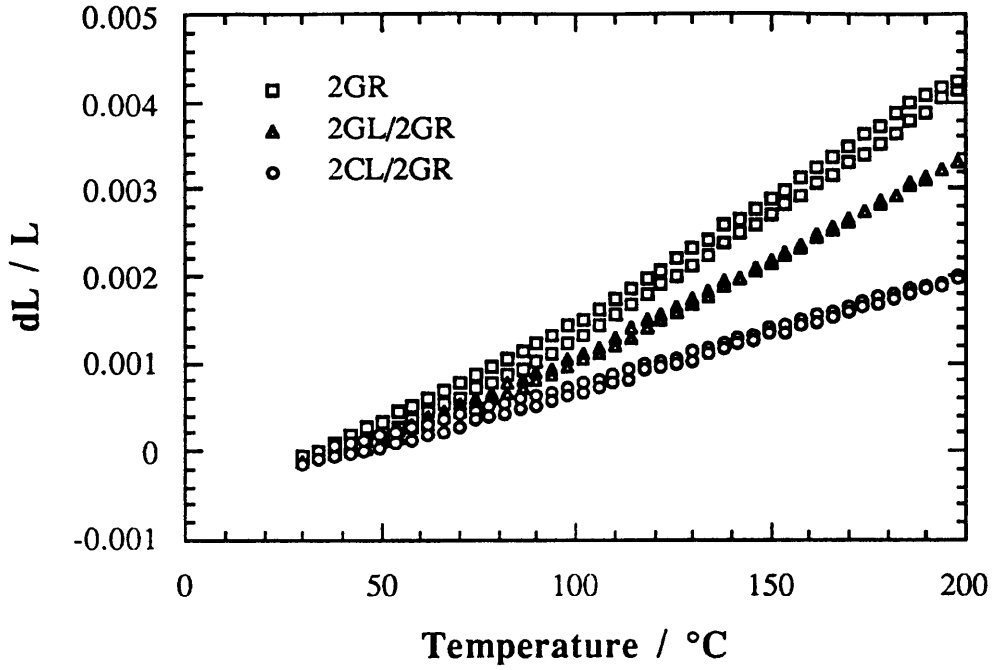

Figure 4.14 Plots of dL / L versus temperature (the second cycle) for 2GR, 2GL/2GR and 2CL/2GR SRIM composites tested in longitudinal direction.

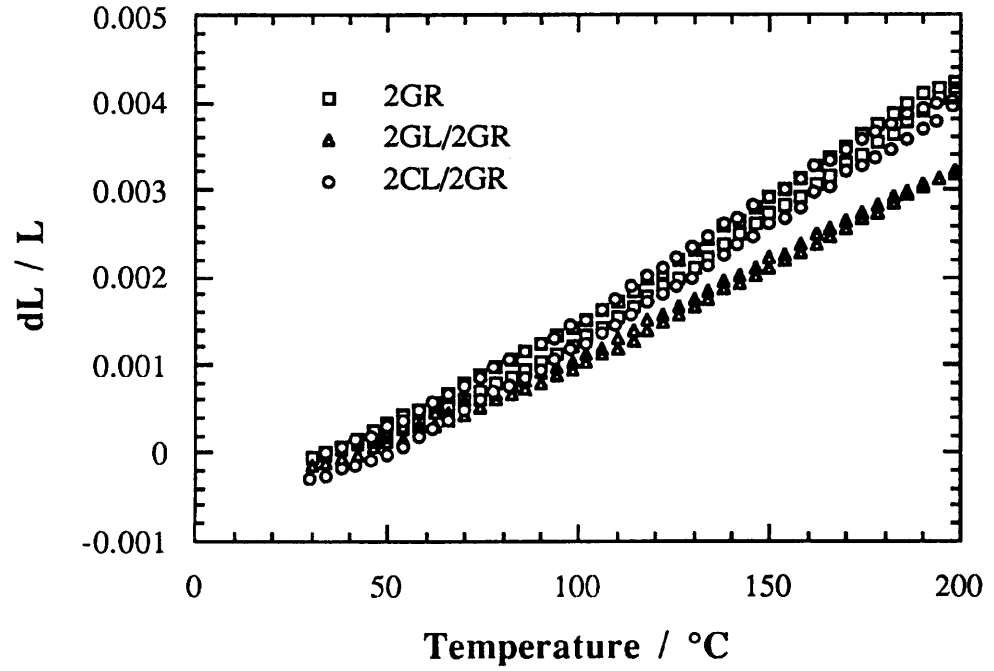

Figure 4.15 Plots of dL / L versus temperature (the second cycle) for 2GR, 2GL/2GR and 2CL/2GR SRIM composites tested in transverse direction.

Table 4.10 A summary of CLTE data of SRIM composites

Temp. / °C	CLTE / 10^{-6} K^{-1}									
	Matrix	2GR		2GL/2GR		2GL/5GR		2CL/2GR		2CL/5GR	
		L*	T*	L*	T*	L*	T*	L*	T*	L*	T*
34	80.1	24.8,	22.2	16.0,	21.7	9.6,	10.4	11.4,	21.3	8.4,	8.2
46	80.4	25.6,	23.7	16.6,	22.0	8.9,	9.7	9.8,	22.6	8.5,	9.8
58	87.9	24.2,	24.2	16.4,	21.0	10.5,	10.4	11.6,	24.5	8.4,	9.4
70	91.2	26.6,	23.7	17.3,	22.2	11.3,	12.0	11.3,	24.5	10.4,	11.3
82	85.3	24.7,	24.2	16.8,	22.6	10.4,	9.7	10.5,	22.7	8.4,	10.3
94	93.1	26.6,	26.1	19.5,	26.2	9.9,	9.9	12.6,	24.4	9.0,	10.7
106	121	29.4,	27.1	24.3,	27.9	11.7,	10.6	13.3,	28.8	11.1,	12.9
118	120	31.4,	30.9	23.6,	29.1	10.7,	13.6	14.9,	29.3	11.2,	13.3
130	122	31.8,	30.4	24.2,	28.5	11.4,	12.6	13.8,	29.4	11.5,	13.6
142	120	32.3,	30.8	24.4,	28.6	10.7,	13.0	13.5,	30.0	11.9,	14.0
154	122	30.6,	30.4	23.9,	28.8	11.2,	13.1	14.3,	29.6	12.3,	14.2
166	123	31.3,	30.4	24.4,	28.3	11.2,	13.2	14.2,	29.2	11.8,	13.5
178	128	30.4,	30.4	24.0,	29.0	10.9,	13.8	14.2,	29.4	12.2,	14.5
190	122	31.1,	30.8	24.5,	30.4	11.9,	13.4	13.5,	29.6	12.5,	13.7
198	122	31.3,	30.9	24.7,	29.8	13.7,	14.0	13.6,	29.2	12.3,	15.0

L* and T* refer to the data of CLTE of SRIM composites in longitudinal and transverse directions.

Table 4.11 The CLTE data of common materials [165]

Materials	CLTE / 10^{-6} K^{-1}
Carbon fibre	-1.2 (27)*
Kevlar fibre	-2 (59)*
Glass fibre	5
Ceramics	5 ~ 9
Iron, steel	11
Copper, brass	18
Aluminium	25
Zinc alloys	27
PE (high density)	130 ~ 200
Nylon 6.6	90
Epoxy resin	60
Polystyrene	70
ABS	80

* referring to the data at radial direction.

From Table 4.10, it is clear that the CLTE of the matrix was greatly reduced by incorporating reinforcement mats, and values of CLTE of SRIM composites varied from 30 x 10^{-6} to 12 x 10^{-6} K^{-1} depending on reinforcement volume fraction, reinforcement type, and specimen direction, presented reductions of 300 to 700% of that of the matrix. Furthermore, the CLTE values match those of common engineering materials shown in Table 4.11.

It is noticed from Fig.4.16 to Fig.4.22, that within the experimental temperature range from 30 to 200 °C, all materials have two CLTE (the values are given in Table 4.12) due to the contribution of matrix, which has the CLTE of 85 x 10^{-6} K^{-1} (30 - 90 °C) and 122 x 10^{-6} K^{-1} (110 - 200). This suggests there is a type of molecular motion around 110 °C, which will be confirmed by the existence of a broad ß peak (80 - 130 °C) during DMA study in section 4.4. As the volume fraction of reinforcements increases, the difference between those two CLTE value decreases.

Table 4.12 The value of CLTE of SRIM composites

Materials	$(CLTE)_L$* x 10^{-6} / K^{-1}		$(CLTE)_T$* x 10^{-6} / K^{-1}	
	30 - 90 °C	110 - 200 °C	30 - 90 °C	110 - 200 °C
Matrix	85	122	85	122
2GR	25	32	24	31
2GL/2GR	17	24	22	29
2GL/5GR	10	12	10	13
2CL/2GR	11	14	23	30
2CL/5GR	9	12	10	14

* L and T refer to the values of CLTE measured in longitudinal and transverse directions respectively.

Figure 4.16 shows that even two layers of random glass-fibre reinforcements greatly reduce the CLTE of the matrix. The CLTE of 2GR in the transverse direction is slightly

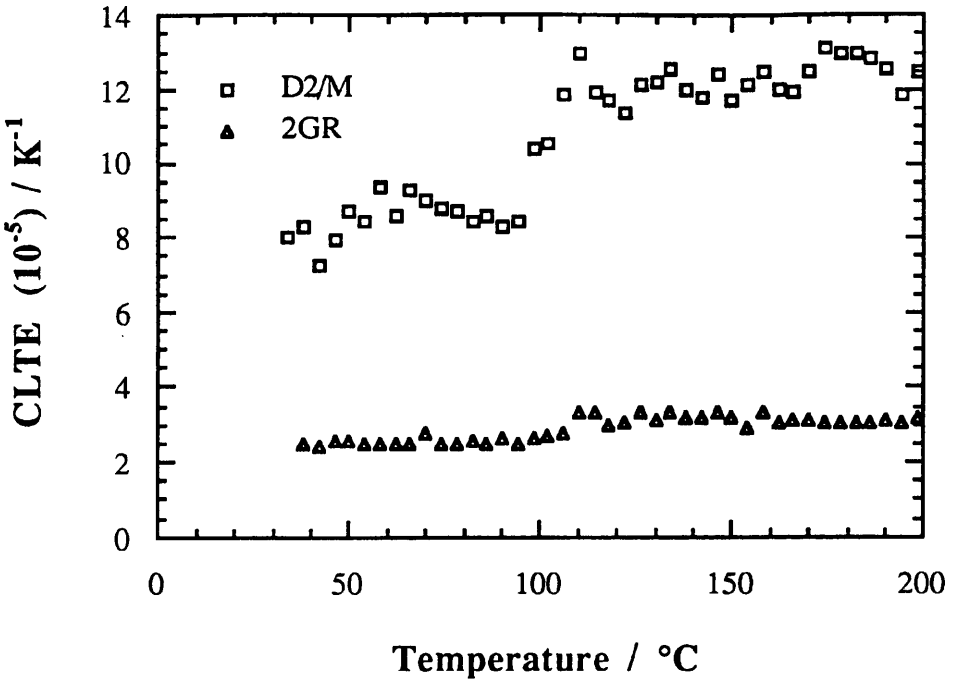

Figure 4.16 The effect of two layers of random glass mats on the CLTE of the matrix

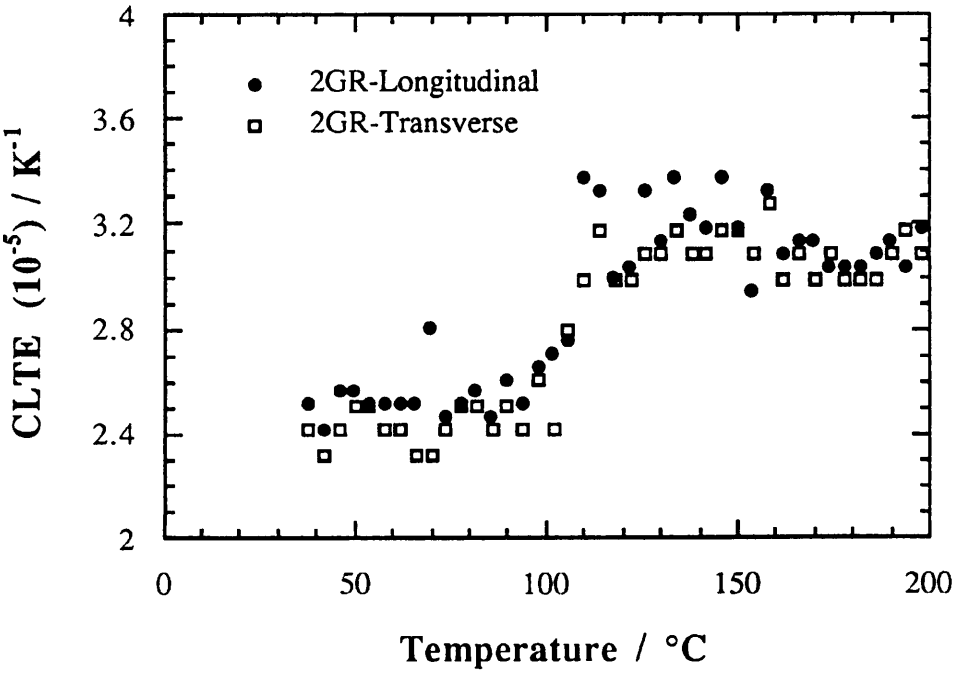

Figure 4.17 The effect of specimen direction on the CLTE of the SRIM composite, 2GR

lower than that in the longitudinal direction (see Fig.4.17), and reflects the small amount of anisotropy caused by movement of the fibres along the mould length due to the flowing resin as was injected into the mould.

Clearly, the matrix is completely isotropic, and SRIM composites are anisotropic. For random glass-fibre mat reinforced composite, 2GR, the value of CLTE in the longitudinal direction is slightly higher than in the transverse direction. As out-layer unidirectional fibre reinforcements are added, the CLTE of SRIM composites in the longitudinal direction are mainly dominated by both out-layers of unidirectional fibre reinforcements and inside-layers of random fibre reinforcements, and the CLTE of SRIM composites in the transverse direction are mainly dominated by inside-layers of random reinforcements and matrix, the CLTE of SRIM composites in the longitudinal direction are much lower than those in the transverse direction (see Table 4.12). Because the CLTE of carbon fibre is negative in axes, much lower than that of glass fibre (see Table 4.11), the CLTE of 2CL/2GR is lower than that of 2GL/2GR in longitudinal direction (see Fig.4.18). However, the CLTE of carbon fibre in radial direction is much higher than that of glass fibre (see Table 4.11), so the CLTE of 2CL/2GR is slightly higher than that of 2GL/2GR in transverse direction (see Fig.4.18). For SRIM composites with unidirectional glass-fibre reinforcements as out-layers, the CLTE of SRIM composites in longitudinal direction depends on both outside unidirectional mats and inside random mats, increasing the number of inside-layers of random fibre reinforcements reduces the CLTE of SRIM composites. That is the reason that the CLTE of 2GL/5GR is much lower than that of 2GL/2GR in longitudinal direction (see Fig.4.19). However, the CLTE of SRIM composites with carbon fibre reinforcements as out-layers is dominated by carbon fibre in longitudinal direction, even increasing inside layer number of random glass fibre mats has almost no effect on it. That is the reason that the CLTE of 2CL/5GR is only slightly lower than that of 2CL/2GR in longitudinal direction (see Fig.4.21).

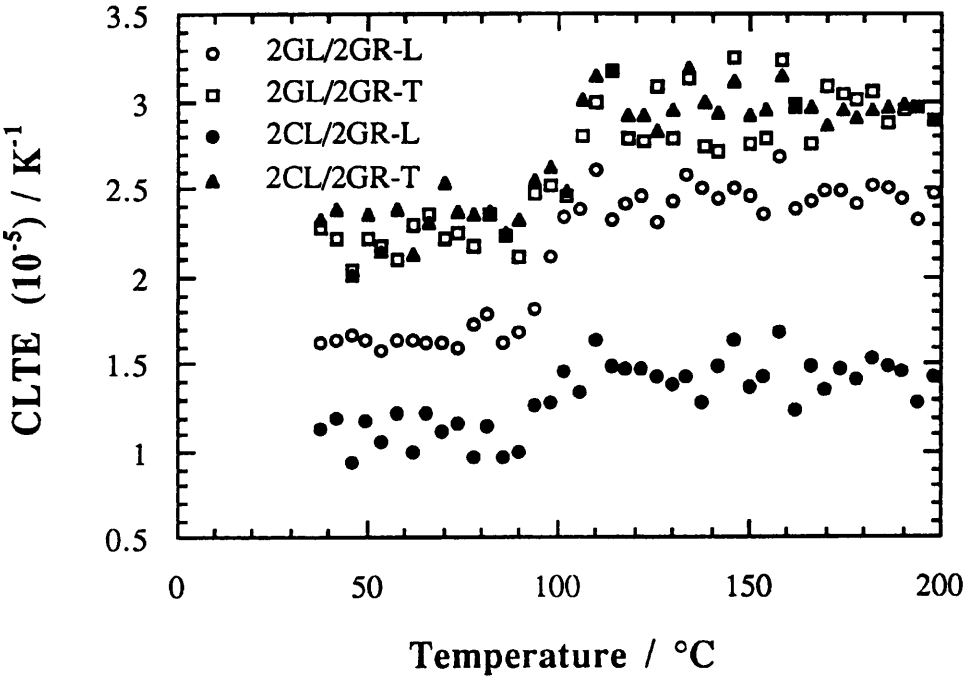

Figure 4.18 The effect of out-layers of fibre reinforcements on the CLTE of SRIM composites (L and T refer longitudinal and transverse directions, respectively).

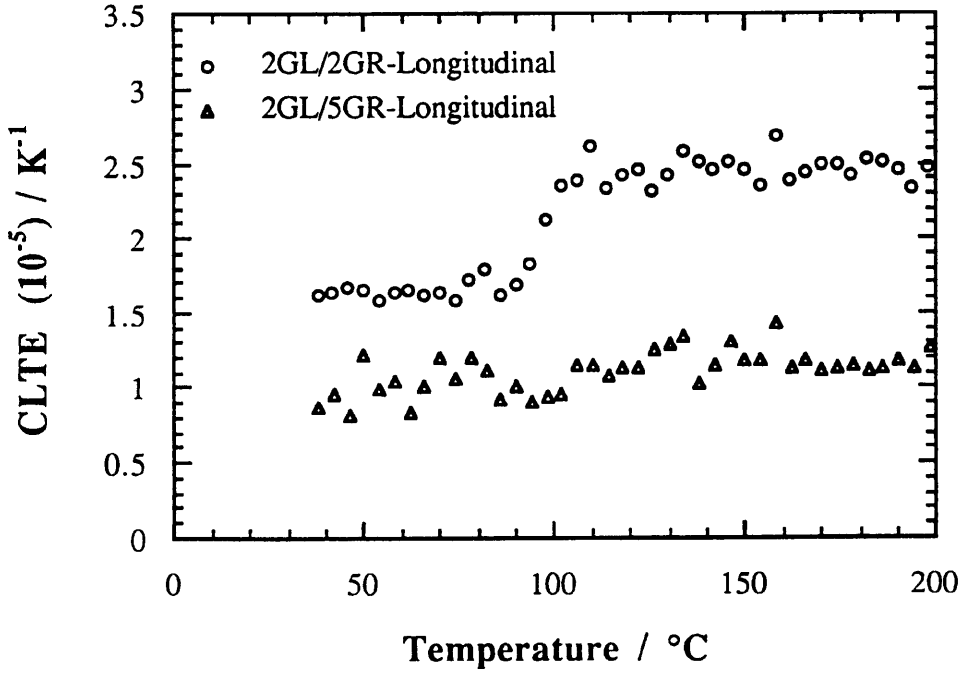

Figure 4.19 Plots of CLTE versus temperature for longitudinal specimens of glass-glass SRIM composites

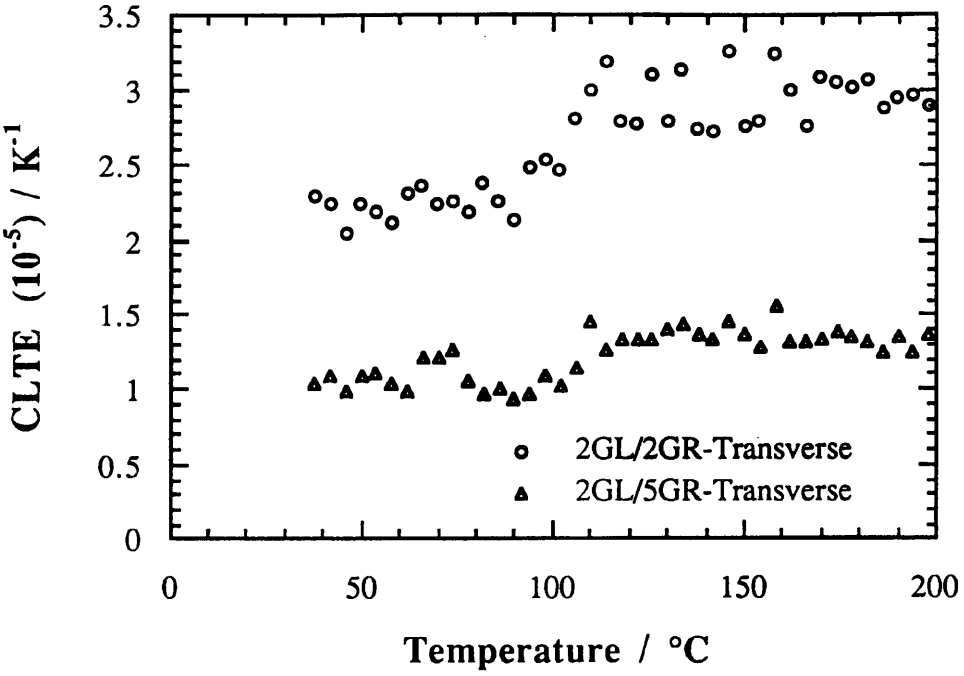

Figure 4.20 Plots of CLTE versus temperature for transverse specimens of glass-glass SRIM composites

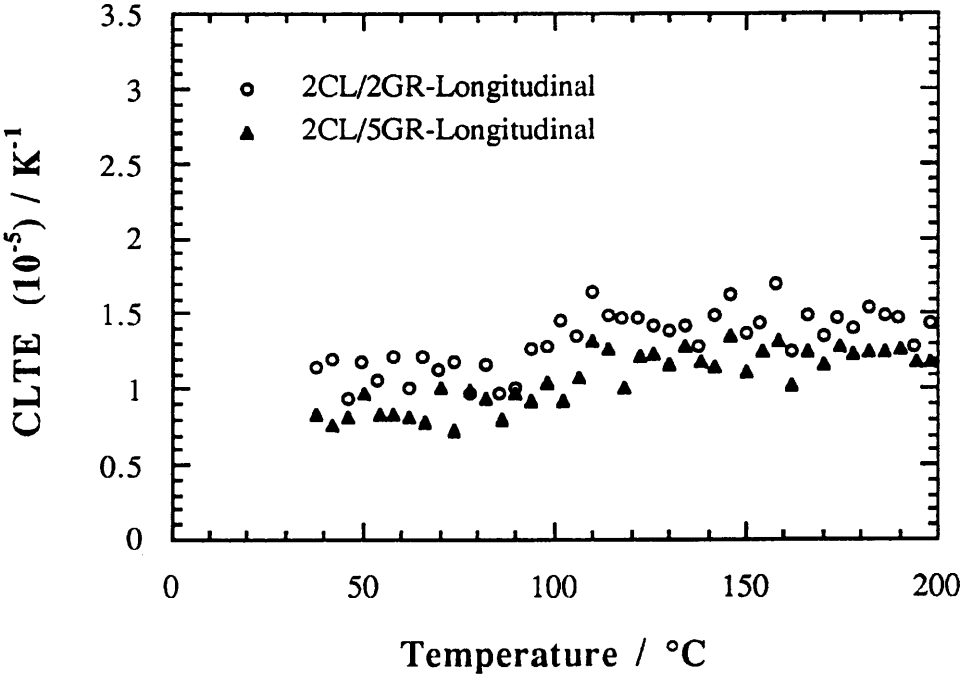

Figure 4.21 Plots of CLTE versus temperature for longitudinal specimens of carbon-glass SRIM composites

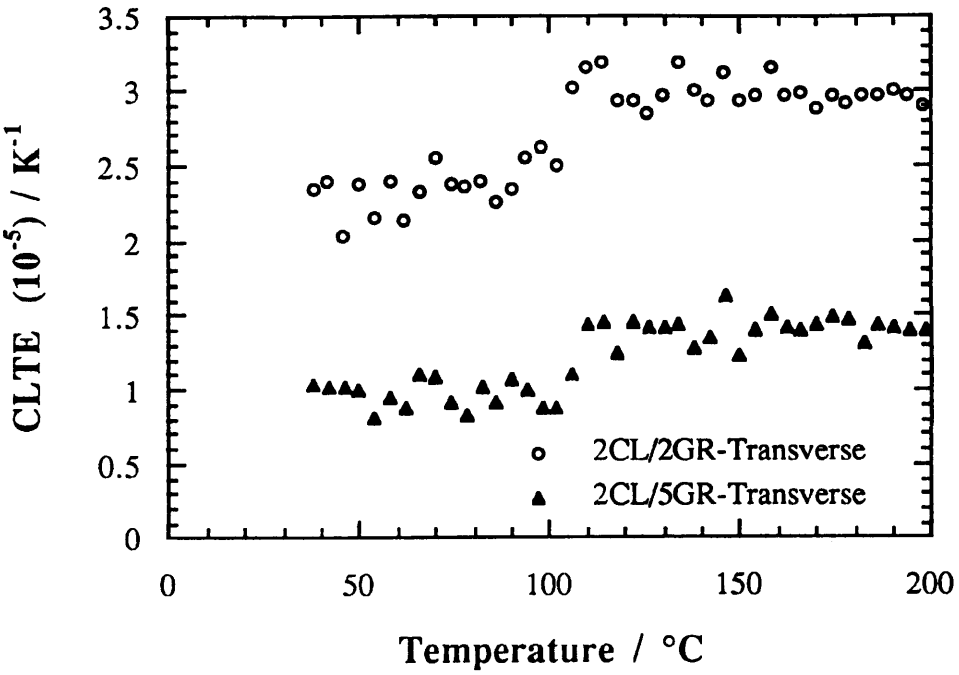

Figure 4.22 Plots of CLTE versus temperature for transverse specimens of carbon-glass SRIM composites

In transverse direction, the CLTE of both glass-glass SRIM composites and carbon-glass SRIM composites mainly depend on the layer number of inside random mats. As the layer number of inside random mats increases, the CLTE of SRIM composites decrease. That is the reason that values of the CLTE of 2GL/5GR and 2CL/5GR are lower than those of 2GL/2GR and 2CL/2GR, respectively, in transverse direction (see Fig.4.20 and 4.22).

4.4 Dynamic Mechanical Analysis (DMA)

The DMA technique is similar to that of DMTA described in Chapter 3. The DMA sample holder is shown in Fig.4.23, with a typical specimen (taken in longitudinal direction from SRIM composites (see Fig.4.2)) of dimensions 50 x 10 x 3.3 mm. The ratio of thickness to span, B / L, was 10. The experimental temperature range used was -100 to 300 °C, and the heating rate was 5 °C / min. at an experimental frequency of 1 Hz. Three specimens of each composite were used to give average DMA data, and all SRIM

composites were tested in the longitudinal direction. The data obtained were as values of log E' (where E' is store modulus of the composite) and tan δ (where tan δ is dissipation of the composite) as functions of temperature.

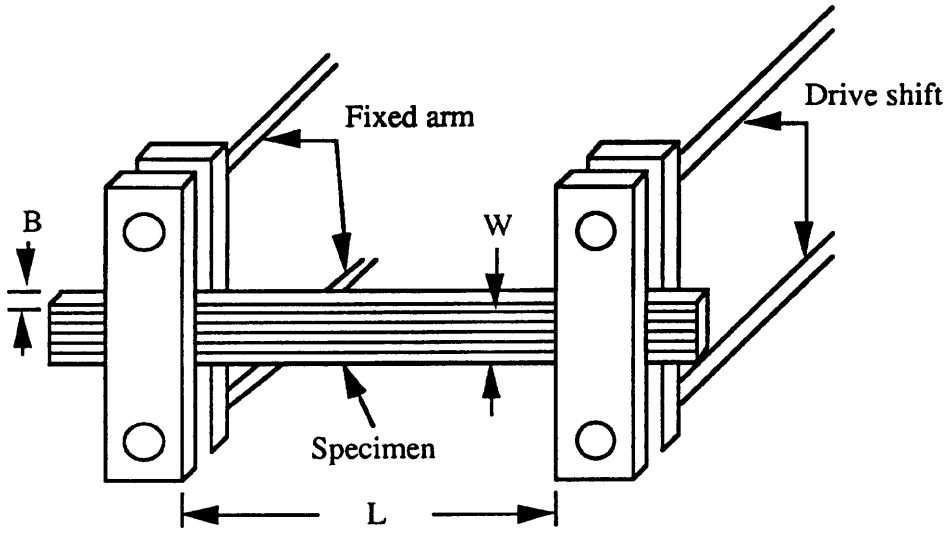

Figure 4.23 The schematic diagram of DMA sample holder and a SRIM composite specimen

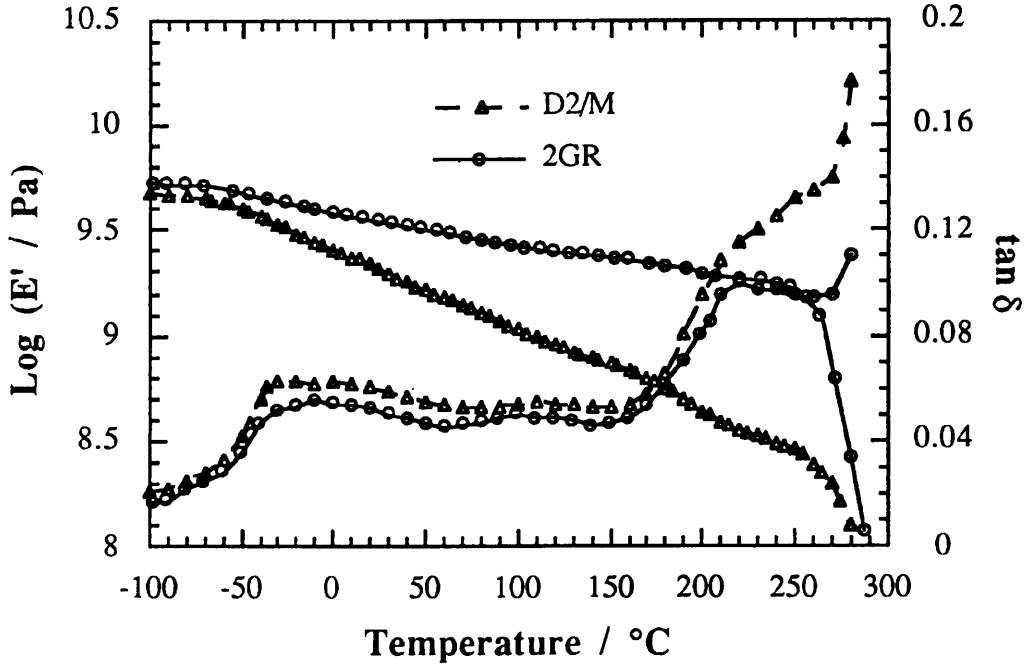

Figure 4.24 The DMA curves of matrix and SRIM composite of 2GR

Fig.4.24 shows the effect of incorporating two layers of random glass-fibre reinforcements on the dynamic thermal mechanical properties of the matrix (The tan δ versus temperature curves show three transitions (α, ß and γ) at the indicated temperatures. These temperatures have been ascribed to different molecular motions in the section 3.1). Because the dissipation factor (tan δ) of glass fibre is very small, the addition of the random glass-fibre mats lowers the energy dissipation of the matrix, resulting in a lower tan δ curve for 2GR. It would be expected that during SRIM processing, frictional heating takes place during mould filling stage, which would result in low reactant mixture viscosity and enhance molecular motion, thus enabling a higher degree of phase separation to take place. However, the thermal mass of the glass fibre would reduce the matrix exotherm, thus reducing molecular motion, and hence reducing phase separation. In addition, the existence of glass fibre would also inhibit molecular motion of the matrix, particularly at the interface. That is why that T_g^S shifts to higher temperature and γ-peak becomes lower and broader (in Fig.4.24) when two layer random glass mats are added. The existence of glass fibre also delays the degradation of the matrix, so that the α-peak of 2GR is much clearly defined than that of the matrix. The transitional behaviour of the matrix and 2GR composites summarised in Table 4.13.

Table 4.13 The effect of random glass mats on the dissipation of the matrix

Sample	γ (T_g^S) / °C	tan δ at T_g^S	ß / °C	α (T_g^H) / °C
D2/M	~ -30	0.063	80 ~ 130	~ 210[a]
2GR	~ -10[a]	0.055	80 ~ 130	~ 220[a]

(a) observed as a shoulder in tan δ, prior to onset of degradation.

The storage modulus, E', of 2GR is not much higher than that of the matrix at lower temperature (< -50 °C) in Fig.4.24; but as temperature increases, the decrease in modulus is much less than for the matrix, because of the good thermal stability of glass fibre. Table 4.14 gives the summary data, which shows superior mechanical-thermal stability of SRIM composites (2GR) to that of the matrix. For example, from -30 to 60 °C, E'(-30 °C) / E'(60

°C) is decreased by 57%; from 60 to 100 °C, E'(60 °C) / E'(100 °C) is decreased by 21%; from 100 to 200 °C, E'(100 °C) / E'(200 °C) is decreased by 81%.

Table 4.14 The effect of random glass mats on mechanical-thermal stability of the matrix

Sample	$\frac{E'\ (-30\ °C)}{E'\ (60\ °C)}$	$\frac{E'\ (60\ °C)}{E'\ (100\ °C)}$	$\frac{E'\ (100\ °C)}{E'\ (200\ °C)}$	tan δ at T_gS
D2/M	2.23	1.42	2.44	0.063
2GR	1.42	1.17	1.35	0.055

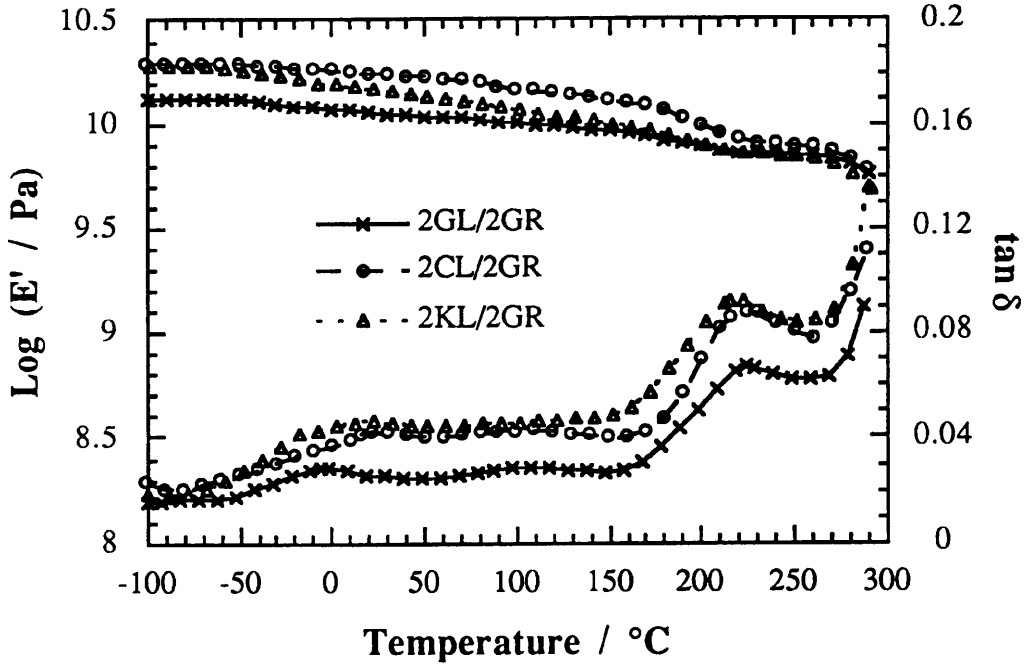

Figure 4.25 The effect of unidirectional mats on DMA curves of SRIM composites

Fig.4.25 shows the effects of addition of unidirectional fibre reinforcements on dynamic thermal mechanical properties of SRIM composites. Due to the organic nature of Kevlar fibre and the typical inorganic nature of glass fibre, the tan δ curve of 2GL/2GR, in Fig.4.25 is lower than that of 2CL/2GR, which is lower than that of 2KL/2GR; and all of them are lower than that of the matrix. A summary data of tan δ is given in Table 4.15. It is noticed that the γ peak of 2KL/2GR and 2CL/2GR are much broader and shifts to higher

temperature than that of 2GL/2GR, maybe because the diameter of Kevlar fibre and carbon fibre is much smaller than that of glass fibre, which would inhibit molecular motion of the matrix more.

Figure 4.25 also shows clearly that the storage modulus of 2CL/2GR, 2KL/2GR and 2GL/2GR are much higher than that of 2GR, and arrange in order of 2CL/2GR > 2KL/2GR > 2GL/2GR, consistent with the fibre modulus order of carbon fibre > Kevlar fibre > glass fibre. The thermal stabilities of 2GL/2GR, 2CL/2GR and 2KL/2GR are also much better than that of 2GR, which can be seen in Table 4.16, and in order of 2GL/2GR > 2CL/2GR > 2KL/2GR.

Table 4.15 The effect of unidirectional mats on dissipation of SRIM

Sample	γ (T_g^S) / °C	tan δ at T_g^S	β / °C	α (T_g^H) / °C
2GR	~ -10	0.056	80 ~ 130	~ 220
2KL/2GR	~ 20(a)	0.046	80 ~ 130	~ 216
2CL/2GR	~ 22(a)	0.042	80 ~ 130	~ 225
2GL/2GR	~ -6	0.028	80 ~ 130	~ 224

(a) observed as a shoulder in tan δ, prior to onset of degradation.

Table 4.16 The effect of unidirectional mats on mechanical-thermal stability of SRIM

Sample	$\frac{E' (-30\ °C)}{E' (60\ °C)}$	$\frac{E' (60\ °C)}{E' (100\ °C)}$	$\frac{E' (100\ °C)}{E' (200\ °C)}$	tan δ at T_g^S
2GR	1.42	1.17	1.35	0.056
2KL/2GR	1.29	1.12	1.48	0.046
2CL/2GR	1.15	1.12	1.49	0.042
2GL/2GR	1.15	1.07	1.31	0.028

Fig.4.26 and Fig.4.27 show the effects of further addition of random mats on dynamic thermal mechanical properties of SRIM. Table 4.17 and Table 4.18 give summary of the data.

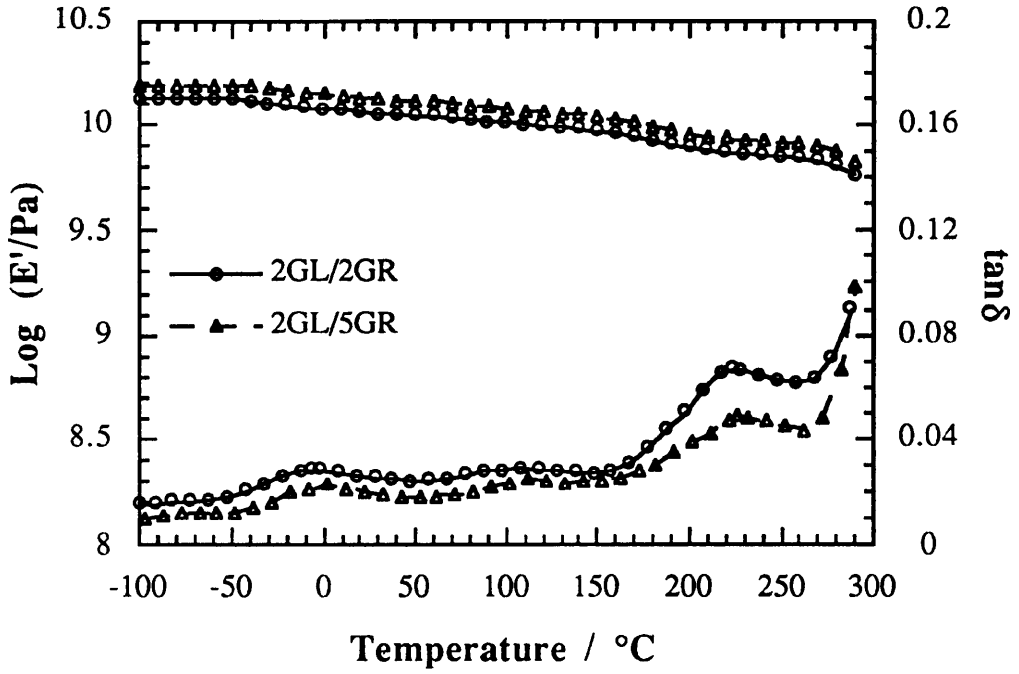

Figure 4.26 The effect of random mats on DMA curves of glass-glass SRIM composites

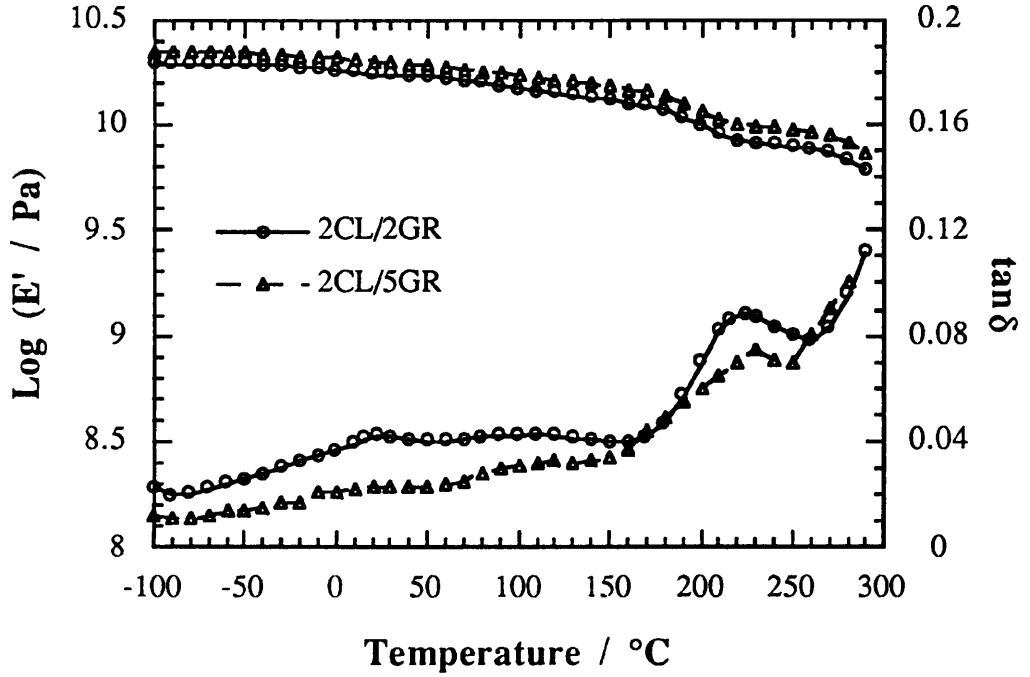

Figure 4.27 The effect of random mats on DMA curves of carbon-glass SRIM composites

Table 4.17 The effect of random mats on dissipation of SRIM

Sample	$\gamma (T_g^S)$ / °C	tan δ at T_g^S	ß / °C	$\alpha (T_g^H)$ / °C
2GL/2GR	~ -6	0.028	80 ~ 130	~ 224
2GL/5GR	~ 2[a]	0.023	80 ~ 130	~ 226
2CL/2GR	~ 22[a]	0.042	80 ~ 130	~ 225
2CL/5GR	~ 20[a]	0.023	80 ~ 130	~ 230

(a) observed as a shoulder in tan δ, prior to onset of degradation.

Table 4.18 The effect of random mats on mechanical-thermal stabilities of SRIM

Sample	$\frac{E' (-30\ °C)}{E' (60\ °C)}$	$\frac{E' (60\ °C)}{E' (100\ °C)}$	$\frac{E' (100\ °C)}{E' (200\ °C)}$	tan δ at T_g^S
2GL/2GR	1.15	1.07	1.31	0.028
2GL/5GR	1.15	1.06	1.30	0.023
2CL/2GR	1.15	1.12	1.49	0.042
2CL/5GR	1.15	1.09	1.47	0.023

Further addition of random mats makes the storage modulus of 2GL/5GR and 2CL/5GR slightly higher than those of 2GL/2GR and 2CL/2GR, tan δ curves of 2GL/5GR and 2CL/5GR lower than those of 2GL/2GR and 2CL/2GR, respectively. And almost no further increase on thermal stabilities of SRIM.

4.5 Summary and Conclusions

Structural composites comprising a PUrI matrix and pre-placed mats of continuous-fibres (surface treated with 0%, 0.1% and 0.5% silane coupling agent) were produced. The mould temperature was 90 °C and SRIM composites were postcured at 150 °C for 1 hour. The matrix (D2/M/0.6), formed from M143 and D2000, showed the best combination of thermal and mechanical properties, and met the basic SRIM processing characteristic of low initial viscosity during mould filling, essential for minimising fibre mat movement whilst

maximising mat penetration and fibre wetting by the PUrI reacting mixture. Various hybrid SRIM composites with fibre contents up to 38 % by volume were produced with single outer layers of unidirectional-fibre mats of either glass, carbon or Kevlar, and different numbers of inner layers of random-fibres of only glass. The main results of thermal property studies of SRIM composites are given as follows:

1 Heat sag studies show that at the experimental condition of 200 mm overhang, the experimental temperature of 200 °C and the heating time of 1 hr, the heat sag of hybrid SRIM composites are negligible., in contrast with the heat sag of 25.49 mm for the matrix, which indicates the significant enhancement on the mechanical-thermal stability of the matrix.

2 Because of the existence of ß-transition, the value of CLTE (85 x 10^{-6} K^{-1}) of the matrix at the temperature below 110 °C is much lower than the value (122x10^{-6} K^{-1}) above 110 °C. But for SRIM composites, the difference between them is slight. The CLTE values (32 to 9 x10^{-6} K^{-1}) of SRIM composites are 300 to 700% lower than that of the matrix, and match the CLTE values of Aluminium, Copper, Iron and Steel as the fibre volume fraction and fibre type vary. The moisture also has effect on CLTE of all the SRIM composites and matrix.

3 The storage modulus of matrix is greatly enhanced by unidirectional mats in order of carbon fibre > Kevlar fibre > glass fibre, which is consistence with the modulus order of those fibres. The γ peak (T_g^S) of matrix is shifted to higher temperature by fibre reinforcements, especially by carbon fibre reinforcements, probably due to reduced phase separation and inhibition of molecular motions of the matrix. The modulus-temperature dependence and energy dissipation of the matrix are also significantly reduced by fibre reinforcements in the order of glass fibre > carbon fibre > Kevlar fibre.

CHAPTER FIVE

DEFORMATION AND FRACTURE STUDIES OF HYBRID SRIM COMPOSITES

5.1 Introduction

The processing and thermal properties of SRIM composites were presented and discussed in Chapter 4. This chapter focuses on the mechanical properties of SRIM composites, obtained by testing specimens taken in both longitudinal and transverse directions from SRIM composites, as described in Fig.4.2. It is well known that for uniaxially-oriented fibre composites, the tensile strength of the composites are affected by three important terms, namely the shear strength, τ, the longitudinal strength, σ_l, and the transverse strength, σ_t. In order to calculate the tensile strength of uniaxially-oriented fibre composites, the shear strength, τ, of the composites must firstly be measured, and the longitudinal strength, σ_l, and transverse strength, σ_t, are obtained or estimated from the tensile properties of the fibres and matrix. In this study, the in-plane shear strength will be used as the shear strength τ, and measured by using the standard ASTM D3846-79 [166].

Fracture toughness is another very important property of composites. Protocols for interlaminar fracture testing for unidirectional composites were drafted in November, 1988 (and last revised in May, 1992) by the Polymer and Composites Task Group / European Structural Integrity Society [167]. The first protocol describes the determination of the delamination resistance of the composites under mode I (opening) loading. The specimen proposed is the Double Cantilever Beam (DCB) (see Fig.5.1) and resistance to the fracture

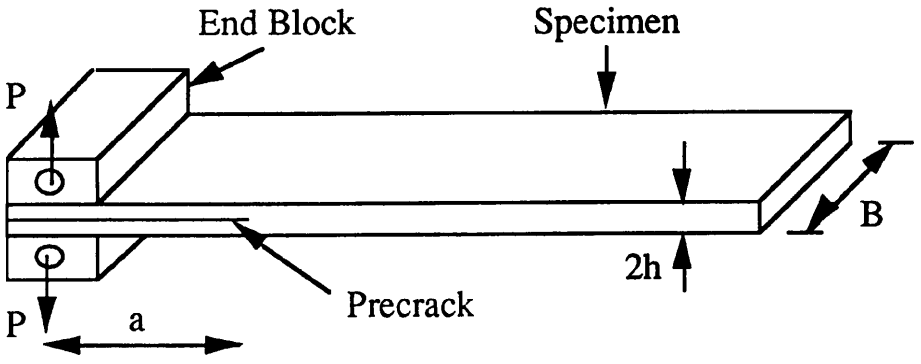

Figure 5.1 Specimen geometry, Double Cantilever Beam (DCB) used to determine G_{Ic}.

initiation (G_{Ic}) of a delamination from an insert (a pre-crack) is calculated by using corrected beam theory, according to the expression

$$G_{Ic} = \frac{3P\delta}{2B(a + \Delta)} \tag{5.1}$$

where P = force, δ = displacement, B = specimen width, a = crack length, and Δ is a correction factor for crack length which may be found experimentally by plotting the cube root of compliance, $C^{1/3}$, as a function of crack length, a (see Fig.5.2).

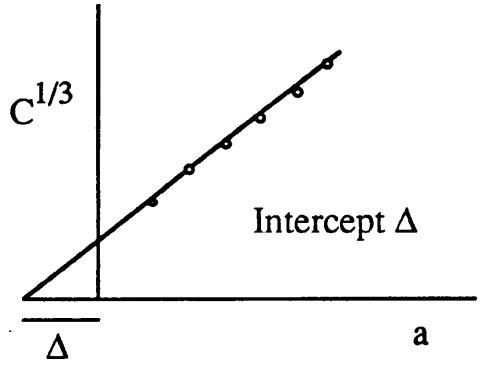

Figure 5.2 Crack length calibration (Δ) by plotting the cube root of compliance, $C^{1/3}$, versus crack length, a.

The second protocol covers the determination of the critical strain energy release rate, G_{IIc}, for initiation of a delamination under mode II (in-plane shear) loading using the End Notched Flexure (ENF) specimen, loaded in three-point bending (see Fig.5.3).

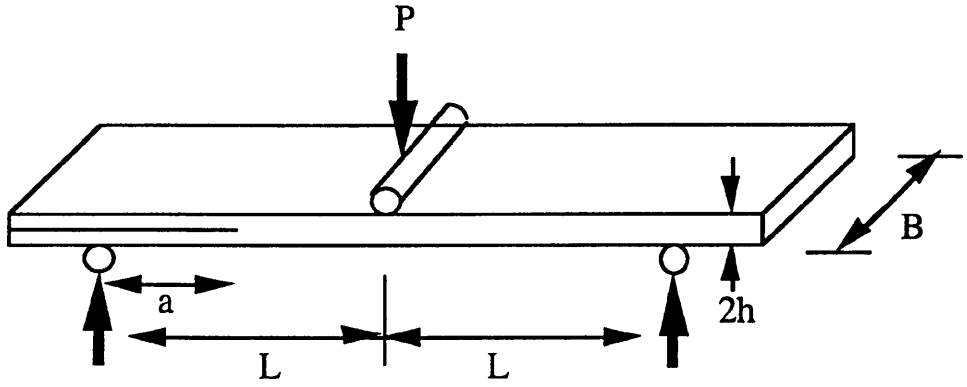

Figure 5.3 ENF specimen geometry used to determine G_{IIc}.

Values of G_{IIc} may be determined by using direct beam theory, according to the expression

$$G_{IIc} = \frac{9\, a^2\, P\, \delta}{2B(2L^3 + 3a^3)} \qquad (5.2)$$

where P = load, δ = displacement, B = specimen width, a = crack length, 2L = span.

The third protocol describes the determination of values of delamination resistance, G_{IIc}, using the End Loaded Split specimen (ELS) under mode II loading. A fourth protocol covers the determination of the critical strain energy release rate $G_{I/IIc}$ for initiation of a delamination under mixed mode (I / II) loading using the Asymmetrical Double Cantilever Beam (ADCB) specimen.

Hitherto, no fracture testing standard or protocol has been reported for randomly-oriented, continuous-fibre reinforced composites in which a pre-crack passes through all of the reinforcement layers of the composite. In the last part of this chapter, an attempt is made to study the fracture toughness of SRIM hybrid composites under mode I loading using Single Edge Notched Bend (SENB) specimens in which a pre-crack propagates cross all the reinforcement layers of the composites (see Fig.5.4).

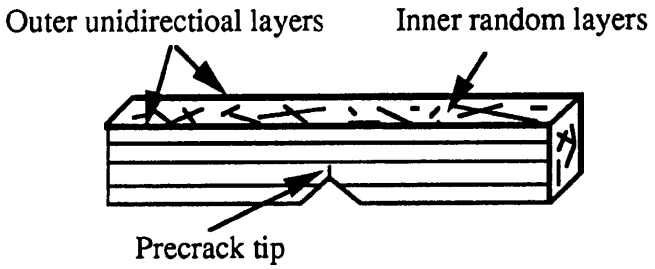

Figure 5.4 Single edge notched bend specimen used to determine G_{Ic} and K_{Ic} for SRIM composites comprising outer layers of unidirectional fibres and inner layers of randomly-oriented, continuous fibres.

5.2 In-Plane Shear Strength

5.1.1 Test Method

There are many kinds of test methods for in-plane shear testing of composite materials [166, 168-170]. The standard ASTM D3846-79 [166] was used to test in-plane

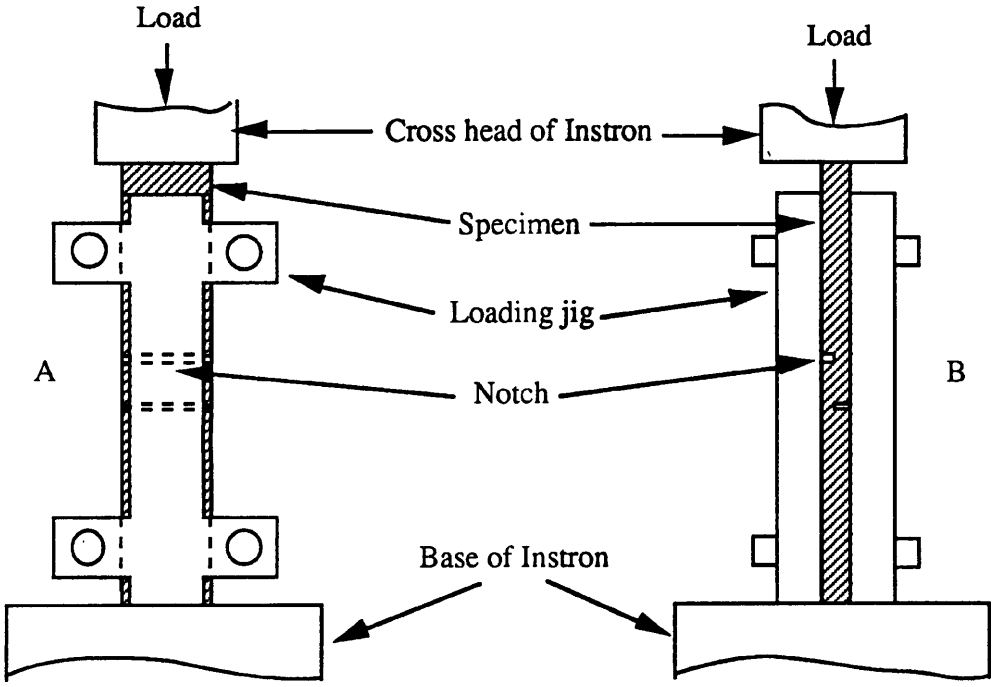

A: A view from the face of the loading jig
B: A view from the side of the loading jig

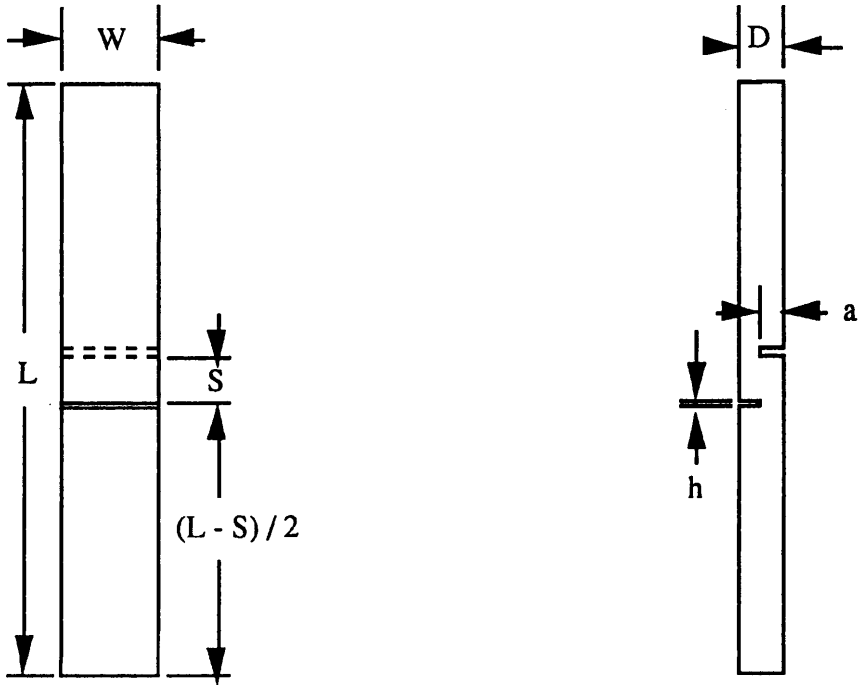

Figure 5.5 Specimen and loading jig used for determining in-plane shear strength.
W = 12.7 mm, L = 79.5 mm, D = 3.3 mm,
$S \approx 6.4$ mm, $D/2 \leq a \leq D/2 + 0.2$ mm, h = 1.02 ~ 1.65 mm.

shear strength of SRIM composites taking into account the cost of fabrication, the cost of testing, data productivity and the accuracy of experimental results. For each SRIM composite, ten specimens (five longitudinal and five transverse specimens) were tested. Specimens with the configuration shown in Fig.5.5 were clamped into a loading jig, details of which are shown in reference[66].

The test procedure was as follows:

1) The width, W, of the specimen between the notches was measured to the nearest 0.025 mm.
2) The specimen was mounted centrally in the supporting jig (Fig.5.5) with its side and bottom flush with the edge of the loading jig. The nuts of the jig were tighten by hand, and the specimen was placed into a assembly in Instron 1185.
3) A cross-head speed of 1 mm / min was used to obtain a force-deflection curve.
4) From the curve, the maximum force, P_{max}, carried by the specimen during the test (this was the load at the moment of failure) was determined.
5) At P_{max}, the sample fractures, which produces two shear fracture surfaces as shown in Fig.5.6. The length, S, of the failed (sheared) area was measured using digital callipers to the nearest 0.025 mm by measurement of either surface.

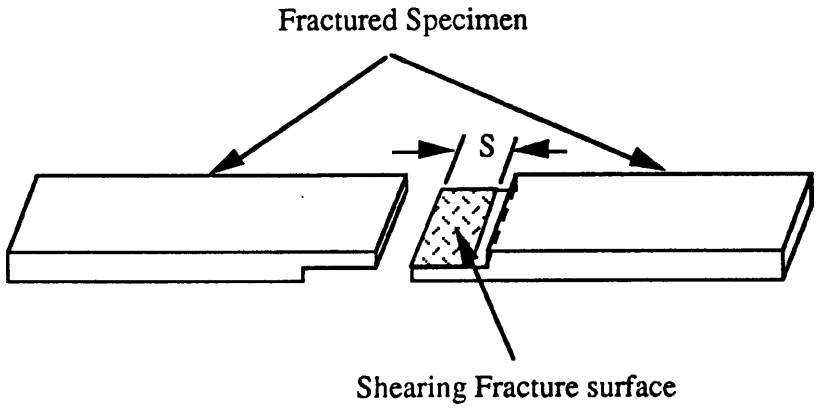

Figure 5.6 A schematic of shearing fracture surface

The value of in-plane shear strength, τ, was calculated using the equation

$$\tau = \frac{P_{max}}{W\ S} \tag{5.3}$$

Values of τ for longitudinal and transverse specimens were essentially similar within experimental scattering. Thus the values of τ obtained for each composite is the mean of ten specimens.

5.1.2 Results and Discussion

Because the SRIM composites studied were hybrid comprising outer layers of unidirectional fibre (glass, carbon or Kevlar) reinforcements, and inner layers of randomly-oriented, continuous-glass fibre reinforcements, M8610, the in-plane shear strength of glass-glass hybrid SRIM composites is assumed to be the same as that of carbon-glass hybrid SRIM composites. Only the former were tested, and the results and discussion are applicable to the latter. The effects of volume fraction of reinforcement and reinforcement surface treatment, with 0.1% and 0.5% silane, on the shear strength of SRIM composites are given in Table 5.1 and Fig.5.7 (All the results are within 95% confidence limit).

Table 5.1 The effects of fibre content and silane surface treatment on the shear strength of SRIM composites

Materials (a)	ϕ_f / % (b)	τ / MPa		
		Control	0.1%	0.5%
2GR	10.7	13.5±1.4	14.1±2.2	14.2±1.0
2GL/2GR	17.7	17.9±1.5	18.6±1.0	(c)
2GL/3GR	23.3	19.7±1.5	22.9±0.7	22.6±1.6
2GL/4GR	27.9	21.0±2.4	22.8±1.2	(c)
2GL/5GR	33.3	24.6±2.8	24.8±2.3	(c)

(a) All materials were post cured at 150 °C for 1 hr.

(b) ϕ_f (= ϕ_{fU} + ϕ_{fR}) is the total volume fraction of reinforcements.

(c) Not determined.

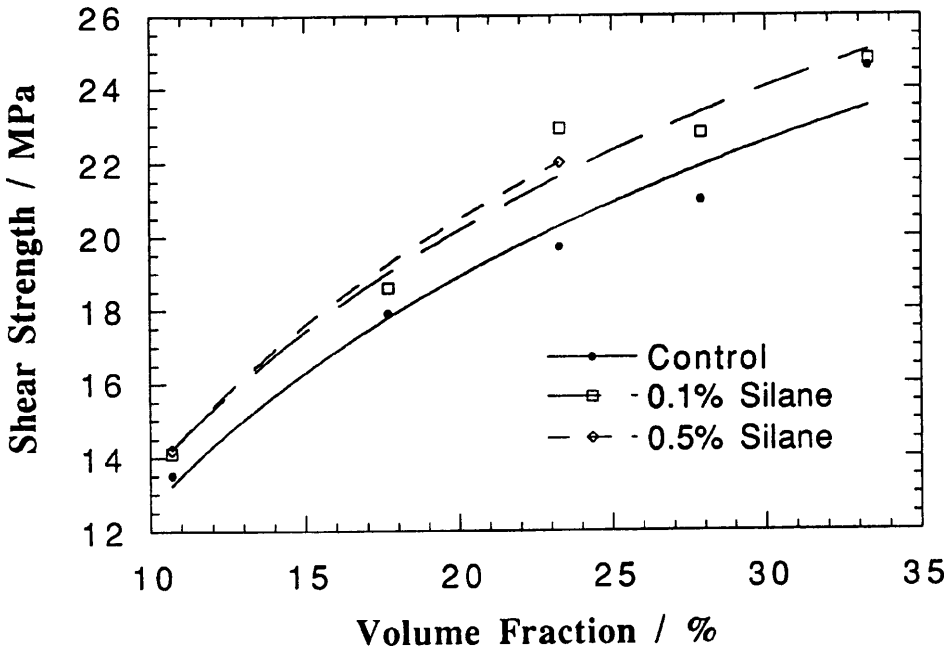

Figure 5.7 The variation of in-plane shear strength with total fibre volume fraction for SRIM composites containing untreated glass fibre mats and glass mats surface treated with different levels of silane coupling agent, Z6120.

Figure 5.7 shows that the in-plane shear strength of SRIM composites increases with the increasing of reinforcement volume fraction. There are two reasons which account for the increase. Firstly, as the reinforcement volume fraction increases, the void volume fraction ϕ_b decreases (see Table 5.2), which is of benefit to the shear strength of SRIM composites. Secondly, as the reinforcement volume fraction increases, the thickness of matrix between reinforcement mats decreases, which also causes the increase in shear strength [172, 191]. in terms of micro-mechanics, a crack always seeks the easiest path for propagation. This means, that in the in-plane shear test of materials, crack propagation is restricted to the region between two adjacent reinforcement mats and to the fibre-matrix interfaces. Decreasing the thickness of the matrix results in a decrease in the probability of occurrence of defects, so that there is an increase in the in-plane shear strength.

Table 5.2 Relationship between ϕ_f and ϕ_b for SRIM composites

Materials	ϕ_f / %	ϕ_b / %		
		Control	0.1%	0.5%
2GR	10.7	19.9	21.1	21.4
2GL/2GR	17.7	14.6	18.9	19.1
2GL/3GR	23.3	14.1	19.4	17.8
2GL/4GR	27.9	12.3	15.0	(c)
2GL/5GR	33.3	12.6	13.4	(c)

(c) Not determined.

When the surfaces of reinforcements are treated with silane, the interfaces between fibres and matrix are improved, as observed by fractography of shear fracture surfaces of composites. Fig.5.8 shows SEM photographs of the shear fracture surfaces of 2GL/2GR and 2GL/2GR/0.1 respectively. In Fig.5.8A, the fibre surfaces are very clean and smooth, which suggests that the propagation of a crack between reinforcement layers involves the clear fracture of fibre-matrix interfaces. However in Fig.5.8B, the fibre surfaces or parts of fibre surfaces are coated with matrix, and the matrix around fibres is obviously plastically deformed by the shear stresses. This means that the crack path is close to the interfaces, but is mainly in the matrix. This results from improvements in interfacial wetting and bonding due to silane surface treatment. Similar τ values for carbon-glass hybrid SRIM composites and Kevlar-glass hybrid SRIM composites are expected, because in all of these SRIM composites, the inner layers of reinforcements were identical to those of glass-glass hybrid SRIM composites, and the in-plane shear test effectively measures the in-plane shear strength within the inner layers of reinforcements.

5.3 Tensile Behaviour

5.3.1 Test Method

Although tensile strength is not an intrinsic property of materials, dominated by the

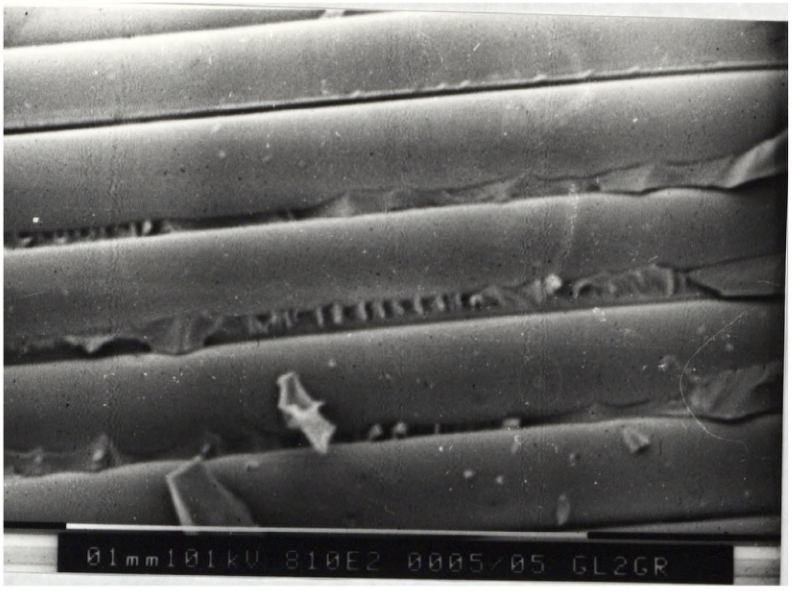

A: Untreated

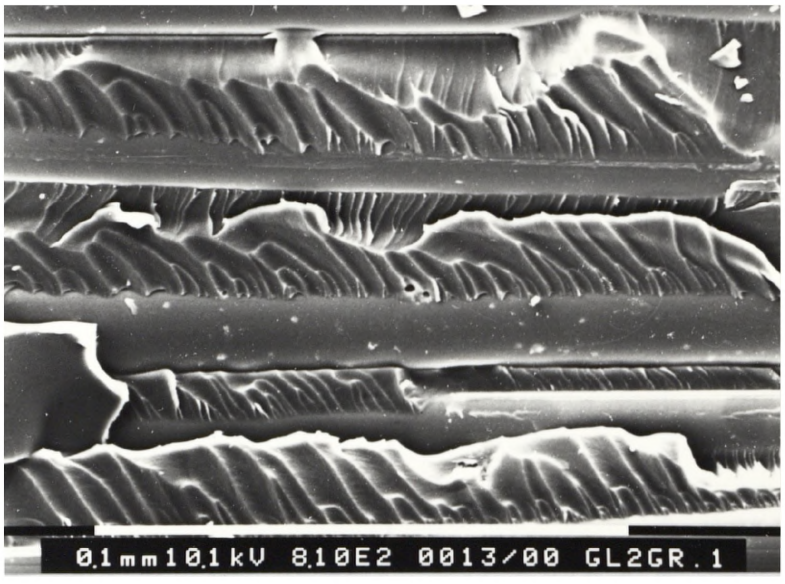

B: Treated with Silane Z-6210 (0.1% w/w)

Figure 5.8 SEM micrographs of in-plane shear fracture surfaces of 2GL/2GR SRIM composites

imperfections present in the materials, the tensile test is a very popular method used to assess materials. In this section, the test method, ASTM D638-91, was used to determine the tensile properties of SRIM composites. The samples were first cut into 150 x 30 x 3.3 mm strip from SRIM composite plaques in both longitudinal and transverse directions, and then milled into dull-bell specimens with the configuration as shown in Fig.5.9. The milled

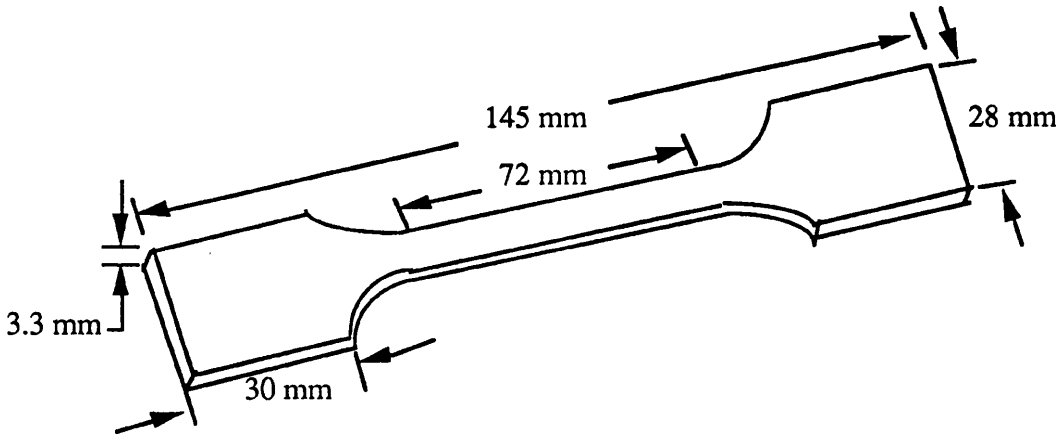

Figure 5.9 The configuration of tensile test specimen

surfaces of specimens were smoothed with 400 and 800 grade sanding papers. Tensile tests were carried out on an Instron 6025 machine with a strain gauge extensometer (Cat. No; 2630036, gauge length; 25 mm, maximum strain; 10%) at 23 ± 2 °C and with a cross head speed of 1 mm / min. The data were recorded using both a computer and a chart recorder attached to the Instron machine. A typical force-strain curve obtained from a tensile test is shown in Fig.5.10, and for all composites, the initial part of the curve was essentially linear. The tensile strength, σ, was calculated by equation (5.4)

$$\sigma = \frac{P_{max}}{B\ W} \tag{5.4}$$

where P_{max} is maximum force, B and W were thickness and width of the gauge length section of specimen. Fracture strain, ε, was the strain at P_{max}. The Young's modulus, E, was calculated using Equation (5.5)

$$E = \frac{\Delta P}{B\ W\ \Delta\varepsilon} \tag{5.5}$$

where ΔP was taken between 5 and 15 N.

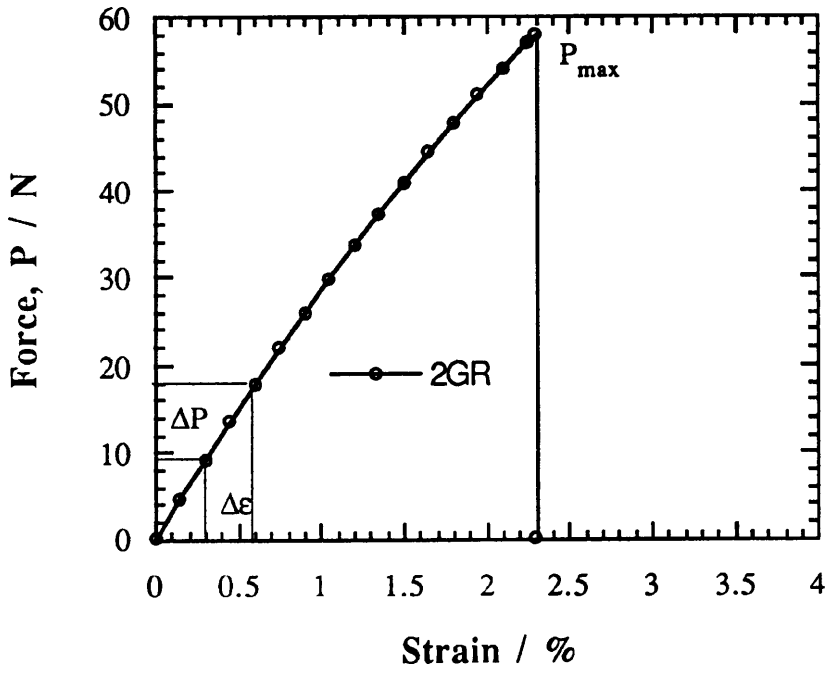

Figure 5.10 A typical tensile force-strain curve of SRIM composite, 2GR

5.3.2 Modelling of Tensile Properties

For a continuous unidirectional-fibre reinforced composites, the longitudinal tensile Young's modulus, E_0, is given by the rule of mixtures:

$$E_0 = E_m \phi_m + E_f \phi_f \tag{5.6}$$

where E and ϕ are the modulus and volume fraction respectively, and subscripts m and f refer to matrix and fibre respectively.

There are several predictive equations [173-183] for he transverse tensile Young's modulus, E_{90}. One of the most commonly used Equations is the Halpin-Tsai [179-181] Equation, as modified by Nilsen [184, 185]

$$\frac{E_{90}}{E_m} = \frac{1 + A\ B\ \phi_f}{1 - B\ \psi\ \phi_f} \tag{5.7}$$

where A = 0.5

and

$$B = \frac{E_f / E_m - 1}{E_f / E_m + A} \tag{5.8}$$

and

$$\psi \approx 1 + \left(\frac{1 - \phi_m}{\phi_m^2}\right)\phi_f \tag{5.9}$$

The factor ψ takes into account the packing fraction, ϕ_m, of the fibres. In the present composites, fibre packing was observed by optical microscopy (see Fig.5.11 and 5.12) to be approximately hexagonal, so that $\phi_m \approx 0.907$.

For a composite containing continuous fibres randomly oriented in a plane, Tsai [186, 187] has developed a simpler method for calculating the tensile Young's modulus, E_{2D}. Namely,

$$E_{2D} \approx \frac{3}{8} E_0 + \frac{5}{8} E_{90} \tag{5.10}$$

were E_0 and E_{90} can be either experimental values obtained from uniaxially oriented fibre composites, or estimated values calculating using Eqs.(5.6) and (5.7).

The rule-of-mixtures can be used to calculated the longitudinal tensile strength of a continuous unidirectional-fibre reinforced composite, according to Eq(5.11).

$$\sigma_0 = \sigma_m \phi_m + \sigma_f \phi_f \tag{5.11}$$

where σ_0 is the longitudinal tensile strength, and σ_m, and σ_f are the tensile strengths of the matrix and fibres.

For uniaxially-oriented fibre composites there are at least three important modes of failure giving three values for tensile strengths, namely, the longitudinal tensile strength, σ_0, the transverse tensile strength, σ_{90}, and the shear strength, τ. The relative importance of an

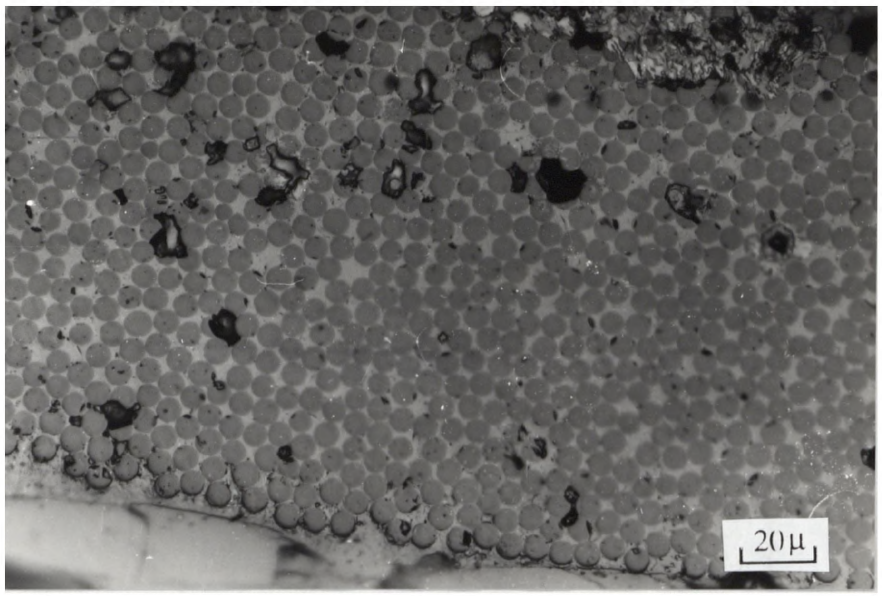

Figure 5.11 Cross section of outer layer of unidirectional carbon fibres in carbon-glass SRIM specimen, taken in the longitudinal direction.

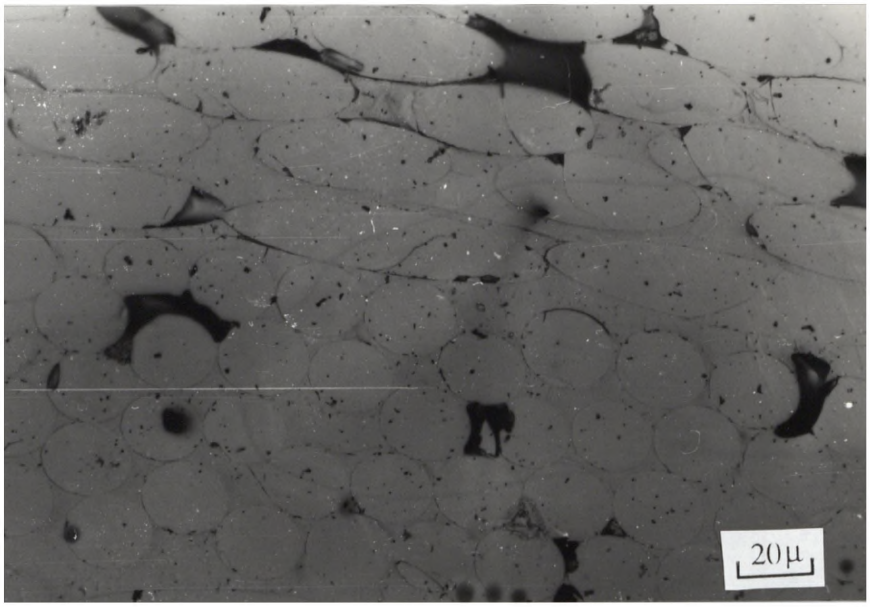

Figure 5.12 Cross section of inner layer of randomly oriented glass fibres in carbon-glass SRIM specimen, taken in the longitudinal direction.

contribution to the observed tensile strength depends on the angle, θ, between the fibres and the applied force (Fig.5.13). Between 0 and ~ 5 °, where a tensile force is approximately parallel to the fibres, the longitudinal tensile strength, σ_0, is the important factor in determining the mode of failure. When θ is between 5 and 45 °, the shear strength, τ, is the important factor in determining the mode of failure. At higher angle (θ is between 45 and 90 °), the transverse tensile strength, σ_{90}, tends to determine the mode of failure. An equation [186], which takes into account all of these factors and often gives reasonable agreement with experimental data as a function of orientation angle θ, is given by Eq(5.12):

$$\frac{1}{\sigma_\theta^2} = f(\phi_f, \phi_m, \theta) = \frac{\cos^4\theta}{\sigma_0^2} + \left(\frac{1}{\tau^2} - \frac{1}{\sigma_0^2}\right)\cos^2\theta \sin^2\theta + \frac{\sin^4\theta}{\sigma_{90}^2} \qquad (5.12)$$

where σ_θ is the tensile strength at an angle θ between the fibre direction and the applied force.

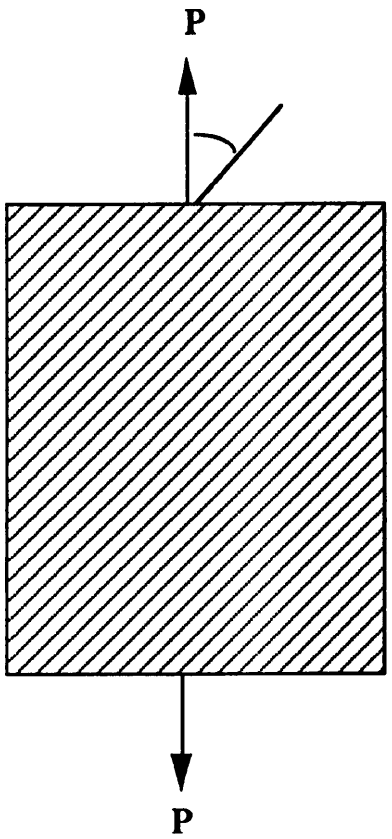

Figure 5.13 Schematic representation of a uniaxially-aligned, continuous fibre composite subjected to a tensile stress, σ_θ, at an angle θ to the fibre axes

For planar randomly-oriented fibre composites, the situation is much more complicated. The three important modes of failure contribute simultaneously to composite tensile strength, and a model based on equation (5.12), was developed in order to calculate the tensile strength of the randomly oriented fibre composites.

The model assumes that a randomly-oriented fibre composite of thickness B, comprises n layers, each containing uniaxially fibres with a particular orientation angle, β_j, limited to narrow range of θ, between 0 and 180 °. Thus for j = 0,.1,.....n-1, the thickness of each layer is B / n and the value of θ for the jth layer is $\beta_j = 180\ j / n$ (see Fig.5.14).

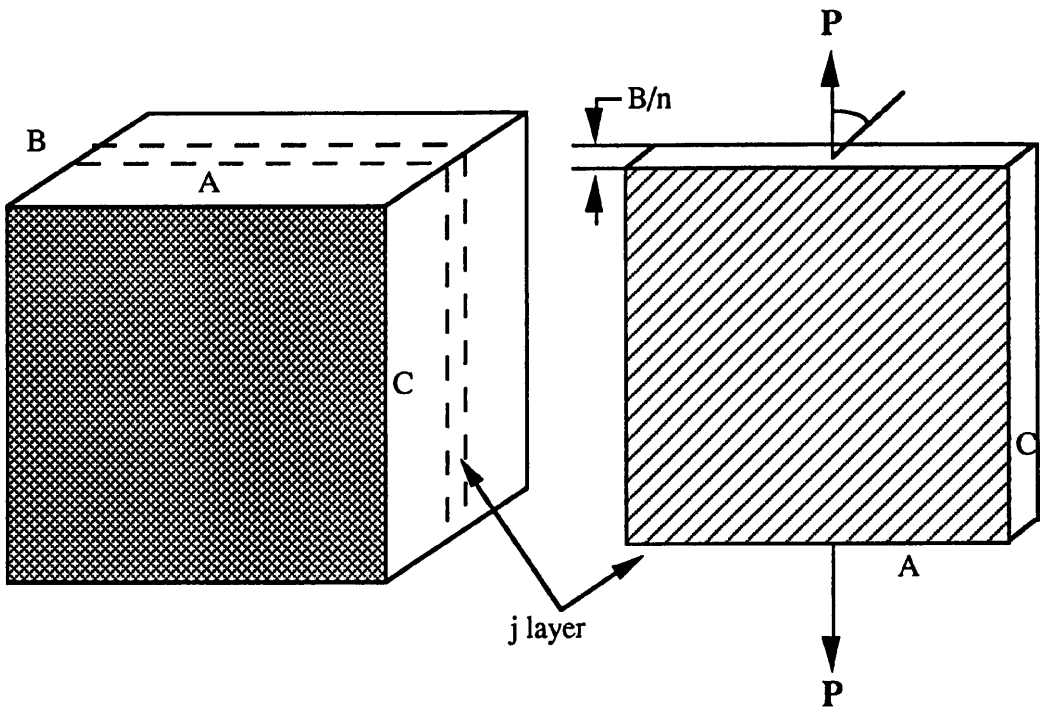

Figure 5.14 Schematic representation of the model used to predict the tensile strength of a randomly-oriented fibre composites

The tensile strength, σ_j, of the jth layer is obtained from equation (5.12), as.

$$\frac{1}{\sigma_j^2} = f(\phi_f, \phi_m, 180\ j / n) \qquad (5.13)$$

and the force, P_j, acting on the jth layer is given as

$$P_j = A_j \sigma_j \tag{5.14}$$

where A_j = B W / n, and W is the width of the composite. Thus, the total force, P_c, acting on the composite is

$$P_c = \Sigma P_j = \frac{B}{n} W \Sigma \sigma_j \qquad j = 0,1,.....n-1 \tag{5.15}$$

Thus, the tensile strength, σ_{2D}, of a 2-dimensional, randomly-oriented fibre composite is given as

$$\sigma_{2D} = \frac{P_c}{B\ W} = \frac{1}{n} \Sigma \sigma_j \qquad j = 1, 2, ...n-1 \tag{5.16}$$

As stated previously, the SRIM composites are hybrid composites with distinct outer layers and inner layers of reinforcements. The outer layers contain unidirectional fibre reinforcement; the inner layers contain continuous, random fibre reinforcement (Fig.5.15). The overall longitudinal tensile strength (Fig.5.15a), σ_l, of SRIM composites is the sum of contribution from unidirectional fibre reinforcement layers, and a composite reinforced with two-dimensional, continuous, randomly oriented fibre reinforcement layers, according to the equation (5.17).

$$\sigma_l = \sigma_{uf}\, \phi_{uf} + \sigma_{2D}(\phi_{rf}, \phi_m) \tag{5.17a}$$

In Eq (5.17a), σ_{uf} is the fibre strength of unidirectional fibre reinforcement, ϕ_{uf} and ϕ_{rf} are the fibre volume fractions of unidirectional fibre reinforcement and continuous, random fibre reinforcement respectively, in SRIM composites, and ϕ_m is the volume fraction of matrix, so that $\phi_{uf} + \phi_{rf} + \phi_m = 1$ (assuming no voids). The second term on the right of Eq (5.17a), $\sigma_{2D}(\phi_{rf}, \phi_m)$, can be calculated by equation (5.16). In the case of transverse specimens (Fig.5.15b), composite failure in the outer layers involves crack initiating and propagating in the matrix and / or along fibre interfaces, but does not, ideally, involve fracture of fibres. Therefore, Eq(5.17a) has to be modified to give approximate expression for transverse

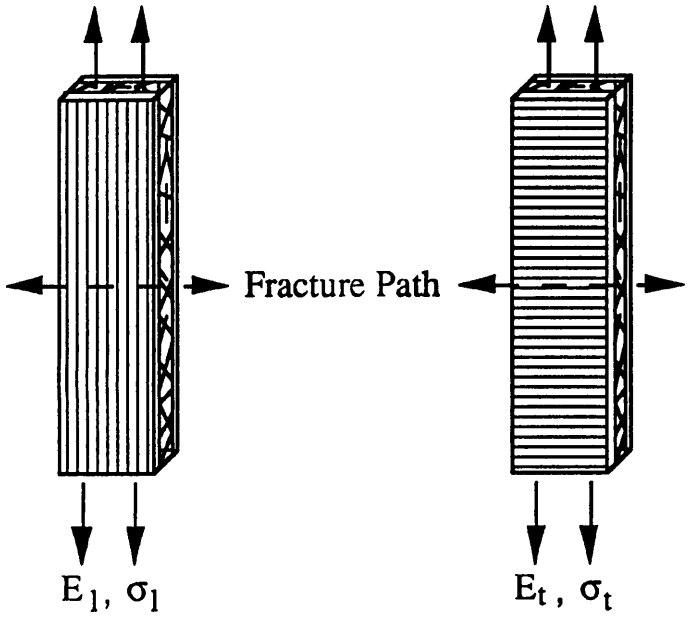

a: Longitudinal Tension b: Transverse Tension

Figure 5.15 A schematic diagram of hybrid SRIM composite specimens under loading
a: a specimen under longitudinal stress; b: a specimen under transverse stress

composite strength (σ_t). That is,

$$\sigma_t = \sigma_{2D}(\phi_{rf}, \phi_m) \tag{5.17b}$$

Using the same model, values of longitudinal tensile moduli (E_l) and longitudinal tensile moduli (E_t) can be predicted based on Eq (5.10). thus,

$$E_l = E_{uf}\,\phi_{uf} + E_{2D}(\phi_{rf}, \phi_m) \tag{5.18a}$$

$$E_t = E_{2D}(\phi_{rf}, \phi_m) \tag{5.18a}$$

where $E_{2D}(\phi_{rf}, \phi_m)$ can be calculated by equation (5.10).

Table 5.3 gives the data which will be used to calculate the tensile strength and Young's moduli of SRIM composites. In using Eqs (5.10) and (5.14) to calculate $\sigma_{2D}(\phi_{rf}, \phi_m)$, values of τ equal to those in Table 5.1 measured for each composite. Also the

value of σ_{90} used in Eq (5.10) was taken to be equal to half of tensile strength of the matrix [190].

Table 5.3 Tensile property data for fibres and matrix used in calculation of SRIM composite moduli and tensile strengths

Materials	E / GPa	σ / MPa	ε / %
E-Glass Fibre [188]	74	3500	4.8
Carbon Fibre [189]	238	3400	1.4
Kevlar Fibre [189]	128	2800	2.0
Matrix	1.5	52	8.6

5.3.3 Results and Discussion

The main tensile stress-strain curves of hybrid SRIM composites are shown in Fig.5.16 - 5.17, and the derived tensile properties are given in Table 5.4. The tensile results

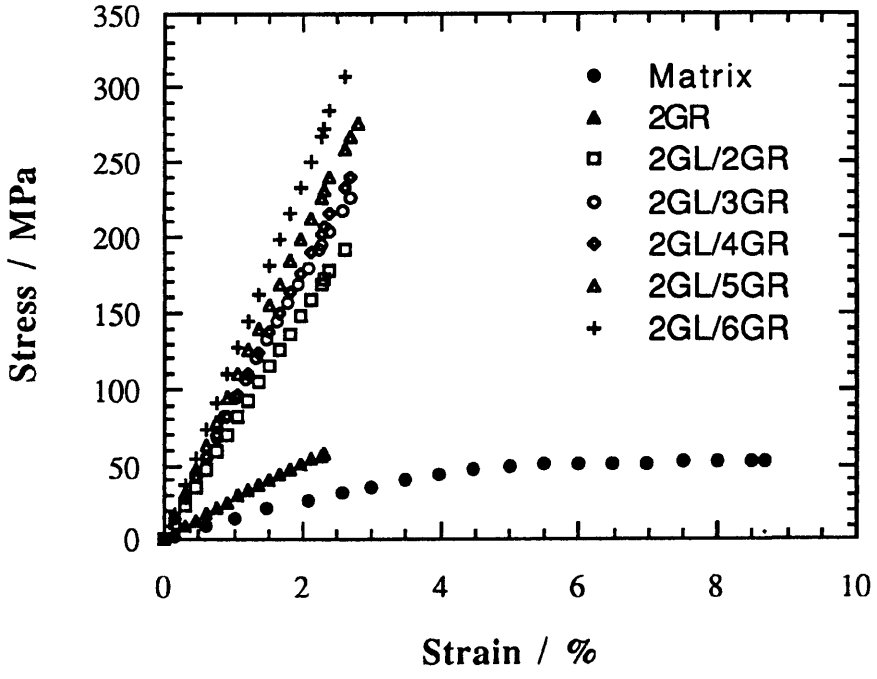

Figure 5.16a Tensile stress-strain curves of glass-glass SRIM composites in longitudinal direction

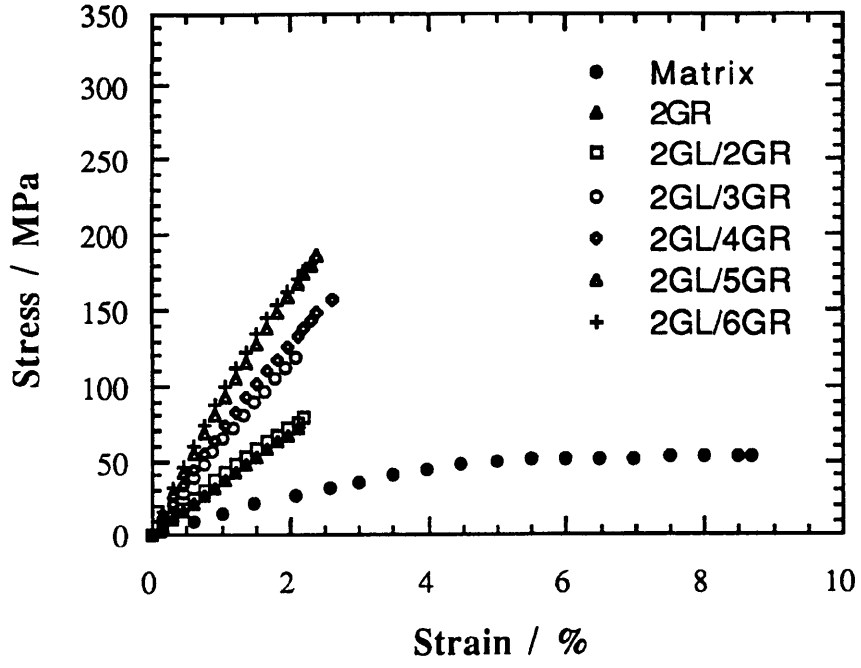

Figure 5.16b Tensile stress-strain curves of glass-glass SRIM composites in transverse direction

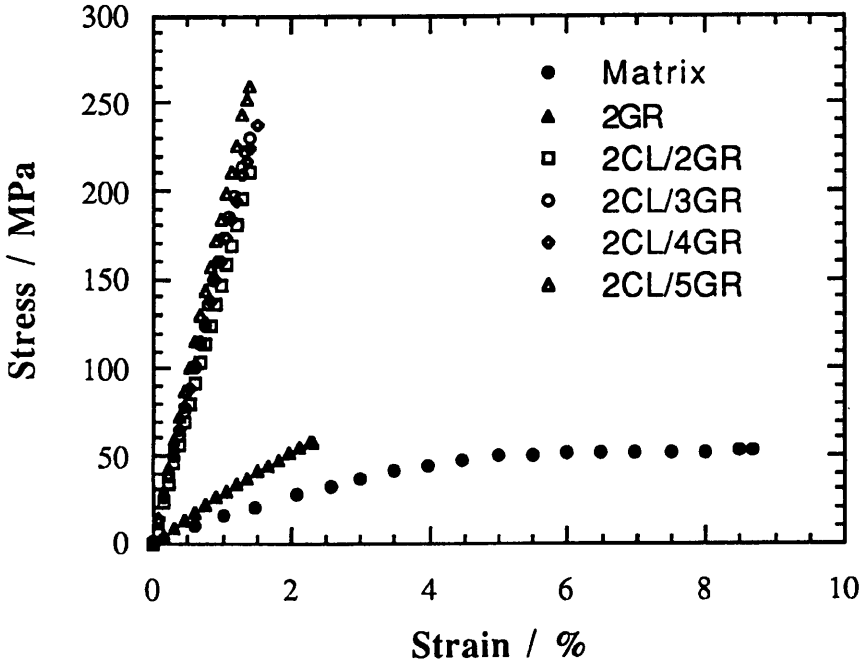

Figure 5.17a Tensile stress-strain curves of carbon-glass SRIM composites in longitudinal direction

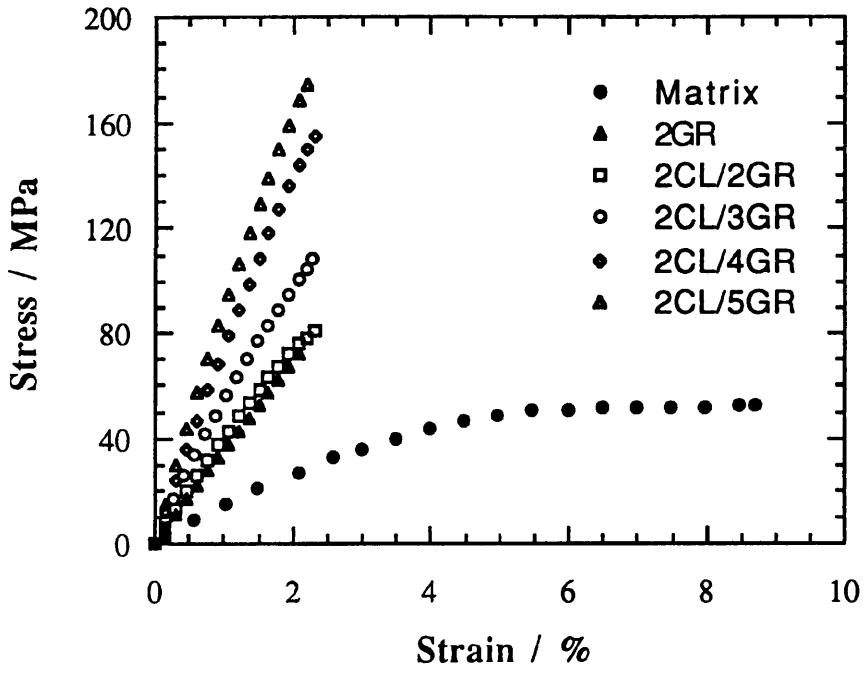

Figure 5.17b Tensile stress-strain curves of carbon-glass SRIM composites in transverse direction

in Table 5.4 show that, as expected, the matrix is isotropic. However, the SRIM composite, 2GR, containing only random glass-fibres is anisotropic with its transverse properties exceeding its longitudinal properties. This suggests that despite the controlled processing conditions used to form the SRIM composites, some compression of the mats along the mould cavity must have occurred, due to the incoming flow of the reactant mixture, resulting in increased orientation of fibres perpendicular to the direction of mould fill. In the hybrid SRIM composites, longitudinal properties are in general determined by the outer layers of unidirectional-fibre mats, and the transverse properties are dominated by the inner layers of random glass-fibre mats. In addition, both the tensile modulus and tensile strength, longitudinal and transverse, increase with increasing volume fraction, ϕ_{rf}, of random glass-fibres.

Table 5.4 Tensile test results of main hybrid SRIM composites

Materials	ϕ_f / %		$E^{(a)}$ / GPa		$\sigma^{(a)}$ / MPa		$\varepsilon^{(a)}$ / %	
	ϕ_{uf}	ϕ_{rf}	l[(b)]	t[(b)]	l	t	l	t
Matrix	0	0	1.5±0.1	1.5±0.1	52±0.8	52±0.8	8.7	8.7±0.8
2GR	0	10.7	3.2±0.3	4.0±0.4	56±8.3	70±13	2.0±0.4	1.9±0.6
2GL/2GR	6.9	10.7	9.6±1.0	5.0±1.2	193±6.3	77±13	2.2±0.2	2.0±0.6
2GL/3GR	7.0	16.3	10.0±0.5	5.5±0.6	236±16	113±13	2.7±0.4	2.6±0.4
2GL/4GR	6.8	21.1	10.7±0.7	7.6±2.0	253±6.5	150±14	2.7±0.1	2.4±0.7
2GL/5GR	6.8	26.5	11.4±1.2	8.3±2.2	284±16	164±16	2.6±0.3	2.6±0.6
2GL/6GR	6.6	30.9	12.3±2.2	10.8±0.9	308±12	182±24	2.6±0.2	2.3±0.3
2CL/2GR	6.4	10.7	15.4±1.5	4.6±1.0	211±23	81±8.3	1.4±0.1	2.3±0.3
2CL/3GR	6.4	16.0	16.8±2.1	5.8±1.1	229±15	108±9.0	1.4±0.2	2.3±0.4
2CL/4GR	6.3	21.2	17.9±1.2	8.2±1.7	237±19	155±14	1.5±0.2	2.3±0.5
2CL/5GR	6.4	26.3	19.8±1.6	10.1±1.7	260±27	174±26	1.4±0.4	2.2±0.4
2KL/2GR	6.3	10.7	12.5±1.1	(c)	210±11	(c)	1.7±0.3	(c)
2GW/2GR	7.5	10.7	9.0±1.7	(c)	189±8.1	(a)	2.2±0.4	(c)
Alternating[(d)] GR/CL(5)	6.7	16.8	16.9±2.0	6.4±0.9	245±28	140±23	1.5±0.1	2.5±0.6
Alternating[(e)] CL/GR(7)	13.4	16.5	26.2±3.7	6.2±0.9	422±30	126±17	1.6±0.2	2.6±0.5

(a) E, σ, and ε are Young's modulus, tensile strength and failure strain respectively; (b) values of l and t refer to the values for longitudinal and transverse specimens respectively; (c) not determined; (d) hybrid mat geometry: GR/CL/GR/CL/GR; (e) hybrid mat geometry: CL/GR/CL/GR/CL/GR/CL.

The longitudinal modulus, E_l, is particularly dependent on the unidirectional-fibre mats, and the differences, at essentially constant overall volume fraction (2GL/2GR, 2CL/2GR, 2KL/2GR), reflects the differences in moduli of the individual fibre types, viz., glass (74 GPa), carbon (238 GPa) and Kevlar (128 GPa) (only limited data were obtained for Kevlar-glass hybrid SRIM composite, because of the difficulty in processing the testing specimens. Thus, only longitudinal tensile properties of Kevlar-glass hybrid SRIM composite, 2KL/2GR, were obtained. However, it is interesting to compare the effect of changing the outer layer mats on the tensile properties of hybrid SRIM composites, which is shown in Fig.5.18)). The transverse modulus, E_t, however, depends mainly on the matrix

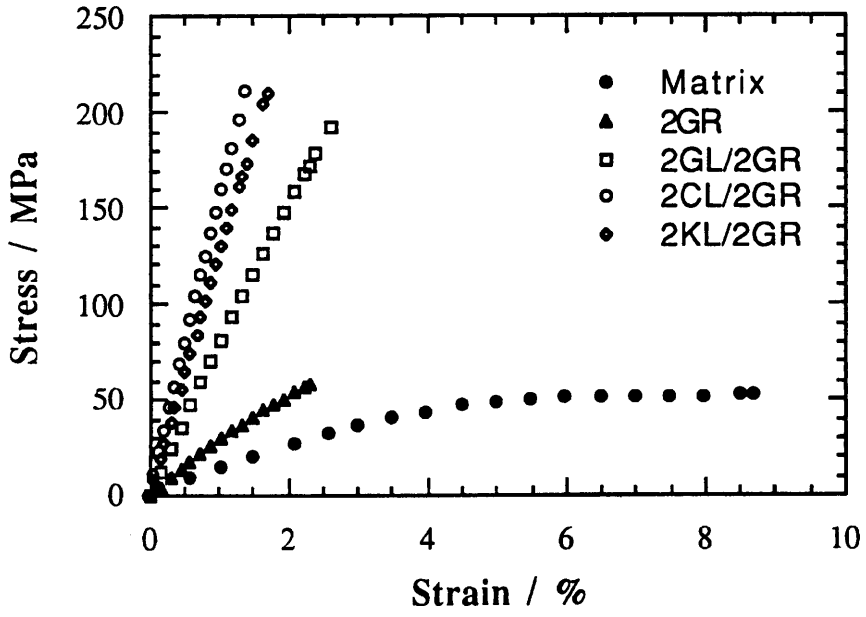

Figure 5.18 The effect of varying the outer unidirectional reinforcement mats on the longitudinal tensile stress-strain curves of hybrid SRIM composites.

and the random glass-fibre content, ϕ_{rf}, and is essentially independent of the type of unidirectional fibre used. The longitudinal tensile strength, σ_l, again is dominated by the presence of the outer unidirectional fibre mats and increases with random glass-fibre content,

ϕ_{rf}, although there is little difference between the hybrid composites at constant overall volume fraction. This is because, unlike their moduli, the tensile strengths of the different fibre types are similar (2800 to 3500 MPa). The transverse tensile strength, σ_t, is dominated by the matrix and random glass-fibre content, ϕ_{rf}, and again is essentially independent of the type of unidirectional fibres used. Similarly, longitudinal failure strains, ε_l, reflect the failure strains of the different types of unidirectional fibres, viz., glass (~5%), carbon (~1.4%) and Kevlar (~2%). Transverse failure strains, ε_t, are essentially constant for all the SRIM composites studied with values between 2.1 and 2.6% being determined by the inner layers of random glass-fibres.

The experimental data are now interpreted in terms of the composite laminate model and the various equations derived in the previous section. Values of composite tensile strengths were calculated using Eq(5.17a) and (5.17b), respectively, for longitudinal and transverse specimens. The calculated values of longitudinal tensile strengths, σ_l, and transverse tensile strengths, σ_t, are shown as the solid and dashed lines, respectively, in Fig.5.19 and 5.20, for glass-glass hybrid SRIM composites and carbon-glass hybrid SRIM composites. The corresponding experimental data are also shown for direct comparison. From Fig.5.19 and 5.20, it is very clear that calculated values of transverse tensile strengths fit experimental data well for both glass-glass and carbon-glass hybrid SRIM composites. However, calculated values of longitudinal tensile strengths only fit experimental data well for glass-glass hybrid SRIM composites. The calculated values of longitudinal tensile strengths for carbon-glass hybrid SRIM composites are higher than their experimental data. This is mainly attributed to the following reason: when Eq(5.17a) was used to calculate longitudinal tensile strengths, σ_l, it was implied that outer layer mats and inner layer mats broke at the same failure strain. For glass-glass hybrid SRIM composites, it was approximately true. However, for carbon-glass hybrid SRIM composites, the failure strain of outer layer mats, unidirectional carbon fibre reinforcements, is ~1.4%, much lower than that of inner layer mats (~2.3%). That is why the experimental data of longitudinal tensile strengths for carbon-glass hybrid SRIM composites are lower than their calculated values.

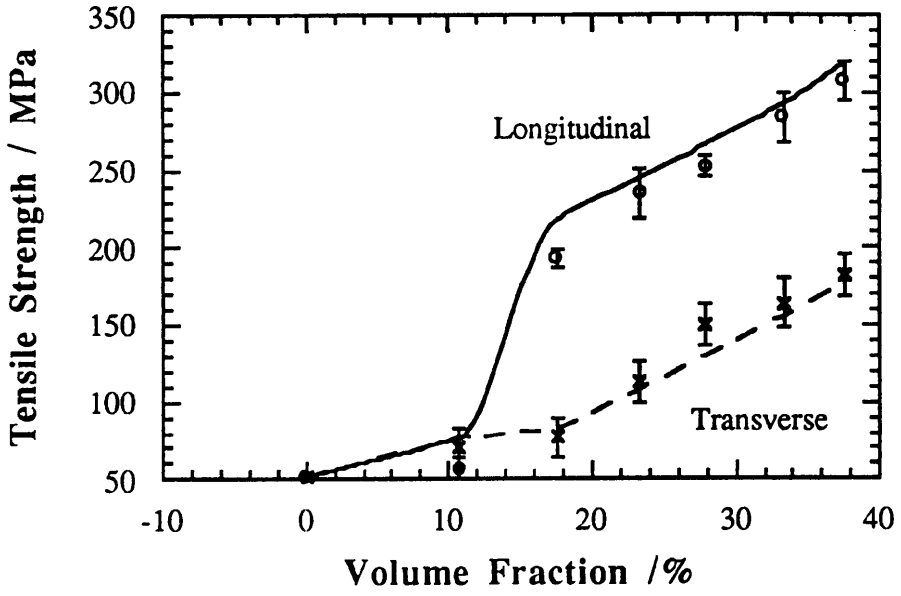

Figure 5.19 The variation of longitudinal and transverse tensile strengths of glass-glass hybrid SRIM composites with total fibre volume fraction ($\phi_f = \phi_{uf} + \phi_{rf}$). Solid and dashed lines are derived from Eqs(5.17a) and (5.17b) respectively.

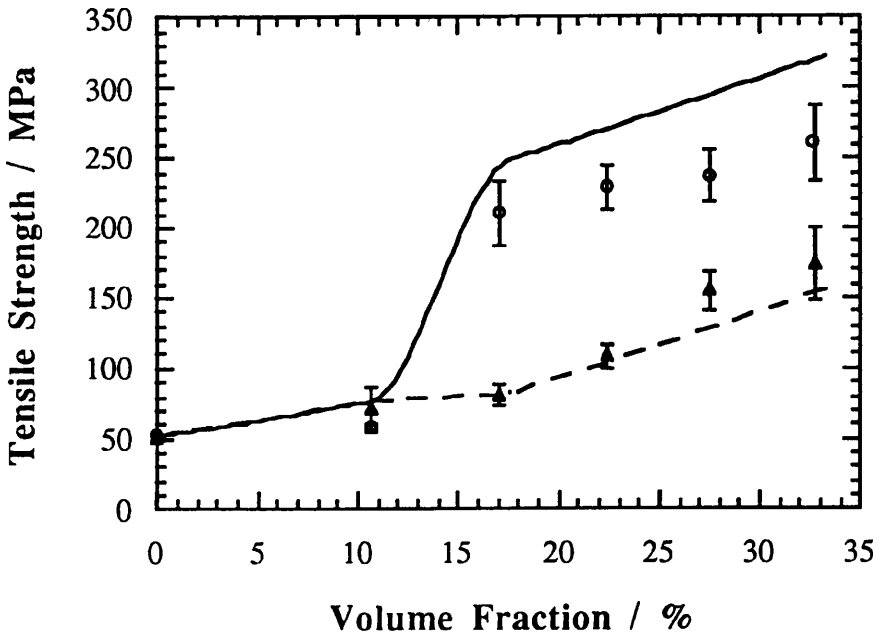

Figure 5.20 The variation of longitudinal and transverse tensile strengths of carbon-glass hybrid SRIM composites with total fibre volume fraction ($\phi_f = \phi_{uf} + \phi_{rf}$). Solid and dashed lines are derived from Eqs(5.17a) and (5.17b) respectively.

Values of composite tensile moduli were calculated using Eq(5.18a) and (5.18b), respectively, for both longitudinal and transverse specimens. The calculated values of longitudinal tensile moduli, E_l, and transverse tensile moduli, E_t, are shown as solid and dashed lines, respectively, in Fig.5.21 and 5.22, for glass-glass hybrid SRIM composites and carbon-glass hybrid SRIM composites. The corresponding experimental data are also shown for direct comparison. In Fig.5.21 and 5.22, the calculated values of transverse tensile moduli fit experimental data well for both glass-glass and carbon-glass hybrid SRIM composites. The calculated values of longitudinal tensile moduli were higher than their experimental data for both of them. Slightly off-axis of unidirectional fibre mats in longitudinal direction and locally buckling of unidirectional fibres are probably attributed to it.

The reinforcements untreated and treated with 0.5 % silane aqueous solution were also used to process similar SRIM composites, and similar tensile tests were also carried out. The results are little different from those mentioned above, probably due to high volume fraction of voids existed in the SRIM composites (see Table 5.2).

5.4 Fracture Behaviour

Traditionally, the performance of engineering plastics is often assessed by tensile, flexural test under the most favourable conditions and often shows ductile behaviour with high elongations. Unfortunately, unexpected brittle fractures usually arise in materials that give ductile fracture in the tension test since they would not be used if the tension tests were brittle. This problem was recognised in the last century when the increasing performance demands of railway construction gave rise to many brittle fracture problems. The impact tests (both Chappy and Izod) are practical solutions to these problems because compared with tensile test, they test materials on the most severe test conditions. The specimens are notched and then struck at high rate in bending, with the notch in tension. Such a combination is likely to induce brittle failure so that if a material performs well, as indicated by high energy absorption, then it is judged to be tough. But the results from impact tests depends on specimen geometry and dimensions, is not a fundamental materials property.

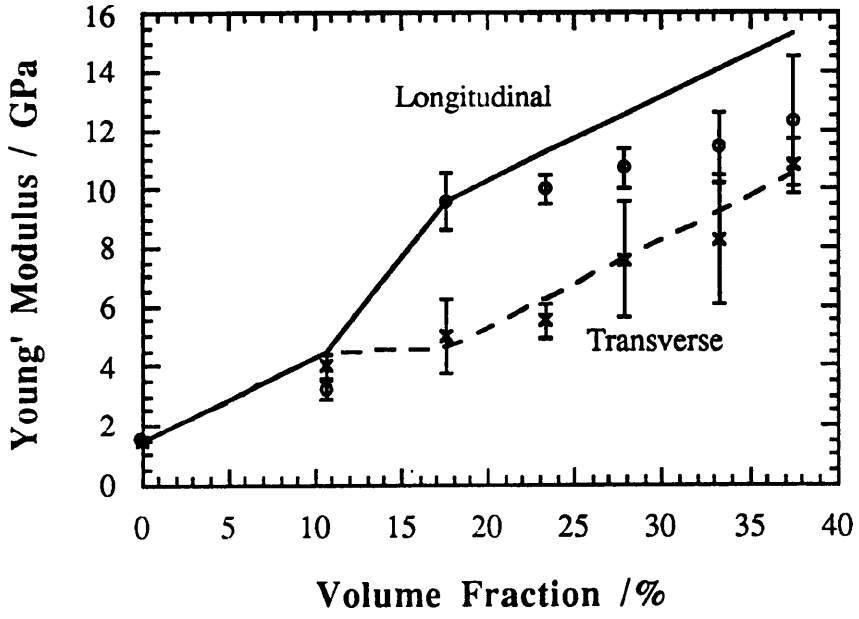

Figure 5.21 The variation of longitudinal and transverse tensile moduli of glass-glass hybrid SRIM composites with total fibre volume fraction ($\phi_f = \phi_{uf} + \phi_{rf}$). Solid and dashed lines are derived from Eqs(5.18a) and (5.18b) respectively.

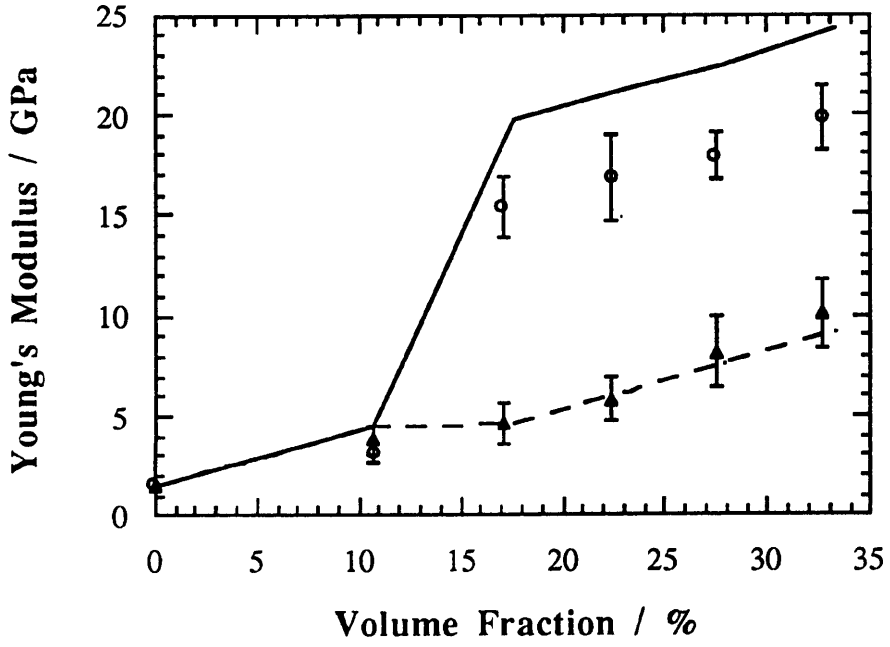

Figure 5.22 The variation of longitudinal and transverse tensile moduli of glass-glass hybrid SRIM composites with total fibre volume fraction ($\phi_f = \phi_{uf} + \phi_{rf}$). Solid and dashed lines are derived from Eqs(5.17a) and (5.17b) respectively.

All the tests mentioned above are empirical and try only to describe failure in a simple way. If yielding occurs the yielding stress is a useful parameter but the fracture stress and the impact energy are of limited value if they are not for the type of failure which happens. It is the occurrence of brittle fracture in practice, when the tests lead one to expect ductile behaviour, which is the essence of the problem and the tests mentioned above do little to help. It is here that Fracture Mechanism becomes important.

5.4.1 Fracture Micromechanisms of Composites

In addition to the strength and modulus which fibre reinforcements bring to composites, another very important property of a composite is its resistance to fracture. The fracture energies of various materials are ranked in decreasing order in the schematic shown in Fig.5.23.

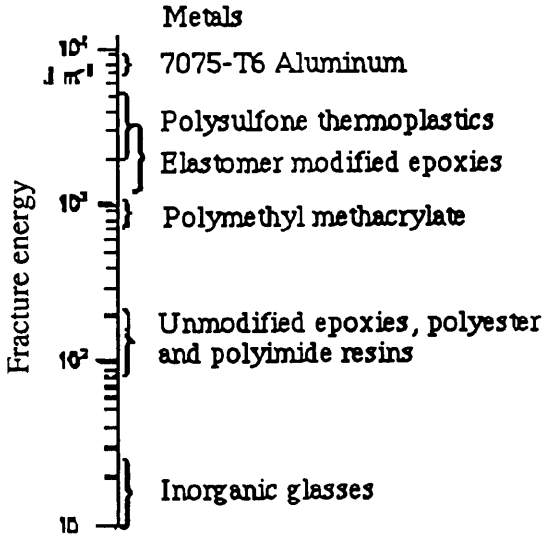

Figure 5.23 Fracture energies (J m^{-2}) for some common materials [192]

A measure of the fracture resistance of a material is given by the specific work of fracture, or fracture toughness, and is defined here as the energy required to create unit area of new transverse fracture surface of composite [193]. When a composite is loaded, there is widespread microscopic damage throughout the material. Extensive damage can be

sustained up to a critical point at which failure occurs by the propagation of cracks. These cracks are much more complicated in nature than those in homogeneous materials. The failure of a composite involves the fracture of load-bearing fibres, matrix and a complex combination of cracks propagated along the interfaces. Fracture toughness of a composite therefore depends not only on the properties of the constituents but also significantly on the interfacial properties or bonding. The various micro-failure mechanisms constituting the total fracture toughness, R, are discussed in the following sections. It is important to notice that except for pseudo-isotropic short fibre composites, the critical energy release rate, Gc, is not necessarily equal to R. Most of the theories of fracture toughness of fibre composites have hitherto been concerned with unidirectional fibres. Characterisation of various origins of fracture toughness in composites may be derived from a consideration of the sequence of microscopic fracture events that lead to the propagation of a macroscopic crack under monotonically increasing loads. In order to distinguish the individual micromechanisms of toughening, it is convenient to consider a model where a crack travelling in the matrix approaches an isolated fibre (Fig.5.24) [194].

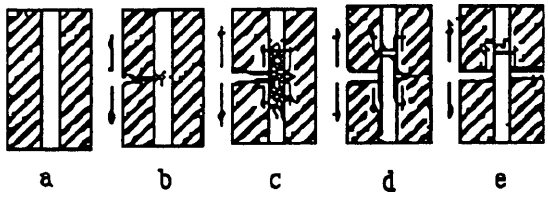

Figure 5.24 Model of the crack-fibre interaction in a simple composite.
(a) In the uncracked composite the fibre is gripped by the matrix. (b) A matrix crack is halted by the fibre, and increasing the load allows the crack to pass around the fibre without breaking the interfacial bond. (c) Interfacial shearing and lateral contraction of the fibre result in debonding and a further increment of crack extension. (d) After considerable debonding, the fibre breaks at some weak spot within the matrix and further crack extension occurs. (e) The broken fibre end must be pulled out against the frictional grip of the matrix if total separation of the composite is to occur [194].

5.4.1.1 Fibre-Matrix Debonding Theory

For a composite in which the fracture strain of fibre is greater than that of matrix (i.e. $\varepsilon_f > \varepsilon_m$), a crack originating at a point of stress concentration (e.g. air bubbles or inclusions) in the matrix is either halted by the fibre if the current level of stress is not high enough or it may pass around the fibre without destroying the interfacial bonding (Fig.5.24b). As the load applied to the composite is increased, the fibre and matrix attempt to deform differentially and a relatively large local stress builds up in the fibre. This causes local Poisson contraction and eventually the level of shear force developed at the interface will exceed the total static interfacial shearing strength, resulting in interfacial debonding at the crack plane which will extend some distance along the fibre (Fig.5.24c). The debonding toughness, R_d, first given by Outwater and Murphy [195], can be inferred to be the total elastic strain energy stored in the fibre over the debond length. l_d, at its breaking stress, σ_f, divided by the cross-section area of the composite [193]:

$$R_d = \frac{V_f \sigma_f^2 l_d}{2E_f} \tag{5.19}$$

where E_f and V_f are the elastic modulus and volume fraction of the fibres. The established view is that the debonding process is frequently a major contributor to the total fracture toughness of GFPR [196], although there may be some confusion as to the exact nature of the energy absorption mechanism. It is important to notice that R_d represented by Eq (5.19) appears to be a consequence of debonding rather than the debonding itself [194].

If the interfacial bonding is very weak compared to matrix tensile strength, tensile debonding may occur at the interface ahead of crack tip as the result of the lateral stress concentration, as proposed by Cook and Gorden (Fig.5.25) [197]. But many investigators [198 - 202] have recognised the occurrence of this failure mechanism in unidirectional fibre composites, and longitudinal splitting at the weak interface is more likely caused by the large shear stress component parallel to the fibre developed in the crack tip region as result of the high anisotropy of a high V_f composite than the tensile stress component [194].

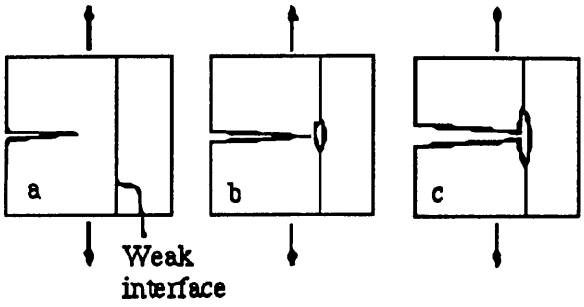

Figure 5.25 The Cook-Gordon Mechanism: Crack tip is effectively blunted [197].

5.4.1.2 Post-Debonding Friction

After interface debonding has taken place, the fibre and matrix move relative to each other as the crack continues to propagate. Kelly [200] has proposed that energy dissipated due to the post-debonding friction is equal to the frictional shear force times the differential displacement between fibre and matrix. Approximating the displacement to the product of the average l_d and the differential strain, $\Delta\varepsilon$, of the fibre (ε_f) and matrix (ε_m), the post-debonding friction toughness, R_{df}, is

$$R_{df} = \frac{2V_f \tau_f l_d^2 \Delta\varepsilon}{d} \tag{5.20}$$

where τ_f is the frictional shear strength. Harris [194] assumed that $\Delta\varepsilon \approx \varepsilon_f$ since ε_m can be neglected in brittle matrix composites.

5.4.1.3 Stress Redistribution

After considerable debonding the continuous fibre is loaded to failure over the debonded length. It can break at a weak point within this region near the main fracture plane. Upon failure, the fibre instantly relaxes and regains its original diameter, so that the ends are again gripped by the matrix (Fig.5.24d). Another source of toughness of fibre composites have been given by Piggott [203] and Fitz–Randolph et al [204], proposing that the energy dissipating mechanism after fibre fracture is the redistribution of strain energy from the fibre to the matrix. Assuming that the stress builds up linearly from the broken end over a distance $l_c / 2$, the strain energy lost from the fibre due to stress redistribution, R_r, is:

$$R_r = \frac{V_f \sigma^2 l_c}{3 E_f} = \frac{V_f \sigma^3 d}{6 E_f \tau_f} \tag{5.21}$$

which is ($2 l_c / 3 l_d$) times the Outwater–Murphy debonding toughness in Eq(5.19).

5.4.1.4 Fibre Pull-out Theory

As the crack propagates, pull-out of the broken fibre from the matrix occurs, giving rise to a continuation of the post-debonding friction work (Fig.5.24e). This additional component of work of fracture, known as the Cottrell [205]-Kelly [206, 207] pull-out work, is the work done against sliding friction in extracting the broken fibre. From the work done by the friction shear stress, τ_f, which is assumed constant over a pull out distance l_{po} the fibre pull out toughness, R_{po}, is:

$$R_{po} = \frac{2 V_f \tau_f l_{po}^2}{d} \tag{5.22}$$

5.4.1.5 Total Fracture Toughness Theory

Atkins and co-workers [208, 209] have developed a new theory based on the co-existence of the three major sources of fracture toughness, i.e. stress redistribution (R_f of Eq(5.20)), fibre pull-out (R_{po} of Eq(5.21)) and generation of new surfaces (R_s) which is the sum of the energies absorbed in creating new surfaces in fibre, R_f, matrix, R_m, and at the interface, R_i, divided by the nominal transverse area (neglecting the cylindrical interface area), i.e.

$$R_S = V_f R_f + (1 - V_f) R_m + V_f \left(\frac{l_c}{d}\right) R_i \approx V_f \left(\frac{l_c}{d} - 1\right) R_m \tag{5.23}$$

Therefore, the total fracture toughness, R_t, is:

$$R_t = R_r + R_{po} + R_S = \frac{V_f \sigma_f}{\tau_f} \left[\frac{\sigma_f d}{6} \left(\frac{1}{4} + \frac{\sigma_f}{E_f}\right) \frac{R_m}{2}\right] + (1 - V_f) R_m \tag{5.24}$$

It should be noted that R_S includes the debond toughness, R_d. R_f is neglected and R_i is approximately equal to R_m in Eq(5.24). Figure 5.26 plots the variation of tensile strength of

composites, σ_c, against R_t or $1/\tau_f$ according to Marston et al [198]. For high τ_f, tensile strength of composites, σ_c, is determined by the presence of the small Griffith cracks (i.e. $\sigma_c^2 \propto R_t$) while, for low τ_f, σ_c decreases linearly with $1/\tau_f$, or R_t ($\sigma_c = b - a R_t$, where a and b are constant). They proposed that both high strength and high toughness can not be achieved simultaneously in fibre composites although the strength and toughness can be optimised as indicated by the point A in Fig.5.26.

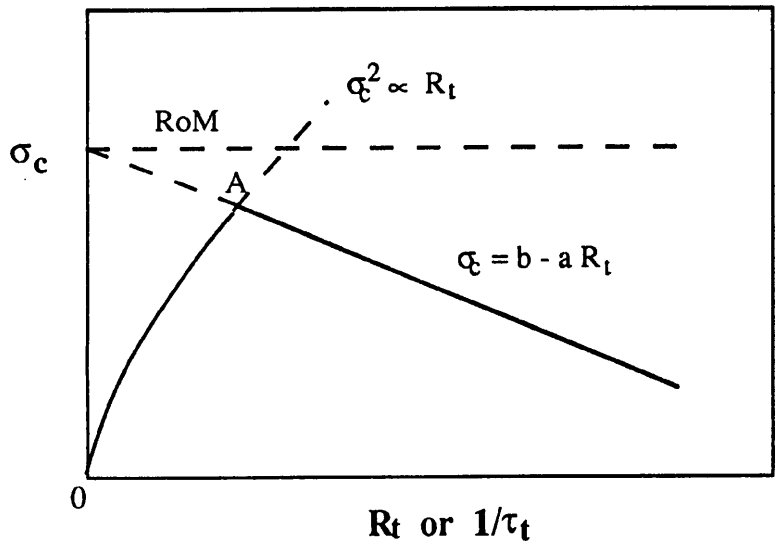

Figure 5.26 The relationship between composite strength, σ_c, and total fracture toughness, R_t, or the inverse of frictional shear strength, $1 / \tau_f$ [198].

For randomly oriented fibre composites, the situation is more complicated, and other factors need consideration, such as, the matrix is fragmented to allow pull out of non–aligned fibres, as shown schematically in Fig.5.27.

Much research on composites has been done in various aspects by researchers would wide. In some of the early research, Irwin [210], Pagano and Tsai [211], Wu [212] gave their reviews about the application or potential application of fracture mechanics and micromechanics to composite failure. Waddoups [213] in 1968 reported the characterisation (tensile, compression, flexural, and shear tests) of laminar composites and micromechanics analysis. Purslow [214-216] applied fractography to the study of the failure mode, failure

sequence and the initial cause of break-down of composites. Herakovich [217] studied in detail the influence of fibre orientation on crack growth in unidirectional, resin matrix composites. For fracture toughness, most of attention was paid to composites in which the cracks were parallel to the fibre direction or between laminates, so that Linear Elastic Fracture Mechanics (LEFM) can be used as exemplified by the studies carried out by Donaldson [218], Hine and Brew [219], Zhang [220], Nikpur [221], Kolle [222], Bathias [223], Bascom [224]. Harris [225] however, suggested that the LEFM parameter, critical stress intensity factor, K_{IC}, has no meaning. Until now, due to the variety of composites, no universal model is available for composite fracture.

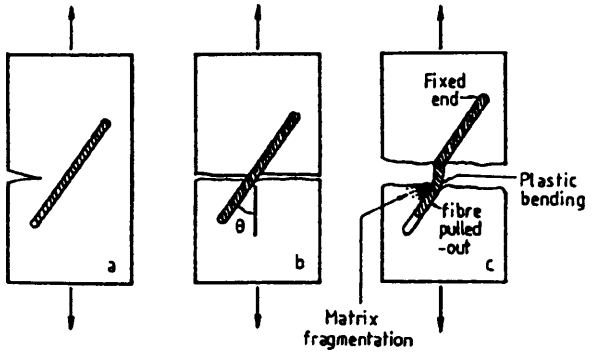

Figure 5.27 A model for plastic bending of fibre and fragmentation of matrix during fracture of randomly oriented fibre composites.[208, 209].

5.4.2 A Linear Elastic Fracture Mechanics (LEFM) Approach

Fracture Mechanics is a most useful tool to describing brittle fracture and was originally introduced by A. A. Griffith [226] to explain why the strength of glass fibres increased with decreasing diameter. His conclusion was that the smaller fibres had smaller flaws and hence were stronger and from this some general principles evolved. Firstly the approach assumes that all materials bodies contain cracks or flaws and that fracture is the condition when these start to grow; i.e. when fracture initiates.

The driving force for this growth comes from the release of stored elastic energy in the body as the crack grows and the generic solution is for a large plate containing a crack of length $2a$ and loaded remotely with a stress σ as shown in Fig.5.28.

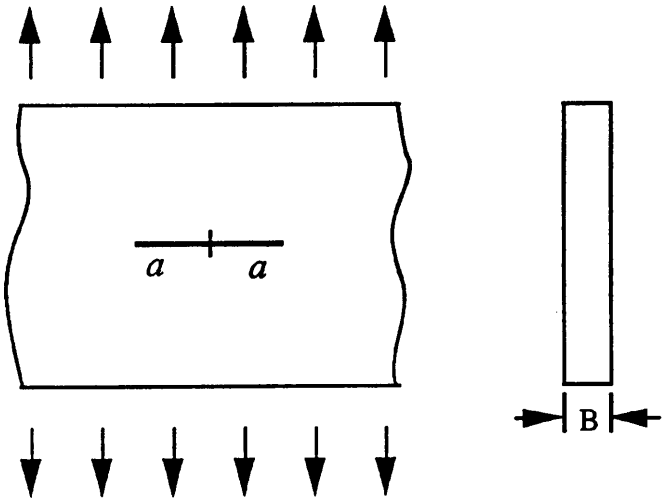

Figure 5.28 A crack in a uniformly loaded plate

The energy release rate, G, is given by,

$$G = \frac{\sigma^2 \pi a}{E} \tag{5.25}$$

where E is the Young's Modulus and π is geometry factor. For fracture, this energy per unit area must equal that required to create the new surfaces, G_C, so we have the fracture condition;

$$G = G_C$$

and,
$$K_C^2 = E\, G_C = \sigma^2 \pi a \tag{5.26}$$

where K_C is defined as the critical stress intensity factor and is used because it comes directly from σ and a, and does not require a knowledge of E. For other geometries and loading systems such as bending or different crack shapes, the parameter π is replaced by a calibration factor Y^2, which is usually a function of (a /w), where w is the specimen width. There is a large number of these functions [227] so that almost any real system can be

analysed using the functions or alternatively, calibrating the system using finite element analysis.

The whole essence of the method of Fracture Mechanics is embodied in Eq (5.24) in that the toughness is characterised via G_c or K_c by a test specimen with a known crack length a. If σ is determined, then K_c may be found and, if E is known, G_c may be determined. The design method is then to examine a given component for which Y^2 ($\equiv\pi$) can be found so that if a is known a critical stress can be found and similarly, if σ is known, the critical stress which can be tolerated before fracture can be calculated. An important point here is that the failure stress σ is not a material property but depends on a and it is K_c or G_c which controls the relationship between σ and a. Thus conventional tensile or flexural tests on un-notched samples give a failure stress appropriate to the flaw size which happens to be present. This is the origin of the well known problem of the variability of strength in conventional tests.

5.4.3 LEFM Test Method and its Application to SRIM Composites

ASTM E399-83 [228] and A Linear Elastic Fracture Mechanics (LEFM) Standard for Determining Kc and Gc for Plastics (testing protocol - March 1990, drafted by J. G. Williams, based on the activities of the EGF Task Group on polymer and composites) [229] are used as the main references.

1. Specimen Preparation and testing:

Three-point bend (also called single-edge notched bend, SENB) geometry was used. For each material, five specimens of 60 x 10 x 3.3 mm were cut in the longitudinal direction, and another five 60 x 10 x 3.3 mm specimens were cut in the transverse direction, respectively, from the same SRIM plaque (see Fig.4.2). Each specimen was notched using a milling machine and a natural crack at the tip of a notch was made by tapping a new razor blade placed in the tip of the notch. The final specimen geometry is shown in Fig.5.29.

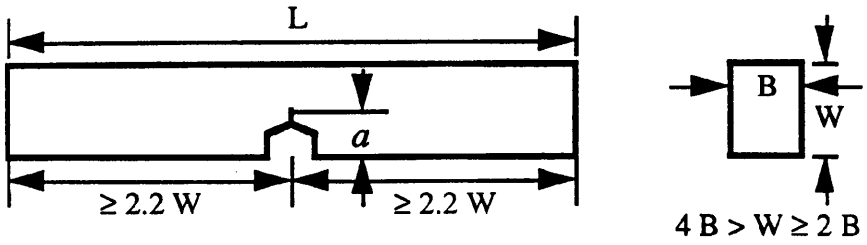

Figure 5.29 Three-Point Bend Specimen (SENB).

a = 5 mm, W = 10 mm (0.45 < a / W < 0.55), B = 3.3 mm, L = 60 mm.

The SENB specimens were tested using a specially-constructed testing rig shown in Fig.5.30. An externally-applied, displacement measuring device was used, and the displacement was taken at the load point, immediately above the crack tip.

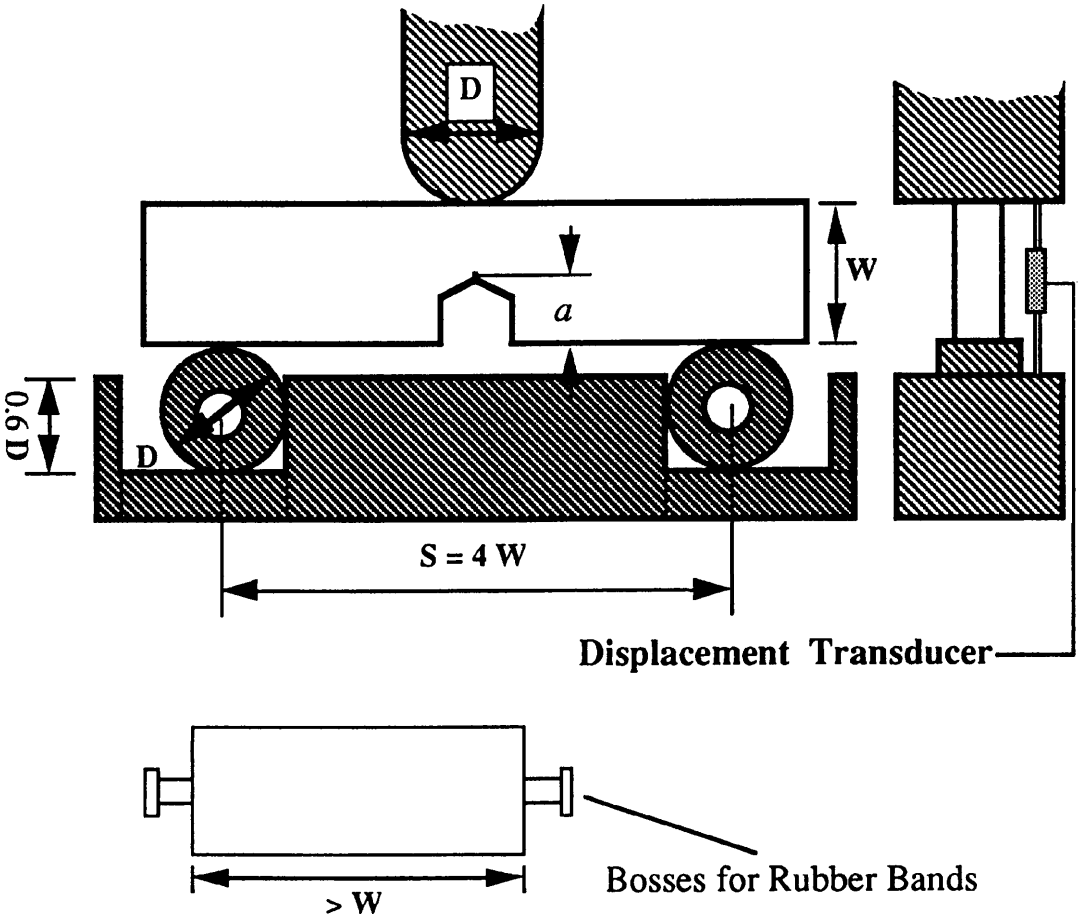

Figure 5.30 The loading rig for Three-Point Bend test.

D = 6 mm, S = 40 mm

A test configuration as shown in Fig.5.31 using identically-prepared, but unnotched specimens, was used to correct the measured displacement for indentation effects, which were allowed for in the calculation of G_c values.

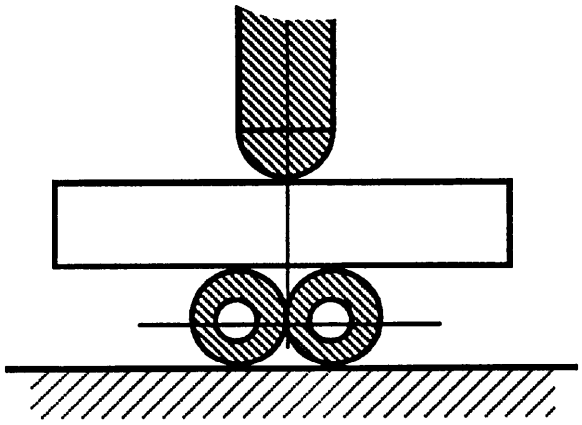

Figure 5.31 Arrangement for finding Indentation Displacement

The effect of the displacement transducer on the measured force used to deform the SENB in the testing rig shown in Fig.5.30, was determined by using the same rig but without a SENB specimen as shown in Fig 5.32. A force-deflection curve from the test (Fig.5.32) was obtained, and the values of force were subtracted from those obtained from the test involving a composite specimen (Fig.5.30).

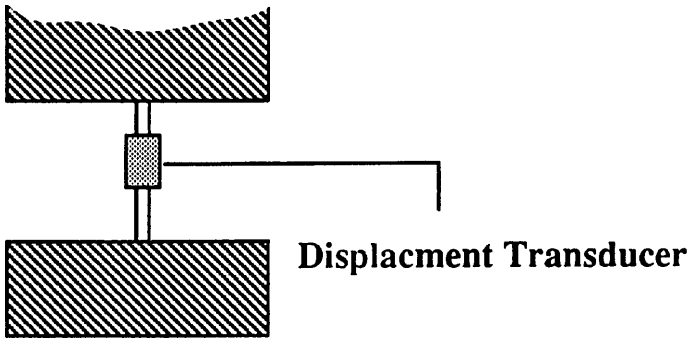

Figure 5.32 Determination of the displacement transducer force-deflection curve.

2. Test Procedure

An Instron 1185 equipped with displacement transducer (C. O. D. Gauge (10/4) / Instron), accurate to ± 0.1% strain, were used to obtain force-deflection data up to fracture, and Macintosh II with a A / D board was used to collect the data. The Instron 1185 was calibrated electronically and displacement transducer was calibrated manually. The test was performed at a cross head speed of 2 mm / minute. In the ideal case, linear force-deflection data were obtained with an abrupt drop of force to zero at the instant of crack growth initiation, and an apparent value of the stress intensity factor K_Q can be determined from the maximum force using Eq(5.27). However, in most cases, some non-linearity in the force-deflection data was observed due to effects such as plastic deformation at the crack tip, non-linear elasticity, general visco-elasticity and stable crack growth after initiation but prior to instability. The first three effects violate the LEFM assumption and the fourth one means that the true initiation force is not defined by the maximum. Indeed it is doubtful if an exact definition of initiation could be made and with a need for simplicity in mind, the arbitary modification to the analysis as described in ASTM E399-83 [228] is used. Considering the general curve shown in Fig.5.33 (the initial curvature is due to machine compliance and the true zero deflection point is obtained by extrapolating the tangent to the linear part of the curve, to the point 0'), a best straight line is drawn to determine the initial compliance C as shown. This is then increased by 5% and a further line drawn. If P_{max} falls within those

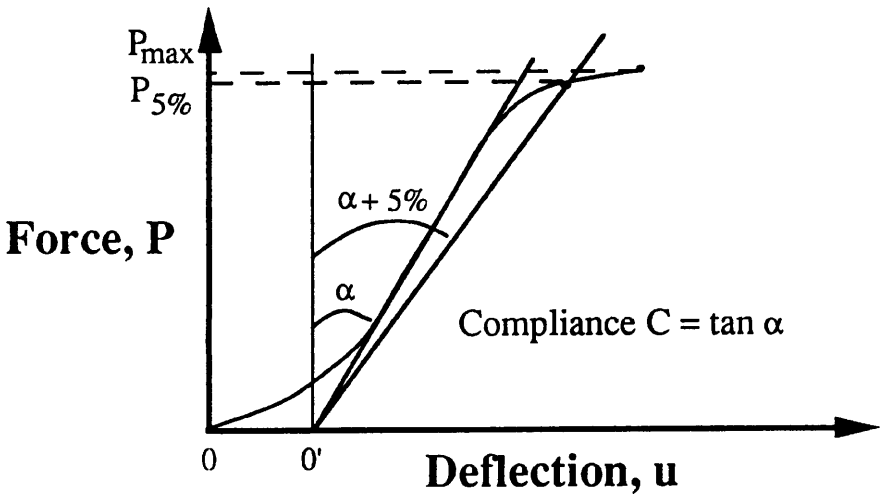

Figure 5.33 Determination of P5% and C.

two lines, then P_{max} is used to calculate K_Q. If the C + 5% line intersects the force curve, then $P_{5\%}$ is determined and this is taken as the force at crack initiation. To study within the LEFM condition it is further specified that:

$$P_{max} / P_{5\%} < 1.1$$

i.e. a 10% non-linearity is allowed. If $P_{max} / P_{5\%} > 1.1$ then the test is invalid. If $P_{max} / P_{5\%} < 1.1$ then $P_{5\%}$ is used to calculate K_Q and G_Q, or Pmax is used if it falls within the two lines.

Values of K_Q are calculated using Eq(5.27),

$$K_Q = \frac{f\ P_Q}{B\ \sqrt{W}} \tag{5.27}$$

where f is calibration factor which depends on the ratio *a*/w as given in Table 5.5, and *a* is the original crack length which is determined from the fracture surface after testing.

The validity of K_Q should be checked via the size criteria, namely,

$$B, a, (W - a) > 2.5 (K_Q / \sigma_y)^2$$

where σ_y is the uniaxial tensile yield stress usually determined from the maximum force. If these criteria are met then, $K_Q = K_{Ic}$.

G_C is determined directly from the energy derived by integrating the force-deflection curve. The procedure to be followed is similar to that used for validity testing and determination of the energy, U_Q, up to the same force point as used for K_Q (as shown in Fig.5.34a). The correction curve, as sketched in Fig.5.34b, is usually quite linear and the energy from indentation, U_{cor}, is determined up to the same force as used for U_Q. The true fracture energy is

$$U = U_Q - U_{cor} \tag{5.28}$$

then G_{Ic} is calculated from this energy U via [230]

$$G_{Ic} = U / B\, w\, \phi \tag{5.29}$$

where values of energy calibration factor, ϕ, defined as $\phi = C / dC / d(a/w)$, are shown in Table 5.5.

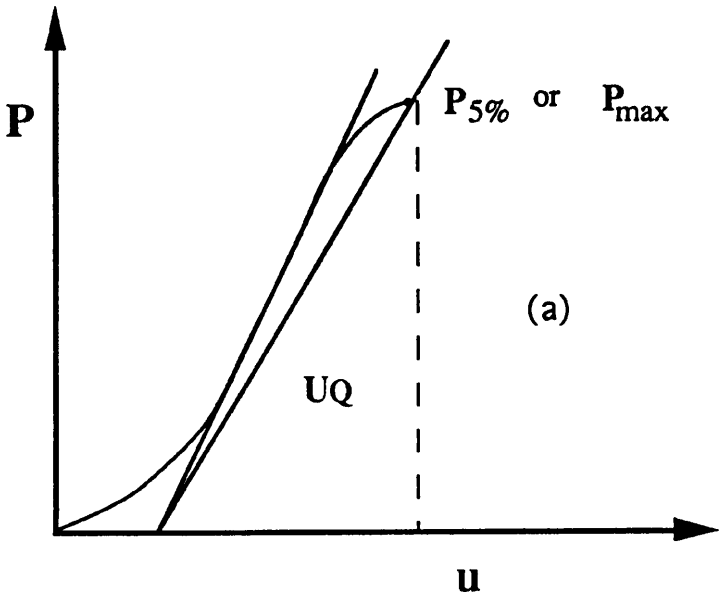

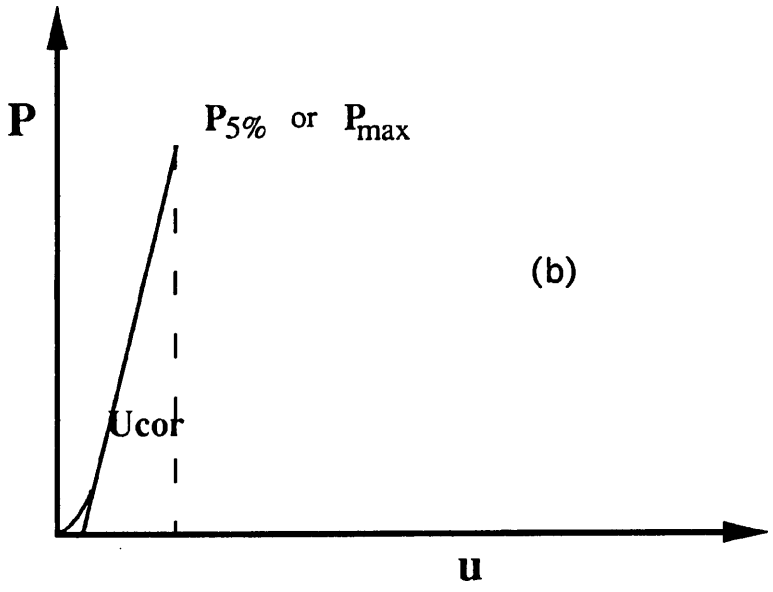

Figure 5.34 Schematic force-deflection curves for SENB test specimens.
(a) fracture test of SENB. (b) indentation test on SENB specimens

Table 5.5 Calibration Factor (SENB*, S / w = 4)

a / w	f	ϕ
0.40	7.93	0.307
0.41	8.16	0.300
0.42	8.38	0.293
0.43	8.63	0.287
0.44	8.88	0.281
0.45	9.14	0.275
0.46	9.42	0.269
0.47	9.70	0.263
0.48	10.01	0.258
0.49	10.32	0.252
0.50	10.65	0.247
0.51	11.00	0.241
0.52	11.36	0.236
0.53	11.74	0.231
0.54	12.15	0.226
0.55	12.57	0.221
0.56	13.02	0.215
0.57	13.49	0.210
0.58	13.99	0.205
0.59	14.52	0.200
0.60	15.09	0.195

* Values calculated using A. Bakker compatible compliance and Stress Intensity Expression for the standard three-point bend specimen (230).

5.4.4 Results and Discussion

Figure 5.34 shows the force versus deflection curves for both non-postcured and postcured matrix. Both curves are initially linear with a rapid decrease of force following crack growth initiation. Values of K_{1c} and G_{1c} were calculated following Eqs (5.27) and (5.29). The results obtained from SENB fracture tests for matrix, D2/M/0.6, were considered in terms of the size criteria, B, a , (W - a) > 2.5 $(K_Q/\sigma_y)^2$, and the LEFM condition, $P_{max} / P_{5\%} < 1.1$. Criteria and the LEFM condition were met, so that it may be concluded that tests were done under the condition of plane strain. Thus K_{Ic} and G_{Ic} can be used to describe critical stress intensity factor and critical energy release rate. Further confirmation that fracture was obtained under condition of plain strain was obtained from Fractography of D2/M/0.6 specimens. The micrographs in Fig. 5.35 for D2/M/0.6 are essentially featureless and typical of brittle fracture as reported, for example, by Hertzberg [231].

Table 5.6 gives the results of the fracture tests of matrix. Post curing has little effect on the value of K_{Ic}, but slightly lowers the value of G_{Ic}. The morphology of D2/M/0.6 was shown in chapter 3 to be co-continuous, and post curing was shown to increase phase separation and the size of microdomain, but to decrease the size of interphase. These morphologic changes are responsible for the decrease of the resistance of the matrix to crack growth initiation. Figure 5.36 and 5.37 show higher magnification SEM photographs of the fracture surfaces in Fig.5.35. In the non-postcured specimen (Fig.5.36), there is evidence of the river markings all over the fracture surfaces, but was

Table 5.6 K_{Ic} and G_{Ic} of matrix

Matrix	K_{Ic} / MPa $\sqrt{m}$	G_{Ic} / kJ m^2	2.5 $(K_{Ic} / \sigma_y)^2$ / mm
D2/M/0.6/up	1.07 ± 0.14	0.91 ± 0.18	1.98
D2/M/0.6/pc	1.08 ± 0.05	0.76 ± 0.05	1.08

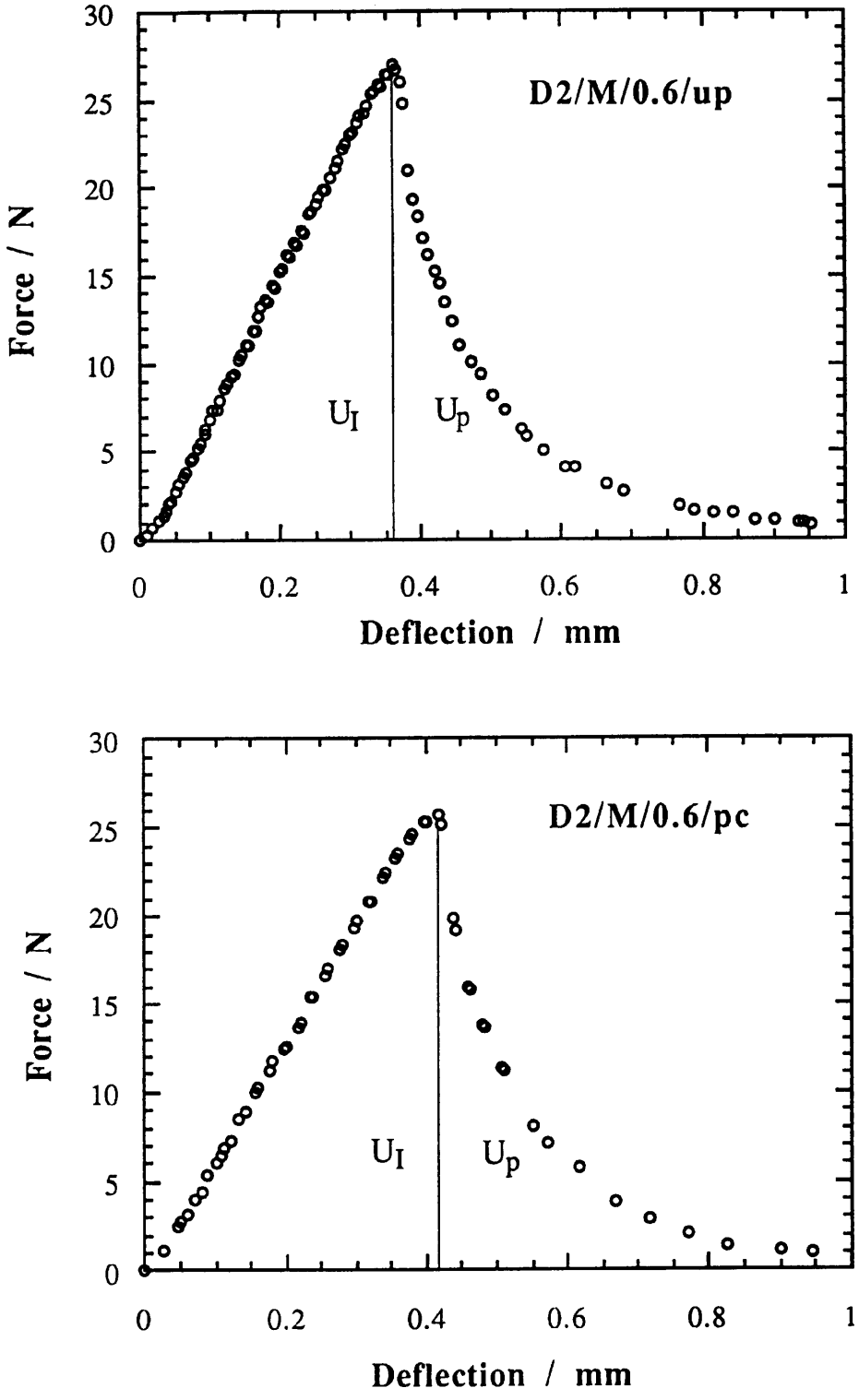

Figure 5.34 Comparative force-deflection curves for non-postcured (up) and postcured (pc) matrix, D2/M/0.6

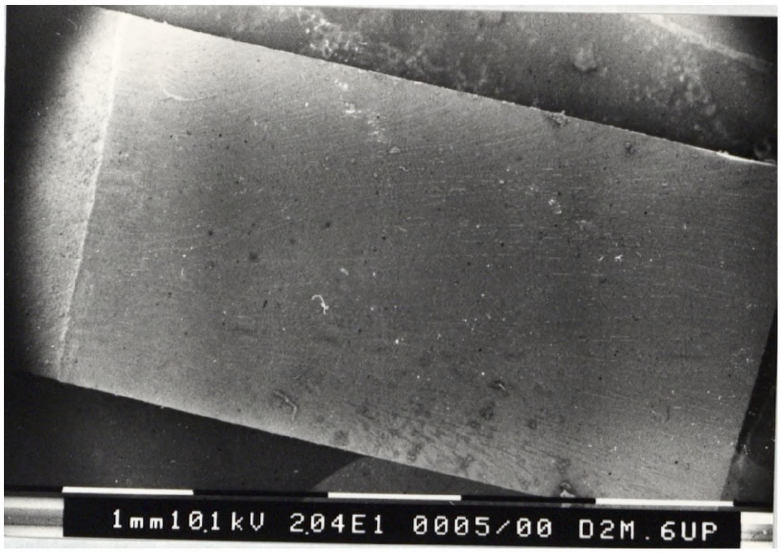

A: D2/M/0.6/up

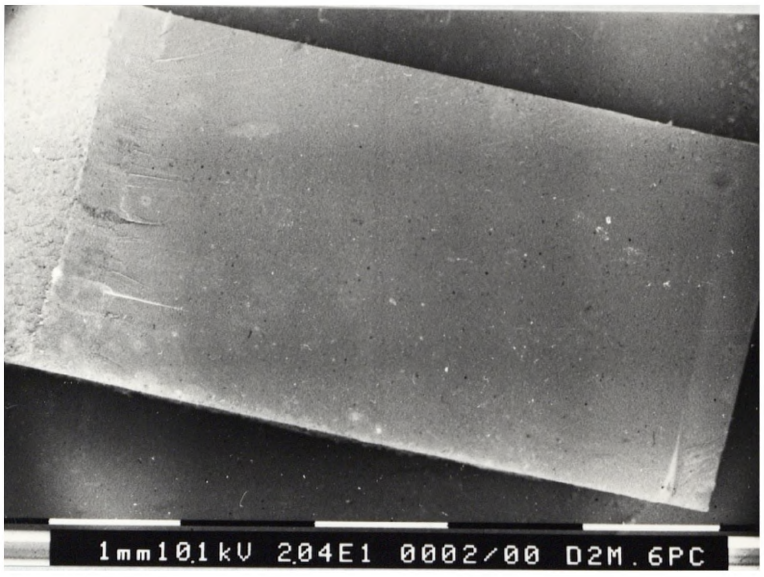

B: D2/M/0.6/pc

Figure 5.35 SEM micrographs of SENB fracture surfaces of D2/M/0.6 matrix.
(a) un-postcured (b) postcured

Figure 5.36 River markings in the fracture surface of D2/M/0.6/up. Crack propagation is from left to right of the micrograph.

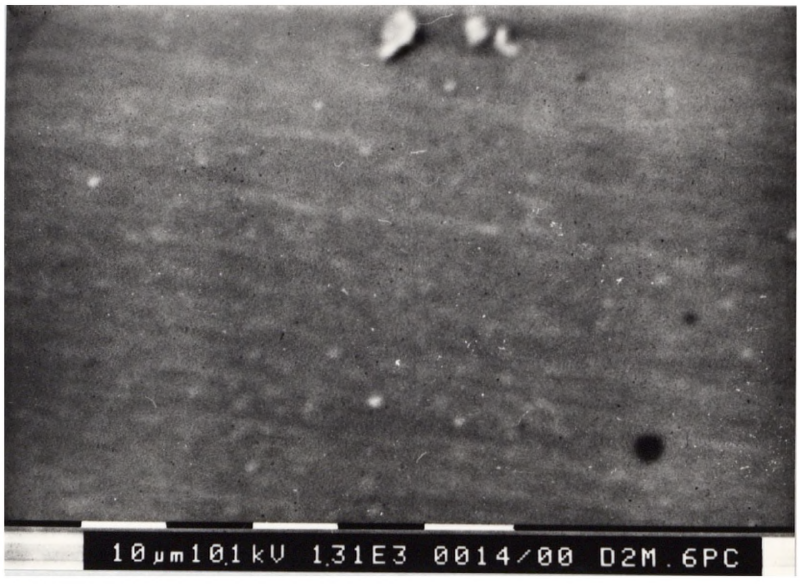

Figure 5.37 Relatively smooth and featureless fracture surface of D2/M/0.6/pc. Crack propagation is from left to right of the micrograph.

only observed in notch-tip regions of the fracture surface of post cured matrix. most of the area of post cured matrix fracture surface was quite smooth as shown in Fig.5.37. The river markings are consistent with a higher value of G_{Ic} of non-post cured matrix. Also the increase in modulus, E, and decrease in strain (plasticity) caused by postcuring, and consideration of the relationship between K_{Ic} and G_{Ic}, $G_{Ic} = (1 - \gamma^2) K_{Ic}^2 / E$, for plain strain, explain why K_{Ic} remains constant but G_{Ic} decreases.

The incorporation of random, continuous glass fibre reinforcement mats and unidirectional glass reinforcement mats in the matrix to make hybrid composites, makes the interpretation of fracture data and failure mechanisms more complicated. Fibres exist at the tip of a crack and bridge the crack at different angles (as shown schematically in Fig.5.38).

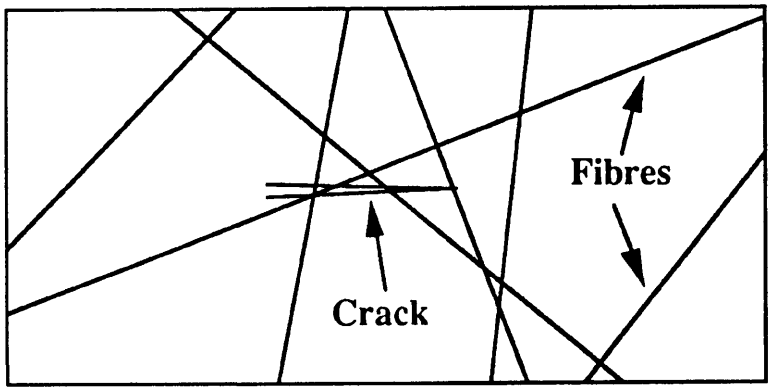

Figure 5.38 A schematic of a crack in SRIM composites

K_{1c}, the critical stress intensity factor, defined in LEFM for homogeneous materials has no validity for heterogeneous, anisotropic materials, such as SRIM hybrid composites [232-235]. So throughout this section, the values of K_{Ic} are given only as reference values, all discussions focus on the values of G_{Ic} obtained for various SRIM composites.

A typical force-deflection curve of SENB for a specimen of 2GR SRIM composite is shown in Fig.5.39. Compare it with Fig.5.34 for matrix, it is noticed that the peak force which is used to calculate K_{Ic}, U_I which is used to calculate G_{Ic}, and failure strain in Fig.5.39 are much greater than those in Fig.5.34, and so does U_p, which is the energy to propagate a crack. Table 5.7 and Fig.5.40 show the effects of reinforcement mats and force

direction on the fracture toughness of SRIM hybrid composites. Fig.5.40 shows clearly that G_{Ic} of matrix increases significantly from 0.76 to 12.5 kJ m^{-2} on incorporation two

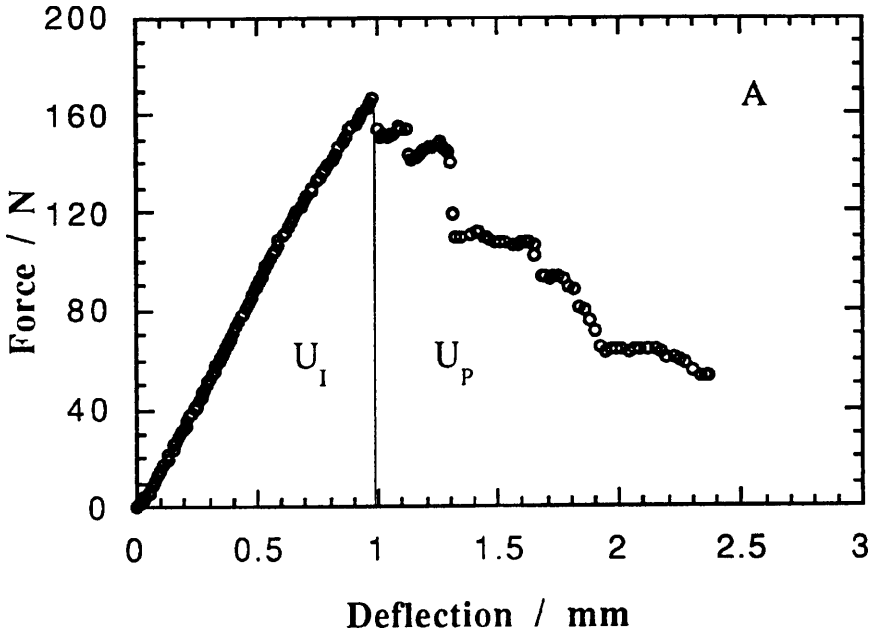

Figure 5.39 A typical force-deflection curve of SENB for a specimen of 2GR SRIM composite

Table 5.7 The effect of Reinforcement Mats on K_{Ic} and G_{Ic} of SRIM composites*

Materials	V_f** (%)	Longitudinal		Transverse	
		K_{Ic} / MPa $\sqrt{m}$	G_{Ic} / kJ m^{-2}	K_{Ic} / MPa $\sqrt{m}$	G_{Ic} / kJ m^{-2}
D2/M/0.6/up	0	1.07±0.14	0.91±0.18	1.07±0.14	0.91±0.18
D2/M/0.6/pc	0	1.08±0.05	0.76±0.05	1.08±0.05	0.76±0.05
2GR	11	5.5 ± 0.60	11.8±2.0	5.8±0.47	12.5±1.6
2GL/2GR	18	8.2 ± 0.48	14.2±2.3	5.3±0.66	10.6±1.9
2GL/3GR	24	10.0± 1.4	15.6±1.6	8.1±0.73	14.2±3.0

* Reinforcement Mats were coated with 0.1% silane aqueous solution.

** V_f is total volume fraction of reinforcements

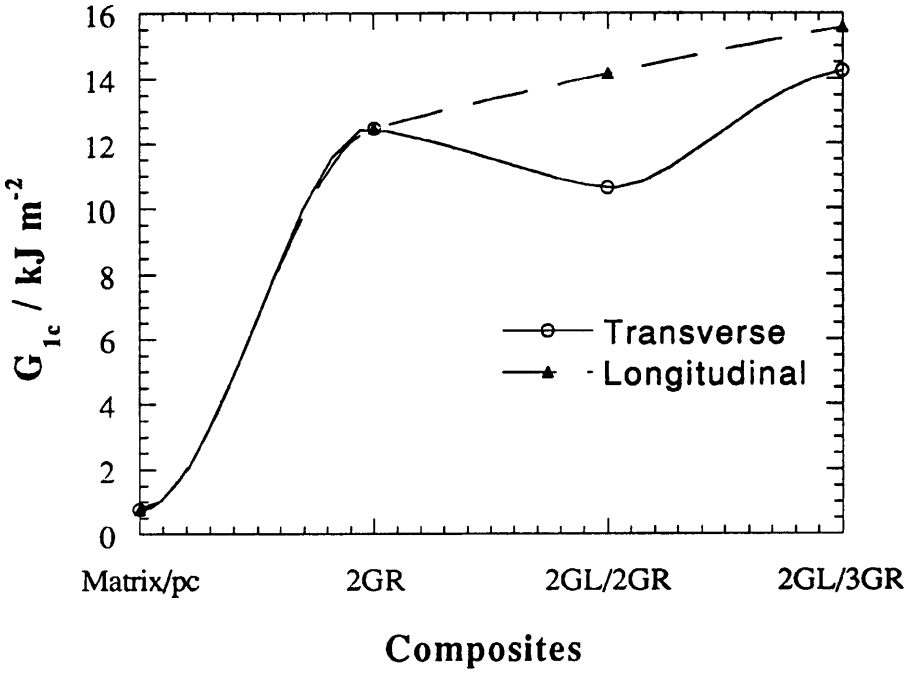

Figure 5.40 The effects of reinforcement mats and force direction on the values of G_{Ic} of SRIM composites

continuous, random reinforcement mats (2GR). However further incorporation of unidirectional mats produced only a gradual increase in G_{Ic} for the longitudinal specimens, and in the case of transverse specimens, G_{Ic} decreases from 12.5 (2GR) to 10.6 (2GL/2GR) kJ m^{-2} before increasing to 14.2 (2GL/3GR) kJ m^{-2}.

The fibre pull-out fracture mechanism dominates the fracture of SRIM composites as confirmed by the SEM of SENB fracture surfaces in Figs.5.41 and 5.42. Thus debonding of fibre-matrix interfaces, post-debonding friction and fibre breakage are the major contributions to G_{Ic} of SRIM composites, in contrast to the fracture work of the matrix which makes only a miner contributions to the value of G_{Ic} of SRIM composites.

In general, cracks in composites follow the path of least resistance during propagation. In the case of the SRIM composites containing only random mats, the crack

path was quite uneven, unlike that in unfilled matrix, in which the path was linear in direction perpendicular to the force direction. Comparative crack propagation paths are shown in Fig 5.43a and 5.43b. Addition of unidirectional mats as the outer layers of SRIM composites constrained the crack path, so that the crack path was essentially linear again perpendicular to the force direction. For longitudinal specimens of SRIM hybrid composites made with outer layers of unidirectional mats and inner layers of random mats, outer unidirectional fibres were broken first as crack growth initiated. Thus, fracture of the unidirectional fibres dominated the crack growth initiation. This explains why the G_{Ic} of 2GL/3GR (15.6 kJ m^{-2}) is only slightly higher than that of 2GL/2GR (14.2 kJ m^{-2}), which was much lower than expected. Fig.5.44 shows that around the tip of crack, the fibres of outer layer unidirectional mats were debonded and broken.

The outer layer unidirectional mats result in more voids in SRIM composites (see Chapter 4). And for transverse SRIM composite specimens, there are more fibre-matrix interfaces parallel to force direction, which decrease the toughness of composites. That is reason that the G_{Ic} of 2GL/2GR (10.6 kJ m^{-2}) was slightly lower than that of 2GR (12.5 kJ m^{-2}) in transverse direction, but it was expected that the G_{Ic} of 2GL/3GR (14.2 kJ m^{-2}) was much higher than that of 2GL/2GR in transverse direction. Fig.5.45 shows clearly how a crack propagation through a transverse SRIM composite specimen.

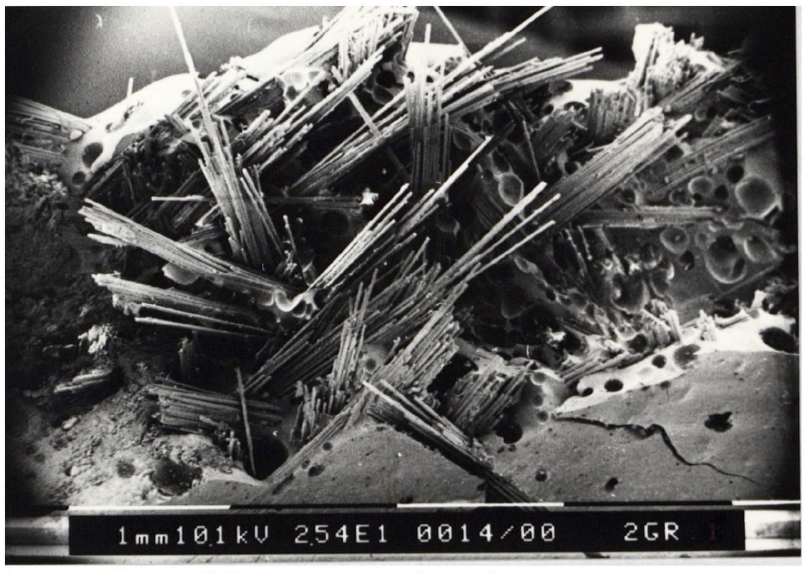

Figure 5.41 Fractography of SRIM composites of 2GR

A: Longitudinal

B: Transverse

Figure 5.42 Fractography of SRIM composites of 2GL/2GR

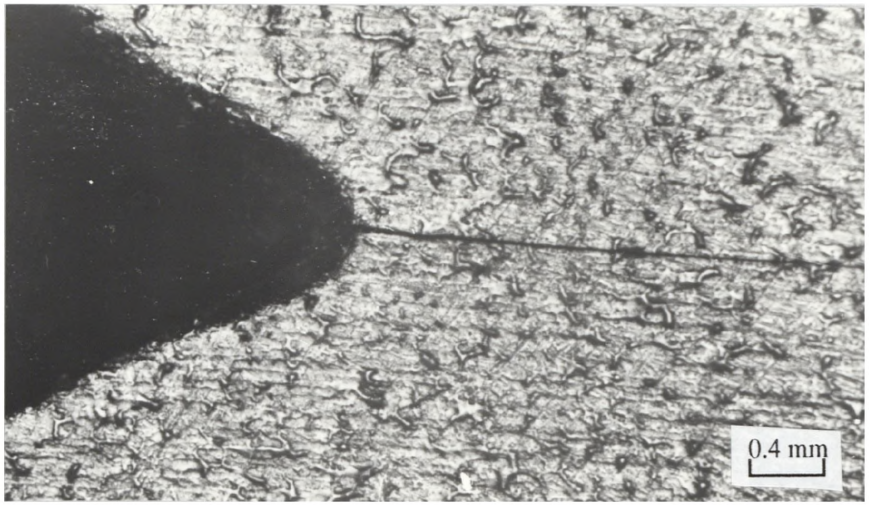

a: Matrix

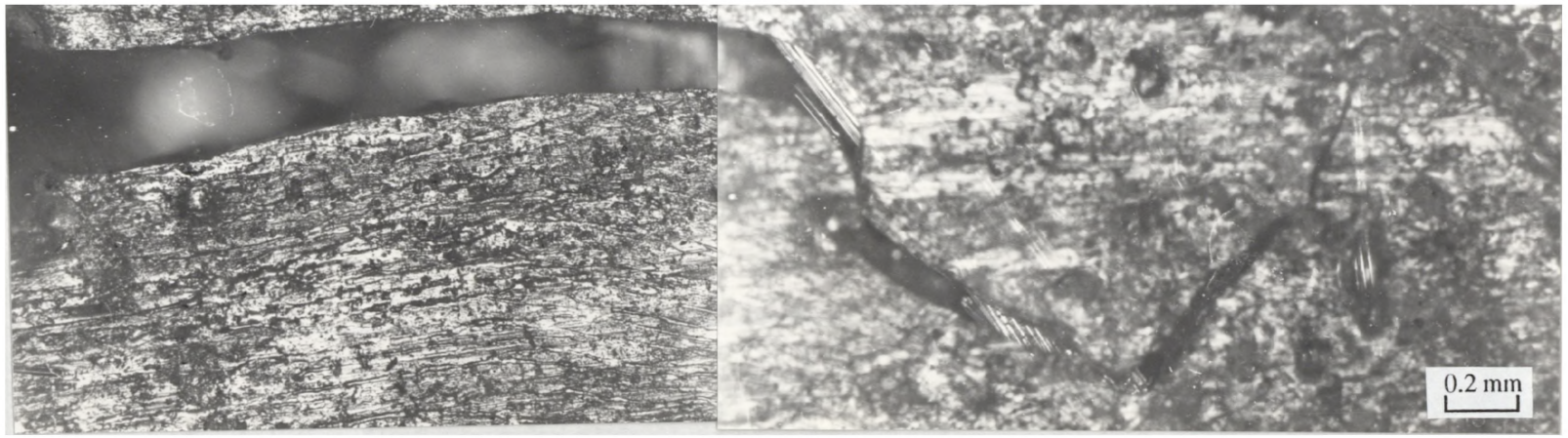

b: 2GR

Figure 5.43 Crack propagation path in SENB specimens, (a) unfilled D2/M/0.6 matrix and (b) 2GR SRIM composite.

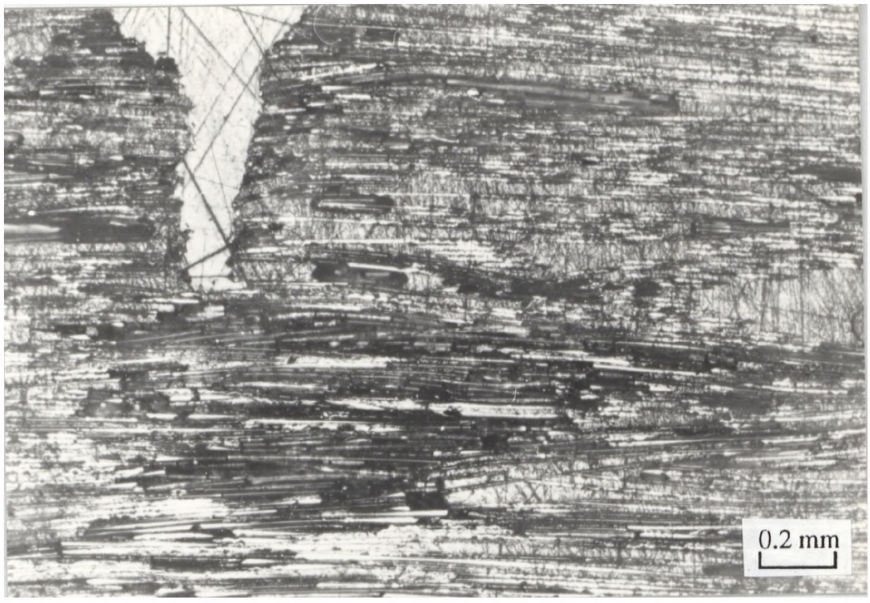

A: Lower magnification

B: Higher magnification

Figure 5.44 Damaged zone around the tip of the crack in a longitudinal specimen of 2GL/2GR

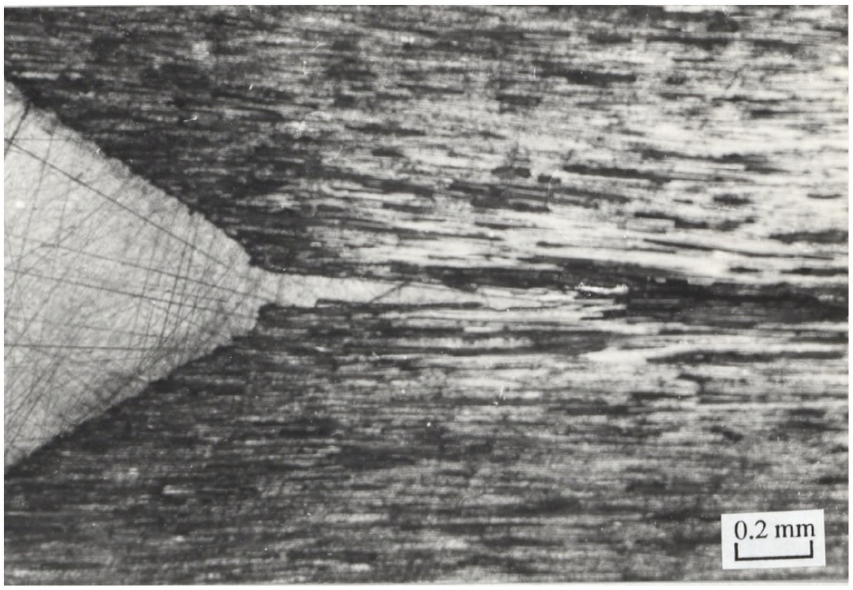

A: Lower magnification

B: Higher magnification

Figure 5.45 Crack propagation path in a transverse specimen of 2GL/2GR

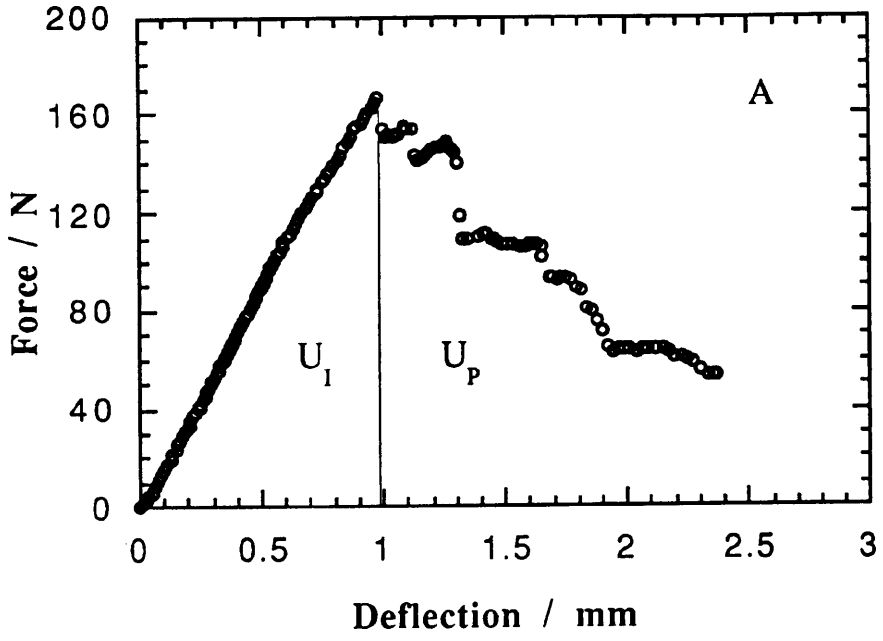

Figure 5.46 A force-deflection curve from SENB tests on a typical SRIM composite, 2GR

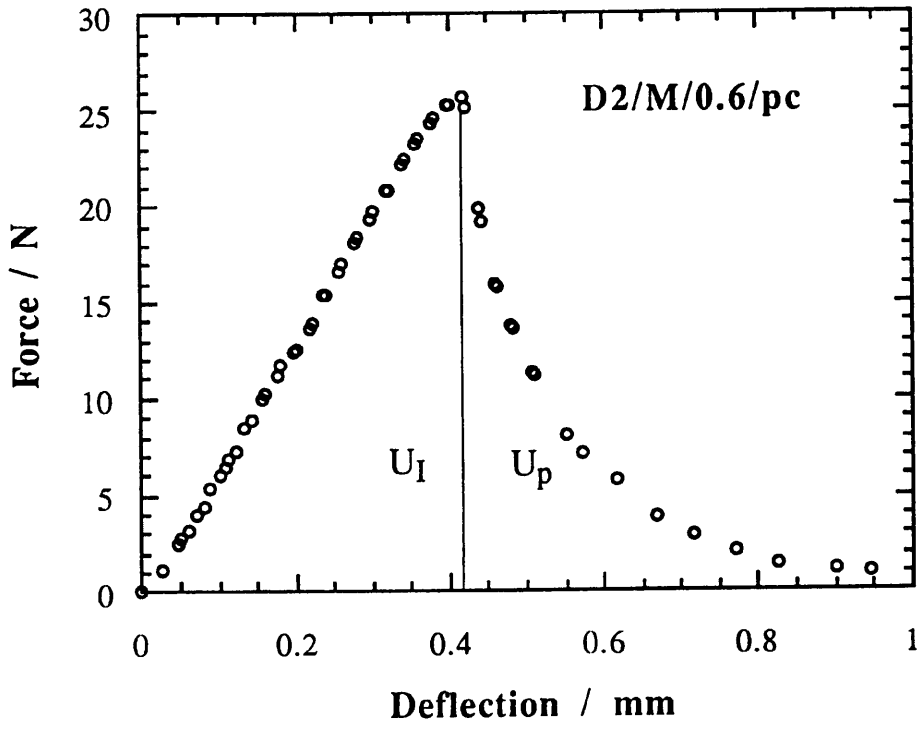

Figure 5.47 A force-deflection curve from SENB tests on the matrix, D2/M/0.6/pc

Not only is there a significant increase in the value of G_{Ic} on incorporating continuous reinforcements, but there is also significant resistance of SRIM composites to crack propagation (after peak force) compared with matrix. Fig.5.46 shows a typical force-deflection curve from SENB fracture tests for SRIM composites, in which U_I is the energy up to crack initiation, and Up the energy for subsequent crack propagation. It is very clear that after crack initiation, significant energy is still required for crack propagation. This is especially true for SRIM hybrid composites loaded in the longitudinal direction, in which the outer layers of unidirectional mats dominate crack initiation, whereas the inner layers of random mat dominate crack propagation. By comparison, the matrix (see Fig.5.37), after crack initiation, required little energy to propagate the crack, and the material failed almost immediately.

In order to study the effect of fibre surface treatment on the fracture properties of SRIM composites, SENB fracture tests were also carried out on the SRIM composites reinforced with untreated fibres and with the fibres coated with 0.5% silane aqueous solution, and the results are given in Tables 5.8 and 5.9. Comparison of the values of G_{Ic} in Table 5.8, and in Table 5.9 shows that fibre surface treatment increases the values of G_{Ic} of SRIM composites slightly in both longitudinal and transverse directions.

The SEM photograph in Figure 5.48 shows a bundle of pull-out fibres in the fracture surface of 2GR (control), in which the reinforcement mats were not coated with silane. The fibre surfaces in Fig.5.48 are essentially clean, which suggests that debonding occurred along the matrix-fibre interface, compared to the fibre surfaces from the fracture surfaces of 2GR/0.1 and 2GR/0.5 shown in Fig.5.49, in which reinforcement mats were coated, respectively, with 0.1% and 0.5% silane aqueous solutions. Figure 5.49 shows there to be significant residual resin and hackle marks [236] on the fibre surfaces, which suggests that some of debonding occurred within the matrix, but close to the matrix-fibre interfaces. Thus more fracture energy is required, and value of G_{Ic} of SRIM composites are increased with fibre surface treatment.

Table 5.8 The effects of silane treated fibres on K_{Ic} and G_{Ic} of SRIM composites. Data are for longitudinal direction.

Composites	K_{Ic} / MPa $\sqrt{m}$			G_{Ic} / kJ m^{-2}		
	Control	0.1%	0.5%	Control	0.1%	0.5%
2GR	4.9 ± 0.59	5.5 ± 0.6	5.6 ± 1.1	10.8 ± 2.6	11.8 ± 2.0	12.1 ± 2.0
2GL/2GR	7.3 ± 1.1	8.2 ± 0.48	7.3 ± 0.71	13.6 ± 3.0	14.2 ± 2.3	13.5 ± 3.2
2GL/3GR	9.5 ± 1.4	10 0 ± 1.4	10.2 ± 0.9	14.7 ± 1.6	15.6 ± 1.6	18.5 ± 3.1

Table 5.9 The effects of silane treated fibres on K_{Ic} and G_{Ic} of SRIM composites. Data are for transverse direction.

Composites	K_{Ic} / MPa $\sqrt{m}$			G_{Ic} / kJ m^{-2}		
	Control	0.1%	0.5%	Control	0.1%	0.5%
2GR	5.1 ± 0.65	5.8 ± 0.47	5.7 ± 1.3	11.0 ± 2.4	12.5 ± 1.6	12.2 ± 4.3
2GL/2GR	4.6 ± 0.40	5.3 ± 0.66	4.8 ± 0.51	10.4 ± 0.7	10.6 ± 1.9	11.9 ± 1.6
2GL/3GR	7.4 ± 1.1	8.1 ± 0.73	9.5 ± 0.83	14.4 ± 2.8	14.2 ± 3.0	17.5 ± 2.4

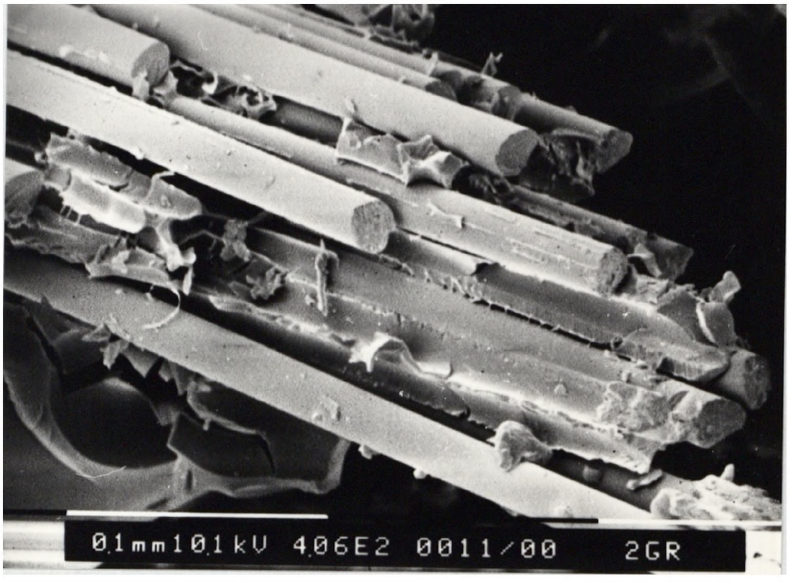

Figure 5.48 A SEM micrograph of part of the fracture surface of 2GR (control), showing a bundle of pull-out fibres.

A: 2GR/0.1

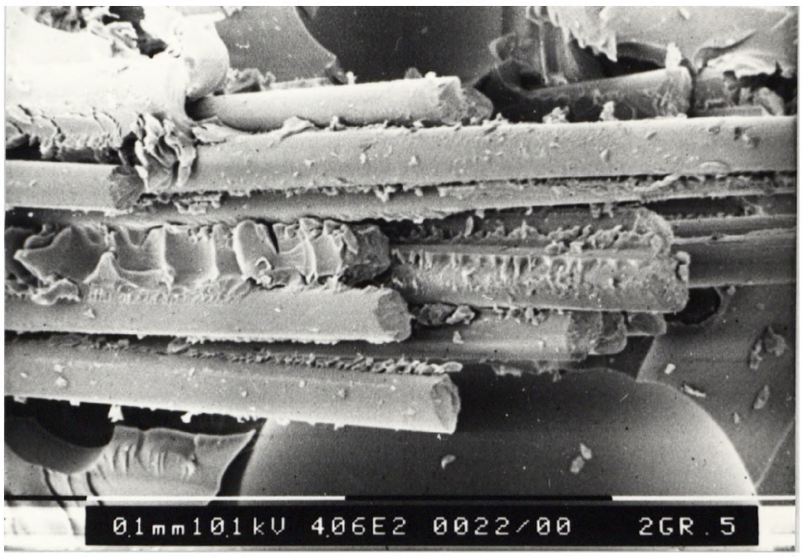

B: 2GR/0.5

Figure 5.49 SEM micrographs of parts of the fracture surfaces of 2GR/0.1 and 2GR/0.5, showing bundles of pull-out fibres.

For longitudinal specimens of carbon-glass hybrid SRIM composites, the carbon fibres were damaged during SENB testing. Damage occurred before crack initiation, caused by compression due to the very poor compressive properties of carbon fibres. For transverse specimens of carbon-glass hybrid SRIM composites, the inner layers of random glass mats dominated the fracture toughness of SRIM hybrid composites, and the values of G_{Ic} and K_{Ic} obtained were similar to those for transverse specimens of glass-glass hybrid SRIM composites. The experimental results are given in Table 5.10.

Table 5.10 Values of K_{Ic} and G_{Ic} results obtained from transverse specimens of carbon-glass hybrid SRIM composites

Composites	V_f / %	K_{Ic} / MPa $\sqrt{m}$		G_{Ic} / kJ m^{-2}	
		Control	0.1%	Control	0.1%
2CL	11	4.9 ± 0.59	5.8 ± 0.47	10.8 ± 2.6	12.5 ± 1.6
2CL/2GR	17	4.4 ± 0.95	6.4 ± 0.90	9.9 ± 3.6	12.7 ± 1.8
2CL/3GR	23	7.1 ± 1.2	7.6 ± 1.3	12.9 ± 2.6	13.9 ± 3.6
2CL/3GR	27	(a)	9.1 ± 1.6	(a)	14.3 ± 3.7

(a) not determined

5.5 Summary and Conclusions

The mechanical properties of the matrix are significantly enhanced by incorporating carbon, glass and Kevlar fibre reinforcements. By using a hybrid lay-up structure, the matrix is reinforced in all directions by the inner layers of randomly-oriented, glass-fibre reinforcements, and is strengthened in a designed direction by the outer layers of unidirectional fibre reinforcements. For SRIM composites containing 7% (v/v) unidirectional glass fibres and 26% (v/v) randomly oriented glass fibres, the modulus and tensile strength of SRIM composite are 11 GPa and 284 MPa, respectively, in the longitudinal direction, which are 700% and 500% higher than those of the matrix, and are 8 GPa and 165 MPa respectively in the transverse direction, which are 500% and 300% higher than those of the matrix. The modulus and tensile strength of the matrix is only 1.5

GPa and 56 MPa, respectively. The reinforcing effect of carbon fibres is even better. For the SRIM hybrid composite containing 13% (v/v) unidirectional carbon fibres and 17% randomly oriented glass fibres, the modulus and tensile strength of the composite are 26 GPa and 422 MPa, respectively, in the longitudinal direction, which are 1700% and 800% higher than those of the matrix.

A composite laminate model was successfully developed in section 5.3.2 to predict the tensile strengths and moduli of SRIM composites. Values of composite tensile strengths were calculated using the derived equations of Eq(5.17a) and (5.17b), respectively, for longitudinal and transverse specimens. The calculated values of transverse tensile strength fit experimental data well for both glass-glass and carbon-glass hybrid SRIM composites. However, calculated values of longitudinal tensile strengths only fit experimental data well for glass-glass hybrid SRIM composites, and are higher than the experimental data for carbon-glass hybrid SRIM composites. This is attributed mainly to the lower failure strain of carbon fibres. Values of composite tensile moduli were calculated using the derived equations of Eq(5.18a) and (5.18b), respectively, for both longitudinal and transverse specimens. The calculated values of transverse tensile moduli fit experimental data well for both glass-glass and carbon-glass hybrid SRIM composites. However, the calculated values of longitudinal tensile moduli were higher than the corresponding experimental data. In some cases, slightly disorientation of the unidirectional fibres in the outer layers resulted in localised buckling of the unidirectional fibres during deformation of apparently unidirectional specimens.

The fracture toughness, G_{Ic}, of matrix (0.76 kJ m^{-2}) is significantly increased by fibre reinforcement, despite the brittleness of glass fibres (G_{Ic} = 0.8 kJ m^{-2}). For instance, for the 2GL/2GR SRIM composites, G_{Ic} in the longitudinal and transverse directions are 14 kJ m^{-2} and 11 kJ m^{-2} respectively, which are 1700% and 1300% higher than that of the matrix.

As the volume fraction of fibre reinforcements increases, the in-plane shear strength of SRIM composites increases probably due to the decrease in void content. Fractography

showed that fibre-matrix interfacial bonding is improved by surface treatment of fibres with silane. However, the in-plane shear strength and fracture toughness, are increased only slightly, due probably to the high volume fraction of voids in the SRIM composites. Experimental results also showed that the surface treatment of fibres with silane had little effect on tensile properties of SRIM composites, again due probably to high volume fraction of voids in SRIM composites.

CHAPTER SIX

CONCLUSIONS AND SUGGESTIONS FOR FUTURE WORK

6.1 Conclusions

Novel copoly(isocyanurate-urea)s, PUrI, have been produced by reaction injection moulding, RIM. The materials were formed from ≈ 2:1 weight ratio of polyisocyanate to amine-functionalised polyoxypropylene, POP, in the presence of an organic trimerisation catalyst (TMR), a quaternary ammonium carboxylate. Diamine- and triamine-POP, namely, D2000 and T5000 (M_n~2,000 and 5,000 g mol^{-1} respectively) were used and the polyisocyanate, Isonate M143, was based on 4,4'-diphenylmethane diisocyanate. In some cases an aromatic diamine chain extender, either 3,5-diethyltoluene diamine, DETDA, or methylene-bis-2,6-diisopropylaniline, MDIPA, was also used. Stoichiometric ratios, [NCO] / [NH_2], ranged from 7 to 30, and the reactant and mould temperatures used in RIM were 36 and 90 °C, respectively. Gel times were controlled by varying the catalyst concentration, and gel times as short as 5 s were achieved at 90 °C. Nine PUrI materials produced by RIM have been studied in terms of the rheological behaviour of the reactants used, the reaction kinetics, and the mechanical and dynamic mechanical-thermal properties of the PUrI materials.

Structural composites comprising a PUrI matrix and pre-placed mats of continuous-fibres were produced by RIM in cycle times of < 60 s. The mould temperature was 90 °C and SRIM composites were postcured at 150 °C for 1 hour. The matrix (D2/M/0.6), formed from M143 and D2000, showed the best combination of thermal and mechanical properties, and met the basic SRIM processing characteristic of low initial viscosity during mould filling, essential for minimising fibre mat movement whilst maximising mat penetration and fibre wetting by the PUrI reacting mixture. Various hybrid SRIM composites with fibre contents up to 40 % by volume were produced with single outer layers of unidirectional-fibre mats of either glass, carbon or Kevlar, and different numbers of inner layers of random-fibres of only glass. The fracture, mechanical, mechanical-thermal and thermal expansion properties of the SRIM composites have also been studied.

6.1.1 Rheology of Reactant Blends and Reaction Kinetics of the RIM Process

The reactant blends used to form PUrI were characterised in terms of their rheological behaviour. This provided the data necessary for calculating Reynolds number (Re), the parameter used to define the efficiency of impingement mixing prior to mould filling during RIM processing, and also provided the data necessary to assess the penetration of the pre-placed reinforcements mats by reactant mixtures during SRIM processing. The rheological measurement of reactant blends were carried out with a parallel-plate fixture (Fig. 2.9). The study showed that addition of the chain extenders, DETDA and MDIPA, increased the viscosities of polyamine blends, designated T5/20D, D2/20D, D2/20MD, due to increases in molecular interactions between amines and ether oxygens. Increasing molecular weight or changing molecular structure (from linear to branched) of the polyamine also increased the viscosities of the blends. Viscosity was shown to be an important parameter in RIM processing, and the viscosities of reactant blends decreased in a decreasing order of T5/20D > T5 > D4 > D4-D230 > D2/20MD > D2/20D > D2, and the value of Re increased in an increasing order of T5/20D < T5 < D4 < D4-D230 < D2/20MD < D2/20D < D2. The value of viscosity was used to assess penetration of reactant mixtures into pre-placed mats, and penetration followed the increasing order T5/20D < T5 < D4 < D4-D230 < D2/20MD < D2/20D < D2.

The reaction kinetics of PUrI formation during RIM processing have also been studied by an adiabatic temperature rise (ATR) technique. Based on an energy balance approach for the reactions involved, equations were developed to calculate the fractional conversion of the limiting reactant and the heats of reaction for the case of n sequential reactions. The equations derived to analyse the ATR experimental data were as follows:

$$\alpha = (\alpha_j - \alpha_{j-1}) \frac{a\,(T - T_{j-1}) + \frac{b}{2}(T^2 - T_{j-1}^2)}{a\,(T_j - T_{j-1}) + \frac{b}{2}(T_j^2 - T_{j-1}^2)} + \alpha_{j-1} \qquad t_{j-1} < t \leq t_j \qquad (6.1)$$

$$-\Delta H_j = \frac{\rho}{(\alpha_j - \alpha_{j-1})\, C_o} [a\,(T_j - T_{j-1}) + \frac{b}{2}(T_j^2 - T_{j-1}^2)] \qquad (6.2)$$

where α, α_{j-1}, α_j are the fractional conversions of the limiting reactant at times t, t_{j-1}, t_j, respectively; t_{j-1} and t_j are, respectively, the initial and final times of the jth reaction, where j=1, 2.....n; α_o(=0) and α_n(=1) are, respectively, initial and final conversions. T, T_{j-1} and T_j are, respectively, adiabatic temperatures at times t, t_{j-1}, t_j; T_n, the temperature rise for the final reaction corresponds to the measured (total) maximum adiabatic temperature, T_{ad}. ΔH_j is the heat of reaction of the jth reaction, ρ is the density of reactant mixture, C_o is the concentration of limiting reactant, and a and b are constants. The two equations were successfully applied to the present systems. The analysis results of ATR data showed that copolymerisation occurred via a two-step (or three-step) process involving rapid polyether-urea, soft segment (SS) formation followed by NCO-trimerisation to form a glassy polyisocyanurate, hard segment (HS) phase. The T5-based reaction systems had longer gelation times than D2-based systems. Increasing the molecular weight distribution of the polyamine as in D4-D230 blend, or adding chain extenders to D2, increased the gelation times of the reaction systems. However, for T5-based systems, adding chain extender had little effect on gelation times. The reaction kinetics studies showed that for all PUrI reaction systems, very low fractional conversions of isocyanate groups were achieved during initial stages, which therefore limited the viscosity build-up during initial stages of the RIM process. This control of the viscosity-time profile was shown to be very important for the successful production of SRIM composites.

6.1.2 Structure-Property Relationships in Block Copoly(urea-isocyanurate)s

The structures and morphologies of PUrI materials were studied using DMTA, TEM, and SAXS, and were shown to significantly influence materials properties. The PUrI were characterised by a non-equilibrium morphologies which resulted from the competition between polymerisation kinetics, chemical gelation and (micro)phase separation occurring during RIM processing. DMTA confirmed the existence of a (micro)phase separated morphology, the scale of which was determined by TEM and SAXS. The degree of segmental mixing, inferred from the DMTA modulus-temperature

dependence between polyether (≈ -50 °C) and isocyanurate (160-200 °C) glass transition temperature, was in good agreement with that measured by the invariant Q' from SAXS. The addition of chain extenders DETDA, especially MDIPA made PUrI more thermally stable and tougher. The functionality of the polyamine had a tremendous effect on the morphology of PUrI and, therefore, on their properties. TEM studies showed D2/M/1.6 system (formed using linear polyether diamine) to possess an isotropic, co-continuous morphology (1-d ≈ 100 Å) comprising soft-segments and hard-segments, and was therefore much stiffer (E = 1.4 GPa) and more mechanical-thermal stable (E'(-50 °C) / E'(200 °C) = 5.5) than T5/M/1.6 (formed using branch polyether triamine) system (E = 0.7 GPa, and E'(-50 °C) / E'(200 °C) = 6.8), which had a morphology comprising a continuous soft-segmental phase with a random distribution of spherical hard-segmental inclusions. The morphology and properties of D2/M/0.6 PUrI were also affected by annealing (150 °C / 1 hr, 180 °C / 1 hr, 200 °C / 1 hr). Tensile stress-strain data showed that annealing increased Young's modulus (from 1.26 to 1.45 GPa) and reduced ultimate elongation (from 10% to 8.7%), due to increase in crosslinking density. The DMTA (sharper and higher γ (T_g^s) peaks), in good agreement with the SAXS (Q' increased from 180 to 257) and TEM(clearer definition of morphology), showed enhancements of phase purity on annealing.

6.1.3 Processing, Thermal and Mechanical Properties of SRIM Composites

The PUrI system, D2/M/0.6, was shown to have low initial viscosity during RIM processing, better thermal and mechanical properties, compared with T5-, DETDA- and MDIPA- based systems. D2/M/0.6 was therefore selected to be the matrix resin for SRIM composites. SRIM composites were successfully processed with total fibre volume fractions up to 38%, using randomly-oriented continuous glass fibres as inner layers, and hybrid combinations of unidirectionally oriented glass fibres, carbon fibres, or Kevlar fibres as outer layers.

The mechanical-thermal stability of matrix was remarkably enhanced by the reinforcements. Heat sag study showed that at the experimental condition of overhang of

200 mm, experimental temperature of 200 °C and heating time of 1 hr, the heat sag of hybrid SRIM composites were negligible, in contrast with the heat sag of 25.49 mm of the matrix, which indicates the significant improvement on the mechanical-thermal stability of the matrix. The same conclusion was reached by DMA study, in which the modulus-temperature dependence of matrix was reduced from 7.7 to 1.6 by the reinforcements in the temperature rang of -30 °C to 200 °C in the longitudinal direction. The DMA study also showed that the storage modulus of matrix was greatly enhanced by unidirectional mats in the longitudinal direction in the order carbon fibre > Kevlar fibre > glass fibre (which was in good agreement with tensile testing results), which was consistence with the modulus order of those fibres. The γ peak (T_g^S) of matrix was shifted to higher temperature by fibre reinforcements, especially by carbon fibre reinforcements, probably due to decreasing phase separation and inhibiting molecular motion of the matrix. The mechanical-thermal stability and energy dissipation of the matrix were also significantly improved by fibre reinforcements in the order, glass fibre > carbon fibre > Kevlar fibre. The thermal expansion study showed that the value (85 x 10^{-6} K^{-1}) of CLTE of the matrix at the temperature below 110 °C was much lower than the value (122 x 10^{-6} K^{-1}) above 110 °C, due to the existence of ß transition. However for SRIM composites, the difference between them was slight. The CLTE values (9 to 32 x 10^{-6} K^{-1}) of SRIM composites were 300 to 700% lower than that of the matrix, and matched the CLTE values of Aluminium, Copper, Iron and Steel as the fibre volume fraction, fibre type and sampling direction varied. The moisture also has effect on CLTE of all the SRIM composites and matrix.

The mechanical properties of matrix were also significantly enhanced by carbon fibre, glass fibre and Kevlar fibre reinforcements. By means of hybrid lay up structure, matrix was reinforced in any direction by the inner layers, randomly oriented fibre reinforcements, and was strengthened in a particular direction by the outer layers, unidirectional fibre reinforcements. For the SRIM composite containing 7% (v/v) unidirectional glass fibres and 26% (v/v) randomly oriented glass fibres, the modulus and tensile strength of SRIM composite were 11 GPa and 284 MPa respectively in longitudinal

direction, which were 700% and 500% higher than those (1.5 GPa and 56 MPa) of the matrix, and were 8 GPa and 165 MPa respectively in transverse direction, which were 500% and 300% higher than those of the matrix. The reinforcing effect of carbon fibres was even better in the longitudinal direction. For the SRIM hybrid composite containing 13% (v/v) unidirectional carbon fibres and 17% randomly oriented Glass fibres, the modulus and tensile strength of the composite are 26 GPa and 422 MPa, respectively, in longitudinal direction, which were 1700% and 800% higher than those of matrix. A composite model was developed in section 5.3.2 to calculate the tensile strengths of hybrid SRIM composites. The following equations were derived from the model:

$$\sigma_l = \sigma_{uf}\,\phi_{uf} + \sigma_{2D}(\phi_{rf}, \phi_m) \tag{6.3}$$

$$\sigma_t = \sigma_{2D}(\phi_{rf}, \phi_m) \tag{6.4}$$

$$\sigma_{2D} = \frac{P}{B\,A} = \frac{1}{n}\Sigma\,\sigma_j \qquad j = 1, 2, ...n\text{-}1 \tag{6.5}$$

$$\sigma_j = \sqrt{\frac{1}{f(\phi_f, \phi_m, \frac{180}{n}j)}} \tag{6.6}$$

$$f(\phi_f, \phi_m, \theta) = \frac{1}{\sigma_\theta^2} = \frac{\cos^4\theta}{\sigma_0^2} + \left(\frac{1}{\tau^2} - \frac{1}{\sigma_0^2}\right)\cos^2\theta\,\sin^2\theta + \frac{\sin^4\theta}{\sigma_{90}^2} \tag{6.7}$$

where σ_l and σ_t were the tensile stress of SRIM composites in the longitudinal and transverse directions, respectively, σ_{uf} and ϕ_{uf} was the tensile stress and volume fraction of fibres of the unidirectional reinforcements; ϕ_m was volume fraction of matrix, $\phi_{rf} = \phi_f$ was fibre volume fraction of random reinforcements, $\theta = 180\,j / n$, n was 8 in the present study; $\sigma_0 = \sigma_{rf}\,\phi_{rf} + \sigma_m\,\phi_m$, σ_{rf} and σ_m were fibre tensile stress of random reinforcements and tensile stress of matrix respectively; τ was shear stress between fibres and matrix, and was equal to half value of σ_m in the present study. Eqs (6.3) and (6.4)

were applied to predict the tensile strengths of hybrid SRIM composites, and fitted experimental data

The transverse-cross fracture toughness, G_{Ic}, of matrix was measured by Single Edge Notched Bending test which was developed from William's protocol for plastics. The study showed that G_{Ic} of matrix was greatly improved by fibre reinforcements, mainly due to fibre bridging at the crack tip, fibre pulling out and breaking during crack initiation and propagation, in spite of brittleness of glass fibres (G_{Ic} = 0.8 kJ m^{-2}). For instance, for 2GL/2GR SRIM composite, its G_{Ic} in longitudinal and transverse directions were 14 kJ m^{-2} and 11 kJ m^{-2} respectively, which are 1700% and 1300% higher than that (0.8 kJ m^{-2}) of the matrix.

The effects of fibre surface treatment with silane was also studied. Although fractography showed that the fibre-matrix interface was much improved by surface treatment of fibre reinforcement with silane, the properties of SRIM composites were little improved, which was quite unexpected, maybe due to high volume fraction of Voids.

6. 2 Suggestions for Future Work

Following are a few suggestions for future work:

1. More work needs to be done to optimise formulations of D2-based PUrI, such as changing the stoichiometric ratio of isocyanate groups to amine groups, and the content of chain extender.

2. Measurements of the heats of reactions of M143 (diisocyanate) with D2000, MDIPA, DETDA, T5000 need to be made to compare with the values predicted by the kinetics model.

3. Some modification could be done on HP-15 RIM machine, for example, the recirculation system, in order to reduce the void contents in SRIM composites.

4. Other testing methods for fracture toughness, such as Compact Tension test, Single Edge Notched Four Point Bending test, could be used to measure the transverse-cross fracture toughness, G_{Ic}, of SRIM composites, in comparison with the results from Single Edge Notched Three Point Bending test used in the present study.

5. Appropriate fracture tests and fracture mechanics analysis need to be developed to provide more meaningful and absolute fracture properties in terms of specimen and test geometry-independent values of K_{Ic} and G_{Ic}.

REFERENCES

1. C. W. Macosko, RIM / Fundamental of Reaction Injection Moulding, Hanser Publisher, 1989.
2. L. J. Lee, Rubber Chem. Tech., 53, pp542–599, 1980
3. W. E. Becker, "Reaction Injection Moulding", Ed. Becker, Van Nostrand, USA, 1979.
4. C. Hepburn, "Polyurethane Elastomers", Applied Science, London, 1982.
5. J. A. Sneller, Modern Plast., 60, No 3, pp24–25, 1983.
6. J. Harreis, Kunststoffe, 59, pp398–402, 1969.
7. F. W. Pahl, K. Schluter, Kunststoffe, 61, pp540–544, 1971.
8. H. Wirtz, J. Cellular Plast., 2, pp324–330, 1966.
9. H. Wirtz, J. Cellular Plast., 5, pp304–309, 1969.
10. H. Piechota, Kunststoffe, 60, pp7–14, 1970.
11. W. E. Ranz, AIChE J., 25, 41, 1979.
12. S. D. Fields, E. L. Thomas, J. M. Ottino, Polymer, 27, 1432, 1987.
13. P. D. Wickert, C. W. Macosko, W. Z. Ranz, Polymer, 28, pp1105–1110, 1987.
14. S. C. Machuga, H. L. Midje, J. S. Peanasky, C. W. Macosko, W. E. Ranz, AIChE J., 34, 1988.
15. H. Boden, K. Schulte, H. Wirtz, Chapter 4 in 'Polyurethane Handbook', Ed. by G. Oertel, Hanser, Munich, FDF (1985).
16. German Patent 2007935 (1970), Krass–Maffei, A.G.
17. K. Schulte, US Patent 3 975 128 (1976).
18. J. A. Molnar (Jr), L. J. Lee, J. Appl. Polym. Sci., 37, 2295 (1989).
19. R. B. Bird, W. E. Stewart, E. L. Lightfoot, 'Transport Phenomena', Wiley, New York, USA (1960).
20. A. J. Ryan, Ph.D Thesis, Victoria University of Manchester, UK (1988).
21. L. T. Nguyen, N. P. Suh, Polym. Proc. Eng., 3 (1 & 2), 37 (1985).
22. D. J. Sandell, C. W. Mackosko, Polym. Proc. Eng., 3 (1 & 2), 57 (1985).
23. D. H. Sebastian, S. Baukobbal, Polym. Proc. Eng., 4 (1), 53 (1986).
24. M. Nelson, L. J. Lee, J. Appl. Polym. Sci., 37, 251 (1989).

25. J. L. Koenig, Adv. Polym. Sci., 54, 87–147 (1983).

26. E. B. Richter, C. W. Macosko, Polym. Eng. Sci., 18, (13), 1978.

27. R. E. Camargo, C. W. Macosko, M. Tinell, S. T. Wellinghoff, Polym. Comm., 24, (1983).

28. J. S. Osinski, Polym. Eng. Sci., 23, (13), 1983.

29. R. E. Camargo, Ph.D Thesis, University of Minnesota (1984).

30. H. Ishida, C. Scott, J. Polym. Eng., 6, (1–4), 208 (1986).

31. T. J. Hsu, L. J. Lee, Polym. Eng. Sci., 28, (15), 955–963 (1988).

32. W. P. Yang, C. W. Macosko, Makromol. Chem. Macromal. Symp., 25, 23–44 (1989).

33. R. E. Camargo, V. M. Gonzalez, C. W. Macosko, M. Tinell, Rubber Chem. Tech., 56, (4), 774–783 (1983).

34. S. D. Lipshitz, C. W. Macosko, J. Appl. Polym. Sci., 21, 2029–2039 (1977).

35. E. Broyer, C. W. Macosko, F. E. Critchfield, L. E. Lawler, Polym. Eng. Sci., 18, (5), (1978).

36. E. C. Steinle, F. E. Critchfield, J. M. Castro, C. W. Macosko, J. Appl. Polym. Sci., 25, 2317–2029 (1980).

37. M. C. Pannone, C. W. Macosko, Polym. Eng. Sci., 28, (10), (1988).

38. N. P. Vespoli, L. M. Alberino, A. A. Peterson, J. H. Ewen, Proc. SPI 29th Ann. Tech. Conf., Reno, Nevada (1985).

39. N. P. Vespoli, L. M. Alberino, J. H. Ewen, Polym. Proc. Eng., 3 (1–2), 127–147, (1986).

40. D. Nissen, R. A. Markovs, J. Elast. Plest. 15, 96 (1983).

41. M. C. Pannone, C. W. Macosko, J. Appl. Polym. Sci., 34, 2409–2432 (1987).

42. A. A. R. Sayigh, H. Ulrich and W. J. Farrissey, (Jr.), Chapter 5 in "Condensation Monomers", Ed. J. K. Stille and T. W. Campbell, Wiley, New York, 1972.

43. R. Richter and H. Ulrich, Chapter 17 in "The Chemistry of Cyanates and Their Thio Derivatives", Part 2, Ed. S. Patai, Wiley, New York, 1977.

44. D. H. Chdwick and T. H. Cleveland, Vol. 13, p789, in "Kirk Othmer Encyclopedia

of Chemical Technology", 3nd edn., Ed. M. Grayson and D. Eckroth, Wiley, New York, 1981.

45. K. Findeisen, K. Konig and R. Sundermann, Band E4, P738, in "Houben–Weyl Mothoden der Organischen Chemie", 4th edn., Ed. H. Hagemann, Thieme Verlag, Stuttgart, 1983.

46. J. H. Saunders and K. C. Frisch, Chapter 3 in "Polyurethanes Chemistry and Technology, Part 1 Chemistry", Interscience, New York, 1962.

47. J. H. Saunders and K. C. Frisch, Chapter 4 in "Polyurethanes Chemistry and Technology, Part 1 Chemistry", Interscience, New York, 1962.

48. Fabrizio Parodi, "Isocyanate–derived Polymers" in Comprehensive Polymer Science, Vol 5: Step Polymerization, Ed. G. Allen, J. C. Bevington, G. C. Eastmond, 1989, Pergamon Press.

49. L. M. Alberino, T. R. McClellan, "The future of RIM in the United State ", in Reaction Injection Moulding, Ed. J. E. Kresta, Am. Chem. Soc. Symp. Series 270, 1985

50. P. S. Carleton, J. H. Ewen, H. E. Reymore,"High–modulus polyisocyanurate elastomers", US Patents, 4,126,741 and 4,126,742, 1978.

51. P. S. Carleton, D. P. Waszecick, L. M. Alberino, "MM/RIM: RIM composite using preplaced reinforcement", Soc. Plast. Ind. Urethane Technical/Marcket Conf., 1985, p154–160.

52. N. A. Ward, MSc. Thesis, UMIST, 1989.

53. Don Nelson, 31st Intern. SAMPE Symp., April 7–10, 1986, p1049–1063.

54. C. L. Wang, D. Klempner and K. C. Frisch, J. Appl. Polym. Sci., Vol 30, 4337–4344, 1985.

55. C. L. Wang, D. Klempner and K. C. Frisch, Polym. Materials Sci. and Eng., 49, 38, 1983.

56. F. E. Kresta, K. H. Hsieh and C. L. Wang, RIM + FAST Polymerization Reactions, 1981, PST Series 18.

57. D. Klempner, K. C. Frisch and C. L. Wang, Adv. Ureth. Sci. tech., 1984, 9, p102–129.

58. A. J. Ryan and J. L. Stanford, "Polyureas" in Comprehensive Polymer Science, Vol 5, Step Polymerization, Ed. G. Allen, J. C. Bevington, G. C. Eastmond, 1989, Pergamon Press

59. J. H. Saunders, K. C. Frisch, "Polyurethanes: Chemistry and Technology; Part I and II, Interscience, New York, USA, 1962.

60. H. J. Twitchett, Chem. Soc. Rev., 3, 209, 1974.

61. H. R. Gillis, A. T. Hurst, L. J. Ferrarini, A. Watts, J. Elast. Plast., 16, 291, 1984

62. K. Schauertre, Chpt. 33 in "Polyurethane Handbook", Ed. G. Oertel, Hanser, Munich, FDR, 1985.

63. A. J. Birch, PhD Thesis, 1991, The University of Manchester.

64. R. W. Lenz, "Organic Chemistry of Synthetic High Polymers", J. Wiley, New York, USA, 1967.

65. G. Good, "Flexible Polyurethane Foams: Chemistry and Technoloy", Applied Science, UK, 1982.

66. Texaco Chemicals, U.S. Patent, 3 654 370, 1972.

67. R. E. Camargo, C. W. Macosko, M. Tirrell, S. T. Wellinghoff, Polym. Eng. Sci., 22, 719, 1982.

68. A. Damusis, T. B. Lin, Chpt. 5 in "Reaction Injection Moulding: Structure property Relationships in Polyurethanes", Ed. J. E. Kresta, Am. Chem. Soc., Washington, USA, 1985.

69. P. Koldodziej, W. P. Wang, C. W. Macosko, S. T. Wellinghoff, J. Polym. Sci. Polym. Phys., 24, 2395, 1986.

70. R. E. Camargo, J. S. Andrews, C. W. Macosko, S. T. Wellinghoff, Polym. Preprints, Aug., 294, 1984.

71. A. J. Ryan and J. L. Stanford, R. H. Still, Proceedings Rolduc polymer Meeting – 2, Holland, April 25, 1987.

72. J. P. Casey, W. F. Burgoyne, J. E. Lewis, J. Cell. Plast., 22, 464, 1986.

73. W. R. Willkomn, Z. S. Chen, C. W. Macosko, D. A. Gobran, E. L. Thomas, Polym. Eng. Sci., 28 (14), 888, 1988.

74. J. H. Ewen, J. Elast. Plast., 17, 281, 1985.

75. A. J. Ryan and J. L. Stanford, A. N. Wilkinson, Polym. Bull., 18, 517, 1987

76. W. R. Willkomn, Ph. D. Thesis, University of Minnesota, USA, 1990.

77. UK Patent, 1 148 454.

78. D. Nissen, R. A. Markovs, Proceedings Soc. Plast. Indu., 27th Ann. Tech/Mark. Conf., 1982.

79. J. L. Stanford, A. N. Wilkinson, D. K. Lee, A. J. Ryan, Plast. Rubb. Proc. Appl., 13(2), 111, 1990.

80. S. L. Cooper, A. V. Tobolsky, J. Appl. Polym. Sci., 10,1837, 1966.

81. A. J. Ryan, J. L. Stanford, R. H. Still, Plast. Rubb. Proc. Appl., 13(2), 99, 1990.

82. R. J. G. Dominguez, Polym. Eng. Sci., 21, (18), 1981.

83. A. J. Birch, J. L. Stanford, A. J. Ryan, Polym. Bull., 22, (5/6), 629–636, 1989.

84. L. H. Pebbles, Macromolecules, 7, 872, 1974.

85. P. J. Flory, J. Chem. Phys., 10, 51, 1942.

86. M. L. Huggins, J. Phys. Chem., 46, 151, 1942.

87. J. S. Higgins, Makromol. Chem. Macromol. Symp., 15, 201, 1988.

88. R. Koningsveld, Polym. Eng. Sci., 25 (7), 1118, 1985.

89. J. N. Owens, I. S. Gancarz, J. T. Koberstein, T. P. Russell, Macromolecules, 22, 3388, 1989.

90. A. J. Ryan, Polymer, 31, 707, 1990.

91. T. Hashimoto, Y. Tsukahara, K. Tachi, H. Kwai, Macromolecules, 16, 648, 1983.

92. A. J. Ryan, J. L. Stanford, X. Tao, "Morphology and Properties of Novel Copoly(isocyanurate–urea)s Formed by Reaction Injection Moulding", Summited to Polymer in April, 1992.

93. M. M. Cross, A. Kaye, J. L. Stanford, R. F. T. Stepto, "Rheology of polyols and polyol slurries for use in reinforced RIM" in Reaction Injection Moulding, Ed. J. E. Kresta, Am. Chem. Soc. Symp. Series 270: Washington D.C., 1985, p97–110.

94. P. D. Coates, A. I. Sivakumar, A. F. Johnson, Plast. Rubb. Proc. Appl., 1987, 7, p19–28

95. R. M. Gerkin, L. F. Lawler, E. G. Schwartz, J. Cell. Plast., 15, 51–58, 1979

96. J. Ferrarini, S. Cohen, Mod. Plast., 59 (10), 68–77,1982.

97. D. M. Rice, R. J. G. Dominguez, J. Cell. Plast., 19, 114–120, 1983.

98. G. H. Slocum, N. H. Nodelman, C. E. Fluharty, D. W. Schumacher, "Structural RIM: successful combination of RIM process and fiber reinforcement", Am. Soc. Mat., Adv. Composites Conf., Detroit, Nov., 1986.

99. M. Begemann, G. Menges, W. Michaeli, J. Cell. Plast., 25, 409–419, 1989.

100. V. M. Gonzalez, J. M. Castro, C. W. Macosko, "Reaction Injection Moulding Filling and Curing with situ Fiberglass Mats", Soc. Plast. Eng. Tech. Paper, 39:519 ff (1981).

101. G. K. Batchelor, "An Introduction to Fluid Mechanics", Cambridge University Press, Cambridge, UK, 1967.

102. G. O. Martin, J. S. Son, "Fluid mechanics of mould filling for fiber reinforced plastics", Am. Soc. Mat., Adv. Composites Conf., Dearborn MI, Nov., 1986.

103. M. J. Short and R. C. Rains, "Class A - structural RIM: Polyurethane Technology for Automotive Body Panel Applications", Processing of the Eight Annual ASM / ESD Advanced Composites Conference, Chicago, USA, 2-5 November 1992.

104. F. Hostettler, G. C. McCormick, Plastics Technology Associates Inc., Contract No. NSF–C–ERS77–19711, National Science Foundation 1978, U.S. Department of Commerce, National Technical Information Service, PB–278979.

105. R. J. G. Dominguez, D. M. Rice, Polym. Comp., 4 (3), 185–189, 1983.

106. D. Nelson, Plast. Eng., 43 (11), 29–32, 1987.

107. I. R. Kleinholz, PRI RRIM Conf., Solihull, UK (1981).

108. N. Barksby, J. L. Stanford, "Unpublished work" (1983).

109. R. D. Farris, H. E. De La Mare, R. H. Overcashier, W. G. Gottenberg, Polym. Plast. Technol. Eng., 21 (2), 129–157, 1983.

110. H. G. Waddill, 35th S.P.E. Ann Tech. Conf., Reinforced Plast. / Comp. Inst. SPE (1980).

111. R. H. Overcashier, W. G. Gottenberg, 37th S.P.E. Ann Tech. Conf., Reinforced Plast./Comp. Inst. SPE (1982).

112. K. L. Forsdyke, Paper 6, PRI RRIM Conf., Solihill, UK (1981).

113. G. L. Brode, W. F. Hale, US Pat. 4 403 066 (1983).

114. G. L. Brode, M. J. Michno, S. W. Chow, ACS Polym. Preprint, 24 (2), pp. 194~195, 1983.

115. T. C. Wilkinson, S. F. Chappel, W. L. Kelly, 6th SPI, Int. Tech. Mark. Conf., SPI, 1983.

116. T. C. Wilkinson, J. H. Eckler, Jnl. Elast. Plast., 18, (3), pp128~135, 1986.

117. Ashland Chemicals, Tech. data bulletin 1595, 1986.

118. J. Leadbitter, P. D. Coates, J. Cerotti, J. Hynds, F. Johnson, J. Ryan, 5th Int. Conf. Reactive Proc. Polym., University of Bradford, UK, 1985.

119. P. S. Carleton, D. P. Waszeciak, L. M. Alberino, J. Cell. Plast., Nov–Dec., 1985, p409–415.

120. A. N. Wilkinson, Ph. D. Thesis, UMIST, 1990.

121. G. M. Slocum, N. H. Nodelman, D. W. Schumacher, M. F. Hurley, Proc. 3rd SPE Ann. Conf. Adv. Comp., ASM Int., 1987.

122. G. Ferber, SPE Nat. Tech. Conf., 1979.

123. V. M. Gonzalez, C. W. Macosko, Polym. Comp., 4, 190–195, 1983.

124. R. Mohan, Proc. 3rd SPE Ann. Conf. Adv. Comp., ASM Int., 1987.

125. B. C. Mazzoni, P. Corradi, Polyurethane Would Congress, Aachen, FDR, SPI/FSK, pp. 865~872, 1987.

126. J. V. Scrivo, Proc. 3rd SPI Ann. Conf. Adv. Comp., ASM Int., 1987.

127. J. Burkus, U.S. Patent 2,993,870 (to U.S. Rubber Co.) (1961).

128. K. C. Frisch, K. J. Patel and R. D.Marsh, J. Cell. Plast. 6,203 -214 (1970).

129. H. E. Reymore, P. S.Jr, Carleton, , R. A. Kolakowskiand, A. A. R. Sayigh, J. Cell. Plast. 11, 328 - 344 (1975).

130. Daniel Cohn and Karl Lance, Polymer Communication, Vol.28, 226 -228, Aug. 1987.

131. P. S. Carleton, D. P. Waszeciak and L. M. Alberino, J. Cell. Plast. 409 - 416, 21,1985.

132. V. M. Gonzalaz, J. M. Castro and C. W. Macosco, "Proceeding of the 2nd Would Congress of Chemical Engineering", Montreal, Canada (October 4-9, 1981).

133. V. M. Gonzalaz, "Study of Reactive Polymer Processing with Fiber Glass Reinforcement", Ph. D. Thesis, University of Minnesota, USA (December 1983).

134. A. J. Ryan, R. H. Still and J. L. Stanford, Plast. Rubb. Proc., 13, p90, 1990.

135. A. J. Ryan. and J. L. Stanford, "pp427, Chapter 23, Volume 5 (Synthesis - Step Polymerization) in Comprehensive Polymer Science, Eds. Allen, G. and Bevington, J. C., Pergamon Press, Oxford, UK, 1988.

136. R. J. G. Dominguez, J. Cell. Plast., 20, p433, 1984.

137. Dow Chemical Company Limited, Middlesex UB11 1BE, Certificate of Analysis (Dow Ref. No. 704813) and Material Safty Data Sheet, May 1991.

138. A. J. Birch, M.Sc. / Ph. D. Transfer Report, Man. Mat. Sci. Cent., UMIST, 1988.

139. Lonza, A. G., Amine Tech. Data Sheet (1981).

140. G. C. Plane, J. L. Stanford and R. H. Still, Unpublished Work.

141. J. L. Stanford, R. H. Still and A. N. Wilkinson, Unpublished Work.

142. L. E. Nielsen, Polymer Rheology, Marcel Dekker, Inc. (1977).

143. D. D. Barksky, A. Kaye, J. L. Stanford. and R. F. T. Stepto, Chapter 6 in Reaction Injection Moulding: Structure Property Relationship in Polyurethances", Ed. J. E. Kresta, Am. Chem. Soc., Washington (1985).

144. F. W. Schneider, in "Reaction Injection Moulding and Fast Polymerization Reactions", Ed. J. E. Kresta, Am. Chem. Soc., Washington, USA (1985).

145. P. D. Coates, University of Bradford, UK, "Private Communication".

146. Texaco Chemical Company, Technical Services Bulletin, 1991.

147. L. M. Alberino, J. Appl. Polym. Sci., Vol. 23, pp2719 - 2727 (1979).

148. A. J. Birch, Research Report to Kobe Steel - UMIST, May - September 1990.

149. Vespoli, N.P., Alberino, L.M., *Polym. Process. Eng.*, 1985, **3**, 127.

150. Gibson, P.E., Vallance, M. A., Cooper, S.L. In *Developements in Block Copolymers-1*, Goodman, I., Ed. Applied Science, London,UK, 1982.

151. Abouzahr, S., Wilkes, G.L.,*Processing, Structure and Properties of Block Copolymers*, Ed. Folkes,M.J., Elsevier, New York, USA, 1985.

152. Ryan, A.J., Stanford, J.L., Wilkinson, A.N., PCT Patent Application #GB90/21917: filed for Kobe Steel Europe Limited, 9 October 1990.

153. Stagg, H.E., The Analyst, 1946,**71**, 557; ASTM D1638m

154. Baltá-Calleja, F.J., Vonk, C.G., *X-ray Scattering of Synthetic Polymers*, Elsevier, Amsterdam, The Netherlands, 1989.

155. Porod, G., *Kolloid-Z*, 1951, **124**, 83; 1952, **125**, 51; 1952, **125**, 108.

156. Cullity, D.B.pp127-131 in *Elements of X-ray Diffraction,* 2nd ed., Addison Welesly: Reading, UK, 1978.

157. Cahn, J.W., Hilliard, J.E., *J. Chem. Phys.*, 1958, **28**, 258.

158. Chen-Tsai, C.H.Y., Thomas, E.L., MacKnight, W.J., Schneider, N.S., *Polymer,* 1986, **27**, 659

159. Olabisi, O., Robeson, L.M., Shaw, M.T., *Polymer-Polymer Miscibility*, Academic Press, New York,USA, 1979.

160. De Gennes, P.G., *Scaling Concepts in Polymer Physics*, Cornell University Press, Ithaca, USA, 1979.

161. Helfand, E.; Waserman, Z.R.; In *Developements in Block Copolymers-1*, Goodman, I., Ed. Applied Science, London,UK, 1982.

162. Flory, P.J., *Principles of Polymer Chemistry*, Cornell University Press, Ithaca, USA, 1953.

163. E. J. Roche and E. L. Thomas, Polymer, 1981, vol. 22, March, p333-341

164. Heinso Company, Technical Data, 1990

165. Thermophysical Properties of Matter, Vol.12 (Thermal Expansion, Metallic Element and Alloys), 1975; and Vol.13 (Thermal Expansion, Nonmetallic Solids), 1977, New York, London, IFI / Plenum, distributed by Heyden.

166. ASTM Standards, D3846-79 (Reapproved 1985)

167. Protocols for Interlaminar Fracture testing of Composites, Polymer & Composites Task Group / European Structural Integrity Society, May, 1992

168. S. Lee and M. Munro, Composites, Vol. 17, No. 1, 1986, pp13 - 22.

169. ASTM Standards, D4255-83

170. ASTM Standards, D2344-84

171. ASTM Standards, D695-89

172. Zhang, S. Y.; Soden, P. D.; Soden, P. M.; Composites, Vol. 17, No. 2, April 1986, pp100 - 110

173. S. W. Tsai, Structural Behavior of Composite Materials, NASA Rept. CR-71, 1964

174. Z. Hashin and B. W. Rosen, J. Appl. Mech., 31E, 223 (1964)

175. Z. Hashin, AIAA J., 4, 1411 (1966)

176. Hermans, J. J.; Proc. Koninkl. Nederl. Akademie Van Wetenschappen, Amsterdam, 70B, 1 (1967)

177. J. M. Whitney, Textile Res. J., 37, 1008 (1967)

178. C. C. Chamis and G. P. Sendeckyj, J. Composite Mater., 2, 332 (1968)

179. S. W. Tsai, U. S. Dept. Commerce Rept. AD834851 (1968)

180. J. E. Ashton, J. C. Halpin, and P. H. Petit, Primer on Composite Analysis, Technomic, Stanford, Conn., 1969.

181. J. C. Halpin, J. Composite Mater., 3,732 (1969)

182. T. S. Chow and J. J. Hermans, J. Composite Mater., 3, 382 (1969)

183. B. W. Rosen, Proc. Royal Soc., A319, 79 (1970)

184. L. E. Nielsen, J. Appl. Phys., 41, 4626 (1970)

185. T. B. Lewis and L. E. Nielsen, J. Appl. Polymer Sci., 14, 1449 (1970)

186. S. W. Tsai, Mechanics of Composite Materials, Air Force Materials Lab. Rept. AFML-TR-66-149 (1966)

187. S. W. Tsai and N. J. Pagano, Composite Materials Workshop, S. W. Tsai, J. C. Halpin and N. J. Pagano, Ed., Technomic, Stanford, Conn., 1968, pp233.

188. Composite Materials Series, Vol. 2, Fibre reinforcement for Composite Materials, Ed. by A. R. Bunsell, Published by Elsevier, 1988.

189. Heinsco Ltd, Private communication, 1991.

190. L. E. Nielsen, Mechanical Properties of Polymer and Composites, Vol. 2, p466.

191. N. Sela, O. Ishai, and L. Banks-sills, Composites, Vol. 20, No. 3, May 1989, pp257-264.

192. K. K. Chawla, Composite Materials, p66

193. Jang–Kyo Kim, Yin–Wing Mai, Copm. Sci. Technol., 41, 333–378, 1991

194. B. Harris, Metal Science, 14, 351, 1980

195. J. O. Outwater, M. C. Murphy, Proc. 24th Conf. SPI, 1969, Paper 11C

196. M. C. Murphy, J. O. Outwater, Proc. 28th Conf. SPI, 1973, Paper 17A.

197. J. Cook, J. E. Gordon, Proc. Roy. Soc. Lond., A282, 508, 1964

198. T. U. Marston, A. G. Atkins, D. K. Felbeck, J. Mater. Sci., 9, 447, 1974

199. A. G. Atkins, J. Mater. Sci., 10, 819, 1975

200. A. Kelly, Proc. Roy. Soc. Lond., A319, 95, 1990

201. J. Tirosh, ASME Trans. E, J. Appl. Mech., 40, 758, 1973

202. A. S. Tetelman, Fracture Process in Fibre Composite Materials, ASTM STP–460, p473, 1969

203. M. R. Piggott, J. Mater. Sci., 5, 669, 1970

204. J. Fitz–Randolph, D. C. Phillips, P. W. R. Beaumont, A. S. Tetelman, J. Mater. Sci., 7, 289, 1972

205. A. H. Cottrell, Proc. Roy. Soc. Lond., A282, 2, 1964

206. A. Kelly, W. R. Tyson, J. Mech. Phys. Solids, 13, 329, 1965

207. A. Kelly, Strong Solids, Oxford University Press, Oxford, 1966

208. J. L. Helfet, B. Harris, J. Mater. Sci., 7, 494, 1972

209. P. Hing, G. W. Groves, J. Mater. Sci., 7, 427, 1972

210 G. R. Irwin, "Force Concepts in Relation to Fracture Behaviour of Composite Materials", Composite Materials Workshop, Ed. S. W. Tsai, J. C. Halpin, N. J. Pagano, 1968

211. N. J. Pagano,S. W. Tsai, "Introduction to Micro Mechanics", Composite Materials Workshop, Ed. S. W. Tsai, J. C. Halpin, N. J. Pagano, 1968

212. E. M. Wu, "Fracture Mechanics of Anisotropic Plates", Composite Materials Workshop, Ed. S. W. Tsai, J. C. Halpin, N. J. Pagano, 1968

213. M. E. Waddoups, "Characterization and Design of Composite Materials", Composite Materials Workshop, Ed. S. W. Tsai, J. C. Halpin, N. J. Pagano, 1968

214. O. Purslow, Composites, 241–247, Oct., 1981

215. O. Purslow, Composites, Vol. 19, No 2, 115–126, March 1988

216. O. Purslow, Composites, Vol. 19, No 5, 358–366, Sept., 1988

217. C. T. Herakovich, "Modeling Fracture of Resin Matrix Composites", Mechanics of Plastics and Plastics Composites, AMD–Vol. 104, Ed. V. K. Stokes, 1989

218. S. L. Donaldson, Composites, Vol. 16, No. 2, 103–112, April 1985

219. P. S. Hine, B. Brew, R. A. Duckett, I. M. Ward, Comp. Sci. Technol., 33, 35–71, 1988

220. S. Y. Zhang, P. D. Soden, P. M. Soden, Composites, Vol. 17, No. 2, 100–110, April 1986

221. K. Nikpur, Y. F. Chen, J. L. Kardos, Comp. Sci. Technol., 38, 175–191, 1990

222. J. J. Kolle, K. Y. Lin, C. C. M. Eastland, A. C. Mueller, Mechanics of Plastics and Plastics Composites, AMD–Vol. 104, Ed. V. K. Stokes, 1989

223. C. Bathias, R. Esnault, J. Pellas, Composites, 195–200, July 1981

224. W. D. Bascon, J. L. Bitner, R. J. Moulton, A. R. Siebert, Composites, 9–18, Jan. 1980

225. B. Harris, S. E. Dorey, R. G. Cooke, Comp. Sci. Technol., 31, 121–141, 1988

226. Griffith, A. A., Phil, Trans. R. Soc. H211 (1920) P163 - 198

227. Rook, D. P., Cartwright, D. J., Compendium of Stress Intensity Factors, HMSO (1976)

228. ASTM Standard E399 -- 83

229. A Linear Elastic Fracture Mechanics (LEFM) Standard For Determining K_C and G_C For Plastics, Testing Protocal -- March, 1990

230. Bakker, A., Inter. J. of Fatigue and Fracture of Eng. Mat. and Struc. (march 1989)

231. Hertzberg, R. W., "Fracture Surface Micromorphology in Engineering Solids" in Fractography of Modern Engineering Materials -- Composites and Metals, MASTERS/AU Editors, STP948, 1985

232. "Fracture Mechanics of Engineering Materials" Ed. by metal physics section of Beijing Iron and Steel Institute

233. Droutman, L. J., "Chapter 5 Fracture and Fatigue" in Composite Materials, Ed. by Droutman, L. J. and Krock, R. H., 1974

234. Cherepanov, G. P., Mechanics of Brittle Fracture, 1974

235. Harris, B., Dorey, S. E. and Cooke, R. G., "Strength and Toughness of Fibre Composites", Composites Science and Technology, 31(1988) 121 --141

236 Morris, G. E., "Determining Fracture Directions and Fracture Origins on failed Graphite/Epoxy Surface, in Nondestructive Evaluation and Flaw Criticality for Composite Materials, STP696 (American Socioty for Testing and Materials, PA,1979) P.274